# Synthesis and modeling of III-As nanowires by SAG-HVPE : towards infrared and energy conversion devices

Emmanuel Chereau

**UNIVERSITE CLERMONT AUVERGNE**

**ECOLE DOCTORALE DES SCIENCES FONDAMENTALES**

# THESE

présentée pour obtenir le grade de

## DOCTEUR D'UNIVERSITE

*Spécialité : Milieux denses et matériaux*

Par CHEREAU Emmanuel

# Synthesis and modeling of III-As nanowires by SAG-HVPE: towards infrared and energy conversion devices

Soutenue publiquement le 15 mars 2024 devant le jury :

| | |
|---|---|
| **Mme. Laurence MECHIN**<br>Directrice de recherche, GREYC, Caen | Président du jury |
| **M. Ludovic DESPLANQUE**<br>Maitre de conférences HDR, IEMN, Lille | Rapporteur |
| **M. Guillaume SAINT-GIRONS**<br>Directeur de recherche, INL, Lyon | Rapporteur |
| **M. Gabin GREGOIRE**<br>Ingénieur de recherche, III-V Lab, Palaiseau | Examinateur |
| **Mme. Yamina ANDRE**<br>Maitre de conférences HDR, Institut Pascal, Aubière | Directeur de thèse |
| **M. Ray LAPIERRE**<br>Professeur des universités, McMaster University, Canada | Co-directeur de thèse |
| **Mme. Evelyne GIL**<br>Professeur des universités, Institut Pascal, Aubière | Encadrant |

# Acknowledgements / Remerciements

*Ce travail a bénéficié du soutien du Centre International de Recherche « Systèmes Innovants pour les Transports et la Production » de l'I-SITE CAP 20-25.*

*En premier lieu, j'aimerais remercier les membres de mon jury de thèse. Merci à* ***Monsieur Ludovic DESPLANQUE*** *et à* ***Monsieur Guillaume SAINT-GIRONS*** *d'avoir accepté d'être les rapporteurs de mon travail de thèse, ainsi que d'avoir consacré du temps à la lecture, à l'analyse et à la critique de mon manuscrit. Merci également à* ***Madame Laurence MECHIN*** *et à* ***Monsieur Gabin GREGOIRE*** *d'avoir accepté de participer à ce jury et d'examiner ce travail.*

*Ensuite, j'aimerais remercier mes encadrants. Je tiens à remercier ma directrice de thèse* ***Yamina ANDRE*** *de m'avoir proposé ce sujet et de m'avoir accompagné scientifiquement et humainement tout au long de ce projet. Tu as toujours été bienveillante et disponible, et je t'en remercie. Je souhaite également remercier mon co-directeur de thèse* ***Ray LAPIERRE****. Ray, I sincerely thank you for your kindness and for your involvement in this work. You made me feel very welcome during my stay in Hamilton and I had a great time in Canada. I wish you all the best for the future. Enfin, je tiens à remercier* ***Evelyne GIL*** *pour son encadrement. Merci pour tes relectures et ton implication dans ce travail. Je sais que tu aurais aimé être plus présente mais tu as toujours été à l'écoute et su trouver les mots justes.*

*J'aimerais remercier toutes les personnes avec qui j'ai collaboré pendant ma thèse et sans qui ce travail n'aurait été possible. Tout d'abord, merci aux collaborateurs de l'université McMaster qui ont beaucoup œuvré dans ce travail de thèse :* ***Amanda THOMAS, Ethan DIAK, Curtis GOOSNEY*** *et* ***Nebile GOKTAS****. Qu'ils trouvent ici ma profonde gratitude, Thank you all! J'aimerais sincèrement remercier le professeur* ***Vladimir DUBROVSKII*** *qui nous a aidé dans l'élaboration des modèles de croissance. Travailler à ses côtés fut très plaisant et enrichissant. Merci également aux collaborateurs d'IBM Zurich :* ***Heinz SCMHID****,* ***Philipp STAUDINGER*** *et* ***Kirsten MOSELUND****, ainsi que ceux de l'Université de Bath :* ***Philip SHIELDS****,* ***Andy MOSKALENKO*** *et* ***Pierre-Marie COULON****,*

*pour l'élaboration des substrats patternés. Je remercie également* ***François REVERET****,* ***Catherine BOUGEROL****,* ***Gwénolé JACOPIN****,* ***Thierry TALIERCIO*** *et* ***Eric TOURNIÉ*** *pour leurs caractérisations des nanofils. Enfin, merci* ***Arnaud DALLÉ*** *pour les séances MEB mais aussi pour les séances d'escalade. Maintenant que tu es un runner confirmé, j'espère qu'on fera beaucoup de trails ensemble !*

*Mes remerciements se tournent maintenant vers les membres de l'équipe.* ***Geoffrey****, je tiens sincèrement à te remercier pour tes enseignements et tes conseils. De par ta connaissance des réacteurs et de l'épitaxie, j'ai été très bien formé et c'est grâce à toi que j'ai pu obtenir les résultats qui sont présentés dans ce manuscrit. L'équipe a de beaux jours devant elle à tes côtés, merci pour tout le Djoff'.* ***Elias****, mon co-doctorant, celui avec qui nous partageons tout depuis le début : les rires, les coups durs, les conférences mais aussi les entraînements. À cause de toi, je vais devoir recourir un marathon car j'ai une revanche à prendre ! Merci pour ton aide, que ce soit pour la thèse ou pour les à-côtés. J'espère qu'on fera encore de nombreuses courses ensemble.* ***Arthur****, ou plutôt Carbur pour les intimes, tu nous as rejoint dans ce bureau et tu t'es fait une place permanente. Merci d'avoir été là pendant ma dernière année, nous avons eu de beaux moments ensemble et je te souhaite le meilleur pour la suite.*

*J'ai une pensée particulière pour* ***Gabin*** *qui m'a accueilli et formé lors de mon arrivée. Tes connaissances du réacteur arséniure et ton expérience m'ont beaucoup aidé et je t'en suis très reconnaissant. Je tiens également à remercier* ***Jihen*** *qui a été présente au début de ma thèse. Merci pour ton aide et bon courage pour la suite. Merci aussi* ***Ahmed*** *pour ton aide sur l'exploitation des résultats, je te souhaite bon courage pour ta thèse. Enfin, merci* ***Jean-Chriso*** *pour ta bonne humeur et ta sympathie.*

*J'ai tiens également à remercier les doctorants que j'ai côtoyés durant ma thèse :* ***Léo, Léa, Loïc, Hiba, Guy, Romain, Salma*** *et* ***Ismaël****. Plein de belles choses à tous et bon courage pour ceux qui finissent. Merci aussi à mes amis* ***Pierre, Maxime, Sacha, Tristan, Maëlys*** *et* ***Léa*** *pour tous les moments passés ensemble, je vous souhaite mes meilleurs vœux pour la suite.*

*Au cours de ces années de thèse, j'ai eu l'opportunité d'enseigner là où tout a commencé : à l'IUT Clermont Auvergne. Merci tout d'abord à* ***Agnès*** *et* ***Damien*** *qui m'ont permis d'enseigner à l'IUT. Merci également* ***Rémi, Vincent, Hubert*** *et les autres pour votre accueil chaleureux et votre gentillesse. Merci également aux personnes de l'Institut Pascal avec qui j'ai partagé des moments agréables :* ***Pierre, Hamadou, Martine, Guillaume, Françoise*** *et les autres.*

*Enfin, je souhaite finir ces remerciements avec mes proches. Je remercie chaleureusement mes amis de toujours* ***Ronan*** *et* ***Kilian****. Je remercie sincèrement* ***ma famille*** *et* ***ma belle-famille*** *pour leur soutien inconditionnel et leur joie de vivre. Ces moments de partage sont précieux au quotidien et sont des atouts majeurs pour mener à bien une thèse. Enfin, je souhaite terminer ces remerciements avec la personne qui est à mes côtés depuis le début, celle qui m'accompagne, qui m'encourage et qui prend soin de moi au quotidien.* ***Alison****, tu es un pilier de ma vie et je n'y serai pas arrivé sans toi. Merci d'être à mes côtés, cette thèse est aussi la tienne.*

# Table of contents

# Résumé

Ce travail porte sur la croissance sélective (SAG) de nanofils (NFs) III-As par épitaxie en phase vapeur par la méthode aux hydrures (HVPE). Dans un premier temps, nous avons étudié la SAG de NFs de GaAs sur des substrats de GaAs. Des études systématiques portant sur les conditions de croissance ont mis en évidence une suppression de la croissance sous atmosphère riche en arsenic. Ces observations ont été appuyées par un modèle cinétique qui, pour la première fois en HVPE, prend en compte la diffusion des adatomes de Ga sur les facettes latérales des NFs. Puis, une étude préliminaire du dopage des NFs a été conduite, ainsi que des croissances de jonctions p-i-n dans des NFs. Les résultats sont encourageants quant à la réalisation de dispositifs à base de NFs par HVPE. Dans un second temps, nous avons étudié la SAG de NFs d'InAs et d'InGaAs sur des substrats de GaAs et Si. Il s'est avéré que la suppression de la croissance se produit également pour les NFs d'InAs. Concernant l'InGaAs, des réseaux de NFs de compositions variées ont été obtenus avec succès. Un modèle de croissance a été développé révélant que la composition des NFs est contrôlée par la cinétique de croissance plutôt que par des facteurs thermodynamiques. Cela simplifie considérablement le contrôle de la composition dans une large gamme de paramètres HVPE. Ces résultats montrent la capacité de la HVPE pour la fabrication de réseaux de NFs d'InGaAs homogènes avec des compositions facilement ajustables.

**Mots clés** : HVPE, nanofils III-As, croissance sélective, épitaxie, modèles de croissance.

# Abstract

This work focuses on the selective area growth (SAG) of III-As nanowires (NWs) by hydride vapor-phase epitaxy (HVPE). First, we have studied the SAG of GaAs NWs on GaAs substrates. Systematic studies according to growth conditions have demonstrated a growth suppression effect under arsenic-rich atmosphere. These observations were supported by a kinetic model which, for the first time in HVPE, takes into account the diffusion of Ga adatoms on the NWs side facets. Then, a preliminary study of the doping of NWs was carried out, as well as the growth of p-i-n junctions in NWs. The results are encouraging regarding the fabrication of NW-based devices by HVPE. Secondly, we have studied the SAG of InAs and InGaAs on GaAs and Si substrates. It turned out that growth suppression also occurs for InAs NWs. As for InGaAs, NW arrays with various compositions have been successfully obtained. A growth model was developed revealing that the NWs composition is controlled by growth kinetics rather than thermodynamic factors. This greatly simplifies the control of the composition across a wide range of HVPE parameters. These results show the capability of HVPE for the fabrication of homogeneous InGaAs NW arrays with widely tunable compositions.

**Key words** : HVPE, III-As nanowires, selective area growth, epitaxy, growth modeling.

# General introduction

Over the last decades, III/V semiconductor nanowires (NWs) have attracted much attention due to their unique physical properties and potential applications in nanoelectronics and optoelectronics. A wide variety of NW-based devices have been developed, including transistors, solar cells, lasers and photodetectors. To date, the main techniques used to grow NWs are molecular beam epitaxy (MBE) and metal organic vapor phase epitaxy (MOVPE). In this thesis, I used hydride vapor phase epitaxy (HVPE). This process has been developed at Institut Pascal since the 1980s for the growth of III-V planar layers. In the last decade, the group has successfully demonstrated the growth of III-As and III-N NWs whether by catalyst-assisted growth [1, 2, 3] or by catalyst-free growth [4, 5].

My thesis work was part of two research projects. First, the beginning of my thesis was part of the project ENNORA (2017-2022) (*Epitaxie de Nanofils semiconducteurs pour l'ENergie. PrOpriétés StRucturales, Optiques et de TrAnsport Electrique*) funded by the region AURA (*Pack Ambition Recherche*). This project involved four French laboratories (CEA-INAC, INSA-INL, Institut Néel and Institut Pascal). The project objective was the growth and characterization of III-As and III-N NWs for energy conversion applications. Within the project, Institut Pascal was in charge of the HVPE growth of InGaAs NWs. Another part of my thesis work was developed within the project NANOSPRING (2021-2024) (*NANOfils III-V HVPE pour des diSPositifs pouR l'INfrarouGe)* funded by the region AURA (*Pack ambition international NanoSpring*) and by the International Research Center "Innovation Transportation and Production Systems" of the I-SITE CAP 20-25. This project is in collaboration with Professor Ray LaPierre from McMaster University and aims to produce InAs and InGaAs NWs for infrared applications. This collaboration also explores the growth of GaAs NWs for betavoltaic cells. To summarize, my thesis work focuses on the selective area growth of III-As NWs and is detailed in this manuscript which contains three chapters.

The chapter I introduces the context of the thesis and the HVPE method. First, the key advantages of the NW geometry are discussed as well as the main growth methods used for the growth of III-As NWs, namely catalyst-assisted growth, catalyst-free growth and selective area growth (SAG).

The state-of-the-art is discussed regarding the particular properties of III-As NWs and the resulting wide range of applications. From this, the main motivations for the growth of III-As NWs at Institut Pascal are presented: GaAs NWs for betavoltaic cells, and InAs and InGaAs NWs for infrared photodetectors. Such applications require the growth of regular arrays of long NWs (several μm). One of my thesis objectives was the achievement of such arrays in perspective of potential NW-based devices grown by HVPE. Then, the HVPE method is described, with the experimental set-up as well as the calculation of the vapor phase composition as a function of the initial gas flows. Afterwards, the thermodynamics and kinetics aspects of HVPE, essential to understand the growth mechanisms, are introduced. Finally, the issues related to the supply of appropriate high quality patterned substrates are discussed, which impacted the number of substrates available for the thesis work.

The chapter II focuses on the SAG of GaAs NWs on GaAs(111)B substrates. The NW morphology is investigated versus the growth conditions and template geometry. The growth study reveals that As-rich conditions are highly undesirable for SAG of GaAs NWs by HVPE due to the formation of As trimers on the NW top facet that suppresses the NW axial growth. Consequently, optimal conditions for the growth of long NWs are determined which result in long NWs ($\sim$ 6 μm) with a high aspect ratio of around 50. These observations were supported by a dedicated kinetic model which takes into account the diffusion of Ga adatoms from the NW sidewalls to the top. Secondly, we report the first study of doping of catalyst-free GaAs NWs by HVPE. The influence of dopants on NW morphology, optical and crystallographic properties is discussed. These preliminary results made it possible to conduct the first growth of a p-i-n junction NW by HVPE. The NWs obtained were then processed to make a photovoltaic device at McMaster University. Unfortunately, the observed efficiencies were very poor but this study highlights several ways of improvement with a perspective of growing future p-i-n junctions by HVPE. Finally, a new p-i-n junction prototype is tested with a very high flow of n-dopant. This was characterized by cathodoluminescence and shows two distinct areas seeming to correspond to the different doping area. These results are encouraging for the realization of NW p-i-n junction by HVPE.

The chapter III presents the SAG of InAs NWs on Si(111) substrate and InGaAs NWs on GaAs(111)B and Si(111) substrates. To begin with, optimal conditions for growing long InAs NWs are determined which allows obtaining $\sim$ 15 μm long NWs. These preliminary experimental results will be the base of the development of multispectral photodetector devices which will be performed during a forthcoming collaboration with McMaster University. Regarding InGaAs NWs, the demonstration of feasibility on GaAs(111)B substrate shows a remarkably high growth rate (more than

50 µm/h) and indium-rich NWs with an estimated average indium composition of $x = 0.84$ by EDX (energy-dispersive X-ray spectroscopy) and $x = 0.78$ by PL (photoluminescence). Then, SAG of InGaAs NWs was successfully demonstrated on Si(111) substrate. A wide range of InAs fractions in InGaAs NWs was obtained from $x = 0.34$ to $x = 0.90$. The EDX mapping of individual NWs confirmed the homogeneous composition along the entire NW length. A dedicated growth model was developed and the NW composition was shown to be controlled by the growth kinetics rather than thermodynamic factors, which considerably simplifies the compositional control in a wide range of HVPE parameters. Overall, these findings reveal the capability of the cost-effective HVPE technique for the fabrication of regular arrays of InGaAs NWs on Si with widely tunable and spatially uniform compositions.

Chapter I

# HVPE of III-As nanowires

This first chapter introduces the HVPE method for growing III-As semiconductors. For convenience in this manuscript, III-As notation is used to refer to GaAs, InAs and InGaAs materials. The chapter is divided into two parts.

The first part provides a brief background of III-As materials and their properties. In particular, the advantages of the nanowire geometry are discussed and the state-of-the-art of III-As nanowires growth is introduced. Then, the motivations and target applications of my thesis work are presented.

In the second part, a presentation of the HVPE reactor is made with its operating principle. The main issues that can be encountered for SAG at nanoscale and the details of the patterned substrates used in this work are discussed. This is followed by an introduction of the thermodynamic and kinetic models of growth by HVPE.

# I.1 Main advantages of nanowire geometry

**What are nanowires?** Nanowires (NWs) are quasi-1D structures with a diameter of the order of several nm up to tens of nm and with a high aspect ratio. Thanks to their geometry, NWs have very specific properties in terms of strain relaxation, light interaction and electrical transport. Therefore, since their discovery in 1964 by Wagner and Ellis [6], the interest in the growth of NWs has steadily increased. As we will show later, NWs have already proven to be very efficient in many fields of application such as solar cells, light-emitting diodes (LEDs) or photodetectors [7, 8, 9]. The main advantages of NWs are described below.

**Solving the lattice mismatch:** The major issue regarding the epitaxial growth of semiconductors material on heterosubstrate is the difficulty of growing defect-free crystal. The lattice mismatch between the substrate and the as-grown semiconductor causes strain at the interface between the two materials. In thin film epitaxy, this results in extremely poor quality of heterointerfaces with high density of misfit dislocations. These dislocations act as non-radiative recombination centers which strongly impact electrical and optical properties of the grown material. Nevertheless, this is not the case for NWs. Thanks to NW small lateral size, strain is relaxed through the free-lateral facets as shown in Figure I.1. Thus, even in high lattice-mismatched systems such as epitaxy of III-V semiconductors on Si substrate, dislocation-free materials can be grown [10, 11]. The lattice mismatch of the main materials used in this work are: GaAs/Si (4.1%), InAs/GaAs (7.2%) and InAs/Si (11.6%) [12].

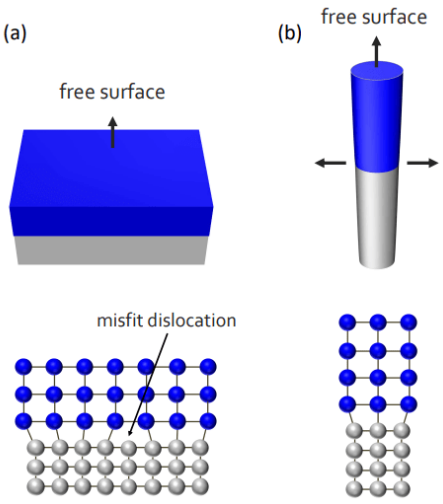


Figure I.1 – *Schematic of a) planar growth and b) NW growth on heterosubstrate. Strain relaxation results in misfit dislocation for the 2D layer, while strain is relaxed through the free-lateral facets of the NW. From [13].*

**Growth of axial and radial heterostructures:** The NW geometry allows the formation of two different types of heterostructures: axial heterojunction and radial or core/shell heterojunction where semiconductor materials can be grown around a core NW [14, 15]. To obtain these particular structures, it is necessary to control the growth conditions in order to increase the radial growth at the expense of the axial one. In catalyst-assisted growth (see section I.2.1), this can be done by controlling the properties of the catalyst droplet. In MBE, this is usually achieved at low growth temperatures and a low V/III beam equivalent pressure ratio whereas in MOVPE, axial nanowire growth is inhibited at higher growth temperatures and/or increased reactant concentration in the vapor phase. The different possibilities of NW heterojunctions are schematized in Figure I.2.

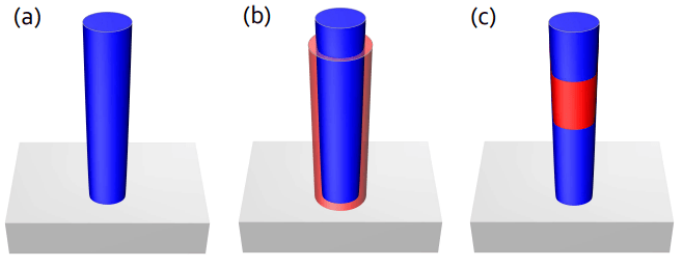


Figure I.2 – *Schematic illustration of different NW heterostructure configurations: a) single NW on a substrate, b) radial (core/shell) heterostructure and c) axial heterostructure. Adapted from [13].*

**Light-trapping:** Due to their small size, light-absorption by NWs cannot be treated using ray optics. NWs behave like antennas, concentrating the incoming light in their small volume [16]. Resonant absorption mechanisms occur in NW arrays related to Fabry-Pérot modes, or waveguide modes, which results in enhanced anti-reflection properties, and light-trapping into the NW array. As will be explained in more detail further (section I.3.4.2 on page 25), depending on NW length, NW diameter and array pitch, the reflection can be minimized and effective broadband absorption can be reached, which was studied theoretically [17, 18, 19, 20, 21, 22] and experimentally [23, 24, 25, 26]. High absorption even for large incident angles [18, 24] makes NWs attractive to collect diffuse light.

Thanks to these specific properties, a strong interest has been developed on the growth of NWs semiconductors and more particularly on III-V NWs. Thus, many studies have been realized on the growth of nitrides III-N and arsenides III-As NWs. Glas et al. [27] demonstrated through theoretical considerations that for a given lattice mismatch percentage, a critical diameter exists below which NWs are dislocation-free. In their work, the critical NW length above which dislocations become energetically favorable, is calculated as a function of the NW initial radius and for different lattice mismatch values. Thus, for a given lattice mismatch, there is a critical radius $r_0$ below which infinitely

long NWs with dislocation free interfaces can be grown. These results are presented in Figure I.3. Obviously, the larger the lattice mismatch, the smaller the critical diameter. For example, the growth of dislocations free highly mismatched GaAs/Si NW heterostructures with a lattice mismatch around 4% is theoretically possible for radii below 40 nanometers.

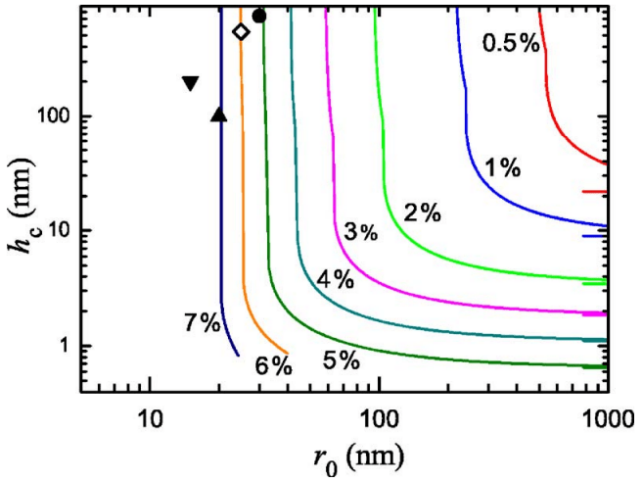


Figure I.3 – *Dependence of the critical thickness $h_c$ on the NW radius $r_0$ for different lattice mismatch given in %. From [27].*

Due to these advantages, NW geometry offers a suitable solution to design active III-V devices on mismatched substrates. Moreover, the possibility of growing heterojunctions (axial or radial) opens up new possibilities for the realization of NW-based devices. In the next section, we present the different methods that are reported for the growth of III-V NWs.

# I.2 Nanowires growth methods

In order to grow NWs, two main categories exist which are the top-down and the bottom-up approaches. We will only detail the bottom-up approach which is the point of the thesis. Nevertheless, it should be mentioned that the top-down approach consists in etching a bulk material from a particular pattern. It has the advantage of easily controlling the position and dimension of the NWs but the multiple etching processes can randomly cause defects on the surface of NWs and make this approach complex to implement.

Regarding the bottom-up approach, NWs are grown by addition of material onto the substrate. The most commonly used techniques for this approach are: molecular beam epitaxy (MBE), metal organic vapor phase epitaxy (MOVPE) and hydride vapor phase epitaxy (HVPE). Two different ways are used for the growth of NWs: catalyst-assisted growth and catalyst-free growth.

## I.2.1 Catalyst-assisted growth

Several methods have been developed to grow NWs with a high material quality. To date, the most common method is the vapor-liquid-solid (VLS) growth promoted by a metal catalyst [7, 9, 28]. The VLS growth was first investigated by Wagner and Ellis in 1964 [6]. They demonstrated that one-dimensional silicon structures, i.e. NWs, can be grown on silicon substrate by means of a pre-deposited gold catalyst seed as illustrated in Figure I.4. Gold droplets are obtained by depositing a thin solid Au layer which is annealed before the growth. Afterwards, the growth of NWs takes place below liquid Au droplets and not on the bare substrate. The growth direction of nanowires is usually $\langle 111 \rangle$, which means that the crystal axis is perpendicular to the (111) substrate. The final diameter of the nanowires depends on the initial Au particle diameter and annealing conditions. Since this pioneering experience, most of NWs are grown by the VLS mechanism using Au nanoparticle catalysts.

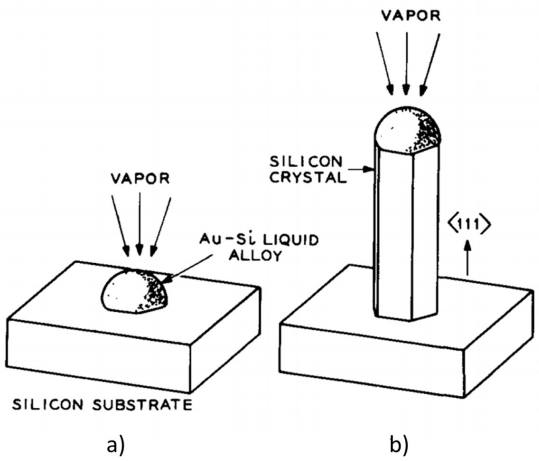


Figure I.4 – *Illustration showing the growth of a Si whisker by VLS: a) Au-Si droplet on the Si substrate at the initial stages of growth, b) growth of pure Si crystal under the droplet. From [6].*

Thanks to Au-assisted growth, many III-V semiconductors have been integrated on various substrates and especially on Si with a perspective to integrate III-V devices on the silicon electronic platform. Regarding III-As semiconductors (GaAs, InAs et InGaAs), high quality NWs were successfully grown by adjusting the growth conditions, the temperature or the size of the droplet [29].

Nonetheless, it was reported that Au atoms can incorporate into NWs and act as an impurity by introducing deep level recombination centers. This results in a significant degradation of electrical and optical properties of NWs [30, 31]. Consequently, much effort has been put on growing Au-free NWs in the self-catalyzed VLS approach, in which Au is replaced by the group III metal as the

catalyst. The group III element can be deposited before growth, or it can be formed directly on the substrate during the NW growth. The key parameters governing III-assisted growth of III-As NWs by MBE are: the As flux controlled by the $As_2$ or $As_4$ pressure [29] which limits the axial growth rate, the group III adatoms flux at the droplet which increases the growth rate [32] and the oxide layer which provides nucleation sites and wetting characteristics which promote the droplets formation [33, 34]. Self-assisted growth avoids the incorporation of impurities and allows the growth of high purity NWs compatible with the Si platform technology.

## I.2.2 Catalyst-free growth

Catalyst-free growth occurs without the use of any seed particles. Thereby, the precursors condensate directly on the substrate via vapor-solid mechanism (VS) or incorporate after diffusion along the lateral facets. Unlike VLS mechanism where the catalytic nanoparticle mainly drives the NW growth, specific growth conditions are used in order to obtain an anisotropic growth with a high axial growth rate. Indeed, growth anisotropies are governed by the surface energies of the respective facets which are very sensitive to the chemical potential $\mu$ and are therefore strongly governed by growth conditions. These growth anisotropies depend only on the orientation of NWs facets and are independent of the nature of the substrate whether heteroepitaxy (GaAs NWs on Si for example) or homoepitaxy (GaAs NWs on GaAs). The absence of a catalyst particle induces major differences in the nucleation process. As an example, in selective area growth (which is further described below), NWs exclusively nucleate on oxide free surface. Nonetheless, on a fully oxide-free substrate, large islands nucleate due to the high mobility of the group III adatoms [35]. These islands have a considerably reduced axial growth rate, preventing the NW growth. The NWs density and morphology can be adjusted by a meticulous control of apertures formation in the oxide layer. This can be realized by an etching of the pre-deposited oxide layer [35, 36, 37]. Although the density of NWs is controllable, the NWs still grow randomly on the substrate.

## I.2.3 Selective area growth (SAG)

In self-organized growth (on unpatterned substrate), the NWs grow randomly on the substrate. The random arrangement and size of the NW growth seeds lead to inhomogeneity of the NW ensembles in terms of their diameter, length, position, and growth direction. This randomness induces inhomogeneities of the electronic and optical properties, making the fabrication of devices very difficult. In order to overcome these problems, selective area growth (SAG) has been developed. SAG con-

sists of growing NWs in pre-defined locations which makes it possible to have very homogeneous NW arrays on large scales. These NWs can be obtained either by VLS or VS growth.

This technique requires the pre-deposition of a dielectric mask layer ($SiN_x$, $SiO_x$) on the substrate. Afterwards, apertures with specified diameter and pitch are obtained using lithography technique. Today, electron beam lithography (EBL) provides holes of a few tens of nanometers resulting in very dense NW arrays. An example of a SAG growth process is illustrated in Figure I.5.

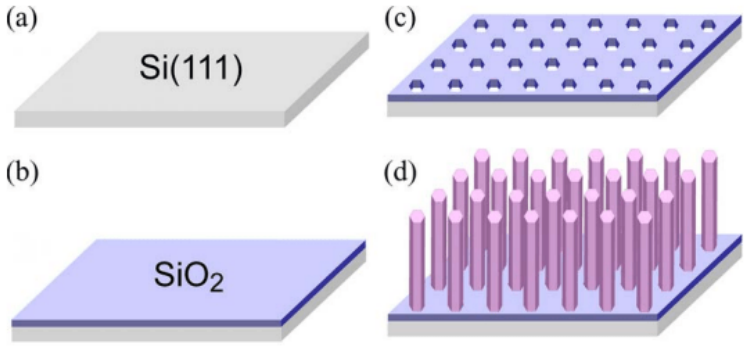


Figure I.5 – *Illustrations of a SAG process: (a) Bare Si(111) substrate cleaned. (b) Deposition of $SiO_2$ dielectric mask film on Si(111) substrate. (c) Definition of pattern by EBL and wet chemical-etching. (d) NWs growth. Adapted from [7].*

SAG is a major asset for the realization of NW-based devices because it allows the control of the NWs size and density over a large area. This allows to synthesize homogeneous NW arrays over the entire substrate's area which is essential for the realization of NW-based devices. We will further detail the interest of SAG compared to self-organized growth on the properties of NWs. Now that we have presented the different ways to grow NWs, we discuss the state-of-the-art of the growth of III-As NWs in the next section.

# I.3 State-of-the-art of III-As nanowires growth and target applications

## I.3.1 III-As material properties

Every III-V bulk semiconductor material under ambient conditions have a stable zinc-blende (ZB) crystal structure, except III-N materials which exhibit the wurtzite (WZ) crystal structure. Nevertheless, in the case of semiconductor NWs, pure ZB [38], pure WZ [39] and polytypism (a mixture

of ZB/WZ) can be obtained [40]. Indeed, either ZB phase or WZ phase is stable so a disordered mixture of both crystal structures is often found along NW length. As both phases can appear in NWs, it is essential to define what are WZ and ZB crystal phases. The ZB and WZ crystal structures for GaAs are shown in Figure I.6.

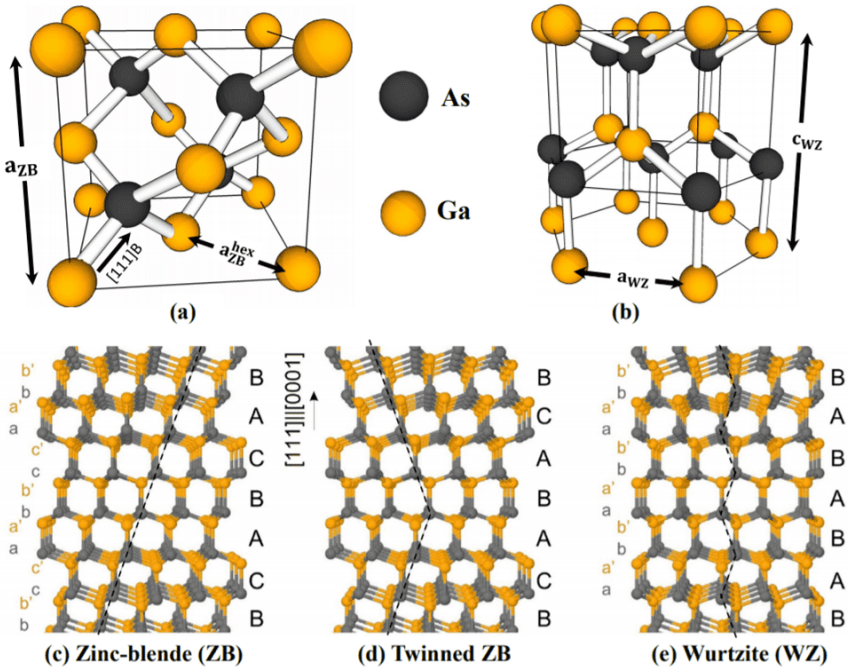


Figure I.6 – *a) Zinc-blende (ZB) lattice and b) wurtzite (WZ) lattice of GaAs crystal. Crystal structure sequences along the* $< 111 > || < 0001 >$ *directions for: c) ZB, d) Twinned ZB and e) WZ. From [41].*

**ZB crystal phase:** The ZB phase corresponds to a face centered cubic (fcc) structure containing two sub-lattices at (0,0,0) and (1/4,1/4,1/4) $a_{ZB}$, filled with group III atoms and As atoms, respectively. III-As material grown along the [111] direction can be terminated either with (In, Ga) atoms corresponding to III-As(111)A, or with As atoms for III-As(111)B. The ZB crystal is a repetition of three bilayers represented as "ABCABC" sequences (Figure I.6.c).

**WZ crystal phase:** The WZ phase corresponds to the penetration of two hexagonal compact (hcp) lattices with "ABAB" stacking sequence, one lattice of III atoms (In,Ga) and one of As atoms. Both lattices have the same axes and are shifted by $3/8c_{wz}$.

As explained previously, both phases can be obtained in NWs. As the surface to volume ratio is much higher for NWs than for layers, the surface energy plays a significant role. Regarding the WZ phase, it has a lower number of dangling bonds on the NW side facets resulting in a lower surface energy. However, the ZB phase has a cohesive energy between an atomic pair about 17 meV lower

than WZ GaAs and 11 meV lower than WZ InAs [42]. From that point, regarding the growth of NWs, it can be easily imagined that there is a competition between these two crystal phases.

As the growth of III-As NWs takes place layer-by-layer, stacking faults and rotational twins are often observed along the growth direction. A rotational twin is defined as an inversion of the "ABC" sequence into the "CBA" sequence. This corresponds to a rotation of the "ABC" sequence of the ZB by 180° around the growth axis (see Figure I.6.d). This results in the formation of a WZ monolayer with an "ABA" stacking sequence. Therefore, a ZB lattice can be fully transformed into WZ if rotational twins occur every two monolayers. This is represented by the dashed line on the Figure I.6.e.

As the ZB crystal phase is the main phase observed for the growth of III-As NWs, we will focus on the properties of this one. Cubic III-As semiconductors have a direct bandgap, the minimum of the conduction band and maximum of the valence band are located at the center of the Brillouin zone at k = 0 as illustrated in Figure I.7. Near the Γ-symmetry point, the valence band is composed of a heavy hole band, a light hole band, and a split-off band. The heavy hole and light hole bands are degenerate at the Γ-point. Measuring energy from the top of the valence band at the Γ-point, the split-off energy is $E_{so}$ = - 0.34 eV in GaAs and $E_{so}$ = - 0.41 eV in InAs [12]. Due to the direct gap, the probabilities of generation and radiative recombination of carriers are very important. Therefore, III-V semiconductors are very efficient at converting light energy into electronic energy and reciprocally. This represents a major advantage compared to Si material which has an indirect bandgap which limits the optical absorption.

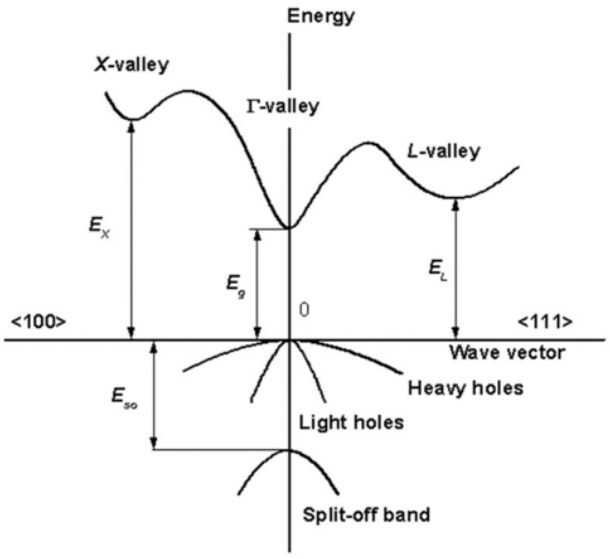


Figure I.7 – *Typical band structure of cubic III-As material near k = 0. Adapted from [43].*

At 300 K, the respective bandgap energies $E_g$ for InAs and GaAs are 0.354 eV and 1.424 eV, respectively. Thus, the interest in InGaAs material lies mainly from its tunable bandgap between these two values. This corresponds to a large infrared wavelength range extending from 880 nm to 3500 nm. Indeed, the bandgap energy of InGaAs can be tuned by controlling In (or Ga) fraction. Paul et al. [44] have proposed an equation for the bandgap $E_g$ of $Ga_xIn_{1-x}As$ according to GaAs fraction in the solid $x_{Ga}$ and the temperature $T$:

$$E_g(x_{Ga},T)=0.42+0.625x_{Ga}+[\frac{5.8}{(T+300)}-\frac{4.19}{(T+271)}].10^{-4}T^2x_{Ga}-\frac{4.19.10^{-4}T^2}{(T+271)}+0.475x_{Ga}^2 \quad \text{(I.1)}$$

This equation is mainly used to estimate the composition from the bandgap deduced, for example, from photoluminescence or cathodoluminescence spectra. Note that this equation has been verified for unstrained cubic ZB material. According to this equation, the evolution of the InGaAs bandgap energy as a function of the indium concentration at different temperatures (5 K and 300 K) is shown in Figure I.8.

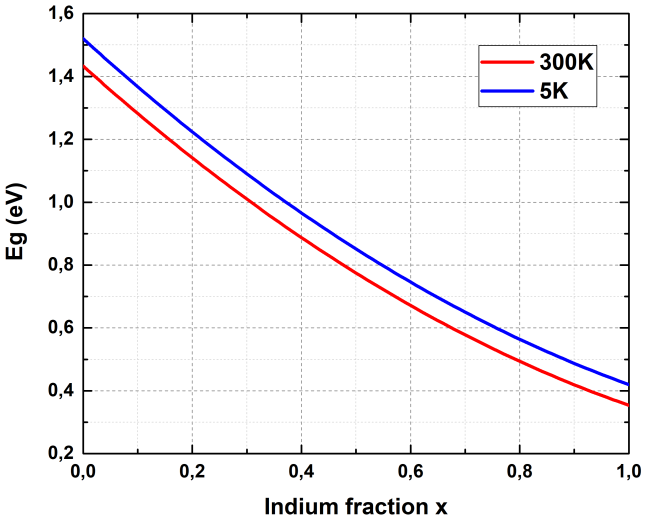


Figure I.8 – *InGaAs bandgap energy $E_g$ as a function of the indium concentration at 5 K (in red) and at 300 K (in blue).*

Now that we have presented the main properties of III-As materials, we will be able to present the main results obtained for the growth of III-As NWs.

## I.3.2 GaAs and InAs nanowire growth

The growth of binaries GaAs and InAs NWs has been widely studied by MBE and MOVPE. Since Au-catalyzed growth was the first which succeeded to grow NWs, it is the most documented method to grow III-As NWs. Presently, for all these growth techniques, the relationships between

the size of Au droplet, the growth thermodynamics and the growth kinetics have been investigated [45, 46]. In MBE and MOVPE, it appears that the NWs growth is significantly impacted by diffusion of the element III adatoms. Dubrovskii et al. [42] demonstrated the length dependence of GaAs NWs on the size of gold catalyst particles. They concluded that the growth of NWs with diameters lower than 100 nm was essentially a diffusion-induced growth. In other words, the diffusion of adatoms from the substrate to the top of NWs greatly increases the NWs length, especially for low diameters. In addition, Harmand et al. [47] have investigated the effect of the Ga diffusion length on the NWs morphology. At low temperature, the diffusion length of Ga is small which favors nucleation on the sidewalls before the adatoms reach the top of the NWs. Consequently, the NWs exhibit a conical shape as illustrated in Figure I.9.a. At higher temperature, the diffusion length of Ga is increased, adatoms can reach the gold particle at the NWs top and NWs become more cylindrical as illustrated in Figure I.9.b.

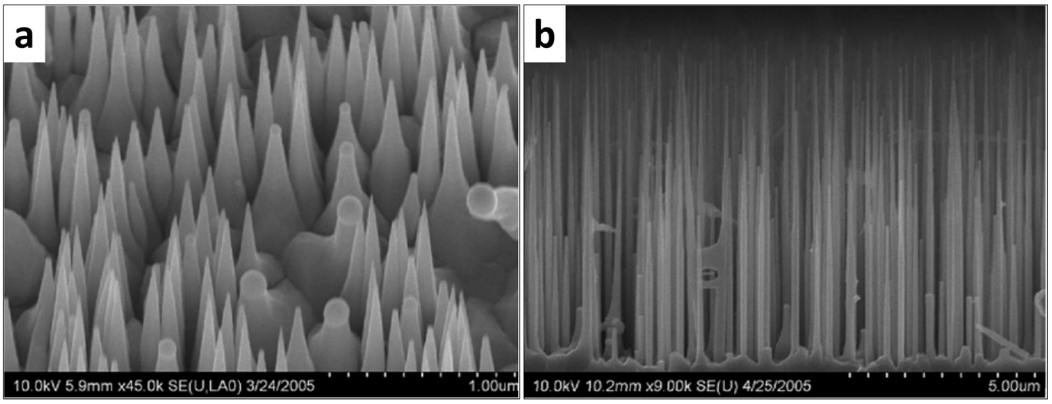


Figure I.9 – *SEM images of Au-catalysed GaAs NWs grown by MBE at a) 420 °C and b) 580 °C. Adapted from [47].*

The same behavior has been observed for gold-catalysed InAs NWs grown by MOVPE when diffusion of adatoms dominates the growth rate, and chemical reaction is negligible [48]. In addition, high-quality GaAs NWs have been obtained by Au-assisted growth in MBE [49] and MOVPE [50]. In the case of Au-catalyzed InAs NWs, MBE has succeeded in growing pure ZB NWs [51, 52]. The high crystalline quality is correlated to the very small NWs diameter of 20 nm [51]. Concerning the HVPE growth method, pure ZB GaAs NWs with exceptional length has been obtained by Au-catalyzed growth [1]. At 715 °C with a III/V ratio of 5, a high grow rate of 170 µm/h has been observed. This is explained by the high material input ($3 \times 10^{-3}$ atm for $GaCl_g$ and $3 \times 10^{-3}$ atm for $As_{4g}$) and the high dechlorination rate of the element III precursor (GaCl) in HVPE. Nevertheless, as explained previously in section I.2.1, Au has been reported to act as impurity that creates deep level

recombination centers in NWs which deteriorate the electrical and optical properties of materials. Therefore, effort have been dedicated to grow gold-free III-As NWs through self-catalyzed growth method.

Self-catalysed growth of GaAs NWs was successfully demonstrated by MBE, MOVPE and HVPE [30, 53]. Recently, Becdelievre et al. demonstrated the growth of ultra-long self-catalyzed GaAs NWs up to 80 µm by MBE, however, this required a significant growth time of 12 h [54]. Regarding MOVPE, Breuer et al. [30] have investigated the self-catalyzed growth of GaAs NWs on Si(111) substrates. They observed that by using a low III/V ratio ($<1$), the nucleation can occur at 600 °C. Nevertheless, the density and homogeneity of the grown structures are still not controlled. Concerning HVPE, similar observations were found by Dong et al. [53]. For VPE processes, the main challenge is linked to the temperature required for cracking chemical precursors (such as organometallic precursors), combined with arsenic rich atmosphere in the reactor. Under such conditions, both the initial nucleation and the subsequent stability of liquid gallium droplets are not favored [55, 56]. Considering these limitations, it is very difficult to obtain adequate conditions for Ga-catalyzed growth and the length of GaAs NWs is so far limited to less than 1 µm. On another side, the growth of self-catalysed InAs NWs has been successfully demonstrated by MBE [32, 57, 58] and MOVPE [59, 60]. However, it is not quite obvious whether a droplet is present during growth or not. In practice, indium droplets are seldom observed at the end of the growth, in particular in MOVPE growth. An example of self-catalysed InAs NWs grown by MBE is shown in Figure I.10.

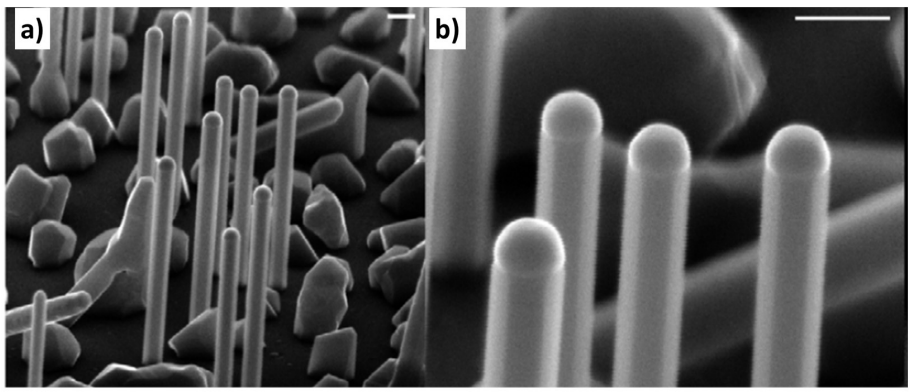


Figure I.10 – *Tilted-view SEM images of self-catalysed InAs NWs grown by MBE. In droplets are visible at the NWs tip and the contact angle is almost 90°. Scale bars are 200 nm. Adapted from [32].*

Meanwhile, numerous studies focused on the growth of catalyst-free III-As NWs. As for catalysed growth, the morphology of the NWs is controlled by changing the growth parameters [61, 62]. Whether for self-catalyzed growth or not, many studies showed the importance of the surface prepara-

tion before the growth, in particular the optimization of the oxide layer for NWs nucleation. Regarding the growth on Si(111) substrate, Tomioka et al. [14, 63], reported that an arsenic pre-treatment of the Si(111) surface is mandatory to ensure the vertical growth of III-As NWs along the [111]B direction.

To produce periodic NW arrays, selective area growth (SAG) was developed where growth occurs on pre-determined sites on a patterned substrate. As detailed previously in section I.2.3, SAG can be made with or without a catalyst. Thus, large-scale arrays of NWs with homogeneous properties can be obtained [64, 65]. SAG of GaAs and InAs NWs has been demonstrated by MBE and MOVPE on various substrates [14, 66, 67, 68, 69, 70]. Diverse studies reported a strong relationship between the apertures diameter and the final morphology of GaAs and InAs crystals grown on GaAs (111)B and Si(111) substrates [71, 72]. Yoshida et al. have reported that the GaAs crystal morphology changed from hexagonal NW to truncated tetrahedra when the aperture diameter is higher than $\sim$ 500-1000 nm [72]. These observations were further corroborated experimentally and supported by a theoretical model based on the variation of the Gibbs free energy by Ikejiri et al. [69]. Nevertheless, Wang et al. [73] reported a different behavior with InAs NWs when increasing the apertures diameter (Figure I.11). They have shown that by increasing the aperture diameter, the number of NWs per aperture increased as well. In smaller opening, once a NW nucleates, it acts like a sink for adsorbed species and suppresses the formation of other nuclei. Over a particular apertures diameter, the number of adsorbed species is sufficient to allow multiple NWs nucleation.

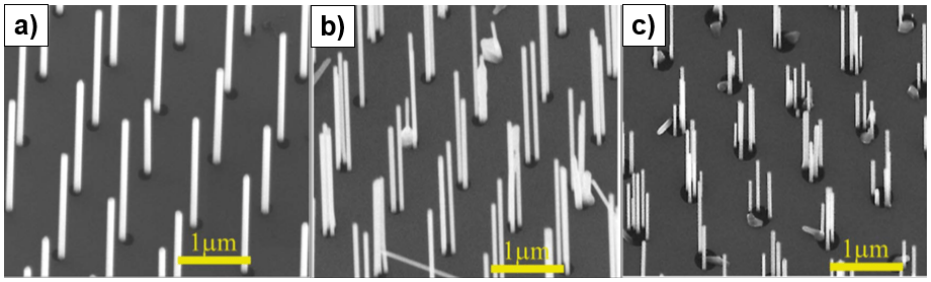


Figure I.11 – *Tilted-view SEM images of InAs NW arrays on Si(111) grown by MOVPE. The apertures diameter is: a) 160 nm, b) 200 nm, c) 300 nm. Adapted from [73].*

SAG of catalyst-free GaAs and InAs NWs on GaAs (111)B and Si(111) substrates has been recently demonstrated by HVPE [4, 74]. For both materials, the main observations highlighted are: a pre-treatment of substrate surface under arsenic atmosphere is crucial to nucleate on Si(111) substrate and to obtain vertically aligned NWs; growth conditions and pattern geometry make it possible to control the NWs morphology; and finally, NWs grown along [111]B direction exhibit a high density of random stacking faults related to the ZB/WZ polytypism.

Regarding GaAs results, NWs and platelets have been obtained thanks to various growth conditions and different apertures diameters (350 nm vs 500 nm). These platelets exhibited a defect-free ZB crystallographic structure. SEM images of NWs and platelets are illustrated in Figure I.12. Several NWs growth conditions have been investigated and two of them are taken as examples with different growth temperatures in Figure I.12.a and Figure I.12.b. The growth conditions between the NWs in Figure I.12.b and the platelets in Figure I.12.c-d are identical, only the openings diameter is different. Thus, the importance of the pattern geometry on NWs morphology has been demonstrated in HVPE. Nonetheless, the NWs obtained in this study are of small length ($\approx$ 1 µm) because of a low axial growth rate (maximum is around 6 µm/h). As it will be addressed later in chapter II, this growth rate is under HVPE capabilities of tens µm/h.

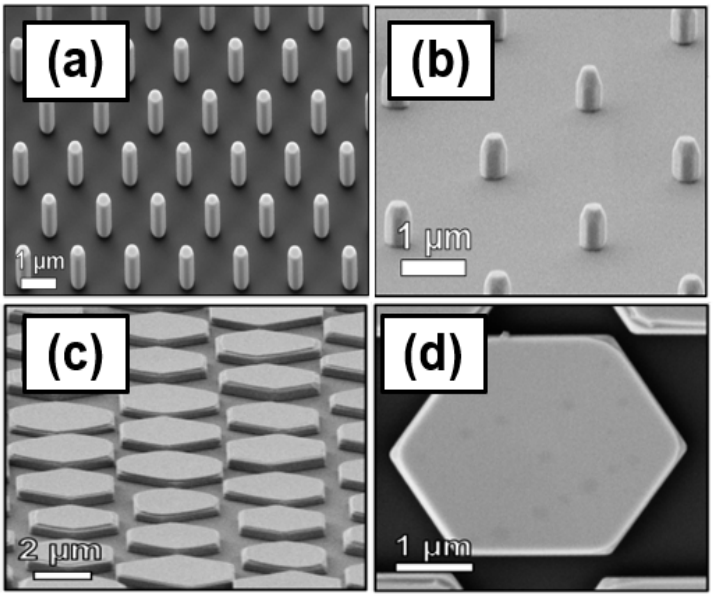


Figure I.12 – *Tilted-view SEM images of GaAs NW arrays grown on Si(111) under different growth temperatures: (a) 785 °C and (b) 760 °C. The openings diameter is 350 nm and the pitch is 1.75 µm. (c) tilted-view SEM images of hexagonal GaAs micro-platelets grown on Si(111). (d) Closer top-view SEM image on a selected micro-platelet showing an hexagonal morphology. The openings diameter is 500 nm and the pitch is 2.50 µm. Platelets were grown under the same growth conditions of (b). Adapted from [74].*

As for the SAG of InAs NWs by HVPE, it has been shown that it is also possible to control the morphology by varying the growth parameters. High axial growth rates of about 30 µm/h can be reached at a growth temperature of 680 °C. SEM images of InAs NWs grown on GaAs(111)B and Si(111) at 640 °C by HVPE are shown in Figure I.13.

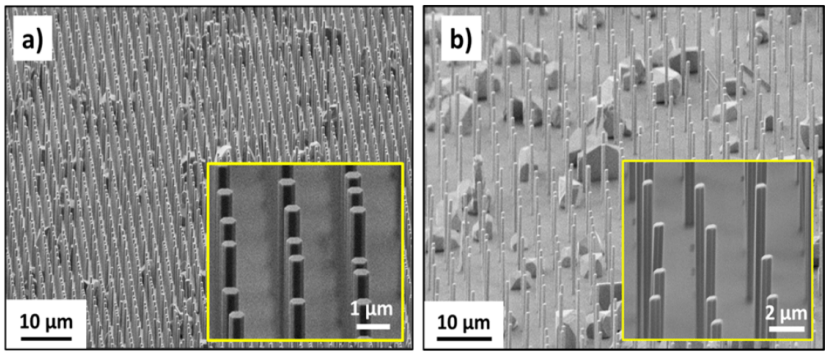


Figure I.13 – *Tilted-view SEM images of InAs NWs grown on: a) patterned GaAs(111)B substrate and b) patterned Si(111) substrate. Openings diameters are 60 nm and 350 nm, respectively. Insets show a magnified view of the NWs. From [4].*

Lastly, it should be noted that one of the main issues of SAG lies in the dielectric mask quality. Parasitic growth may occur depending on the roughness, the thickness variation, the patterning process used and remaining oxide in the openings. As an example, it can be seen in Figure I.13 the presence of non-oriented structures probably due to mask imperfections. To conclude, in SAG, whatever the growth method (VLS or VS), the geometry of the NWs depends both on the growth conditions (temperature and vapor phase composition) but also on the pattern characteristics.

### I.3.3 InGaAs nanowire growth

Several methods have been developed to grow InGaAs NWs. As described in section I.3.1, InGaAs material is of great interest because of its widely tunable bandgap energies or wavelengths (from 880 to 3500 nm) and high electron mobility. In contrast to planar InGaAs heterostructures, for which the composition is restricted to nearly lattice-matched substrates to inhibit strain induced defects like $In_{0.53}Ga_{0.47}As$ on InP [75], the more efficient strain relaxation of NWs allows the integration of InGaAs NWs on diverse substrates with much larger composition tunability. Nonetheless, even if the growth of GaAs and InAs NWs is widely studied, the growth of InGaAs ternary material is less developed as several issues need to be addressed. Indeed, controlling the NWs morphology and the alloy composition is not straightforward, especially because Ga and In atoms have different properties in terms of surface diffusion, kinetics of incorporation and solubility [76]. Thus, several Au-assisted growth studies showed the presence of Ga-rich core and In-rich shell in InGaAs NWs. This can be explained by two reasons:

– **1)** In VLS-growth of InGaAs NWs the species with higher diffusivity (In adatoms) generate an unintentional In-rich shell structure near the bottom of the NW that is responsible for the

compositional non-uniformity [45, 76]. This has also been explained by theoretical transient growth models [77].

– **2)** The In has a higher affinity for the Au catalyst than Ga, which is expected to further modify the composition of ternary InGaAs NWs during VLS growth [78]. Indeed, Guo et al. observed that due to this competitive solubility of In versus Ga adatoms, Au catalysts preferentially transport Ga to the NW growth front, resulting in a segregation of a Ga-rich InGaAs core region (via VLS-mode) and an In-rich InGaAs shell layer (via vapor-solid, VS-mode) [79].

The same observations were made for self-catalyzed growth achieved through a Ga droplet where a significant time delay for the In to precipitate underneath the alloy droplet is observed. The limited precipitation of In atoms and the formation of an In-rich shell structure therefore closely resembles Au-catalyzed growth. Figure I.14.a, from Koblmüller et al. [78], depicts a schematic illustration of the growth model and resultant non-uniform composition distribution of InGaAs NWs as obtained by the catalyst-assisted growth mode. This schematic shows that besides a predominant Ga-rich VLS-type growth in the axial direction, mediated by the preferential precipitation of Ga atoms over In atoms as supplied primarily by surface diffusion fluxes, also an In-rich InGaAs shell layer evolves at the sidewalls in a VS-type growth mode.

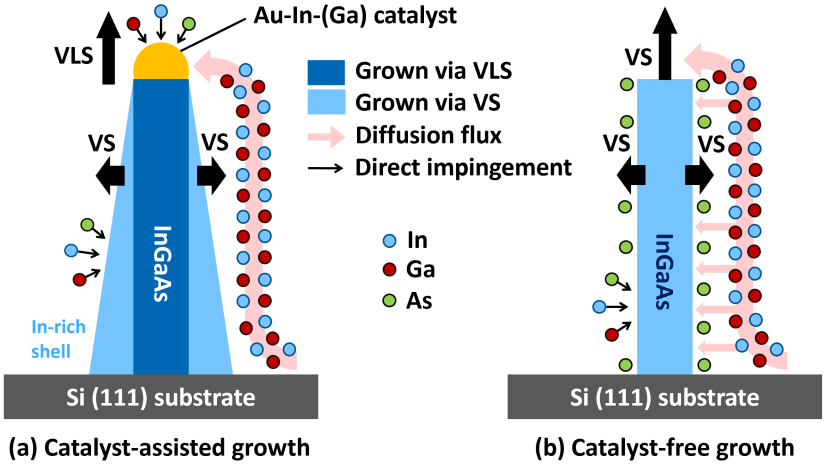


Figure I.14 – *Schematic illustrations of (a) Au-catalyst assisted growth of InGaAs NWs which commonly results in a VLS-type axial growth of a preferential Ga-rich InGaAs core and a VS-grown In-rich shell layer around, and (b) catalyst-free VS-type growth mode which produces typically higher compositional uniformity of InGaAs NWs. This growth mode is achieved mainly via the high anisotropies in growth rates of different facets, i.e., much higher growth rate along the axial [111] facet than compared to the {110} sidewall facets. From [78].*

Therefore, efforts have been made to use catalyst-free vapor-solid (VS) method to grow InGaAs NWs. Nevertheless, self-assembled NWs leads to random distribution and an inhomogeneity in the composition of NWs which deteriorates the electronic and optical properties. Shin et al. [80] demonstrated the growth of untapered and high aspect ratio self-assembled InGaAs NWs on Si substrate by MOVPE. A wide range of indium composition has been obtained varying from 20% to 100%. In comparison with catalyst-assisted NWs, the composition was far more homogeneous. However, despite the good composition homogeneity in a single InGaAs NW, significant composition variations was observed from one NW to another. This phenomenon was explained by the random NWs nucleation on the substrate and, therefore, the density of NWs. Indeed, due to the different diffusion lengths of Ga and In atoms, the incorporation ratio of Ga and In atoms is directly related to the NWs inter-distance. The latter may vary along the substrate due to the random distribution of the nucleation sites. Hertenberger et al. [81] investigated the evolution of the NWs composition and morphology according to growth parameters. In their study, they highlight the benefits of using patterned substrate to optimize composition homogeneity. As can be seen on the XRD spectra in Figure I.15, the full-width-at-half-maximum (FWHM) of the peak is thinner in the case of InGaAs NWs grown by SAG. This means that the NWs composition all over the substrate is far more homogeneous compared to self-assembled NWs.

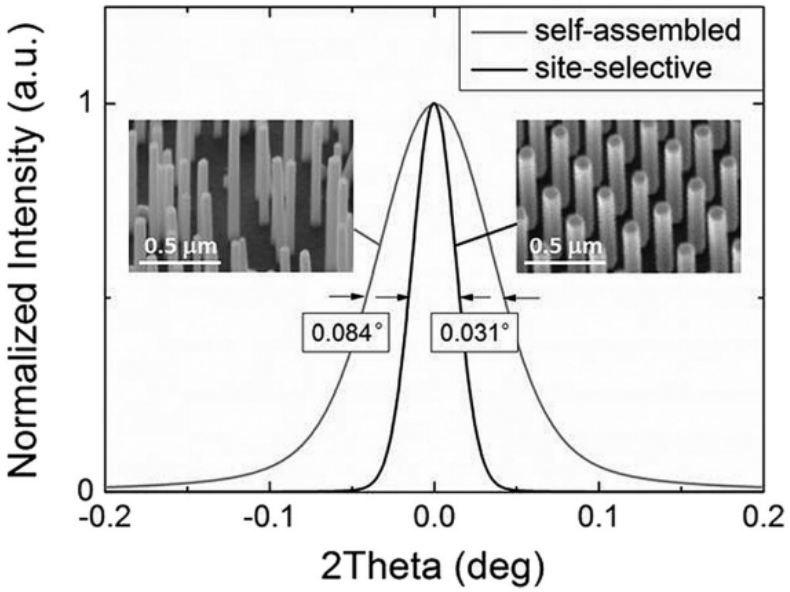


Figure I.15 – *Normalized intensity of the 2θ-InGaAs peak position (fixed at 2θ=0) comparing similarly grown site-selective $In_{1-x}Ga_xAs$ NWs [x(Ga)=0.07, black] and self-assembled $In_{1-x}Ga_xAs$ NWs [x(Ga)=0.08, grey]. Insets illustrate representative SEM images of the two different types of NWs. From [81].*

The SAG of InGaAs NWs with various compositions is still under investigation with few studies published to date. Very recently, Azimi et al. demonstrated the growth of InGaAs NWs with all compositions by MOVPE on GaAs(111)B substrate [82]. Concerning the growth on Si(111) substrate, various compositions were obtained by MOVPE and MBE [83, 84]. To our knowledge, no work on the growth of InGaAs NWs by HVPE is reported.

To conclude, we have discussed on the state-of-the-art of the growth of III-As NWs. In particular, we have shown that SAG of catalyst-free NWs results in homogeneous and well-ordered NWs arrays. This is interesting for both GaAs and InAs but also essential for the InGaAs. Thus, SAG allows NWs to be used as devices in many applications which is the subject of the next section.

## I.3.4 Target applications

As introduced in section I.1 (page 6), the NW geometry gives rise to specific properties, offering a wide range of applications. It allows an integration on low cost Si substrates while keeping high efficiency devices. In this section, we will only focus on target applications for the III-As NWs which are synthesized at Institut Pascal. Nonetheless, it should be noted that various applications can be achieved through III-As NWs such as: solar cells [8, 85, 86], lasers [64, 87], photodetectors [9, 88], field-effect transistors [89, 90] and light emitting diodes [91].

The motivations of growing III-As materials is part of a strong partnership between McMaster University and Université Clermont Auvergne. This collaboration led Institut Pascal, and more precisely the HVPE growth team to collaborate with Professor Ray LaPierre's group, specialized in the field of NWs epitaxy and NW-based devices. HVPE tends to be used for its main advantages, namely that it is a low-cost process with high growth selectivity and the possibility of implementing high growth rates. The two main target applications of my work are: the growth of GaAs NWs for betavoltaic cells and the growth of InAs and InGaAs NWs for infrared photodetectors. My thesis focuses on the growth of III-As NWs by HVPE and these applications are long-term goals. The primary objective is to obtain homogeneous arrays of long NWs over large areas in order to make devices.

### I.3.4.1 GaAs for betavoltaic cells

We will briefly explain the concept of betavoltaic generator without going into specific details. The goal is to understand why it is important to control the growth and the doping of GaAs NWs.

Betavoltaic (BV) generators, or nuclear batteries, are potential power supplies for applications which require a low power and long-lasting source [92]. BVs function similarly to photovoltaics: electron-hole pairs (EHPs) are excited in a semiconductor p-i-n junction and collected to create electricity. However, unlike photovoltaics, BVs harness the energy from $\beta$ particles as opposed to photons [93]. These $\beta$ particles, products of some radioactive decay reactions, provide input energy to the device over the half-life of the radioisotope in question. In addition, because the kinetic energy of the $\beta$ particles are on the order of keVs, thousands of EHPs can be generated from a single decay reaction. Nonetheless, the particle flux is much lower than that of solar photons so the overall device power output is on the order of nano/microwatts [94]. Due to the long half-life of common BV sources (tens to hundreds of years), the low instantaneous power output is offset by the long discharge time, which results in an energy density much higher than that of electrochemical cells [95]. Therefore, BVs fill a unique niche in power supply technologies. Finally, BVs are insensitive to environmental conditions which allows them to function at extreme temperatures or pressures without concern for malfunction or breakdown [96]. Such applications that benefit from BVs include biomedical implants, remote sensors, mobile microelectronics, and space exploration [92, 97, 98]. Challenges in these areas include infrequent access for maintenance, inability to rely on renewable sources (solar, wind), or exposure to conditions that would render electrochemical cells inoperable.

Figure I.16 shows specific energy versus specific power for various energy-storing devices (also called Ragone plot). This clearly shows that the power delivered is lower compared to current cells but that the lifetime of these devices is very long, which is of potential interest for many applications.

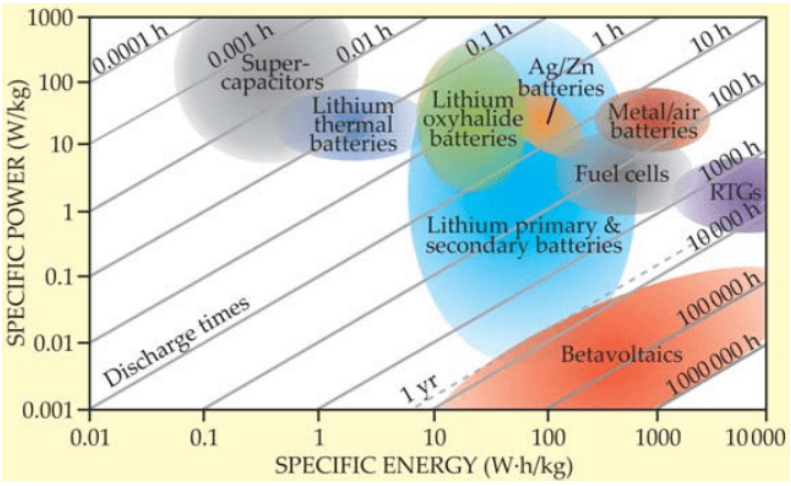


Figure I.16 – *Betavoltaics supply low power over a long lifetime, making them unique among energy-storage devices, including chemical batteries, fuel cells, supercapacitors, and radioisotope thermoelectric generators. From [93].*

The performance of BV devices is a function of radioisotope source characteristics, device geometry, and properties of the semiconductor converter. Where the radioisotope half-life alone determines the ultimate device lifetime, both the activity (the rate of decay multiplied by the number of radioactive atoms present) and the average $\beta$-decay energy dictate the total power input driving the generator [99]. Theoretical studies conducted by Devan Wagner in Professor Ray LaPierre's group highlighted the interest of GaAs as a betavoltaic cell [100]. His work focused on simulations of betavoltaic devices for several semiconductors: Si, GaAs and GaP. The simulated structures that he has performed are shown in Figure I.17.a and the results for the comparison between NWs and planars are shown in Figure I.17.b.

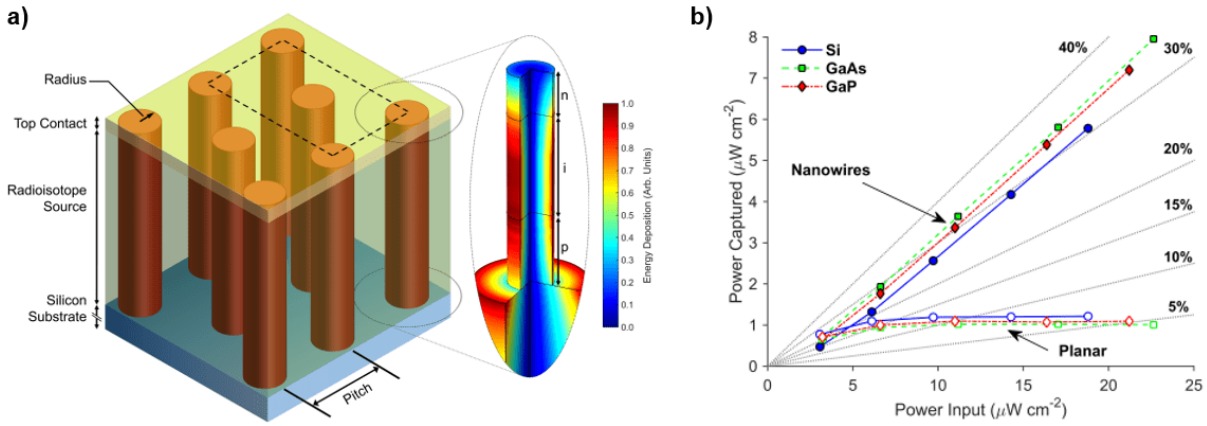


Figure I.17 – *a) Schematic (not to scale) of a NW BV device, showing a portion of the hexagonal array. The dashed box outlines a non-primitive unit cell used to examine radiation interactions, while the dotted circle indicates the outline of a single NW unit cell used in semiconductor charge transport simulations. The single NW on the right shows the various regions of the NW p-i-n diode, while indicating the relative energy deposition distribution within the device. b) A comparison of the captured power for optimized NW devices using nickel-63 and corresponding planar devices with the same power input. The grey lines indicate the energy capture efficiency. Adapted from [99].*

The simulated structure consists of nanowires p-i-n junction surrounded by a radioisotope source (here Nickel 63). The proposed structure is composed of a hexagonal array of axial NW p-i-n junction diodes grown on a Si substrate. It should be noted that radial (core-shell) NW structures are also possible but it has been found that axial NWs currently out-perform radial NWs in photovoltaic applications. Therefore, axial NWs has been the focus of this study [101]. With this design, energy capture can be increased by up to an order of magnitude over planar devices with an equivalent power input [102]. This large increase is achieved because the NW array surrounds the radioisotope, taking advantage of the isotropic $\beta$ particle emission, while the short path-length any $\beta$ particle must travel

to some semiconductor converter volume significantly reduces the self-shielding effect regardless of source activity [102]. In addition, the multiple semiconductor NWs provide $\beta$ particles with multiple opportunities to deposit their energy within the converting medium as they travel through the device. In Figure I.17.b is represented the evolution of the power captured according to the power input between NWs and planar layers for different semiconductors. It immediately appears a better power captured by the NWs. For example, for a power input of 15 μW/cm$^2$, the nanowires will capture 5 times more power than the planar layers. Thus, it is necessary to study the growth of NWs of GaAs but also the influence of doping in order to obtain a good p-i-n junction.

Finally, Dewan Wagner has shown that the length of NWs has a great influence on the efficiency of BV devices. On Table I.1 is given the evolution of the integrated captured power in GaAs NWs with a Nickel-63 source according to NW length.

| **Nanowire length (μm)** | 1.5 | 3.0 | 5.0 | 7.5 | 10 |
|---|---|---|---|---|---|
| **Integrated captured power (nW/cm$^2$)** | 714 | 1932 | 3642 | 5803 | 7953 |

Table I.1 – *Evolution of the integrated captured power in GaAs NWs with a Nickel-63 source according to NW length. Adapted from [100].*

From this table, it clearly appears an increase in the power captured by increasing the length of the NWs. Indeed, with 10 μm long NWs, the power captured is around ten times greater than with 1.5 μm long NWs. As it could be difficult and expensive to grow long NWs in MBE, HVPE is considered to grow long GaAs NWs at low cost. Thus, the objective is to make long NWs and to make the first doping studies of catalyst-free GaAs NWs which has never been done by HVPE. To conclude, it should be noted that in Ray LaPierre's laboratory, a NW-based BV device has been demonstrated for GaP NWs grown by MBE on Si substrate [102]. This first demonstration showed an efficiency of about 0.45%. My collaborative work with Ray LaPierre has enabled the establishment of an ANR project between McMaster University, CEA-IRIG and Institut Néel focusing on wide bandgap semiconductors such as AlN and GaN.

### I.3.4.2 InAs for multispectral infrared photodetectors

Sensing infrared (IR) light has proven valuable in the fields of optical fiber communication, chemical sensing and spectroscopy. Among IR photodetectors, the most widely used material system for IR image sensing is $Hg_{1-x}$ $Cd_x$Te (MCT) [103]. Nevertheless, the main disadvantage of MCT is its substrate. MCT is epitaxially grown on a lattice matched CdZnTe wafers [104, 105, 106].

These wafers are extremely costly, of small sizes and have a different thermal expansion coefficient than Si resulting in integration issues with Si readout integrated circuits (ROIC) [104, 105, 106]. To get an overview, the cost of a 6 inch (15.24 cm) diameter Si wafer is $\sim$ \$100 whereas a 7 x 7 $cm^2$ CdZnTe wafer costs \$10000 [107]. Nonetheless, MCT on Si exhibits higher dislocation density than MCT on CdZnTe [105]. Consequently, CdZnTe is still the preferred substrate for the development of high performance MCT-based IR detectors [106].

To overcome these problems, one solution considered is the multispectral photodetector. A multispectral photodetector has multiple absorption wavelength bands with negligible overlap [107]. Therefore, a multicolored image can be extracted containing the spectral information from each absorption wavelength bands [107]. An IR multispectral photodetector has various absorption bands in the IR spectrum [105, 107]. This multispectral IR detection is of paramount importance as it offers the ability of detecting the differences of temperature in diverse objects allowing a better contrast in the IR [107].

Based on aforementioned properties, NWs possess unique qualities for multispectral IR photodetector applications that are challenging and costly to perform with actual industry material systems and approaches for multispectral photodetectors, that is:

- **A better integration with Si ROIC:** NW-based multispectral photodetectors can be integrated with Si ROIC by directly fabricating them on Si substrate.
- **Inherent multispectral IR detection ability:** Geometry of NW and array pitch can be adjusted to achieve narrow spectral absorption bandwidth. This eliminates the need for supplementary spectral filter array above the photodetector array for multispectral detector design. Moreover, this reduces fabrication challenges. For example, for the bottom-up approach, this can be achieved by defining the pitch in a single lithography step and the NW diameter and length can be modulated by tuning the growth conditions.
- **NWs act as photodetector:** Axial and radial NW heterojunctions can be grown. Therefore, NWs not only absorb strongly light in specific spectral bands, but they can also convert absorbed photons into current.

These specific advantages are expected to significantly enhance multispectral photodetector device performance, but also to reduce device fabrication complexity and overall cost. Theoretical studies conducted by Khalifa Azizur-Rahman in Professor Ray LaPierre's group highlighted the interest of InAs as multispectral photodetector device [108]. The absorptance in vertical NW arrays is

typically dominated by three optical phenomena: (1) radial mode resonances, (2) near-field evanescent wave coupling, (3) and Fabry–Perot (F-P) mode resonances. The contribution of these optical phenomena to InAs NW absorptance was simulated using the finite element method (with COMSOL Multiphysics). The study compared the absorptance between finite and semi-infinite NW with varying geometrical parameters, including NW diameter (D), NW length (L) and array period (P). It should be noted that these simulations were performed for electromagnetic HE modes. The cell of NWs used for the simulations is schematized in Figure I.18.

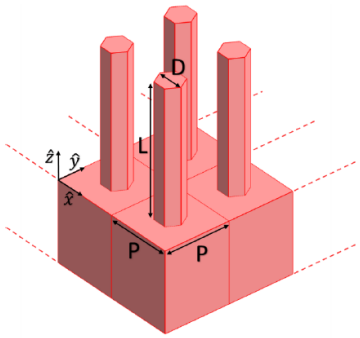


Figure I.18 – *Schematic of a NW array of period (P), NW length (L), and NW diameter (D). From [109].*

The results of the simulations for InAs NWs are presented in Figure I.19 with the absorptance dependence according to NWs diameter in Figure I.19.a and to NWs length in Figure I.19.b.

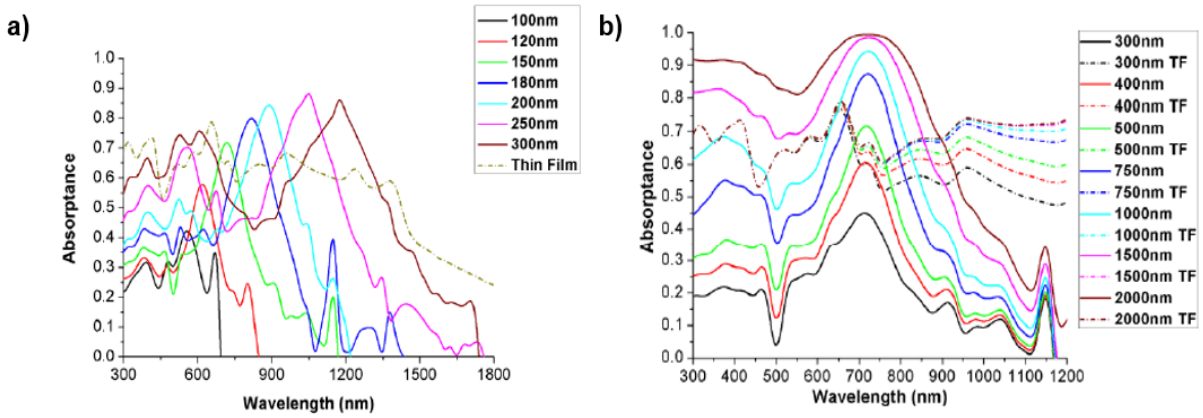


Figure I.19 – *a) Absorptance at L = 500 nm from NW tip in semi-infinite NWs for D = 100 nm to 300 nm for InAs NWs. P = 500 nm. The thin film absorptance of equal thickness is also shown for comparison. b) Absorptance of InAs NWs for different L along the semi-infinite NW axis. L was measured from the NW tip. Thin film (TF) absorptances for the same thickness are also plotted for comparison with the NWs. From [108].*

We can see in Figure I.19.a that the resonance peak wavelength of the HE1n radial modes is red-shifted with increasing D. For example, for NWs with a diameter of 150 nm the absorptance peak is located at approximately 750 nm whereas for a diameter of 300 nm the peak is located at approximately 1200 nm. Therefore, the peaks are located in the visible - short IR wavelength ranges. We can also have peaks in the mid-wavelength range by further increasing the NW diameter (300 to 700 nm) with a larger pitch of 1000 nm. Thus, unlike thin films, the position of the absorptance peak of NWs can be controlled by adjusting NW geometry and array pattern. This naturally makes NW-based multispectral photodetectors attractive because the NW geometry can be tuned to strongly absorb at a specified wavelength without the need for tuning the material bandgap or mounting additional spectral filters on top of the photodetector [110]. This main result shows that if we have NWs with different D and P on the same substrate, we can have absorptance peaks in several wavelength ranges on one and the same substrate. It should be noted that the upper wavelength limit of absorptance being the semiconductor bandgap, it is interesting to investigate low bandgap semiconductors such as InAs, InSb or InAsSb.

In Figure I.19.b we can see that at a specific absorptance wavelength, the absorption increases with the length of the NWs. For example, the absorbance goes from about 0.4 for NWs with a length of 300 nm to an absorptance close to 1 with NWs with a length of about 2 µm. Thus, in the same way that it is important to have long NWs of GaAs for BV applications, it is essential to grow long InAs NWs for IR applications.

### I.3.4.3 InGaAs for infrared applications

As discussed previously, a particular interest lies in the growth of InGaAs material because of its widely tunable bandgap energies or wavelengths (from 880 to 3500 nm) and high electron mobility. As shown previously in Figure I.8 (page 14), the fraction of indium in the ternary alloy makes it possible to modify the bandgap of the material. Therefore, it is possible to cover a wide range in the infrared domain. The main motivation here is that the growth of InGaAs NWs by HVPE has never been thoroughly investigated and published.

To conclude, the majority of applications introduced in this section need particular NWs characteristics with specific length and diameter. The morphology can be tuned by a precise control of the growth conditions. Now that we have presented the main motivations for the growth of III-As NWs by HVPE, we will describe the HVPE reactor used at Institut Pascal.

# I.4 SAG-HVPE of III-As nanowires

## I.4.1 Experimental setup

The reactor used in our laboratory is a home-made hot wall reactor working at atmospheric pressure. The reactor is made of quartz which guarantees a great thermal stability even at high temperature (up to 1000 °C). In order to ensure a laminar flow above the substrate and a homogeneous mixture of the vapor phase, the geometry and the total flow of the reactor are optimized. The reactor is divided into three zones, heated by a six-zone furnace. A schematic of the HVPE reactor is shown in Figure I.20.

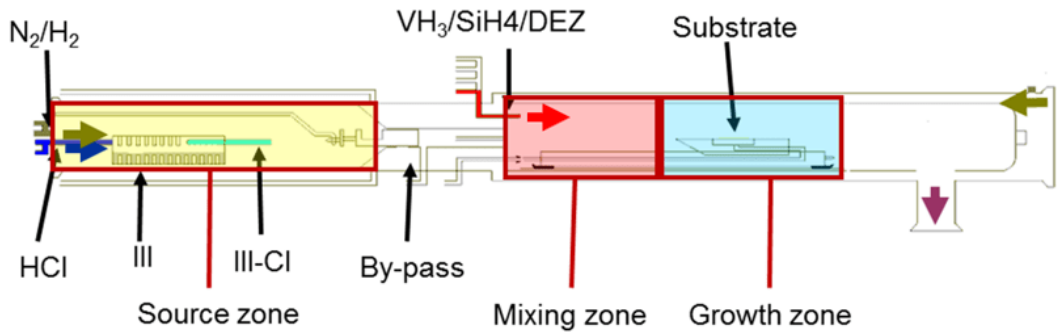


Figure I.20 – *Schematic of the HVPE reactor of Institut Pascal for the growth of III-As semiconductors. The reactor was designed and custom-built by the HVPE team of the laboratory.*

In the source zone (in yellow), $H_2$ carrier gas is introduced and III-chloride gaseous precursors (InCl and GaCl) are produced by reacting HCl gas with liquid indium and gallium at 730 °C. To control the supersaturation (i.e. the thermodynamic driving force) of the growth reaction, additional HCl can be introduced in this zone. The supersaturation is a crucial parameter for the growth by HVPE and will be presented in the next section. Regarding element V precursors, arsine gas ($AsH_3$) is introduced in the downstream mixing zone of the reactor (in red) heated at higher temperature to ensure a homogeneous mixing of the gas phase and to reduce parasitic nucleation upstream of the substrate, since the reactions involving chloride molecules are exothermic. It is possible to dope the sample during growth by introducing diethylzinc (DEZ: $(C_2H_5)_2Zn$) for p-doping or silane for n-doping ($SiH_4$) in this zone. It should be noted that the DEZ is maintained at a certain temperature in a thermostatically controlled bath, therefore, the DEZ flow rate strongly depends on the bath temperature $\theta_{DEZ}$. The last zone is the deposition zone (in blue) which is heated at the lowest temperature so that the reaction is favored on the substrate. The mixing and the deposition zones are connected with the source zone

through a manual-controlled drawer-valve. This latter allows the preparation of the different species without any unwanted deposition upstream of the substrate. Gas flows are manually controlled using valves and flowmeters and the gas flows are distributed in standard cubic centimeters per minute (sccm).

It turns out that SAG-HVPE (selective area growth HVPE) has a major advantage which is the almost non-existent adsorption of chloride precursors on the dielectric mask. Nevertheless, a significant obstacle persists which is to obtain patterned substrates at the nanometric scale, as explained in the following section.

## I.4.2 Foreword on SAG at nanoscale

### I.4.2.1 SAG-HVPE for high selectivity

The low adsorption of chloride precursors on the dielectric mask allows, when the mask is of good quality, to obtain very high selectivity over a large area. As an example, in Figure I.21 is illustrated a remarkable large field SEM images of GaAs NWs obtained during my work (more detailed in section II.2.3 on page 67).

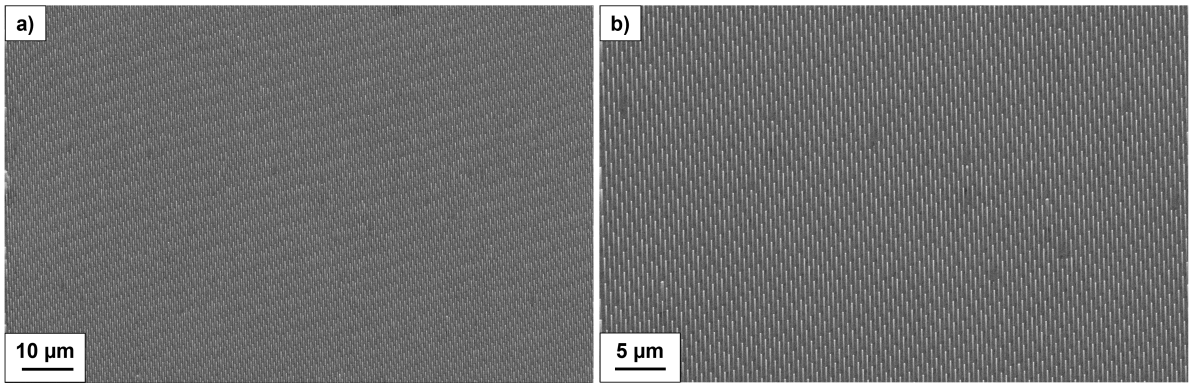


Figure I.21 – *Large field SEM images of p-doped GaAs NW array on patterned GaAs(111)B substrate showing an example of high selectivity obtained by SAG-HVPE.*

Thus, HVPE proves itself to be a powerful tool for obtaining high selectivity which is crucial for the epitaxy of NW-based devices. Nevertheless, the supply of high quality patterned substrate at nanoscale remains a major problem to overcome as we detail in the next section.

### I.4.2.2 The patterned substrate supply problem

When we wish to carry out SAG of NWs at a nanometric scale, a major problem arises which is obtaining good quality patterned substrate. Today, only EBL provides diameter apertures of around ten nanometers but it is a very expensive technique and it is not accessible in all laboratories. Whatever the method used, the process of obtaining patterned substrates is complex, expensive and very sensitive to the different technical parameters. In addition, it is very complicated to procure patterned substrates because there are mainly fabricated by research laboratories and not by industrial ones. Thus very few patterned substrates were available during my thesis work, which limited the extent of the experimental studies that could be carried out. In the following section are presented the details of the patterned substrates that I have used.

### I.4.2.3 Details of the substrates used in this work

SAG was performed on patterned GaAs(111)B and Si(111) substrates. The details of the substrates used in chapters II and III are reported in Table I.2.

| | **Substrate name** | **Substrate nature** | **Pitch (µm)** | **Apertures diameter (nm)** | **Dielectric mask** | **Patterning technique** |
|---|---|---|---|---|---|---|
| **Chapter II** | #Bath | undoped GaAs(111)B | 1 | 340 | 35 nm $SiN_x$ | PECVD + DTL |
| | #IBM1 | p-doped GaAs (111)B | 1 or 2 | 80 | 35 nm $SiO_x$ | PECVD + EBL |
| **Chapter III** | #IBM2 | undoped GaAs(111)B | 2 | 60 | 35 nm $SiO_x$ | PECVD + EBL |
| | #AC121A | p-doped Si(111) | 1.75 or 3.50 | 350 | 100 nm $SiN_x$ / 20 nm $SiO_x$ | PECVD + EBL |

Table I.2 – *Details of the patterned substrates used in this work.*

For all of the substrates, the layers were deposited by plasma-enhanced chemical vapor deposition (PECVD). They were either patterned by displacement talbot lithography (DTL) or by electron beam lithography (EBL). More details of DTL can be found in Coulon et al [111]. The substrate #Bath is the result of collaborations with Philip Shields from the University of Bath and #IBM1 and

#IBM2 are the result of collaborations with Heinz Schmid from IBM Zurich. Due to the lack of good quality Si(111) substrate, I had to use #AC121A which is an old substrate manufactured more than 10 years ago within a collaboration with CEA-Leti in Grenoble. This probably impacted the growth process on Si(111) as we discuss in the next section. Finally, it should be noted that patterned Si(111) substrates were fabricated at McMaster University but did not result in any significant results probably due to the thickness of the dielectric mask or chemical etching issues.

### I.4.2.4 The difficulty of nucleation on silicon substrate

The III/V growth community has always been interested in integration on silicon substrates. Among the motivations for using Si substrates, we can mention the very low cost of the substrates (compared to III/V substrates), the fact that it is the most widely used semiconductor in industry and the desire to integrate III/V into already existing Si platforms. Nevertheless, the heteroepitaxy of III/V materials on Si substrate is still a challenge to overcome due to the lattice mismatch, the difference of thermal expansion coefficients and the difference of polarity. Therefore, growth of III/V materials on Si substrate is a complex task and the nucleation is very sensitive to the chemical etching of the substrate and the purity conditions of the reactor. Moreover, the oxidation of Si is very fast in HVPE because the reactor works at atmospheric pressure. During the studies on GaAs NWs (chapter II), I conducted many experiments on Si(111) substrate which resulted in no growth and it appeared, later, that the $H_2$ purifier was faulty. Consequently, impurities were present in the reactor which could have prevented efficient nucleation in the holes of the patterned substrate. In addition, the $N_2$ generator, which allows a continuous flow of $N_2$ sweeping in the reactor between the growths, broke down several times. This probably brought impurities into the reactor such as oxygen or carbon. Finally, as explained previously, the #AC121A substrates were manufactured more than 10 years ago, which could also have influenced the nucleation step. Consequently, Chapter II focused only on the growth of GaAs NWs on patterned GaAs(111)B substrate.

This section allowed us to present the gaseous species present in HVPE and the issues that appear for the SAG at nanoscale. In order to determine the growth conditions leading to the growth of III-As materials, it is necessary to address the thermodynamic and kinetic considerations of HVPE growth. This is the content of the next section.

# I.5 Thermodynamics of III-As condensation in HVPE environment

HVPE is a near-equilibrium process which involves III-chlorides precursors (GaCl and InCl) and $AsH_3$/$As_2$/$As_4$ as element V precursors. Thermodynamic calculations allow us to establish the gaseous species that interact with the substrate surface, in particular for $AsH_3$ that decomposes into $As_2$/$As_4$ when it arrives in the hot wall reactor. Thermodynamics of the global deposition reaction allows us to determine if either growth or etching of the solid will happen.

## I.5.1 Composition of the vapor phase

The partial pressures of the different gaseous species present in the growth zone are calculated as a function of the gas flows introduced in the reactor. Then, the partial pressures obtained are used to predict the optimal conditions for the growth of III-As materials.

### I.5.1.1 Formation of III-Cl precursors

As explained in section I.4.1, III-chloride gaseous species ($GaCl_g$ and $InCl_g$) are produced in the source zone by reacting HCl gas with liquid gallium and liquid indium heated at 730 °C. It has been shown by V. S. Ban that for temperature above 725 °C, the chemical reactions of gaseous HCl with liquid gallium or indium produce exclusively the mono-chloride species [112]. Consequently, only InCl and GaCl are present in the vapor phase. For InCl, the corresponding equation is written:

$$In_l + HCl_g \rightleftharpoons InCl_g + \frac{1}{2}H_{2g} \tag{I.2}$$

where we can notice that $H_2$ is a product of the reaction.

Hence, an essential point is to estimate the yield of the reaction in order to calculate the number of HCl molecules that do not react with the liquid source. This mostly depends on the source temperature and the gas speed. In our set-up, the gas speed is 0.1 cm/s which is low enough to consider that any material input ($HCl_g$ on $In_l$) pushes the reaction towards equilibrium. Therefore, we can introduce the equilibrium constant of the reaction (I.2) as follows:

$$K_{InCl} = \frac{[InCl]_1 \times [H_2]_1^{1/2}}{[HCl]_1} \tag{I.3}$$

with $[InCl]_1$ the InCl partial pressure at the exit of the liquid indium cell (labelled 1).

Knowing the input flow rates of HCl and $H_2$ ($d^{in}_{HCl}$ and $d^{in}_{H_2}$), the partial pressures at the source output are calculated using the principle of conservation of the different species H and Cl.

For the H atoms:

$$d^{in}_{HCl} + 2d^{in}_{H_2} = d_1([HCl]_1 + 2[H_2]_1) \tag{I.4}$$

For the Cl atoms:

$$d^{in}_{HCl} = d_1([HCl]_1 + [InCl]_1) \tag{I.5}$$

where $d_1$ is the total flow rate at the source output. As the HVPE reactor works at atmospheric pressure, we can write that the sum of the partial pressures at the outlet of the indium source is:

$$[HCl]_1 + [InCl]_1 + [H_2]_1 = 1 \tag{I.6}$$

The system constituted by the equations (I.3) to (I.6) can be solved using the Newton's iterative method. It allows the calculation of the partial pressures of the different species $[InCl]_1$, $[HCl]_1$ and $[H_2]_1$ and the flow rate $d_1$ at the outlet of the In source. The same reasoning is applied to the gallium source to calculate $[GaCl]_2$, $[HCl]_2$, $[H_2]_2$ which are the partial pressures of GaCl, HCl and $H_2$, and $d_2$ which is the total flow rate at the outlet of the Ga source.

### I.5.1.2 $AsH_3$ decomposition

For temperatures above 600 °C, the thermodynamic study predicts an almost complete decomposition of $AsH_3$ [113]. This decomposition (or cracking) takes place in the hot tube that carries the element V species in the mixing zone of the reactor. The corresponding reaction is given by:

$$AsH_{3g} \rightleftharpoons \frac{1}{2}As_{2g} + \frac{3}{2}H_{2g} \tag{I.7}$$

$As_{2g}$ species are in equilibrium with $As_{4g}$ following the equation:

$$\frac{1}{2}As_{2g} \rightleftharpoons \frac{1}{4}As_{4g} \tag{I.8}$$

To calculate the partial pressures resulting from the cracking of $AsH_3$, we have to introduce the cracking yield $r_{As}$ given by:

$$r_{As} = 1 - \frac{N_{AsH_{3g}}}{N^{in}_{AsH_{3g}}} \tag{I.9}$$

with $N_{AsH_3}$ the number of undecomposed $AsH_3$ at the output of the tube and $N^{in}_{AsH_3}$ the number of $AsH_3$ molecules introduced in the reactor. Thus, we can write:

$$N_{AsH_{3g}} = (1 - r_{As})N^{in}_{AsH_{3g}} \tag{I.10}$$

$$N_{As_{2g}} = \frac{1}{2} r_{As} N^{in}_{AsH_{3g}} \tag{I.11}$$

$$N_{H_{2g}} = \frac{3}{2} r_{As} N^{in}_{AsH_{3g}} + N^{in}_{H_{2g}} \tag{I.12}$$

We can deduce the total flow rate ($d_3$) at the tube outlet by using the principle of conservation of arsenic species:

$$d_3 = (1 + r_{As}) d^{in}_{AsH_3} + d^{in}_{H_2} \tag{I.13}$$

where $d^{in}_{AsH_3}$ and $d^{in}_{H_2}$ are the input flow rates of $AsH_3$ and $H_2$.

Therefore, we can determine the partial pressures of $AsH_{3g}$, $As_{2g}$ and $H_{2g}$ at the outlet of the tube according to $d_3$:

$$[AsH_3]_3 = (1 - r_{As}) d^{in}_{AsH_3} / d_3 \tag{I.14}$$

$$[As_2]_3 = \frac{1}{2} r_{As} d^{in}_{AsH_3} / d_3 \tag{I.15}$$

$$[H_2]_3 = (\frac{3}{2} r_{As} d^{in}_{AsH_3} + d^{in}_{H_2}) / d_3 \tag{I.16}$$

Now that we have calculated the partial pressures of III and V precursors in the upstream zones of the reactor, we can calculate the partial pressures of these species in the growth zone.

### I.5.1.3 Partial pressures in the growth zone

Knowing the partial pressures and the flow rates of gaseous species coming from the source zone and the arsenic tube, we can determine the partial pressures and the total flow rate ($d_T$) in the growth zone by solving the following system of equations:

$$d_1 [InCl]_1 = d_T [InCl] \tag{I.17}$$

$$d_2 [GaCl]_2 = d_T [GaCl] \tag{I.18}$$

$$d_1 [HCl]_1 + d_2 [HCl]_2 + d_{HCl_{add}} = d_T [HCl] \tag{I.19}$$

$$d_3([AsH_3]_3 + 2[As_2]_3 + 4[As_4]_3) = d_T([AsH_3] + 2[As_2] + 4[As_4]) \tag{I.20}$$

$$d_3 [AsH_3]_3 = d_T [AsH_3] \tag{I.21}$$

$$K_{As}(T) = \frac{[As_4]^{\frac{1}{4}}}{[As_2]^{\frac{1}{2}}} \tag{I.22}$$

$$2d_1[H_2]_1 + 2d_2[H_2]_2 + d_3(2[H_2]_3 + 3[AsH_3]_3) + 2d_{H_{2vector}} = d_T(2[H_2] + 3[AsH_3]) \tag{I.23}$$

$$[InCl] + [GaCl] + [AsH_3] + [As_2] + [As_4] + [HCl] + [H_2] = 1 \tag{I.24}$$

This system is solved using the Newton's iteration method. As an example for the growth of InGaAs, the evolution of partial pressures of species as a function of temperature is illustrated in Figure I.22. We can see that the partial pressures of InCl, GaCl, HCl and $As_4$ species are constant over the temperature range. The partial pressure of $As_2$ (in pink), considered at equilibrium with $As_4$, increases with the temperature. Nevertheless, its value is very low compared to $As_4$. Consequently only $As_4$ species will be consider for the growth of III-As in this work. Once the partial pressures are determined, we can calculate the partial pressure III/V ratio in the growth zone which is defined as:

$$III/V = \frac{P_{III-Cl}}{P_{As_4}} \tag{I.25}$$

We can also use the atomic III/V ratio, noted $I_3/I_5$, as it is the case in chapter II and III. It is expressed as:

$$\frac{I_3}{I_5} = \frac{1}{4}\frac{P_{III-Cl}}{P_{As_4}} \tag{I.26}$$

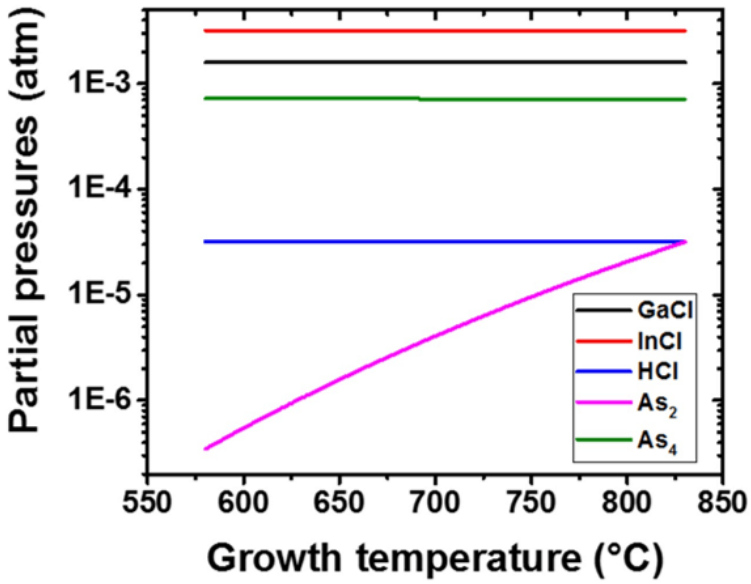


Figure I.22 – *Evolution of partial pressures in the growth zone according to temperature for the growth of InGaAs material.*

Knowing the composition of the vapor phase in the growth zone above the substrate, we can now move to the thermodynamic and kinetic aspects of III-As condensations by HVPE.

## I.5.2 Thermodynamics of III-As growth

### I.5.2.1 GaAs and InAs binaries

Here, we focus on the condensation of InAs and GaAs materials, described by the following equations:

$$GaCl_g + \frac{1}{4}As_{4_g} + \frac{1}{2}H_{2_g} \rightleftharpoons GaAs_s + HCl_g \tag{I.27}$$

$$InCl_g + \frac{1}{4}As_{4_g} + \frac{1}{2}H_{2_g} \rightleftharpoons InAs_s + HCl_g \tag{I.28}$$

These reactions are considered at thermodynamic equilibrium. Therefore, we can write the equality of the chemical potentials of each reaction to determine their respective equilibrium constants. We take the GaAs deposition as an example, given that the same reasoning can be applied to InAs deposition.

The equality of the chemical potentials allows us to write:

$$\mu_{GaAs} + \mu^0_{HCl_g} - \mu^0_{GaCl_g} - \frac{1}{4}\mu^0_{As_{4g}} - \frac{1}{2}\mu^0_{H_{2g}} = +k_B T ln\left(\frac{[As_4]^{1/4}_{eq}[H_2]^{1/2}_{eq}[GaCl]_{eq}}{[HCl]_{eq}}\right) \tag{I.29}$$

with $\mu^0_{i_g}$ the standard chemical potential of species $i$ at equilibrium.

Then, the equilibrium constant for GaAs deposition is defined as:

$$K^{eq}_{GaAs}(T) = \left(\frac{[As_4]^{1/4}_{eq}[H_2]^{1/2}_{eq}[GaCl]_{eq}}{[HCl]_{eq}}\right) \tag{I.30}$$

with $T$ the temperature in the growth zone. The equilibrium constant $K^{eq}_{GaAs}(T)$ is determined from the Gibbs free energy of the reaction $\Delta G(T)$ at the growth temperature T thanks to the following equation:

$$K^{eq}_{GaAs}(T) = exp(\frac{-\Delta G(T)}{RT}) \tag{I.31}$$

$\Delta G(T)$ is calculated from tables of thermodynamic data relative to the species involved in the reaction.

The supersaturation of the vapor phase, noted $\gamma$, determines whether the formation or the etching of the solid GaAs is favored. In other words, whether the reaction (I.27) is driven towards the right or the left side, respectively. This $\gamma$ depends on the equilibrium constant $K^{eq}_{GaAs}(T)$ and the ratio of the partial pressures of the species involved in the reaction [114, 115]:

$$\gamma_{GaAs} = \frac{[GaCl][As_4]^{1/4}[H_2]^{1/2}}{[HCl]K^{eq}_{GaAs}(T)} - 1 \tag{I.32}$$

In the same way as for the formation of GaAs, we can define the supersaturation for the formation of InAs by the expression:

$$\gamma_{InAs} = \frac{[InCl][As_4]^{1/4}[H_2]^{1/2}}{[HCl]K^{eq}_{InAs}(T)} - 1 \tag{I.33}$$

The supersaturation $\gamma$ is the parameter used to measure the deviation of the reaction from its equilibrium. Depending on its sign, we can predict if the growth is favored or not:

- $\gamma = 0$ corresponds to equilibrium between reactants and products.
- $\gamma > 0$ corresponds to the formation of the solid.
- $\gamma < 0$ corresponds to the etching of the solid.

If we consider the deposition of GaAs material, according to Equation (I.32), $\gamma_{GaAs}$ can be varied by controlling the amount of $HCl_g$, $GaCl_g$ or $H_{2g}$ introduced in the reactor. Thus, by introducing additional HCl, it is possible to control the supersaturation. This is why HVPE reactors are often equipped with an independent line of HCl flow. The partial pressures of the gaseous species are obtained from the resolution of the equation of the equilibrium constants, the conservation of mass and total pressure inside the reactor during growth (1 atm).

As mentioned above, HVPE is considered as a near equilibrium growth process. Indeed, according to Stringfellow's calculations for the growth of GaAs material at 1000 K, HVPE exhibits a Gibbs free energy $\Delta G$ of the deposit reaction that is eight times lower than for MOVPE and MBE. As illustrated in Figure I.23, the thermodynamic driving force for growth by HVPE is relatively low in comparison with the far from equilibrium techniques which are MOVPE and MBE [116].

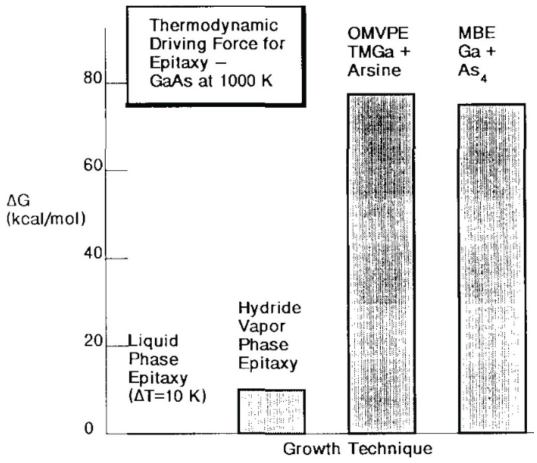


Figure I.23 – *Estimated thermodynamic driving force, Gibbs free energy difference between reactants and products, for several epitaxial growth processes. All calculations are for the growth of GaAs at 1000 K. From [116].*

As the thermodynamic driving force for the growth by HVPE is low, the growth process operates at near-equilibrium conditions. Experimentally it has been shown that by controlling the supersaturation, a wide range of growth rates can be obtained from 3 µm/h to 100 µm/h [1]. This is due to the high dechlorination frequency of element III precursors that allows the system to return quickly to its equilibrium state without any kinetic limitations. That is true whether the supersaturation has a low or high value. Indeed, on increasing the supersaturation, dechlorination frequency is high enough to avoid kinetic limitation; the return to equilibrium, which produces the solid, takes place quickly [117]. By decreasing the supersaturation, a reversible process occurs at the interface due to the volatility of the chlorides. This feature characterizes a near-equilibrium process, which gives the interesting possibility of modulating the growth rate by varying the mass input rate of the reactants. Now that we have presented the thermodynamics for the binaries, we describe the thermodynamics for the ternary InGaAs in the next section.

### I.5.2.2 InGaAs ternary

In the ternary alloy InGaAs, Ga and In atoms are distributed in the sub-lattices of the elements III. The alloy is considered as a pseudo-binary $A_xB_{1-x}$ where $A$ and $B$ are InAs and GaAs, respectively. The interaction energy between atoms of the $AB$ alloy is calculated using the mean-field approximation of Bragg-Williams:

$$E = \frac{N_A}{2} j\phi_{AA} + \frac{N_B}{2} j\phi_{BB} + \nu_{AB}\phi \tag{I.34}$$

where $N_A$ and $N_B$ are the numbers of atoms A and B, respectively. j is the number of first neighbours atoms, and $\nu_{AB}$ is the number of A-B bonds in the structure. $\phi_{lm}$ is the potential energy of interaction between one atom $l$ and one atom $m$:

$$\phi = \phi_{AB} - \frac{\phi_{AA} + \phi_{BB}}{2} \tag{I.35}$$

We can also write E as following:

$$E = E_0 + \nu_{AB}\phi \tag{I.36}$$

where $E_0$ is independent of the atomic distribution.

The number of A-B bonds in the alloy $A_xB_{1-x}$ is given by:

$$\nu_{AB} = xNj(1-x) = N_A j\left(1 - \frac{N_A}{N_A + N_B}\right) \tag{I.37}$$

with N the total number of atoms.

The chemical potential of the atom A is defined using the variation of the free energy F of the system:

$$\mu_A = \left(\frac{\partial F}{\partial N_A}\right)_{N_B} \tag{I.38}$$

where $F = -k_B T ln(Z)$ and Z is the partition function of the system at equilibrium, given by:

$$Z = \frac{N!}{N_A!(N-N_A!)} exp\left(-\frac{E}{k_B T}\right) \tag{I.39}$$

Then, using the regular solution model [118], we can write:

$$\mu_A = \frac{j}{2}\phi_{AA} + j.\phi(1-x)^2 + k_B T ln(x) \tag{I.40}$$

with $x$ the A content in the alloy.

The chemical potential is described by the sum of a standard potential of material A without any interaction ($\mu_A^* = \frac{j}{2}\phi_{AA}$) and an interaction term within the ternary alloy. We define the activity coefficient $\alpha_A$ of A in the alloy $A_x B_{1-x}$ by:

$$\alpha_A = exp\left(\frac{(1-x)^2 j\phi}{k_B T}\right) = exp\left(\frac{(1-x)^2 \Omega}{k_B T}\right) \tag{I.41}$$

with $\Omega = j\phi$, the energy interaction parameter.

Then:

$$\mu_A = \mu_A^* + k_B T ln(x\alpha_A) \tag{I.42}$$

The same approach is used for the binary B. Its chemical potential in the alloy $A_x B_{1-x}$ is given by:

$$\mu_B = \mu_B^* + k_B T ln((1-x)\alpha_B) \tag{I.43}$$

with

$$\alpha_B = exp\left(\frac{x^2 \Omega}{k_B T}\right) \tag{I.44}$$

With these considerations, we can write the variation of the chemical potential of the binaries InAs and GaAs in the alloy $In_x Ga_{1-x}As$:

$$\Delta\mu_{InAs} = \mu_{InAs_s}^* + \mu_{HCl_g}^0 - \mu_{InCl_g}^0 - \frac{1}{4}\mu_{As_{4g}}^0 - \frac{1}{2}\mu_{H_{2g}}^0 - k_B T ln(Q_{InAs}(x,T)) \tag{I.45}$$

$$\Delta\mu_{GaAs} = \mu_{GaAs_s}^* + \mu_{HCl_g}^0 - \mu_{GaCl_g}^0 - \frac{1}{4}\mu_{As_{4g}}^0 - \frac{1}{2}\mu_{H_{2g}}^0 - k_B T ln(Q_{GaAs}(x,T)) \tag{I.46}$$

where:

$$Q_{InAs}(x,T) = \frac{[InCl][As_4]^{1/4}[H_2]^{1/2}}{[HCl]x\alpha_{InAs}} \tag{I.47}$$

$$Q_{GaAs}(x,T) = \frac{[GaCl][As_4]^{1/4}[H_2]^{1/2}}{[HCl](1-x)\alpha_{GaAs}} \tag{I.48}$$

with $[i]$, the partial pressure of species i interacting with the substrate during growth.

Condensation (growth) or sublimation is determined considering the variation of the chemical potential $\Delta\mu$, defined by the extent of the reaction of deposition with respect to its equilibrium:

$$\Delta\mu = \mu^0_{products} - \mu^0_{reactants} - k_B T ln\left(\frac{a_{reactants}}{a_{products}}\right) \tag{I.49}$$

$a_{reactants}$ and $a_{products}$ are the activities of the reactants activity and the products, respectively.

At equilibrium, $\Delta\mu = 0$, thus:

$$\Delta\mu^0 = k_B T ln\left(\frac{a_{reactants}}{a_{products}}\right)_{equilibrium} \tag{I.50}$$

The extent of reaction reads:

$$\Delta\mu = k_B T ln\left(\frac{(a_{reactants}/a_{products})_{equilibrium}}{(a_{reactants}/a_{products})}\right) \tag{I.51}$$

As written, negative $\Delta\mu$ means that growth occurs.

The supersaturation of the vapor phase $\gamma$ is related to the thermodynamic force to restore equilibrium, that is the excess of chemical potential with respect to equilibrium of the reaction at temperature T:

$$\Delta\mu = -k_B T ln(1+\gamma) \tag{I.52}$$

Then:

$$\Delta\mu < 0 \quad \Rightarrow \quad \gamma > 0 \tag{I.53}$$

Thus, as explained previously, the growth takes place for $\gamma > 0$. For the growth of $In_xGa_{1-x}As$, the relative supersaturations of the vapor phase related to InAs and GaAs are given by:

$$\gamma_{InAs}(x,T) = \frac{[InCl][As_4]^{1/4}[H_2]^{1/2}}{[HCl]x\alpha_{InAs}} \frac{1}{K^{eq}_{InAs}(T)} - 1 \tag{I.54}$$

$$\gamma_{GaAs}(x,T) = \frac{[GaCl][As_4]^{1/4}[H_2]^{1/2}}{[HCl](1-x)\alpha_{GaAs}} \frac{1}{K^{eq}_{GaAs}(T)} - 1 \tag{I.55}$$

Finally for the growth of InGaAs material, the composition is a function of the growth rate of the InAs and GaAs binaries in the ternary. The composition can be adjusted by simply changing GaCl and InCl partial pressures. Therefore, from a thermodynamic point of view, it should be possible to grow InGaAs material using HVPE while covering the full range of composition.

To conclude, we have described the thermodynamics that govern growth of III-As materials by HVPE. This allowed us to identify the species involved and to predict the evolution of the reaction as a function of the experimental parameters (growth temperature and composition of the vapor phase). However, thermodynamics only describes the interaction between the vapor phase and the solid. As a matter of fact, thermodynamics fails to predict the evolution of the system at low temperature. Indeed, thermodynamics foretells better growth at low temperature depending on the evolution of adsorption/desorption with temperature, whereas experimentally, no growth or slow growth is observed. Thus, in order to be able to actually describe the system (especially at low temperature), it is necessary to develop kinetic modeling of the elementary steps of the condensation, not only adsorption/desorption of vapor species onto the surface, but also surface diffusion of ad-species and dechlorination frequency of AsIIICl ad-species. Such more accurate description is necessary when it comes to taking advantage of growth anisotropy of the crystal facets to generate micro/nanostructures with various morphologies. The kinetics of HVPE growth is presented in the next section.

# I.6 Kinetics aspect of HVPE process

A kinetic model describing the homoepitaxial growth of GaAs on GaAs(100) substrate has been developed in our group by R. Cadoret, A. Pimpinelli and E. Gil [114, 115]. In this model, the global growth reaction is decomposed into three steps: (1) adsorption of group III and V atoms on the surface, (2) dechlorination step where several mechanisms are proposed as a function of the vapor phase composition and temperature and (3) the diffusion of the adatoms to the nucleation sites in the semi-crystal. The reaction starts with the adsorption of arsenic atoms on the vacant sites of the surface (Figure I.24.a). Then GaCl molecules are adsorbed on the surface, resulting in the formation of a stable chemisorbed As-GaCl complex. The final step is the chlorine desorption from the As-GaCl complex. This step determines the kinetics of the whole process since it is the slowest step. Two different mechanisms are proposed to describe the dechlorination. The first one is the desorption of the Cl atom as $HCl_g$ with the help of $H_{2_g}$. The second one consists in the adsorption of a second layer of GaCl, followed by the desorption of $GaCl_3$. This second mechanism takes place when the adsorption of GaCl molecules is very high. In this work the growth conditions used to grow III-As correspond to growth governed by the first $H_2$ mechanism as illustrated in Figure I.24.a.

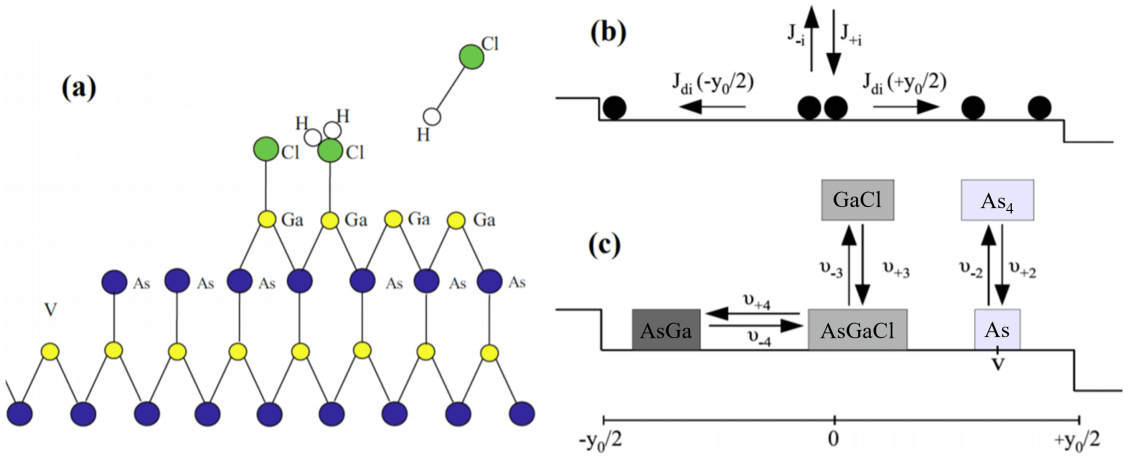


Figure I.24 – *Schematic representation of (a) the $H_2$ dechlorination mechanism of the ad-species AsGaCl, (b) the surface process (adsorption, desorption and diffusion) on a vicinal substrate presenting terraces of width equal to $y_0$ and (c) the growth steps of GaAs from $As_{4g}$ and $GaCl_g$, the adsorption and desorption frequencies of ad-species are represented by $\nu_{+i}$ and $\nu_{-i}$, respectively. The dechlorination and chlorination frequencies of AsGaCl are represented by $\nu_{+4}$ and $\nu_{-4}$, respectively. Adapted from [114].*

The different reactions described in Figure I.24.c can be written as follows:

$$4V + As_{4g} \rightleftharpoons 4As \tag{I.56}$$

$$As + GaCl_g \rightleftharpoons AsGaCl \tag{I.57}$$

$$AsGaCl + H_{2g} \rightleftharpoons AsGa_c + HCl_g + \frac{1}{2}H_{2g} \tag{I.58}$$

where V represents a vacant site, the index g and c indicate gaseous species and incorporated crystal, respectively.

The kinetic model is based on the near-field approximation of Eyring's theory that allows the calculation of adsorption flux $J_{+i}$ and desorption flux $J_{-i}$ of the $i$ molecules. These fluxes are function of the activation energies and the partial pressures of the different gaseous species. The model also takes into account the diffusion flux $J_{di}$ towards the incorporation sites at the steps on the surface (see Figure I.24.b). A similar model will be developed in chapter III for the growth of the ternary InGaAs (see section III.2.3.2 on page 109).

**Adsorption flux** $J_{+i}$: the adsorption flux of the $i$ species is written as:

$$J_{+i} = k_{+i} F_i \theta_{vacant} \tag{I.59}$$

where $\theta_{vacant}$ is the surface coverage ratio in vacant sites, $F_i$ is the mass input considered as element $i$'s partial pressure and $k_{+i}$ is a kinetic constant defined as: $k_{+i} = C_{+i}(T) exp\left(-\frac{E_{+i}}{k_B T}\right)$ with the classical Hernst-Knudsen term $C_{+i} = \frac{1}{\sqrt{2\pi m_i k_B T}}$.

**Desorption flux** $J_{-i}$: the desorption flux of species $i$ is written as:

$$J_{-i} = k_{-i} \theta_i \tag{I.60}$$

where $\theta_i$ is the surface coverage of occupied sites with i-type ad-species and $k_{-i} = C_{-i}(T) exp\left(-\frac{E_{-i}}{k_B T}\right)$ with $C_{-i}(T) \propto \Pi z$ expressed from the partition functions $z$ of the species involved in desorption.

**Net adsorption flux** $J_i$: the net adsorption flux of species $i$, noted $J_i$, corresponds to the amount of atoms that stays on the surface. Thereby, it is the difference between the adsorption flux $J_{+i}$ and the desorption flux $J_{-i}$.

$$J_i = J_{+i} - J_{-i} \tag{I.61}$$

Concerning the diffusion of adatoms, we consider that the surface is composed of steps and terraces. As illustrated in Figure I.24.b, the height of the steps corresponds to a monolayer and the width of the terraces is denoted $y_0$. By assuming that the distance between two steps exceeds widely the diffusion lengths and that the adatoms diffuse faster than the growth rate of the steps (quasi-static hypothesis), we can calculate the diffusion fluxes of different species involved in the growth. On the surface, the conservation of matter gives for species $i$, diffusing towards incorporation sites, the following equation:

$$div(J_{di}) = J_i - J_{i+1} \tag{I.62}$$

where $J_{di}$ represents the diffusion flux of the ad-species $i$ towards the edge of the step, $J_{i+1}$ corresponds to the consumption of the species $i$ during the reaction $i+1$, where species $i+1$ adsorbs on species $i$ according to the net adsorption flux $J_{i+1}$. Thus, for the species involved we can write:

**Diffusion flux of As:**

$$div(J_{d_{As}}) = J_{As} - J_{As+1} = (J_{+As} - J_{-As}) - (J_{+AsGaCl} - J_{-AsGaCl}) \tag{I.63}$$

which, according to reactions (I.56) and (I.57), corresponds to:

(As adsorbing on vacant site of the surface) - (As disappearing because covered by GaCl)

**Diffusion flux of AsGaCl:**

$$div(J_{d_{AsGaCl}}) = J_{AsGaCl} - J_{AsGaCl+1} = (J_{+AsGaCl} - J_{-AsGaCl}) - (J_{+GaAs} - J_{-GaAs}) \tag{I.64}$$

which, according to reactions (I.57) and (I.58), corresponds to:

(GaCl adsorbing on As) - (AsGaCl disappearing because of Cl desorption)

**Diffusion flux of GaAs:** Finally, for GaAs only one equation is involved corresponding to reaction (I.58) which is:

$$div(J_{d_{GaAs}}) = J_{GaAs} = J_{+GaAs} - J_{-GaAs} \tag{I.65}$$

We can express the different $J_{d_i}$ using Fick's law considering the surface concentration $C_i$ of ad-species $i$:

$$J_{di} = -D_i \frac{\partial C_i}{\partial y} \tag{I.66}$$

with $D_i$ the diffusion coefficient of ad-species $i$ and $C_i = N_S \theta_i$, $N_S$ being the number of sites per surface unit.

Now, we can introduce the adsorption and desorption frequencies $\nu_{+i}$ and $\nu_{-i}$ illustrated in Figure I.24.c:

$$\nu_{\pm i} = \frac{J_{\pm i}}{C_i} \tag{I.67}$$

This allows us to write the following system of coupled equations:

$$\nu_{+3} C_{As} - \nu_{-3} C_{AsGaCl} - (\nu_{+4} C_{AsGaCl} - \nu_{-4} C_{GaAs}) = -D_{AsGaCl} \frac{\partial^2 C_{AsGaCl}}{\partial^2 y} \tag{I.68}$$

$$\nu_{+4} C_{AsGaCl} - \nu_{-4} C_{GaAs} = -D_{GaAs} \frac{\partial^2 C_{GaAs}}{\partial^2 y} \tag{I.69}$$

Finally, by considering the time needed to cover the terraces, we can determine the growth rate $V$:

$$V = \frac{h}{t} = h \frac{\dot{y}}{y_0} = \frac{\Omega}{y_0} \left[ -J_{GaAs}(\frac{-y_0}{2}) + J_{GaAs}(\frac{+y_0}{2}) \right] \tag{I.70}$$

where $h$ is the step height, $t = \frac{y_0}{\dot{y}}$ is the time for covering one terrace, $\Omega$ is the molecular volume of GaAs and $J_{GaAs}$ is the diffusion flux of Ga-As ad-species to the step.

We can write this equation according to the concentration of GaAs:

$$V = \frac{\Omega}{y_0} \left[ D_{GaAs} \left| \frac{\partial C_{GaAs}}{\partial y} \right|_{-\frac{y_0}{2}} - D_{GaAs} \left| \frac{\partial C_{GaAs}}{\partial y} \right|_{+\frac{y_0}{2}} \right] \tag{I.71}$$

The concentration of solid GaAs $C_{GaAs}$ is calculated by solving equations (I.68) and (I.69). Afterwards, the growth rate is calculated using Equation (I.71).

The variation of the growth rate as a function of the growth temperature is shown Figure I.25. It follows a typical bell curve. At low temperature, the growth is limited by dechlorination of GaCl ad-molecules, desorption and surface diffusion of ad-species, which are inhibited. The surface is then blocked with undecomposed AsGaCl species. This low temperature domain was defined as the kinetically limited regime by Shaw [119]. When the temperature increases, the dechlorination frequency of GaCl ad-molecules increases, the surface is no further saturated and the number of adsorption sites increases. Consequently, the growth rate increases up to a maximum that takes place at 750 °C, which is predicted by the thermodynamic study. At high growth temperatures, HVPE exhibits the thermodynamically controlled growth regime and the growth rate is determined by the material input rate of the precursors [119]. On the high temperature side of the curve, desorption of GaCl becomes predominant and the growth rate decreases. The overview of the thermodynamics and kinetics of HVPE growth will be useful to discuss growth of III-As NWs.

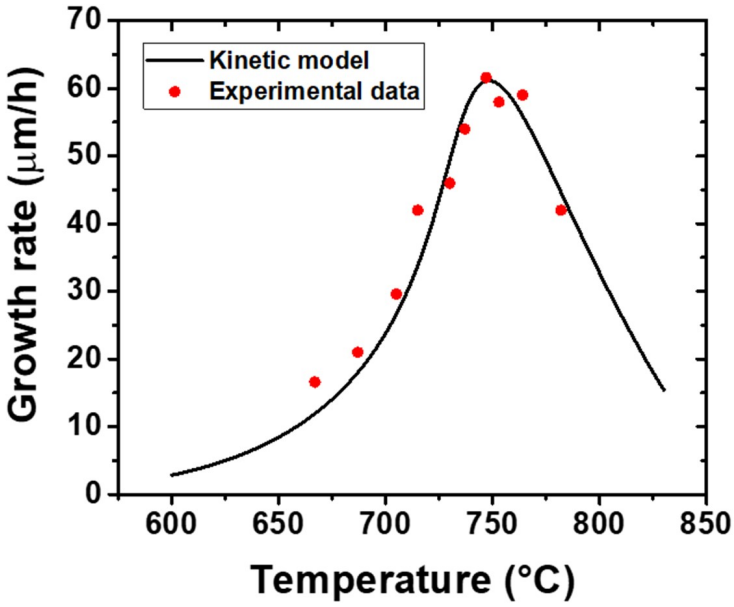


Figure I.25 – *(001) GaAs growth rate in μm/h as a function of the growth temperature T for standard experimental conditions (III/V=4.5). The dots are the experimental points and the full line is the computed theoretical curve according to the kinetic model. Adapted from [114].*

# I.7 Conclusion

In this first chapter, we have presented the main advantages of NWs compared to 2D layers and the resulting advantages for NW-based devices. We have described the different methods that exist to grow these NWs and exposed a brief state-of-the-art of the growth of III-As NWs. In particular, we have discussed the different motivations for my work which are part of a collaboration between Institut Pascal and Professor Ray LaPierre's group. These concern betavoltaic cells for GaAs NWs and multispectral infrared photodetectors for InAs NWs. The growth of InGaAs NWs is also part of this work as ternary alloys have interesting properties for infrared devices. In the last part of the chapter, we have presented the particularities of HVPE growth and detailed the governing thermodynamic and kinetic principles. These are necessary to determine the species interacting during the growth and to control the evolution of the chemical reactions involved. The kinetic approach based on the diffusion of ad-species will be used in chapters II and III.

The next chapter focuses on the SAG of GaAs NWs. In particular, the first doping results will be presented as well as the attempt to make a photovoltaic NW-based device. Chapter III will detail the growth of InAs and InGaAs NWs where various compositions are obtained.

Chapter II

# SAG-HVPE of GaAs nanowires on GaAs(111)B substrate

GaAs NWs arrays for optoelectronic devices with homogeneous electrical and optical properties require a good control of the NWs morphology over large surface substrates. This can be achieved by an adequate control of the vapor phase and a good understanding of the kinetic mechanisms involved during the growth. In this chapter, a complete study of the growth of GaAs NWs is conducted.

Firstly, I demonstrate the growth of long GaAs NWs (several μm long) essential for a good performance of potential NW-based devices by HVPE. Experimental studies are carried out and new phenomena appear like the growth suppression at high partial pressure of $As_4$ leading to a saturation of NWs length. The importance of Ga adatoms diffusion on the lateral facets on the growth of GaAs NWs is shown for the first time in HVPE. Both of these As and Ga effects are supported by a dedicated model described in the chapter. The crystallographic quality of the GaAs NWs was investigated by high-resolution transmission electron microscope (HRTEM).

Secondly, in a perspective to develop a NW-based device, a doping study is carried out. Characterizations by HRTEM and μ-PL (micro-photoluminescence) are carried out. A doping effect on NWs morphology and optical properties is clearly observed.

Finally, the growth of the first p-i-n junctions is described. For the first prototype, a process of NW-based photovoltaic device is conducted. The efficiency obtained is poor but this allows us to discuss possible ways of improvement regarding the growth and fabrication of NW-based device. Another p-i-n junction was grown and cathodoluminescence (CL) characterizations showed promising results for the realization of NW p-i-n junction by HVPE.

# II.1 How to grow long GaAs nanowires by SAG?

As shown in Chapter I, the growth of long GaAs NWs has been widely studied by MBE and MOVPE but the presence of defects in the crystal is still an issue. With the peculiar properties of the HVPE process (high growth temperature, high mass input), it was interesting to determine if defect-free GaAs NWs can be grown using HVPE. The growth of long and defect-free GaAs NWs by HVPE has already been studied at Institut Pascal in the 2010's [1]. However, it was a Au-catalyzed growth and, as explained previously in chapter I (see section I.2.1 on page 9), the foreign Au catalyst can contaminate the NWs by introducing deep level recombination centers, which significantly degrade the electrical and optical properties of GaAs material. Thus, in this study, we focus on the growth of catalyst-free GaAs NWs and the main objective is to obtain NWs of several µm in length.

## II.1.1 Experimental conditions

SAG of GaAs NWs was performed on patterned GaAs(111)B substrates which are #Bath and #IBM1 (see section I.4.2.3 on page 31). $As_4$ and GaCl are used as precursors of element V and III, and corresponding partial pressures are noted $P_{As_4}$ and $P_{GaCl}$ respectively. $H_2$ is used as a carrier gas during the growth. The source zone is kept at a temperature of 730 °C to ensure a constant yield of GaCl formation near 100%. The samples were heated to 740 °C for GaAs deposition in all cases. In order to compare the NW axial growth rate with the 2D growth rate, GaAs layers were grown on unpatterned GaAs (111)B substrates in the same growth run. The atomic III/V ratios, noted $I_3/I_5$, were calculated using Equation (I.26) (section I.5.1.3 on page 36) which is $I_3/I_5 = P_{GaCl}/(4P_{As_4})$, each $As_4$ molecule brings four As atoms to the surface. The morphology of as-grown NWs was studied using a Carl Zeiss Supra scanning electron microscope (SEM) with an acceleration voltage of 3 kV. SEM characterizations were made at *2MAtech* (Aubière, France). NWs length and diameter were deduced from the SEM images. The diameter for tapered NWs was measured at the top just below the tapered section as illustrated in Figure II.1. The uncertainties of the mean diameter and length of the NWs are calculated taking into account the statistical uncertainty and the resolution uncertainty of the SEM.

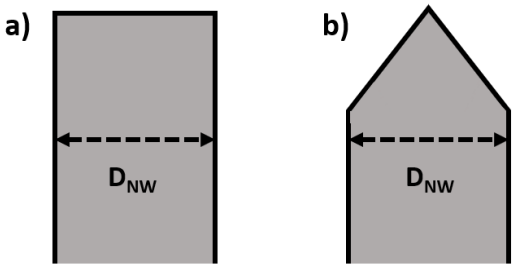


Figure II.1 – *Schematic representation of the NW diameter $D_{NW}$ considered for: a) regular NW and b) NW with a tapered section.*

## II.1.2 Issues raised by a growth time study

The effect of the growth time on the NW morphology was investigated with the aim of growing long NWs. Indeed, usually, the longer the growth time, the longer the NWs. In these growth experiments, the partial pressures $P_{As_4}$ and $P_{GaCl}$ were fixed at $1.0 \times 10^{-3}$ atm and $1.6 \times 10^{-3}$ atm, respectively, yielding a III/V ratio of 0.4. The substrate is #Bath and the growth time was varied between 5 min and 20 min. Figure II.2.a shows the schematics of SAG on patterned $SiN_x$/GaAs(111)B substrates. Figure II.2.b gives the measured evolution of the mean NW length and diameter deduced from the SEM images given in Figure II.2.c-e.

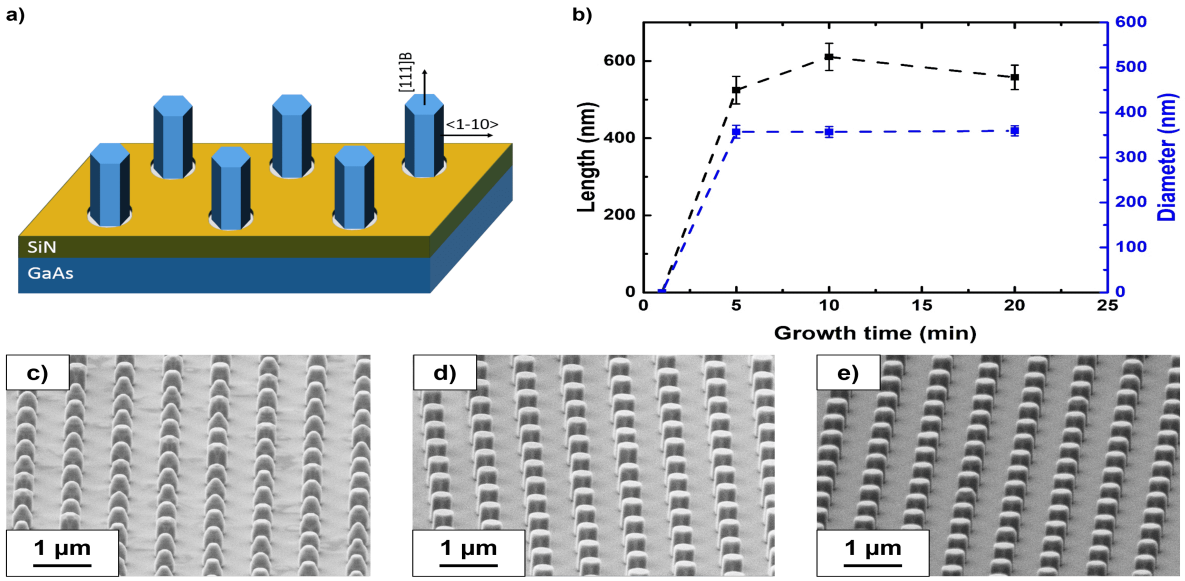


Figure II.2 – *a) Schematic representation of SAG of GaAs NWs on #Bath substrate. b) Measured NW length and diameter as a function of the growth time, deduced from the tilted-view SEM images of GaAs NWs grown for different times: c) 5 min, d) 10 min and e) 20 min. For a growth time of 1 min, no growth was observed. Lines in b) are guides for the eye.*

As expected, the growth is perfectly selective due to the low adsorption of chloride precursors on the mask. The NW growth kinetics exhibits the unusual non-linear behavior shown in Figure II.2.b. After 1 min of GaAs deposition, no NW growth above the mask surface was observed, revealing an incubation time required for: (i) the nucleation of NW seeds in the openings of the $SiN_x$ layer and (ii) filling the openings with GaAs. The processes occurring in the incubation stage include nucleation of a GaAs island, most probably at the edge of the pinhole, its lateral extension and further overgrowth until the NW emerges above the mask layer. The incubation stage results in a delay of NW growth above the mask for a certain time, which equals 1 min on average according to the data. The SEM images reveal that the NWs reach their maximum length of about 550 nm after only 5 min of GaAs deposition. The NWs shown in Figure II.2.c are not clearly faceted and exhibit a tapered morphology. After 10 min and 20 min of GaAs deposition, in Figure II.2.c-d, the NWs have a uniform diameter from base to top, with typical hexagonal cross-section bounded by the {-110} side facets, and the (111)B facet on top [120]. The radial growth rate on the {-110} side facets, which consist of Ga-As rows, is usually very low over a wide range of HVPE conditions because of the low adsorption of GaCl on the {-110} surface [74, 117]. Hence, the radial growth rate of our NWs remains low whatever the growth conditions. The absence of any NW elongation after 5 min is attributed to a growth suppression effect on the (111)B top surface of the GaAs NWs as discussed below.

Two observations support the hypothesis of the NW growth suppression. First, HVPE growth is mainly governed by the adsorption-desorption kinetics of As and GaCl species and the dechlorination rate of the adsorbed AsGaCl species at a given surface. The axial growth rate of NWs should equal at least the growth rate of a layer under the same growth conditions (growth temperature and vapor phase composition), which is not the case here. Indeed, the measured 2D growth rate on the GaAs (111)B surface in these conditions is 305 nm/min (18.3 µm/h), whereas the NWs axial growth rate before the growth suppression is only about 100 nm/min (6 µm/h). In addition, no growth suppression effect on 2D GaAs (111)B surface is observed under the investigated experimental conditions. This shows that the growth suppression is specific for SAG of GaAs NWs on patterned substrates.

## II.1.3 Influence of As and Ga input

To elucidate the origin of the NW growth suppression, a study according to III and V precursors input was conducted. GaAs NWs were grown on #Bath substrate for 10 min at a fixed temperature of 740 °C under different partial pressures of $P_{GaCl}$ and $P_{As_4}$. Figure II.3.a shows the effect of $P_{GaCl}$ variation at a constant $P_{As_4} = 1.0 \times 10^{-3}$ atm, while Figure II.3.b shows the effect of $P_{As_4}$ variation at a constant $P_{GaCl} = 1.6 \times 10^{-3}$ atm.

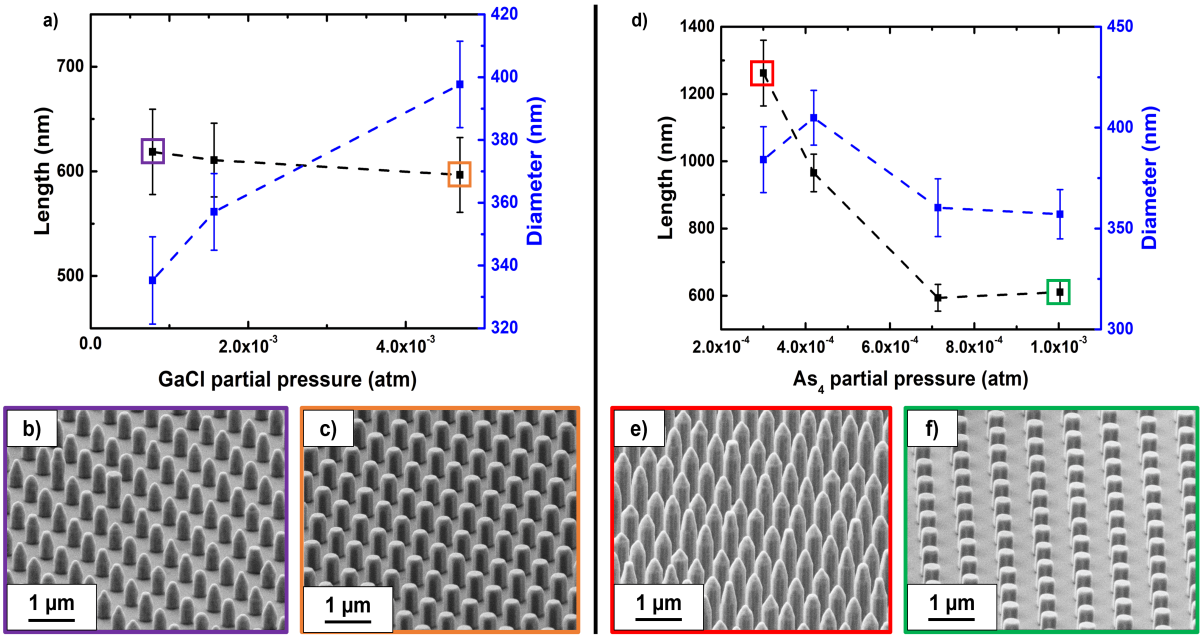


Figure II.3 – *SAG GaAs NWs on #Bath substrate. a) NW length and diameter as a function of* $P_{GaCl}$ *at a fixed* $P_{As_4}$ *of* $1.0 \times 10^{-3}$ *atm. Tilted-view SEM images of GaAs NWs grown at different* $P_{GaCl}$*: b)* $7.8 \times 10^{-4}$ *atm and c)* $4.7 \times 10^{-3}$ *atm. d) NW length and diameter as a function of* $P_{As_4}$ *at a fixed* $P_{GaCl}$ *of* $1.6 \times 10^{-3}$ *atm. Tilted-view SEM images of GaAs NWs grown at different* $P_{As_4}$*: e)* $3.0 \times 10^{-4}$ *atm and f)* $1.0 \times 10^{-3}$ *atm. The regimes yielding the maximum and minimum NW lengths and aspect ratios are highlighted in panels a) and d). Lines in a) and d) are guides for the eye.*

According to Figure II.3.a, the NW diameter increases with $P_{GaCl}$. This effect has already been observed with the thickness of GaAs stripes grown by HVPE [121], and is explained by an increase of Ga adatom concentration on the sidewall surfaces. Different radial growth rates of NWs lead to a change in the NW morphology. At low $P_{GaCl}$, the top part of the NWs is tapered because the intrinsic growth rate of the (111)B facet is greater than the growth rate of the lateral facets. At high $P_{GaCl}$, the opposite occurs, the top facet clearly appears resulting in untapered NW morphology. However, the $P_{GaCl}$ value does not have any significant influence on the NW length at $P_{As_4} = 1.0 \times 10^{-3}$ atm.

According to Figure II.3.d, the $P_{As_4}$ value has a significant impact on the NW length, which strongly decreases for higher $P_{As_4}$. The longest NWs grown at the lowest $P_{As_4}$ of $3.0 \times 10^{-4}$ atm are tapered at the top, as seen in Figure II.3.e, while the shortest NWs grown at the highest $P_{As_4}$ of $1.0 \times 10^{-3}$ atm are untapered. This should be associated with a higher axial growth rate of NWs grown at a lower $P_{As_4}$ and the absence of the growth suppression. The length of these NWs reaches 1262 nm after 10 min of growth, while the length of NWs grown at $P_{As_4} = 1.0 \times 10^{-3}$ atm is only 611 nm. These short NWs should have stopped elongating after 5 min of growth, as we saw earlier in Figure II.2. After that, their tops have been modified by the radial growth to resume the untapered shape, as in Figure II.2.

These data clearly show the importance of the $P_{As_4}$ value for obtaining long GaAs NWs in SAG by HVPE. Longer NWs can only be grown at low $P_{As_4}$ yielding high III/V ratios. According to some studies [120, 122, 123, 124, 125, 126], the growth of the (111)B top facet of GaAs NWs can be suppressed by stable As trimers when the As flux onto the NWs is too high, which suppresses the axial NW growth under very As-rich conditions. For NWs grown at the highest $P_{As_4}$ of $1.0 \times 10^{-3}$ atm (Figure II.3.f), the NW length has saturated at an early stage and hence the top facets of these NWs are fully covered with As trimers. No further growth can occur on such surfaces [127, 128]. For NWs grown at lower $P_{As_4}$, the top (111)B facets can be passivated only partly by As trimers or be completely free of As trimers. The axial growth then occurs on the parts of (111)B surface free from As trimers, or on the whole top facet in the absence of As trimers. This effect will be discussed further in the modeling section of this work (section II.1.4). The passivation of (111)B top facets of GaAs NWs by As trimers under the excessive As input is then suggested to be the reason for the suppression of the NW axial growth far below the 2D level. A higher As input onto the top facets of SAG NWs on the patterned substrates compared to layers on unpatterned substrates is expected to be due to additional $As_4$ species desorbed from the inert mask and NW sidewalls. Therefore, the III/V ratios calculated from the partial pressures provide only the nominal values, while the actual ratio of atomic fluxes impinging on the NW tops may correspond to more As-rich growth conditions.

It is interesting to note that the NWs grown at low $P_{As_4}$ exhibit twelve side facets which belong to the two six-fold families equivalent to {-110} and {11-2} facets [49, 127, 128, 129, 130, 131], as it is shown later in the inset of Figure II.5.a. A schematic of the two families of facets is illustrated in Figure II.4.

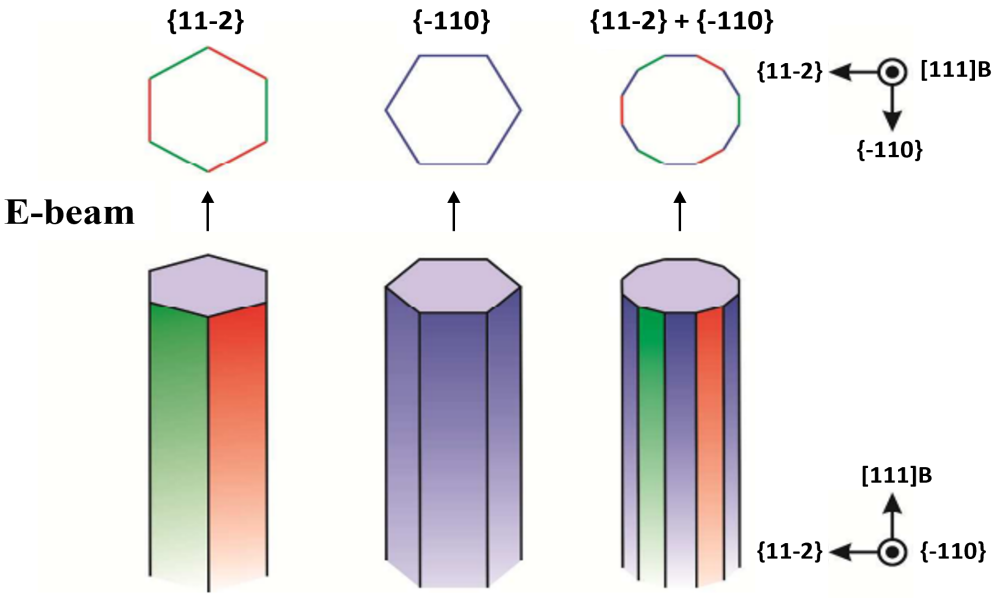


Figure II.4 – *Schematic of the NW cross-sections with possible sidewall facets. With electron beam aligned to be parallel to {11-2} plane referring to the cleavage, possible edges that can be revealed by SEM are shown under each cross-section. Adapted from Supporting Information of [131].*

There are two possible explanations for such a faceting. The NWs may either nucleate with twelve facets initially and then keep this shape due to the equivalent growth rates on both types of facets, or they may nucleate with the energetically preferred six facets and the other facets appear in a later stage for kinetic reasons. If the NWs nucleate with twelve facets, the transition to a hexagonal shape restricted by six {-110} facets, as for NWs grown at higher $P_{As_4}$, may occur by the elimination of the {11-2} facets. For WZ GaAs NWs, the results of Ref. [132] show that the strong binding site found in calculations for GaAs pairs on the {11-20} facets may facilitate nucleation on these sidewalls. Consequently, for NWs with both facet families coexisting, the {11-20} facets may grow out and eventually disappear. Similar behavior may occur in GaAs NWs with predominantly ZB crystal phase, as in our case.

The extreme growth regimes yielding the NWs shown in Figure II.3.e-f result in very different NW morphologies. The crystal structure of these NWs was studied using FEI-TECNAI TEM with an acceleration voltage of 200 kV. The results are shown in Figure II.5.a for a representative NW grown at a low $P_{As_4}$ of $3.0 \times 10^{-4}$ atm, and in Figure II.5.b for a representative NW grown at a high $P_{As_4}$ of $1.0 \times 10^{-3}$ atm. No significant difference in the crystal quality is observed between the two NWs. Both growth conditions yield GaAs NWs with a high density of random stacking faults related to the ZB/WZ polytypism. This polytypism is commonly observed during growth of GaAs NWs along the

[111]B direction [42, 133, 134, 135, 136]. The effect is attributed to a small difference in the internal formation energies of the two phases (around 10 meV), which comes mainly from the electrostatic interaction between the third-nearest-neighbor atoms [42, 133, 134].

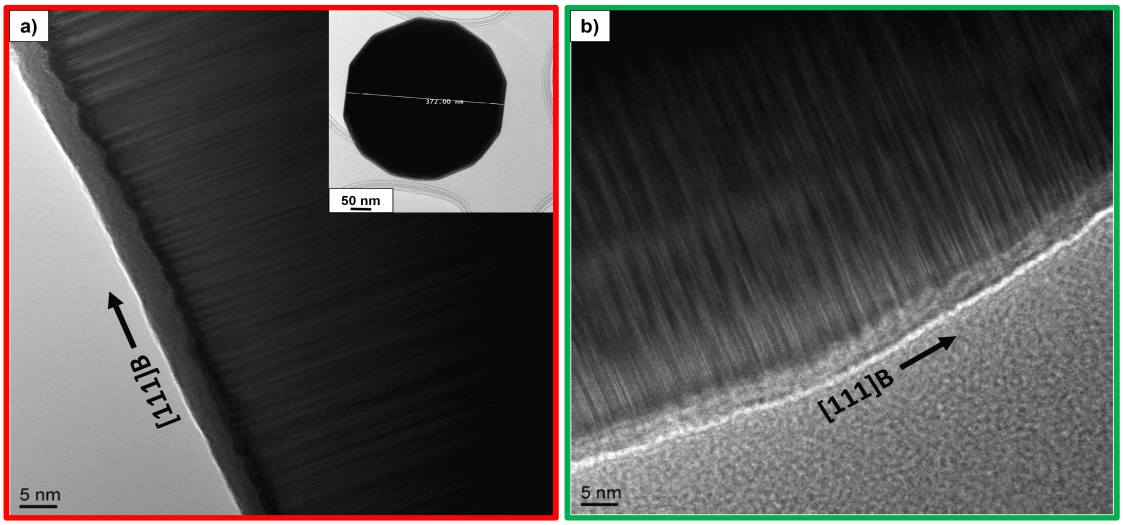


Figure II.5 – *Bright-field HRTEM images of GaAs NWs grown on #Bath substrate at* $P_{As_4}$ *of a)* $3.0\times\ 10^{-4}$ *atm and b)* $1.0\times10^{-3}$ *atm. The shell present on the NWs is an oxide layer. The incident electron beam was along* $\langle 1-10\rangle$*. The inset in panel a) is a TEM image along the [111]B direction showing the twelve side facets.*

In order to confirm that the NW axial growth is not suppressed at low $P_{As_4}$, we have performed the SAG of GaAs NWs on #Bath substrate using two different values of $P_{As_4}$ of $3.0\times10^{-4}$ atm and $4.2\times10^{-4}$ atm for a longer time of 30 min. Figure II.6 shows the SEM images of these NWs. The NW axial growth was still suppressed at $P_{As_4}=4.2\times10^{-4}$ atm, where the NW length was almost the same as that after 10 min of growth (Figure II.3.d), but not suppressed at $P_{As_4}=3.0\times10^{-4}$ atm. The NWs shown in Figure II.6.b exhibit a length of 6800 nm and an aspect ratio of more than 17. Thus, the average axial growth rate of these NWs was 227 nm/min (13.6 µm/h) and is approaching, but still lower than the 2D growth rate on GaAs(111)B substrate of 249 nm/min (14.9 µm/h).

The optimal growth conditions with the partial pressures $P_{As_4}=3.0\times10^{-4}$ atm and $P_{GaCl}=1.6\times10^{-3}$ atm, yielding the longest GaAs NWs on #Bath substrate shown in Figure II.6.b, were used for the SAG of GaAs NWs on a different substrate which is #IBM1 substrate. The dielectric mask was changed to $SiO_x$ and the diameter of circular openings was reduced to 80 nm. Two different pitches of 1 µm and 2 µm were studied. The growth temperature was 740 °C, and the GaAs deposition time was 10 min. Figure II.7 shows the SEM images of the NWs grown in arrays with different pitches with the

insets showing top-view SEM images of hexagonal NWs. Perfect growth selectivity was observed, which is again explained by the negligible adsorption of the chloride precursors on the dielectric mask regardless of its chemical composition. Finally, the average axial growth rate of these NWs exceeded 550 nm/min (33 µm/h), which is 2.2 times larger than the 2D growth rate of 249 nm/min (14.9 µm/h). The NW length reached 5640 nm after only 10 min of GaAs deposition whatever the pitch. With the NW diameter of 144 nm, this yields a high aspect ratio of 39.

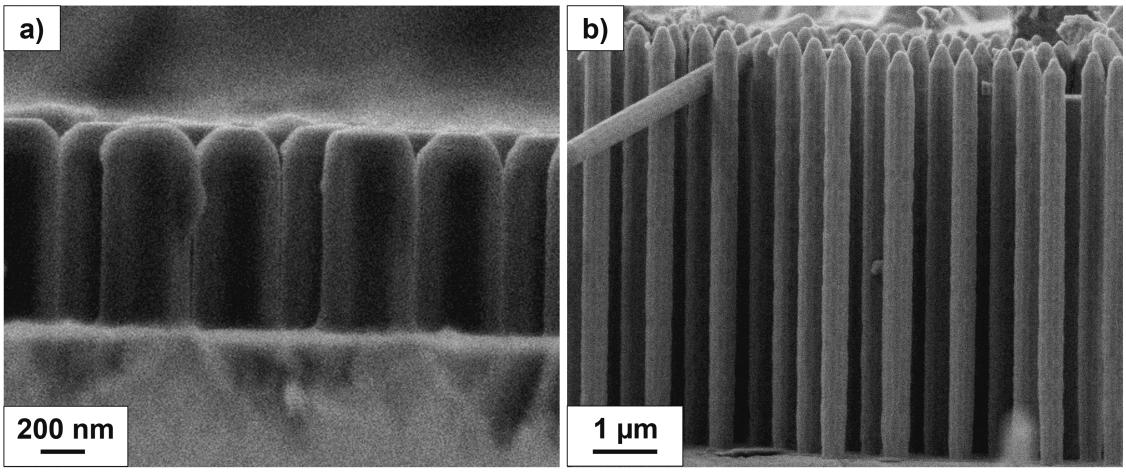


Figure II.6 – *SEM images of GaAs NWs grown on #Bath substrate using $P_{As_4}$ of a)* $4.2 \times 10^{-4}$ *atm and b)* $3.0 \times 10^{-4}$ *atm. The partial pressure $P_{GaCl}$ was* $1.6 \times 10^{-3}$ *atm in both cases.*

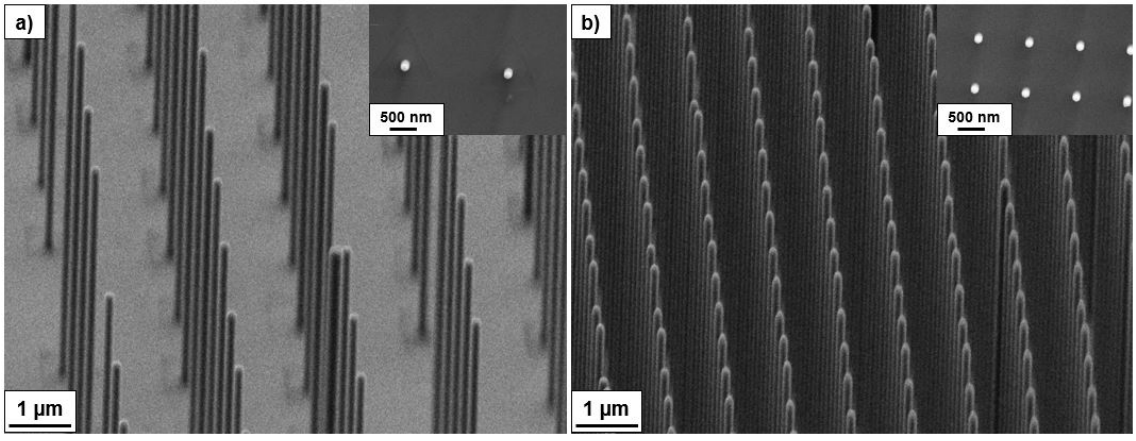


Figure II.7 – *Tilted-view SEM images of GaAs NWs grown for 10 min on #IBM1 substrate with two different pitches of a) 2 µm and b) 1 µm. The partial pressures of precursors were fixed at* $P_{GaCl} = 1.6 \times 10^{-3}$ *atm and* $P_{As_4} = 3.0 \times 10^{-4}$ *atm. The insets show top-view SEM images of the hexagonal NWs.*

Assuming that the axial NW growth is controlled by the Ga transport under As-rich conditions as discussed above, three different Ga fluxes should be considered [137]: (i) the impingement flux arriving onto the NW top directly from vapor, (ii) diffusion flux of Ga adatoms from the NW sidewalls to the top, and (iii) diffusion flux of Ga adatoms from the mask surface to the NW top. These fluxes are illustrated in Figure II.8.

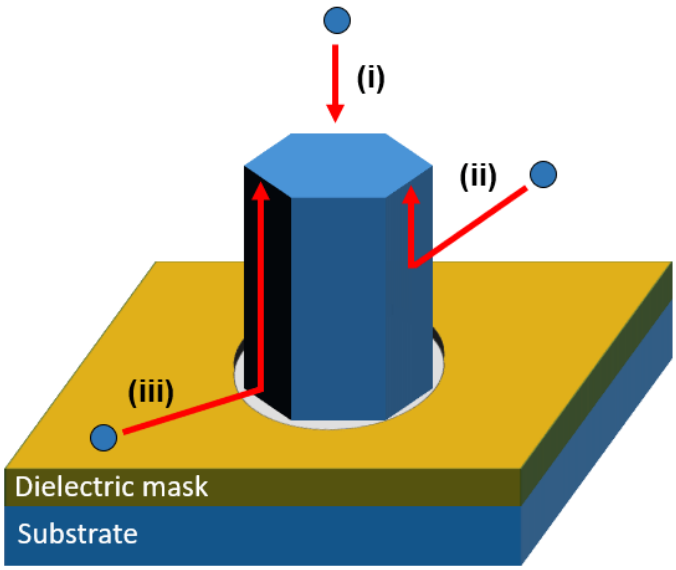


Figure II.8 – *Schematic fluxes for the growth of NW: (i) direct impingement, (ii) diffusion on the NW sidewalls and (iii) diffusion from the dieletric mask.*

The impingement flux (i) is identical for NWs and layers because HVPE growth of GaAs is not limited by the mass transfer [138]. The diffusion flux from the mask (iii) should be absent due to the negligible adsorption of chloride precursors on the mask in HVPE. Therefore, the only reason for the observed increase of the NW axial growth rate above the 2D level is the diffusion flux of Ga adatoms from the NW sidewalls (ii), which has never been considered in HVPE growth.

In conclusion, we are able to experimentally analyze and understand the phenomena governing the growth of catalyst-free GaAs NWs. This allows us to grow long GaAs NWs with a high aspect ratio. In order to better understand what is happening from a kinetic point of view, a model has been developed in collaboration with Professor Vladimir Dubrovskii who helped us to integrate in the model the flux (ii) which is more common in MBE growth.

## II.1.4 Kinetic growth model

In growth modeling, we consider two effects which greatly influence the morphology of SAG GaAs NWs grown by HVPE as discussed above. The model deals with the average values of the NW length and radius, neglecting statistical fluctuations and size distributions in the NW ensemble. First, we account for the axial growth suppression by As trimers under highly As-rich conditions at the NW top, which reduces the axial growth rate below the 2D level. Second, we introduce the possibility for surface diffusion of Ga adatoms from the NW sidewalls to the top, which can enhance the axial growth rate with respect to the 2D level. The model is illustrated in Figure II.9.a. Neglecting the radial growth in the first approximation by taking an average value for the NW radius $R$ throughout the growth run $(R = R_{hole} + R_f)/2$, where $R_{hole}$ is the hole radius and $R_f$ is the measured NW radius after growth, the total change of the NW volume with time $t$ is:

$$\pi R^2 \frac{dL}{dt} = [v_{2D}^{(111)B} \pi R^2 + v_{2D}^{f} 2\pi R \Lambda_3] \frac{S}{S_0} \tag{II.1}$$

Here, $L$ is the NW length above the mask surface, $v_{2D}^{(111)B}$ and $v_{2D}^{f}$ are the 2D growth rates on the top (111)B facet and on the NW sidewall facets, respectively, $\Lambda_3$ is the Ga diffusion length on the NW sidewalls (labelled "3") and $S/S_0$ is the fraction of the top (111)B facet free from As trimers which suppress the axial NW growth. This fraction can equivalently be presented as $S/S_0 = 1 - \theta_5$, where $\theta_5$ is the surface coverage of (111)B facet by As trimers (labelled "5"). The first bracket term describes the direct impingement and desorption of Ga atoms on the top facet, while the second bracket term gives the diffusion flux of Ga adatoms from the NW sidewalls to its top. From Equation (II.1), the NW axial growth rate is given by:

$$\frac{dL}{dt} = v_{2D}(1 + \frac{2\lambda_3}{R})(1 - \theta_5) \tag{II.2}$$

with the effective diffusion length of Ga adatoms $\lambda_3 = \Lambda_3 v_{2D}^{f} / v_{2D}^{(111)B}$, where we write $v_{2D}$ instead of $v_{2D}^{(111)B}$ for brevity. Clearly, the diffusion-induced contribution $2\lambda_3/R$ increases the NW growth rate above the 2D level, while the growth suppression effect on the NW top facet at $\theta_5 > 0$ decreases the NW growth rate below the 2D level.

The coverage of the top NW facet by As trimers is modeled using the simplest form of the Kolmogorov model [139]:

$$\theta_5 = 1 - e^{-(t - t_{inc})/\tau_5} \tag{II.3}$$

with $t_{inc}$= 1 min the incubation time for NW growth above the mask surface as deduced from the growth experiments, and $\tau_5$ the characteristic time for forming As trimers on the top NW facet.

Using this exponential dependence in Equation (II.2) and integrating it with the initial condition $L(t = t_{inc}) = 0$, we obtain:

$$L = v_{2D}(1 + \frac{2\lambda_3}{R})\tau_5[1 - e^{-(t-t_{inc})/\tau_5}] \tag{II.4}$$

At $(t - t_{inc})/\tau_5 \gg 1$, corresponding to the full coverage of the top facet by As trimers ($\theta_5 \to 1$), the NW length saturates to a constant:

$$L \to v_{2D}(1 + \frac{2\lambda_3}{R})\tau_5 \tag{II.5}$$

On the other hand, at $\tau_5 \to \infty$, corresponding to the absence of any As trimers at the NW top under effectively As-poor conditions, the NW length increases linearly with time:

$$L = v_{2D}(1 + \frac{2\lambda_3}{R})(t - t_{inc}) \tag{II.6}$$

This is the usual law of NW elongation enhanced by surface diffusion above $v_{2D}$, as in Refs. [137, 140]. The characteristic time of forming As trimers is expected to be shorter for lower III/V ratios $I_3/I_5$, corresponding to more As-rich conditions. The III/V ratios deduced from the partial pressures of GaCl and $As_4$ give only the nominal values above the substrate. The actual atomic III/V flux ratio on the NW top may be different. Nonetheless, lower $I_3/I_5$ ratios calculated from the partial pressure ratio should correspond to lower atomic III/V flux ratios at the NW top. The III/V balance on the NW top is also changed by the additional Ga adatoms diffusing from the NW sidewalls. It may be assumed that:

$$\tau_5 = \tau_0 \frac{I_3}{I_5}(1 + \frac{2\lambda_3}{R}) \tag{II.7}$$

meaning that $\tau_5$ is simply proportional to the effective atomic III/V ratio at the NW top $(I_3/I_5)(1 + 2\lambda_3/R)$ which includes surface diffusion of Ga adatoms with a constant $\tau_0$. The formation of As trimers should have a barrier character. Therefore, the linear dependence given by Equation (II.7) is expected only in a certain range of effective atomic III/V ratio below a threshold value. Above the threshold, $\tau_5$ should rapidly tend to infinity and the growth suppression effect disappears.

Table II.1 summarizes the partial pressures $P_{GaCl}$ and $P_{As_4}$, the $I_3/I_5$ ratios, the hole diameters $D_{hole}$ and pitches $P$ of the SAG templates, the GaAs deposition times $t$, the measured 2D growth rates on unpatterned GaAs(111)B substrates $v_{2D}$, the lengths $L$ and the average radii $R$ of GaAs NWs used for modeling. The last two columns show the fitting parameters of the model $\lambda_3$ and $\tau_5$ for each datapoint. It is remarkable that the good fits to the data are obtained with the same diffusion length of Ga adatoms of 44 nm. This value is very close to 45 nm, reported for Ga diffusion length on the

sidewalls of GaN NWs grown by MBE in a temperature range from 770 °C to 810 °C [141]. The Ga diffusion length generally depends on the As pressure of III/V flux ratio, as discussed, for example, in previous studies [142, 143, 144]. In the HVPE growth experiments, the partial pressures of group III and V precursors are varied over a limited range such that the $I_3/I_5$ ratio changes from 0.40 to 1.33. The actual ratio of Ga and As fluxes landing on the NWs may be affected by the desorbed growth species. In this limited range, a flux-independent diffusion length of Ga adatoms on the NW sidewalls is usually a good approximation, as noted, for example, in Ref. [141] for the Ga diffusion length on the sidewalls of self-induced GaN NWs. For NWs which have twelve side facets belonging to {-110} and {11-2} families, the previous reports on the growth kinetics of ZB GaAs NWs [49, 137, 140] revealed very similar Ga diffusion lengths on these surfaces. Therefore, using a constant Ga diffusion length of 44 nm for any III/V ratio does not contradict the previous findings and is supported by the fits. The deduced value of the diffusion length is very small. This allows us to safely neglect any pitch-dependent Ga diffusion from the mask, because all Ga adatoms which may have diffused from the mask to the NW sidewalls will re-evaporate before reaching the NW top.

| $P_{GaCl}$ ($10^{-3}$ atm) | $P_{As4}$ ($10^{-3}$) atm | $I_3/I_5$ | $D_{hole}$ (nm) | $P$ (µm) | $t$ (min) | $L$ (nm) | $v_{2D}$ (nm/min) | $R$ (nm) | $\lambda_3$ (nm) | $\tau_5$ (min) |
|---|---|---|---|---|---|---|---|---|---|---|
| 1.6 | 1.0 | 0.40 | 340 | 1 | 5 | 521 | 305 | 174 | 44 | 1.26 |
| 1.6 | 1.0 | 0.40 | 340 | 1 | 10 | 611 | 305 | 174 | 44 | 1.26 |
| 1.6 | 1.0 | 0.40 | 340 | 1 | 20 | 580 | 305 | 174 | 44 | 1.26 |
| 1.6 | 0.7 | 0.56 | 340 | 1 | 10 | 594 | 244 | 175 | 44 | 1.62 |
| 1.6 | 0.4 | 0.95 | 340 | 1 | 10 | 965 | 248 | 186 | 44 | 2.78 |
| 1.6 | 0.4 | 0.95 | 340 | 1 | 30 | 1041 | 248 | 186 | 44 | 2.78 |
| 1.6 | 0.3 | 1.33 | 340 | 1 | 10 | 1262 | 247 | 181 | 44 | 3.47 |
| 1.6 | 0.3 | 1.33 | 80 | 1 | 10 | 5575 | 247 | 60 | 44 | ∞ |
| 1.6 | 0.3 | 1.33 | 80 | 2 | 10 | 5640 | 247 | 56 | 44 | ∞ |

Table II.1 – *Parameters of GaAs NWs grown in different SAG conditions.*

Figure II.9.b shows the fits obtained from Equation (II.4) for the NW lengths with saturation at $I_3/I_5$ = 0.40 and 0.95. The fits are obtained with different $\tau_5$. As expected, the fitting value of $\tau_5$ increases for larger $I_3/I_5$. Figure II.9.c shows the main result of the model. The GaAs NW lengths obtained in 10 min growth experiments under different III/V ratios and in differently sized holes are compared to the 2D growth rates on unpatterned GaAs(111)B under the same growth conditions and

fitted by Equation (II.4) using different $\tau_5$. It is seen that the model reproduces very well the data, including the axial growth suppression by As trimers at low effective III/V ratios and the axial growth increase above the 2D level due to surface diffusion of Ga adatoms to the top of the thinnest NWs.

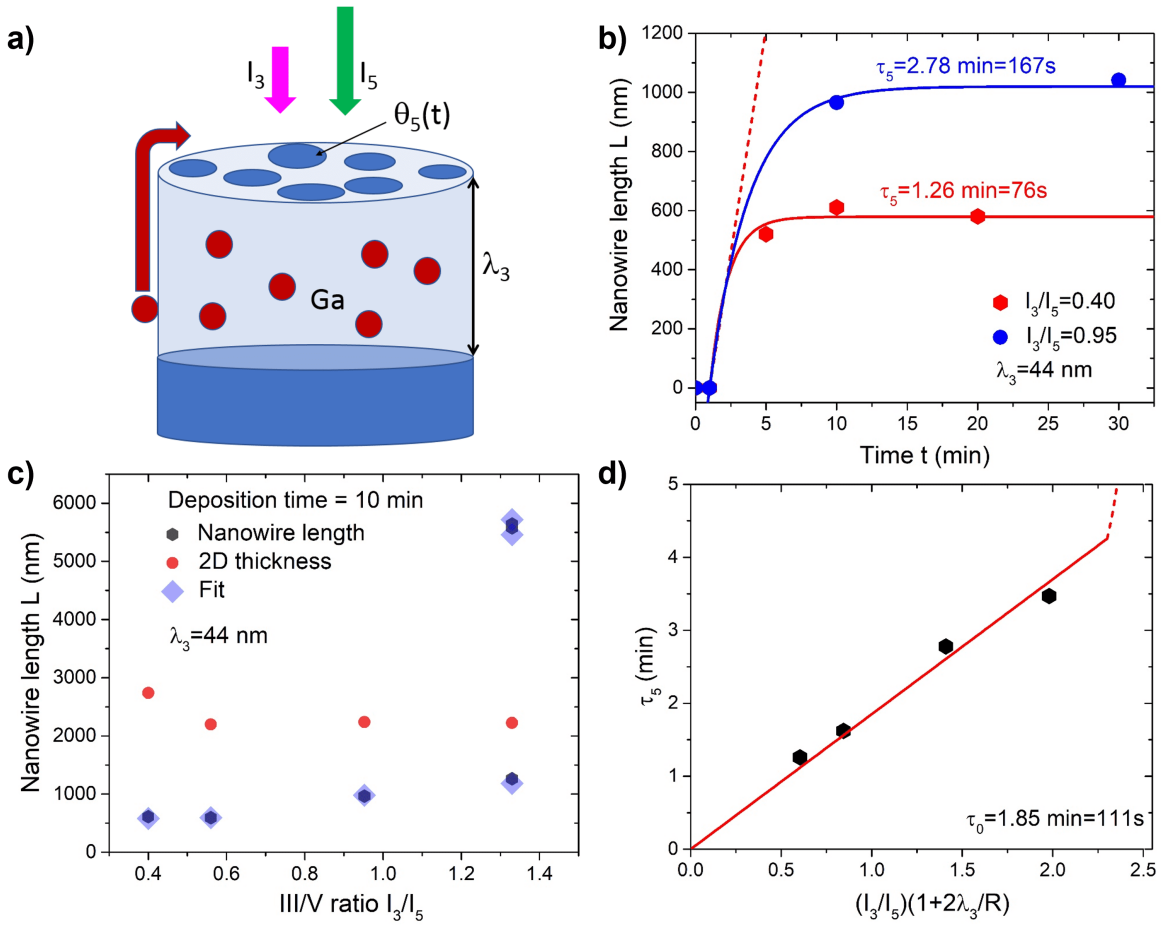


Figure II.9 – *a) Illustration of the model in which the top (111)B NW facet is suppressed by As trimers with a time-dependent coverage $\theta_5(t)$. The effective diffusion length of Ga adatoms on the NW sidewalls equals $\lambda_3$. b) Lengths of GaAs NWs versus time at two different $I_3/I_5$ ratios of 0.40 and 0.95 corresponding to the growth suppression by As trimers at the NW tops (symbols), fitted by the model with the parameters shown in the legend (lines) with $\tau_5$ the characteristic time for forming As trimers on the top NW facet. The dashed straight line corresponds to the layer thickness on unpatterned GaAs (111)B substrate at $I_3/I_5 = 0.4$. c) Lengths of GaAs NWs after t=10 min, fitted by the model and compared to the layer thickness. d) Linear increase of the effective time $\tau_5$ with the III/V input ratio. Dashed line shows a rapid increase of $\tau_5$ for higher III/V input ratios.*

According to Table II.1, the longest and thinnest NWs grown in 80 nm diameter holes in a $SiO_x$ mask at the highest $I_3/I_5$ of 1.33 are modelled with $\tau_5 \to \infty$ meaning that the growth suppression is absent. The small radius of these NWs simultaneously circumvents the unwanted effect of As trimer

accumulation at the NW top and increases the axial NW growth rate far above the 2D level by a more efficient surface diffusion of Ga adatoms. Finally, Figure II.9.d demonstrates the validity of our hypothesis on the linear scaling of the characteristic time $\tau_5$ with $(I_3/I_5)(1+2\lambda_3/R)$ in the range where the growth suppression effect is present. The low value of $\tau_0 = 111$ s obtained implies that the term $(I_3/I_5)(1+2\lambda_3/R)$ must be preponderant to counter the effect of growth suppression.

In conclusion, the experimental results and the kinetic model have brought to light new phenomena that appear during the selective area growth of GaAs NWs by HVPE. This section's content was published in an article [145]. The optimization of the growth conditions made it possible to obtain long NWs which will be used for the rest of this work.

Now that the growth has been optimized to obtain long NWs, the next step is to focus on the doping of GaAs NWs in order to move towards the growth of p-i-n junctions.

# II.2 Doping of GaAs nanowires by HVPE

Doping is essential for any NW-based device because it requires a p-i-n junction. Doping of NWs by HVPE is poorly documented and each reactor being different, it would be pointless to rely on estimates from the literature. At Institut Pascal, p-type doping is done using diethylzinc (DEZ) and n-doping is done using silane ($SiH_4$). Silane comes from a conventional gas cylinder with a direct line to the reactor (0.1% $SiH_4$ concentration in $H_2$). The DEZ is a capsule that is in a thermostatic bath because it is necessary to have a regulated temperature to obtain a gaseous DEZ. This means that if the bath temperature $\theta_{DEZ}$ is different depending on the experiments, the partial pressure of DEZ is changed and thus the amount of dopants changes. As far as our knowledge, this is the first time that a study of doping on catalyst-free III-As NWs has been carried out.

## II.2.1 Doping of GaAs layers

Doping semiconductors is a very delicate task. A very large number of parameters affect the doping such as the growth conditions, the temperature, the structures produced (the doping is different between layers and NWs) or even the nature of the crystallographic orientations. This is why it is necessary to calibrate the doping on layers of GaAs before proceeding to doping the NWs.

As a starting point for doping, we have considered the results previously obtained in our team, in particular during the thesis of Mohamed Ramdani in 2010 [138]. In his work, he performed Hall effect measurements on GaAs (100) dedicated to the epitaxy of p-doped GaAs tips for spin injection.

From these growths of doped GaAs layers, he highlighted the following results: undoped layers appear to be unintentionally p-doped (probably because of residual carbon in the reactor), p-doping with Zn results in doping rates between $1.9 \times 10^{17}$ cm$^{-3}$ and $1.1 \times 10^{19}$ cm$^{-3}$. The same order of magnitude was obtained for n-doping with Si. For this work, I have used the same experimental conditions but I have considered reference GaAs layers for both orientations (100) and (111)B. Here, I present only the results on (111)B layers as this is the NWs grow direction. Photoluminescence (PL) measurements were made solely to check the presence of dopants.

First of all, it should be noted that the growth conditions for layers and NWs are different (in particular the III/V ratio). Moreover, the incorporation of the dopants is different between the layers and the NWs because of the presence of a lateral facet. The layers were grown on semi-insulating GaAs (111)B substrate at 740 °C with $P_{As_4}$ of $1.0 \times 10^{-3}$ atm and $P_{GaCl} = 1.6 \times 10^{-3}$ atm. In order to visualize the influence of doping, PL measurements were carried out in collaboration with François Réveret from the ICCF laboratory of Clermont-Ferrand within the collaboration NANOSPRING. For light excitation, a xenon lamp is used which passes through a monochromator. An excitation wavelength of 550 nm was chosen and a 550 nm band pass filter was used. The samples were immersed in liquid nitrogen to reach a temperature of 77 K. Normalized PL spectra of p-doped and n-doped GaAs (111)B layers are shown in Figure II.10.

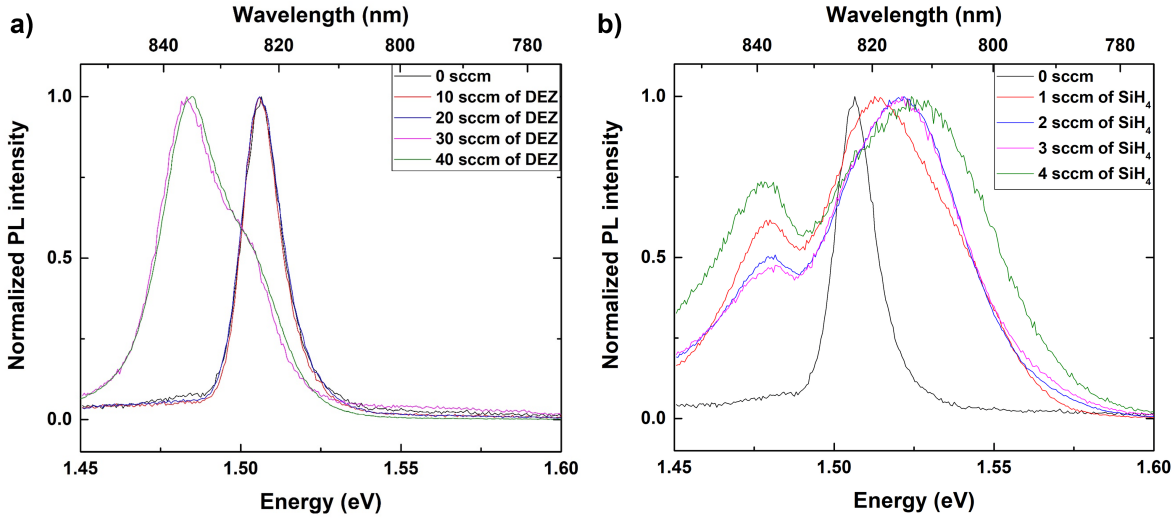


Figure II.10 – *Normalized 77 K PL spectra of GaAs (111)B layers grown by HVPE with different flows of a) p-dopants (DEZ) and b) n-dopants ($SiH_4$).*

The PL intensity has been normalized in order to more easily compare the spectra with each other. To begin with, we can clearly see a redshift for p-doped GaAs layers and a blueshift for n-doped GaAs when dopants flows increase. This phenomenon has already been observed by both PL

and cathodoluminescence (CL). Redshift of the PL/CL spectra in p-type doping have been investigated [146, 147] and is due to the bandgap narrowing effect. On the other hand, the blueshift of the PL spectra, known as the Burstein-Moss effect [148, 149], prevails in n-type III-V semiconductors. According to the recent work of Hung-Ling Chen [150], these phenomena appear for heavy doping in CL spectra ($> 10^{17}$ $cm^{-3}$). This seems consistent with the results from Mohamed Ramdani's thesis [138].

Regarding undoped layer (in black), a main peak is observed at 1.506 eV. This peak could be attributed to the bandgap transition of GaAs since the GaAs bandgap at this temperature is 1.508 eV [151]. Concerning p-doped layers, if we take a closer look at Figure II.10.a, we see that for a flow of 20 sccm of DEZ or less, there is no redshift and no significant difference is observed with respect to the undoped layer. Thus, for low DEZ fluxes, the p-doped and the undoped layers seem to have the same optical transition, confirming the fact that the undoped layer seems to be unintentionally p-doped (due to the presence of impurities in the reactor). Furthermore, from flow at 30 sccm, a redshift clearly appears and a secondary peak arises at 1.50 eV which could be linked to exciton-related transition. Now concerning n-doping in Figure II.10.b, we see an evolution of the position of the peak as a function of the flow rate of $SiH_4$. Indeed, the higher the $SiH_4$ flow, the higher the blueshift. However, a similarity is observed for 2 and 3 sccm. Moreover, a secondary peak is observed at low energies (1.46 eV) whose position does not change with the doping. It seems that this secondary peak is linked to a deep level transition related to silicon [152].

This study does not allow to directly extrapolate the doping rate from the spectra. Indeed, Hall effect measurements are mainly used to determine directly and accurately the doping rate of the doped layers. Hall effect measurements are currently in progress at INSA Rennes. Even if Hall effect measurements are necessary, this study could be considered as a preliminary step to check the effectiveness of the doped precursors before growth of p-i-n junction. Henceforth, we know that it is possible to dope GaAs NWs by our doping setup.

## II.2.2 Experimental conditions and motivations

In this part, it will be reported the exploratory results obtained concerning the doping of GaAs NWs. To our knowledge, this is the first study concerning the doping of catalyst-free GaAs NWs by HVPE. The influence of doping on NWs morphology, structural and optical properties will be discussed. The motivations of growing doped NWs, and more specifically NW p-i-n junction, are part of the objective to make NW-based devices by HVPE.

As explained previously, the best way to estimate doping is Hall effect measurements. This can easily be done for layers but becomes more difficult for NWs. Indeed, it is necessary to have a whole process to planarize the samples before making electric contacts. Thus, only µ-PL will be carried out to visualize the doping.

With the idea of moving towards GaAs NW p-i-n junctions for photovoltaic and betavoltaic applications, a doping study was carried out on GaAs NWs. In order to make contacts for a p-i-n junction with a p-doped core, it is necessary to have a p-doped substrate as well. The #IBM1 substrate wafer was used, it has in particular the property of being a p-doped substrate with small aperture diameters. Four pieces were used: one for undoped NWs, one for n-doped NWs, one for p-doped NWs and the last one for the NW p-i-n junction. The p-i-n junction will be detailed in a next section (section II.3). The patterned area consists of two adjoining squares of 1 $mm^2$ with the same apertures diameter of 80 nm but with a different pitch of 1 and 2 µm. A summary of the substrate pieces and their respective use is shown in Figure II.11.

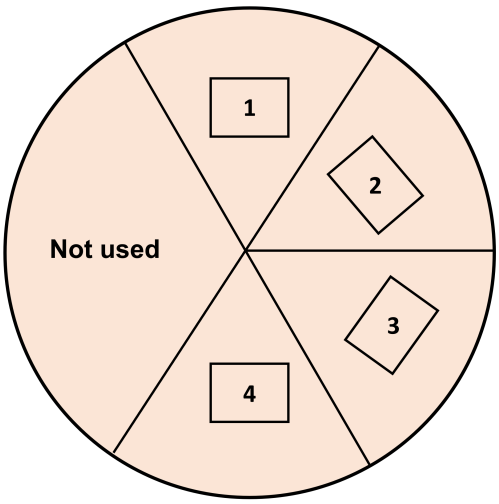


| Sample number | Nature |
|---|---|
| 1 | Undoped |
| 2 | n-doped |
| 3 | p-doped |
| 4 | p-i-n junction |

Figure II.11 – *Summary of the pieces used from the #IBM1 substrate, the numbers corresponding to the growths performed.*

In order to better visualize the squares, a SEM image of the patterned area is shown in Figure II.12. We can clearly see the two distinct squares with a lighter and less dense area which corresponds to the pitch of 2 µm and a denser and darker area which corresponds to the pitch of 1 µm.

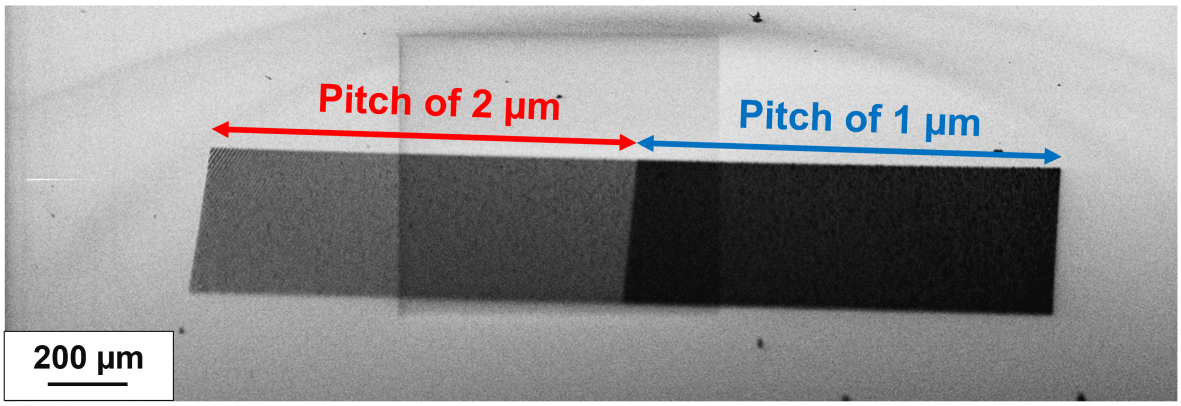


Figure II.12 – *Tilted-view SEM image of the patterned area of the #IBM1 substrate.*

Undoped NWs were grown with $P_{GaCl} = 1.6 \times 10^{-3}$ atm and $P_{As_4} = 3.0 \times 10^{-4}$ atm. Growth was made at 740 °C during 10 min. For the doped NWs, the same growth conditions were kept in order to see a possible effect of doping. The n-doped NWs were grown with 3 sccm of $SiH_4$ and the p-doped NWs were grown with 30 sccm of DEZ.

## II.2.3 Influence on nanowires morphology

We will first study the impact of doping on the morphology of NWs, SEM images of the NWs are shown in Figure II.13. The first observation that can be made is that, whatever the dopants, a perfect selectivity is observed with a very good homogeneity in the morphology of the NWs. Moreover, whatever the pitch, the NWs exhibit a hexagonal shape defined by the family of 6 facets {-110}. In order to better compare the NWs with each other, the mean NWs length and diameter are reported in Table II.2.

| | **Pitch of 1 µm** | | **Pitch of 2 µm** | |
|---|---|---|---|---|
| | Length (µm) | Diameter (µm) | Length (µm) | Diameter (µm) |
| undoped | 5.58 | 0.16 | 5.64 | 0.15 |
| n-doped | 1.30 | 0.43 | *inhomogeneous* | *inhomogeneous* |
| p-doped | 3.16 | 0.17 | 3.23 | 0.17 |

Table II.2 – *Mean length and diameter for undoped, n-doped and p-doped NWs for pitches of 1 µm and 2 µm on #IBM1 substrate.*

To begin with, we note that dopants have an influence on the morphology of NWs. Indeed, the n-doped NWs are much shorter and thicker than the undoped ones. This could be explained by a change in the surface structure due to Si dopants [153]. For the pitch of 1 µm, the NWs exhibit a perfectly hexagonal shape. However, we note that for the pitch of 2 µm, the shape of the NWs is strongly different and the NWs no longer exhibit a hexagonal shape. The only thing that changes between Figure II.13.c and Figure II.13.d being the pitch, a possible hypothesis is that Si atoms adsorb on the mask, unlike chloride precursors, and then diffuse to the NWs lateral facets. If so, this effect would be preponderant for the pitch of 2 µm. Concerning the p-doping, it seems that there is a significant effect on the length of the NWs but not on the diameter. Since the undoped ones are unintentionally p-doped, as discussed previously in section II.2.1 (page 63), it can be assumed that the undoped and p-doped NWs have a similar shape. Finally, according to the data in Table II.2, it would seem that for these corresponding pitches (1 µm and 2 µm) no significant influence on the dimension of the NWs is observed. Thereby, unlike $SiH_4$ which seems to interact with the $SiO_x$ dielectric mask, there does not seem to be a diffusion effect of DEZ at these growth conditions. Finally the results presented here seem to be in agreement with our previous hypotheses. Characterizations of these NWs were made at McMaster University in collaboration with Nebile Goktas, Ethan Diak and Amanda Thomas. Before studying the optical properties of NWs, we will focus on the crystallographic properties.

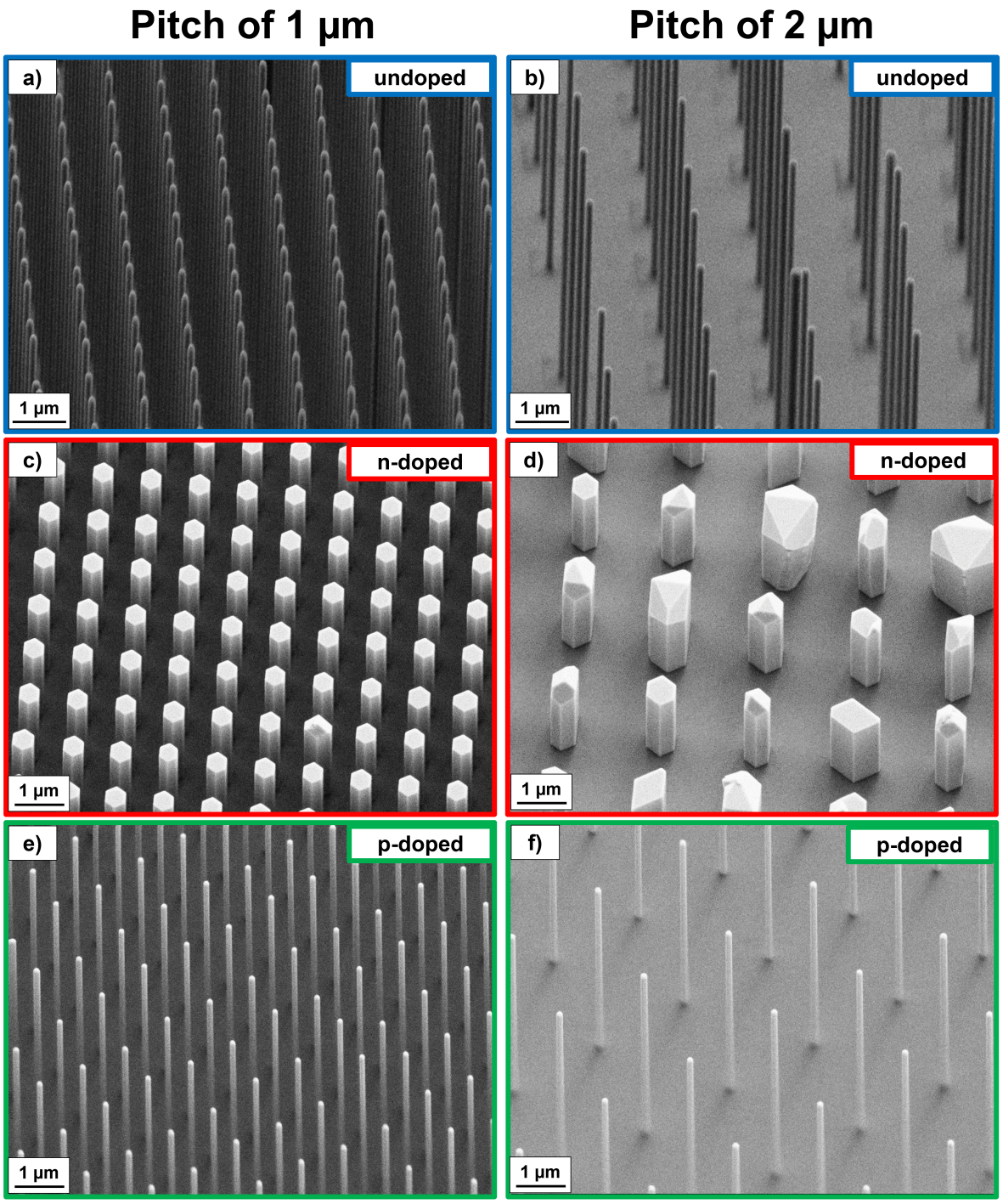


Figure II.13 – *Tilted-view SEM images of: undoped NWs grown on #IBM1 substrate with a pitch of a) 1 µm, b) 2 µm, n-doped NWs with a pitch of c) 1 µm, d) 2 µm and p-doped NWs with a pitch of e) 1 µm, f) 2 µm. The respective flows of n-dopants and p-dopants are: 3 sccm of $SiH_4$ and 30 sccm of DEZ.*

## II.2.4 Structural properties

The NWs were detached in an ultrasonic bath for 2 min. They were then deposited on copper TEM grids for HRTEM analyses. Another part of the NWs was deposited on Si substrate for optical characterization by μ-PL. HRTEM images of NWs are shown in Figure II.14. These images were taken using a Titan 80-300 HB scanning TEM (STEM) operating at multiple accelerating voltages at the Canadian Centre for Electron Microscopy (CCEM) in McMaster University.

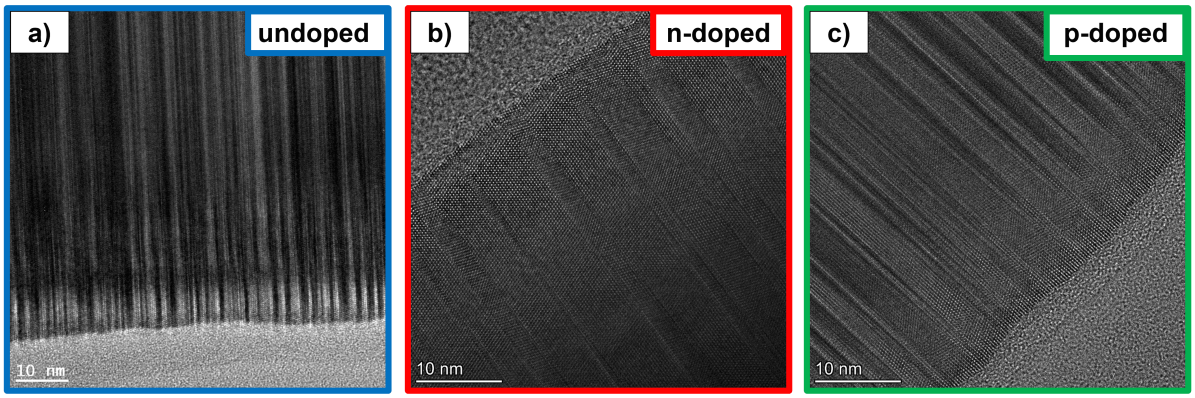


Figure II.14 – *HRTEM images of a) undoped, b) n-doped and c) p-doped GaAs NWs. The shell present on the NWs is an oxide layer. The incident electron beam was along* $\langle 1-10 \rangle$.

Firstly, we observe that the NWs exhibit a high density of random stacking faults related to the ZB/WZ polytypism. As explained previously in section I.3.1 (page 11), this polytypism is commonly observed during growth of GaAs NWs along the [111]B direction. Nevertheless, we note that for the n-doped NWs, larger phase domains appear on NWs. Goktas et. al. have already observed a similar phenomenon in self-assisted GaAs NWs [154]. In their study, they revealed periodic zinc-blende twins, known as twinning superlattices, that are often induced by a high-impurity dopant concentration. They showed that the period of the twinning superlattices increased with the doping concentration and was proportional to the NW radius. However, no significant periodicity in phases was observed in the n-doped NWs presented here. Nevertheless, it would be interesting to see if the same phenomenon appears for higher doping and to provide statistics on the periodicity of ZB/WZ phases. This will be studied in a future work.

## II.2.5 Optical properties

In order to optically characterize these NWs, μ-PL measurements were made on individual NWs. First of all, we have seen that these NWs exhibit a lot of stacking faults which will probably impact the optical properties. Moreover, it should be noted that the observed influence of doping on optical properties can be biased by the doping of the substrate. Indeed, the substrate used is p-doped and there may have a diffusion of charge carriers from the substrate. μ-PL have been made with an illumination from a Melles Griot Argon Ion laser with an excitation wavelength of $\lambda_{exc} = 488$ nm (power in the mW range) and with a 60 × microscope objective. Spectra are collected through a 0.05 mm slit using a 5 s exposure time and come from 3-4 NW sites on each sample. A constant background is subtracted from the spectra to give a zero reference. Room temperature μ-PL measurements were made and no luminescence were observed for the undoped NWs while luminescence was observed for the doped samples. Thus, this suggests that there is an effect of doping on luminescence. We will focus on measurements made at low temperature which provide more exploitable information. 7.5 K μ-PL spectra are shown in Figure II.15.

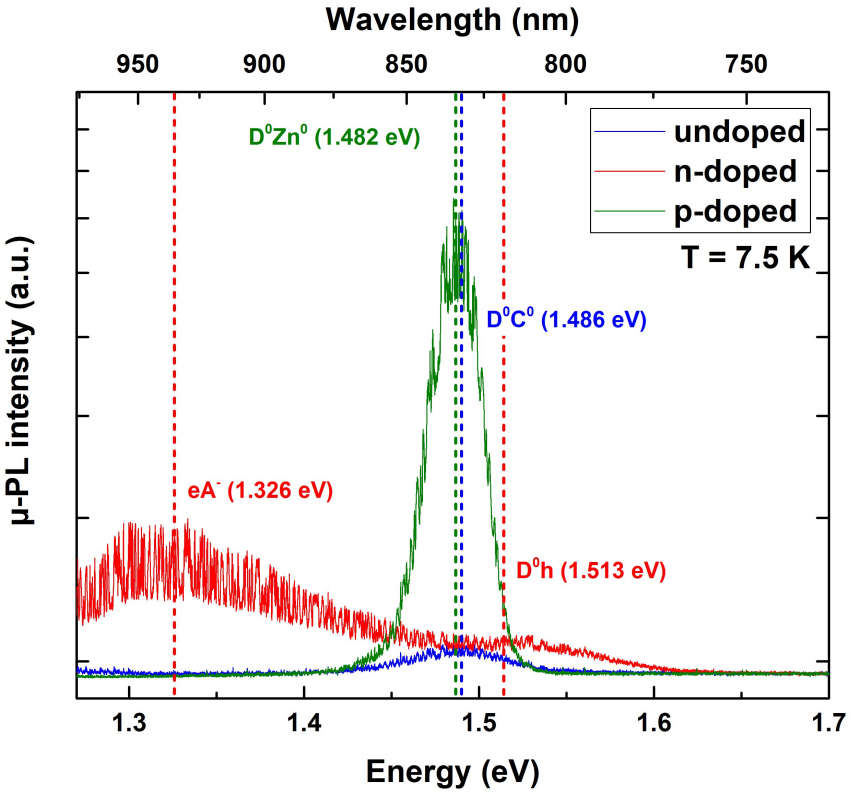


Figure II.15 – *7.5 K μ-photoluminescence spectra of an undoped (blue), n-doped (red) and p-doped (green) single GaAs NW. The y-axis is in logarithmic scale.*

First of all, we note that the PL intensity depends on the doping. The undoped signal has a lower luminescence than the doped ones, which is consistent with a low residual doping. However, it should be specified that, to a lesser extent, the morphology of the NWs can also impact the PL intensity. It can be seen that the undoped NW has a peak which corresponds to a carbon donor-acceptor transition ($D^0C^0$) at 1.486 eV. Thus, as was the case for the GaAs layers, undoped NWs seem to be unintentionally p-doped due to residual carbon in the reactor. This residual carbon probably comes from impurities and from the fact that DEZ which contains carbon ($(C_2H_5)_2Zn$) is used. Recently, this has also been observed in the team on undoped GaAs NWs by Zeghouane et.al [74]. This unintentional doping tends to limit the incorporation of n-dopants. When n-doping the NWs, a compensation effect probably takes place before reaching a certain amount of n-dopants.

Regarding the p-doping, a slight redshift is observed. The peak observed at 1.482 eV tends to correspond to the donor-acceptor transition ($D^0Zn^0$).

Concerning the n-doping, a high energy peak appears at around 1.513 eV corresponding to a $D^0h$ transition. A low energy peak at 1.326 eV appears only for n-doping. Thus, we tend to think that this peak is linked to an effect of the Si dopants. In the literature [152], this peak is associated with free electron to ionized acceptor transition $eA^-$, involving the deep level related to Ga antisites defects.

To conclude, these analyses show that there is indeed an effective incorporation of the dopants, which impacts the optical properties of the NWs. It would be substantial to perform growths with higher flows of dopant precursors in order to have a higher doping rate in the NWs. However, these preliminary results are encouraging for the realization of a p-i-n junction which is the subject of the following section.

## II.3 Towards the first demonstration of p-i-n junction nanowire by HVPE

As explained previously, doping of NWs is a delicate task and the growth of a p-i-n junction is even more so. Even if more doping points are necessary, due to a lack of good quality substrates it was decided to conduct the first reported growth of a NW p-i-n junction by HVPE. To do so, the preliminary results of doping presented above will be used to estimate the growth conditions. Many new challenges come into account for the growth of a NW p-i-n junction and obtaining a junction with a good efficiency requires a large number of tests. As the process to make a betavoltaic device is

ponderous and expensive, it was decided to develop a photovoltaic (PV) device rather than betavoltaic one in order to test the p-i-n junction.

## II.3.1 Choice of the growth conditions

Based on our preliminary doping results, it was decided to conduct the first reported growth of a NW p-i-n junction arrays by HVPE. Even if the transition objective is to make a photovoltaic device, to get an idea of the growth conditions, we base ourselves on the optimal theoretical characteristics for obtaining an efficient betavoltaic cell. These values come from simulations carried out by McMaster University in Devan Wagner's Master's thesis [100]. The optimal conditions for GaAs with a radioactive Ni-63 source are:

- NWs characteristics: height = 10 µm, diameter = 355 nm, pitch = 455 nm
- p-doped core: height = 8.7 µm, thickness = 142 nm, p-doping = $10^{19}$ $cm^{-3}$
- intrinsic-shell : height = 1.2 µm, thickness = 75 nm
- n-doped shell: height = 0.1 µm, thickness = 32 nm, n-doping = $5 \times 10^{18}$ $cm^{-3}$

Based on these characteristics, the optimal NW length is 10 µm. As explained before, my previous work on finding optimal conditions for growing long NWs was of paramount importance because whether for a GaAs or InAs NW-based device, the longer the NWs, the greater the efficiency. Obviously these are theoretical optimal conditions and it will be complicated to get exactly these values. Our lack of knowledge regarding the doping rate makes it even more difficult to obtain a good p-i-n junction. Moreover, we do not know exactly how the growth transition between distinct areas will occur because the HVPE setup does not allow, unlike in MBE, to make abrupt junctions at the nanoscale. Indeed, the high growth rate in HVPE, the persistence of gaseous species in the reactor and the fact that the gas valves are manually controlled do not allow abrupt junctions to be made. Consequently, if we switch the doping from p-doping to n-doping, the gaseous species will remain in the reactor for some time which can affect growth. Furthermore, our pitches are 1 µm and 2 µm and not 455 nm as found optimally. Finally, we do not yet know whether the growth of the p-i-n junction will be axial or radial. Nevertheless, even if it is complicated to make the ideal junction, it is necessary to have these values in order to aim for them at best. As this is the first time that such a study has been carried out, the objective is not to grow the perfect p-i-n junction but to estimate if HVPE process is able to grow a p-i-n junction before subsequently optimizing growth conditions.

Even though the optimal NW length is 10 µm, it was decided to grow a junction of around 3-4 µm. Indeed, the resin deposition process when manufacturing a device, which will be explained later in section II.3.2, becomes more and more restrictive when the NWs are very long. The optimal conditions for making long NWs, namely $P_{GaCl} = 1.6 \times 10^{-3}$ atm and $P_{As_4} = 3.0 \times 10^{-4}$ atm, were implemented. As these values were also used for the growth of the p-doped and n-doped NWs, we can roughly estimate the growth rate of the different areas. Nevertheless, it should be noted that we do not know how the growth will occur and whether the p-i-n junction will be core/shell rather than axial. The growth conditions were set as:

- p-core: 10 min with 30 sccm of DEZ
- i-shell: 30 sec
- n-shell: 2 min and 30 sec with 3 sccm of $SiH_4$

Growth time was 10 min and the temperature was set at 740 °C. SEM images of as-grown NWs are shown in Figure II.16

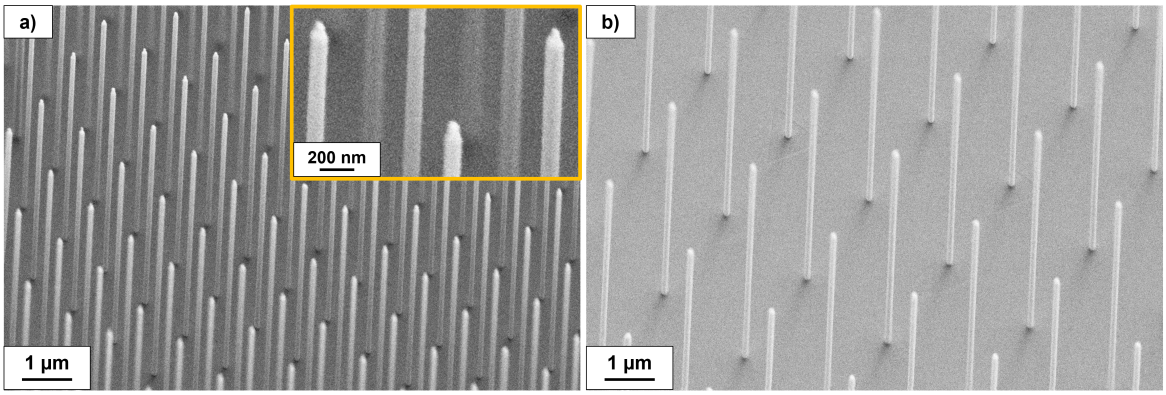


Figure II.16 – *Tilted-view SEM images of the array of NW p-i-n junctions grown on #IBM1 substrate for a) pitch of 1 µm and b) pitch of 2 µm. The inset in a) represent a closer view of the top of the NWs.*

The mean length and diameter are $L = 3.82$ µm and $D = 110$ nm for the pitch of 1 µm and $L = 3.90$ µm and $D = 130$ nm for the pitch of 2 µm. Thus, no significant difference of the NWs dimensions depending on the pitch is observed. Regarding the morphology, the top of the NWs exhibit a "candle" shape with a height of about 80 nm which does not quite match the expected n-doped NWs height. Nevertheless, it still could be the n-doped area. First, we do not know exactly how the growth of n-doped area occurs on the intrinsic area. Consequently, the axial growth rate could be strongly impacted and be different from the purely n-doped NWs growth rate. Moreover, we have seen that the morphology of p-doped NWs and undoped NWs is close, so this reinforces the idea that this "candle shape" could be related to the n-doped area. Therefore, one can expect that this is an axial structure but

the hypothesis of a core-shell structure cannot be ruled out because the radial growth is not controlled. Indeed on the SEM images alone, it is not possible to determine if there has been lateral growth of an n-doped shell. It should be noted that the NWs cannot be passivated inside the HVPE reactor, so the quality of the device may be reduced. Nevertheless, ex-situ passivation of GaAs catalyzed NWs grown by VLS-HVPE has already been carried out in collaboration with the Surfaces & Interfaces team of Institut Pascal and was achieved using $N_2$ plasma [41]. Thus, this option should be considered if future devices were to be performed by HVPE. The device procedure has been set up at McMaster University in collaboration with Amanda Thomas (PhD student at McMaster University).

## II.3.2 Device fabrication

Before trying to make a betavoltaic device, due to technical and financial constraints, it was decided to first make a photovoltaic device to test the p-i-n junction. This is a first time for the HVPE process. The manufacturing process of a device is a difficult task with a large number of delicate steps which makes it difficult to have a good quality device. During my stay at McMaster University, I was able to attend part of the process but due to encountered technical delays I was unable to attend the entire processing. However, I will explain the whole procedure for future p-i-n junction work. To make NW-based devices, it is necessary to mechanically support the fragile NW array before applying top contacts. An electronic resin with favorable light transmission is ideal for photovoltaic applications. A layer of Cyclotene 3022 (BCB) can be applied on top of the sample by repeated spin coating and curing. The cured BCB can then be back-etched to expose NW tips before contact deposition. Then the top and back contacts are added. Typical NW-based p-i-n junction is shown in Figure II.17 with the summary device processing procedure.

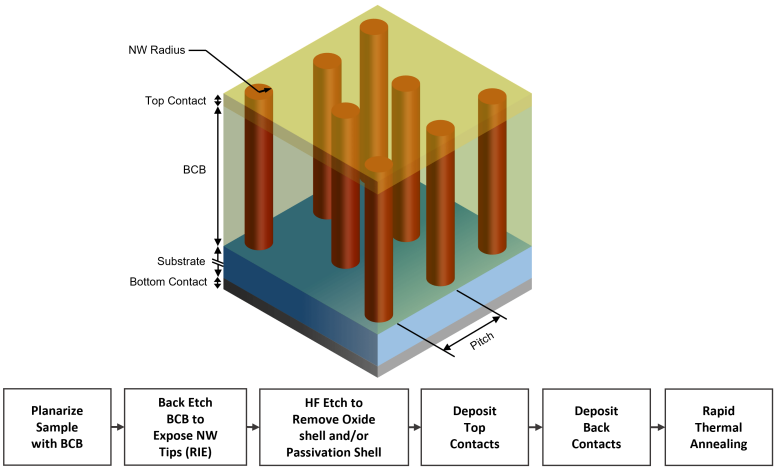


Figure II.17 – *Device processing of an array of NW p-i-n junction.*

The detailed procedure for manufacturing an NW-based device is as follows:

– **Planarization with BCB**: the BCB is deposited by spin coating at 3000-4000 RPM for 30-90 seconds. It may happen that several deposits are necessary in order to completely cover the NWs. BCB films were cured in a nitrogen cabinet to the following program:

| **Set** | **Time (min)** | **Temperature (°C)** |
|---|---|---|
| 1 | 5 | 100 |
| 2 | 5 | 200 |
| 3 | 60 | 250 |

Table II.3 – *Procedure used to cure the BCB.*

– **Reactive Ion Etching - BCB**: Back-etching the BCB is often necessary, because it is difficult to precisely control the BCB thickness relative to the NW heights during spin coating. In addition, there may be edge effects which cause the etching not to be done uniformly over the entire substrate. Samples were etched using a *Technics MICRO-RIE* following the recipe below:

| **$CF_4$ (sccm)** | **$O_2$ (sccm)** | **$N_2$ ( sccm)** | **Power (W)** |
|---|---|---|---|
| 35.8 | 5.4 | 1.8 | 50 |

Table II.4 – *Procedure used for etching by RIE.*

– **Top contact deposition (Sputtering and Metallization)**: As explained previously, it is not possible to perform in-situ NWs passivation in HVPE, so the NWs presented here are not passivated. Nevertheless, it should be noted that passivated NWs require an additional wet etch in $HCl_{(aq)}$ before top contact deposition. The choice of top contact material should be informed by the composition of the NWs. The goal is to achieve an ohmic contact at the metal-semiconductor junction. Material selection is therefore paramount for ensuring a minimal Schottky barrier at the interface. For a generic photovoltaic device, transparent indium tin oxide (ITO) is used for the top contact. The contacts are deposited by photolithography. In general, ITO deposition and metallization require different photomasks to accommodate this requirement. Here 250 nm of ITO has been used to form the transparent top contact layer and 10 nm/200 nm of $Ti/Au$ alloy for top opaque contact. The $Ti$ layer is used as an adhesion layer. Samples were annealed at 400°C for 30 seconds. The top contact deposition procedure is summarized in Figure II.18. The "fingers" make contact with the ITO above the patterned area.

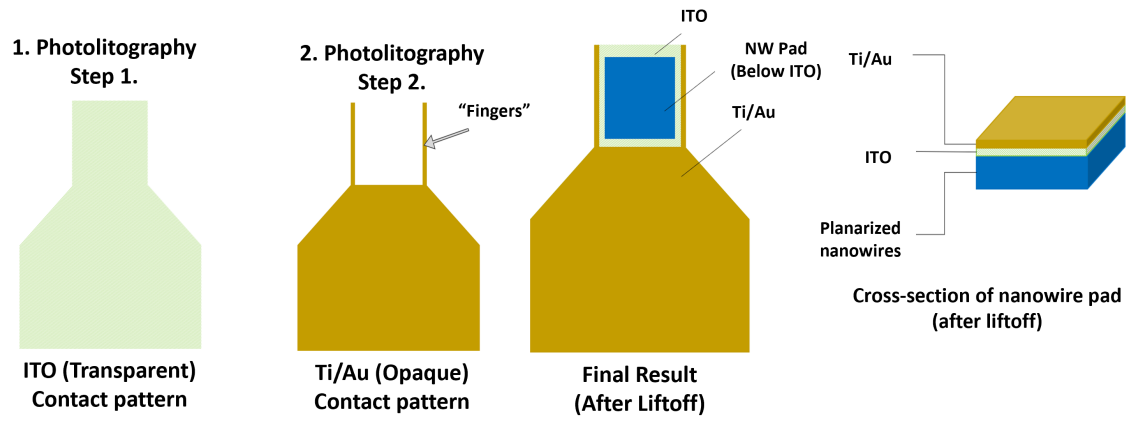


Figure II.18 – *Summary of top contact deposition procedure. The photolithography is done in two steps: 1) deposition of ITO and 2) deposition of Ti/Au layers.*

– **Back Contact Deposition (Sputtering)**: Generally, aluminum is used for the back contact, and can be sputtered using the ITO sputtering system. Nevertheless, the same procedure as for top contacts has been used, namely 10 nm/200 nm of $Ti/Au$ alloy. The back contact completely covers the underside of the sample, so a mask is not necessary. However, it is recommended to apply a thick sacrificial layer of photoresist to the top side to prevent any damage during the back side sputtering process. An HF dip immediately prior to sputtering may be useful to remove native oxide.

– **Rapid Thermal Annealing (RTA)**: Contact quality is generally improved by annealing. Typical rapid annealing times are on the order of 30-60 seconds, with temperatures ranging from 300-500 °C. We have to be mindful of the glass transition temperature of BCB (about 350 °C), when considering longer or hotter recipes. Also note that the ITO film is known to crack under certain annealing conditions. Annealing is recommended prior to all electrical measurements. It primarily serves to: increase the grain size in metal films (thereby improving conductivity), promote alloying of adjacent metal layers (improves top contact) and to promote diffusion of metals into the semiconductor lattice (improves back contact). Here samples were annealed at 400 °C for 30 seconds under $N_2$ atmosphere.

Finally, after the whole process procedure, the cross sectional view of our NW p-i-n junction (assumed to be axial) is represented in Figure II.19.

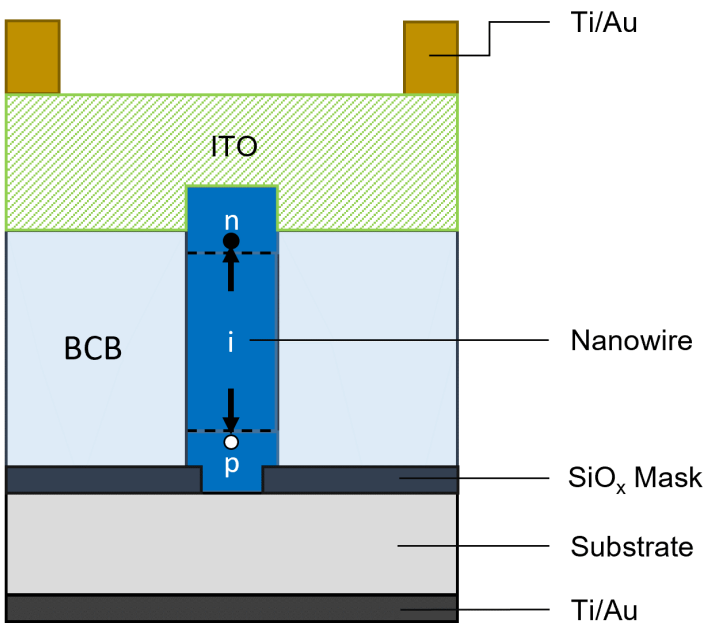


Figure II.19 – *Cross sectional view of an axial NW-based device (not to scale).*

The edge and the center of both pads after the first deposition of BCB by spin coating is shown in Figure II.20.

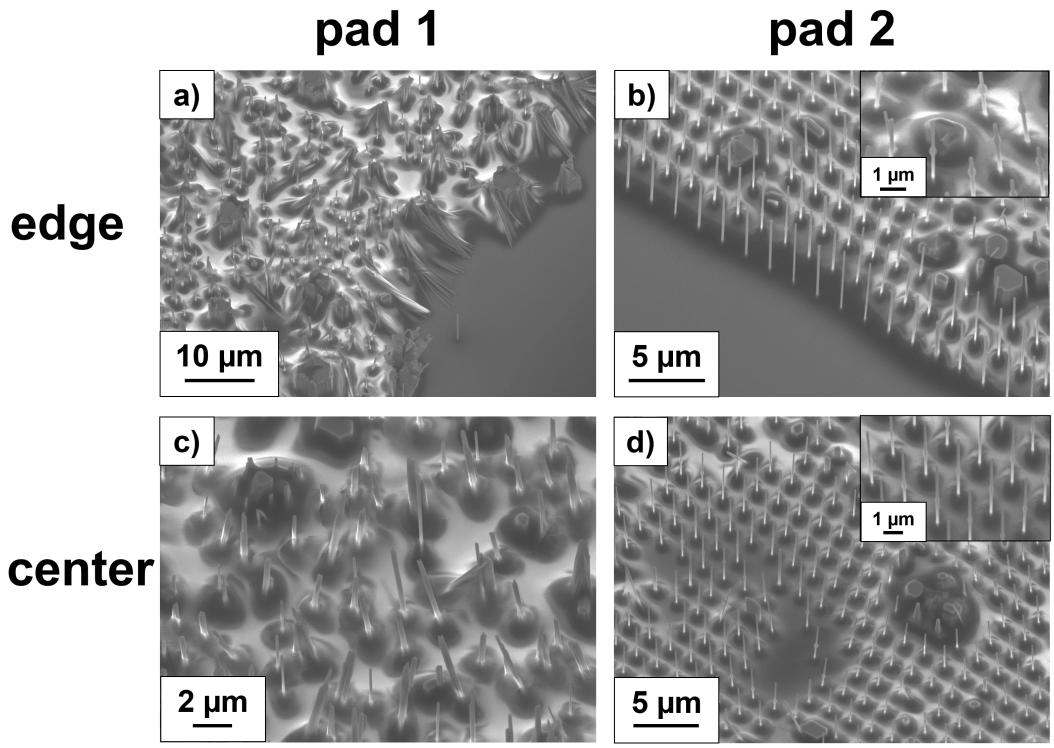


Figure II.20 – *30° tilted-view SEM images of the substrate after the first deposition of BCB: edge of a) pad 1 and b) pad 2, center of c) pad 1 and d) pad 2.*

First, we see the significant edge effect that appears because of the spin coating. Consequently, the thickness of BCB is not constant over all the NW array. For pad 1 (Figure II.20.a), the NWs are removed from the substrate and for pad 2 (Figure II.20.b) there is almost no layer of BCB deposited. Regarding the behavior of the NW arrays at the center, the NWs of pad 1 (Figure II.20.c) look damaged and bent, probably due to the spin coating. Pad 2 (Figure II.20.b) is more consistent with vertical NWs. However, the NWs have a kind of droplet in the middle of their length which seems to be a residue of the initial BCB droplets deposited before the spin-coating.

The procedure to achieve the complete planarization of the NWs was long and complicated. In total, it took four spin coatings and eight etchings by RIE. This large number of steps damages the sample and impacts the quality and efficiency of the device.

Figure II.21 shows the two pads after the final planarization step. We note on pad 1 that few NWs come out and that it is inhomogeneous. On pad 2, we see that the top of the NWs protrude well beyond the BCB but that the surface of the BCB is significantly rough.

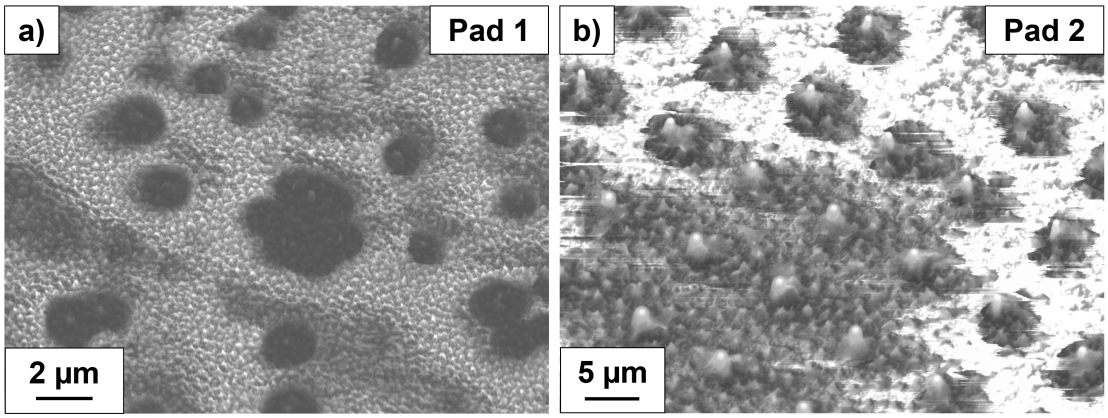


Figure II.21 – *30° tilted-view SEM images of the center of the substrate after the planarization process of a) pad 1 and b) pad 2.*

After planarization, top and back contacts were deposited according to the procedures detailed previously. Now, it is possible to make electrical characterizations which is the subject of our next section.

## II.3.3 I-V characterization

### II.3.3.1 I-V curves and power conversion efficiency

To measure the performance of a device, I-V (or J-V) characterizations are commonly carried out. Two I-V curves, with and without illumination, are generally required for a high-level characterization of PV device quality and performance. Before the I-V measurements, the sample was adhered to copper 24-gauge sheet using *EPO-TEK H20E* silver (Ag) epoxy for electrical characterization. To obtain I-V curve acquisition, a 4-probe arrangement (i.e. a separate current and voltage probe at each contact) is used to minimize the line resistance. Here the sample was characterized using 4-probe I-V measurement test bench setup. Voltage and current sensing has been carried out by a *Keithley 2400* source meter. To illuminate the sample, a AM1.5G solar irradiance spectrum was used using a solar simulator module. The sample contains two different pads corresponding to the two different patterned areas. Pad 1 corresponds to the pitch of 1 µm and pad 2 to the pitch of 2 µm. To better visualize, a photograph of the sample was taken after top contact deposition of pad 1 as illustrated in the Figure II.22.

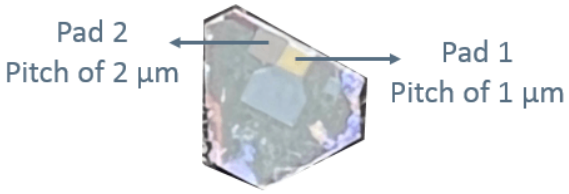


Figure II.22 – *Photograph of the NW-based PV device. Top contact pattern is visible on pad 1.*

J-V curves have been obtained under dark and illuminated conditions for bias voltage sweeps of (-3,+3V). J-V curves of both pads are shown in Figure II.23.

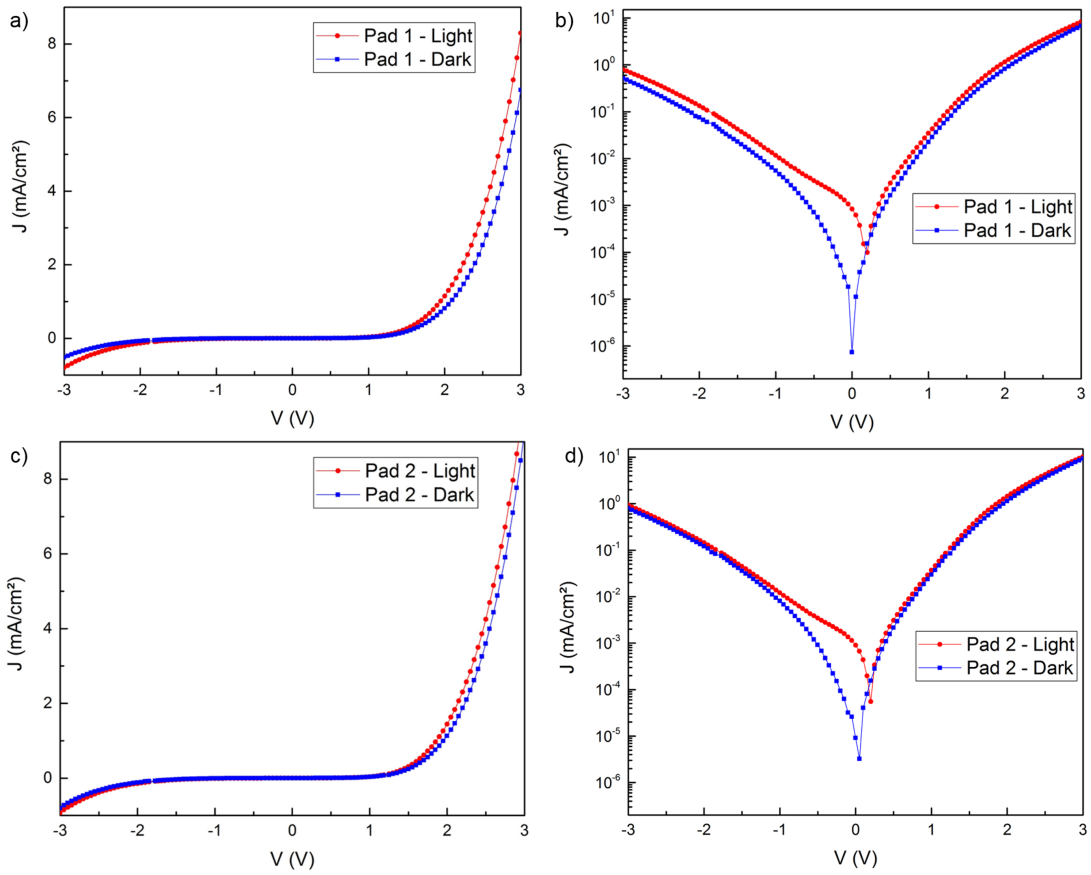


Figure II.23 – *J–V characteristics of the NW ensemble in the dark (blue line) and under illumination (red line) for a) pad 1 and c) pad 2. Corresponding measured semilog dark J–V characteristic of b) pad 1 and d) pad 2.*

The information that can be drawn from these I-V curves is that there is a shift of the minimum position when the sample is under light. This does indicate that there is a response to an illumination with formation of charge carriers which induce a current. Nevertheless, the current values are extremely low (about $10^{-6}$ mA/cm$^2$) which therefore suggests a poor PV efficiency. However, we recognize here a diode response with a rectifying effect. This is linked with the fact that solar cells are often modeled with an electric circuit equivalent to a single-diode. This model is used to fit the dark J-V characteristic based on the following equation:

$$J = J_0\, exp[\frac{V - JR_s}{nV_t}] + \frac{V - JR_s}{R_{sh}} \tag{II.8}$$

with $J_0$ the dark saturation current density, $V_t = kT/q$ the thermal voltage, $R_s$ the series resistance, $R_{sh}$ the shunt resistance and n the ideality factor such as:

$$n = (2.3mV_t)^{-1}\ ,\ m = d\,log(I)/dV \tag{II.9}$$

All these parameters are obtained by fitting the curve close to zero. However, no fit converged suggesting that our diode does not behave like a solar cell. This is not surprising given the low currents obtained. However, it is still possible to determine the series resistance by fitting the high voltage linear response. This gives $R_s = 1.04\ \Omega.\text{cm}^2$ for pad 1 and $R_s = 1.18\ \Omega.\text{cm}^2$ for pad 2. These values are relatively high compared to conventional values of $0.1\ \Omega.\text{cm}^2$ [155]. Several parameters can explain this high value, namely the movement of current through the emitter and base of the solar cell; secondly, the contact resistance between the metal contact and the silicon; and finally the resistance of the top and rear metal contacts. The main impact of series resistance is to reduce the fill factor FF, although excessively high values may also reduce the short-circuit current.

From the I-V curve, PV energy conversion efficiency is deduced by determining the open-circuit voltage $V_{oc}$ and the short-circuit current $Jsc$. The short-circuit current and the open-circuit voltage are the maximum current and voltage respectively from a solar cell. However, at both of these operating points, the power from the solar cell is zero. The "fill factor", more commonly known by its abbreviation FF, is a parameter which, in conjunction with $V_{oc}$ and $J_{sc}$, determines the maximum power from a solar cell. The FF is defined as the ratio of the maximum power from the solar cell to the product of $V_{oc}$ and $J_{sc}$ so that:

$$FF = \frac{V_{mp}J_{mp}}{V_{oc}J_{sc}} \tag{II.10}$$

where $V_{mp}J_{mp}$ is the maximum power from the solar cell.

Thus, using these parameters, one can determine the performance of a PV cell. The most relevant metric for the performance of a PV cell is the power conversion efficiency (PCE) given by:

$$\eta = FF\frac{J_{sc}V_{oc}}{I_{inc}} \tag{II.11}$$

where $I_{inc}$ is the incident irradiance (usually 100 mW/cm² for the simulated AM1.5G spectrum). The various parameters obtained with the corresponding I-V curves are illustrated in Figure II.24.

The efficiencies $\eta$ obtained are of the order of $\sim 5 \times 10^{-5}$ % which is extremely low. Indeed, the maximum value of efficiency of a GaAs NW-based PV device is 15.3% for 1 sun [85]. Several hypotheses can explain these values and will be discussed in the next section.

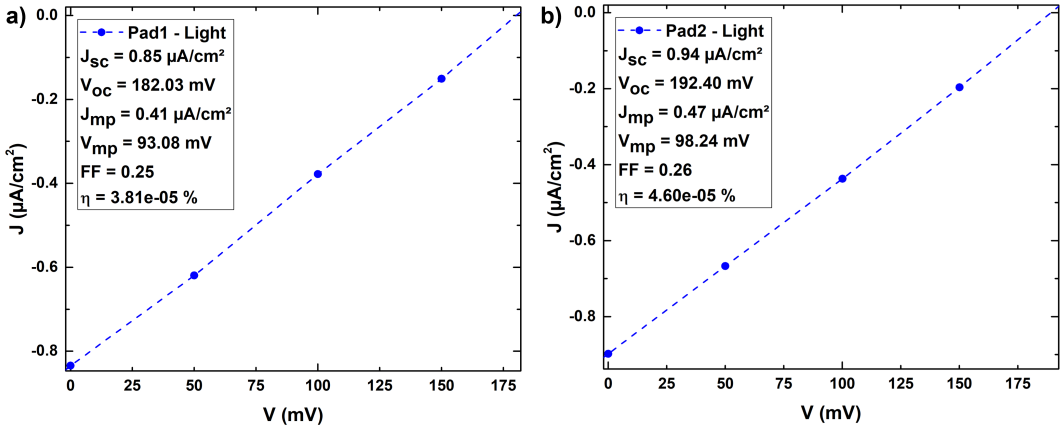


Figure II.24 – *Close I-V curves with the different parameters obtained FF and η for a) pad 1 and b) pad 2.*

Nevertheless, it is possible to quantify the diode rectification using a 'rectification ratio' (RR) defined as:

$$RR(V) = \left| \frac{J+(V)}{J-(V)} \right| \tag{II.12}$$

Thus, RR was calculated for several voltage values: (-1,+1V), (-2,+2V), (-3,+3V) as illustrated in Figure II.25. If we calculate the average rectification ratio $RR_{avg}$ on these 3 pairs of voltages, we obtain $RR_{avg} = 7.33$ for pad 1 and $RR_{avg} = 8.09$ for pad 2. These positive and sufficiently high values clearly show the rectifying effect of the diode

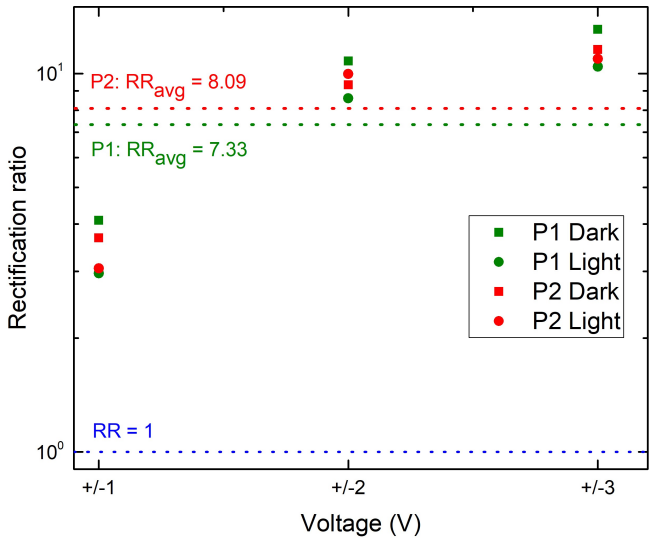


Figure II.25 – *Semi-log rectification ratio (RR) of pads 1 and 2 at +/-1, +/-2 and +/-3V. Their respective average RR is shown in dotted line.*

Despite this good rectification, the efficiency of the device is very poor. Several reasons can explain such values and this is the subject of our discussion.

### II.3.3.2 Discussion and perspectives

As seen before, the efficiency of the device produced is very low. This was the very first device that has been processed from arrays of NW p-i-n junction by HVPE. For the development of future device, several points must be addressed to improve the performance of the device. These points of improvements are divided into two major sub-parts dealing with the growth of the NW p-i-n junction and the device processing.

- **Improve growth of p-i-n junction by HVPE**: First of all, it would be necessary to have a complete quantitative knowledge of doping. It would be necessary to carry out several series of growth with different doping rates on NWs and on layers, and to characterize them by Hall effect. Furthermore, the n-doping used for this p-i-n junction (3 sccm of $SiH_4$) is probably too weak to achieve a good p-i-n junction. Indeed, the intrinsic undoped area being unintentionally p-doped, there is probably a compensation effect. Thus, the junction studied here should not be a p-i-n junction but rather a p+/p- junction which is not sufficient to make it a good junction. Furthermore, the NWs are unpassivated, which causes a lot of leakage currents and a deterioration of the device efficiency. The purpose of this project was first of all to make the first test of growth of p-i-n junction and our observations lead to believe that it is quite possible to carry out such a structure by HVPE. However, my study was preliminary with only few samples available for doping and no information on corresponding doping rates. Finally, these results showed that the collaboration with McMaster University could be fruitful because HVPE succeeds easily in the realization of long NWs and at a low cost. The NWs are homogeneous with a very good selectivity which could be difficult to achieve in MBE. Thus, from these first encouraging preliminary results, we hope that future projects will be carried out in close collaboration with McMaster University for the realization and characterization of NW-based devices.

- **Improve device processing**: Several issues were encountered during the process which probably deteriorated the device quality. Firstly, after the first spin, a poor uniformity has been observed for BCB deposition. Consequently, the subsequent deposited layers are probably non uniform which deteriorate the contact quality. Moreover, several etching of the BCB were necessary with different etching times. Therefore, inhomogeneity of the BCB and etching repetition have induced a great variation of the local thickness of the BCB and roughness on the

BCB surface. Afterwards, issue with the compatibility of NW pad positions with photolithography mask has been encountered. Indeed, it was difficult to align top contact mask pattern to accommodate top contacts for both NW pads on the sample. Finally, residual incomplete opaque top contact remained after the liftoff stage.

## II.3.4 Optimization of a new junction: perspectives

In order to see if the growth of high quality NW p-i-n junction by HVPE is really possible, it was decided to conduct a growth with the maximum flow of n-dopants ($SiH_4 = 10$ sccm). In addition, the substrate used here is #Bath which is undoped, which avoids any diffusion of the carriers from the substrate. A major difference with the previous p-i-n junction is that it was decided to vary $P_{GaCl}$ between each step in order to promote lateral growth. Indeed, as explained previously (section II.1.3 on page 53), an increase in $P_{GaCl}$ promotes an increase in the lateral growth rate. Between each step in order to stabilize the flow of GaCl, a 2-minute growth interruption is done under arsenic atmosphere to avoid the desorption of As adatoms. The growth temperature and $P_{As_4}$ were fixed at 740 °C and $3.0 \times 10^{-4}$ atm, respectively. The growth steps are as follows:

- p-core: 10 min with $P_{GaCl} = 1.6 \times 10^{-3}$ atm and 30 sccm of DEZ
- i-shell: 30 sec with $P_{GaCl} = 3.2 \times 10^{-3}$ atm
- n-shell: 30 sec with $P_{GaCl} = 4.8 \times 10^{-3}$ atm and 10 sccm of $SiH_4$

SEM images of as-grown NWs are shown in Figure II.26. An image with the INLENS detector of the SEM was taken to better visualize the contrast at the top of the NWs.

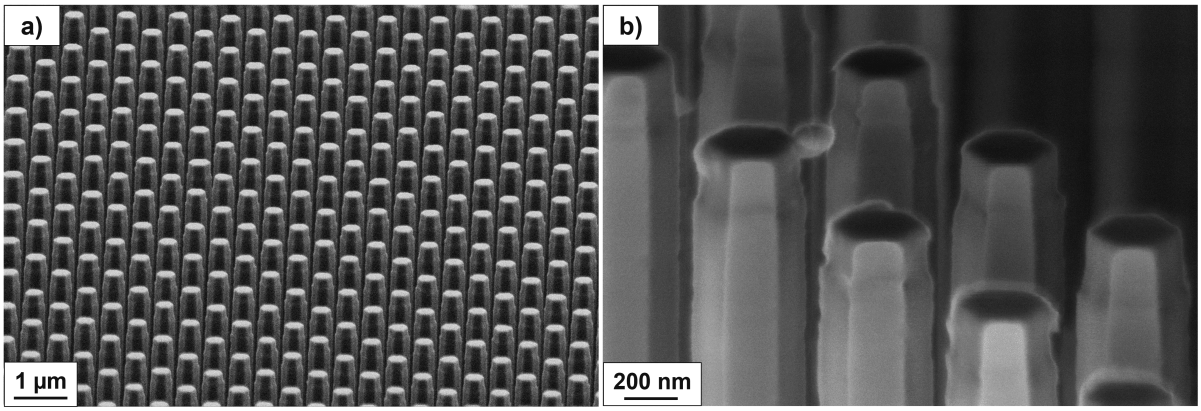


Figure II.26 – *Tilted-view SEM image of p-i-n junction GaAs NWs grown on #Bath substrate at a) large field and b) near-field with SEM INLENS detector.*

First of all, it can be seen that despite several growth interruptions and the use of a high n-dopants flow (the maximum admissible by the $SiH_4$ flowmeter), perfect selectivity is preserved. NWs are homogeneous and exhibited a hexagonal shape. NWs mean length is 3.3 µm and NWs exhibited a significant narrowing of the diameter at the top from 430 nm to 350 nm. The length of this area is about 200 nm. From the SEM images, it is not possible to determine the nature of this narrowing area but based on our previous results, several hypotheses can be submitted. First, undoped NWs and p-doped NWs are very close morphologically. There is no reason for a sudden narrowing to occur except because of n-doping. The $SiH_4$ flow being very strong (10 sccm) it is conceivable that the radial growth rate is strongly impacted. Thus, it seems conceivable that this narrowing area could be the n-doped area. Finally, as radial growth is not fully controlled, we cannot exclude the hypothesis of a n-doped layer deposited on NWs sidewalls, which would make core-shell structures.

In order to determine the nature of this narrowing area, and to know if we are in the presence of a p-i-n junction, cathodoluminescence (CL) measurements were carried out by Gwénolé Jacopin at Institut Néel in Grenoble. The interest of CL for characterising p-i-n junctions is that we can investigate both spectral and spatial resolutions as detailed below. The experimental setup of the CL is illustrated in Figure II.27.

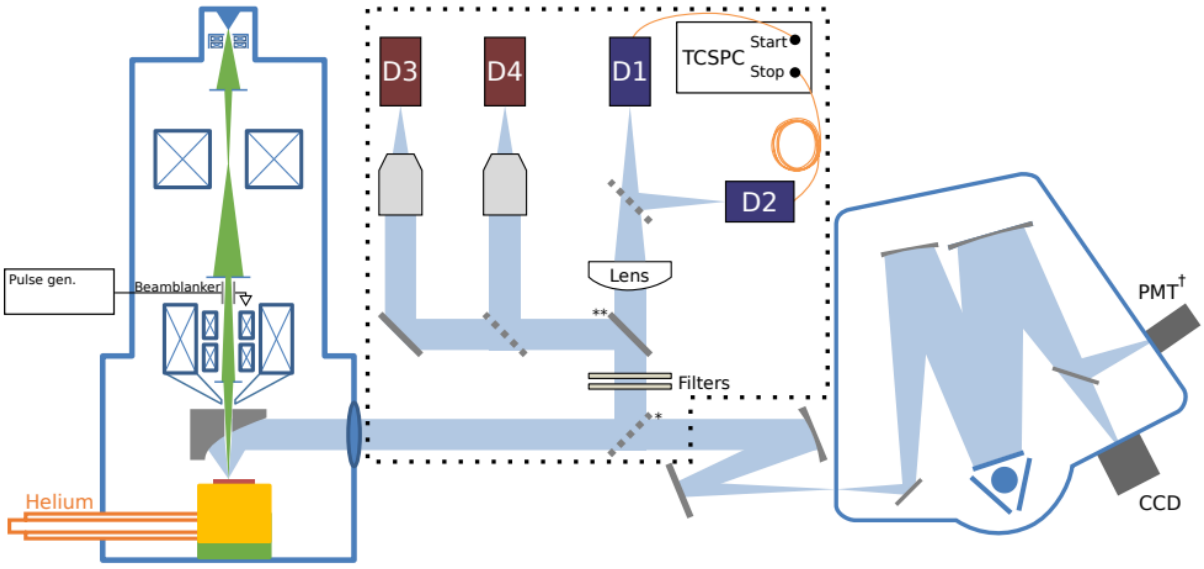


Figure II.27 – *Schematic of the experimental setup of the cathodoluminescence at Institut Néel. The part surrounded by a dashed box was not used during the measurements. Two exit ports are available with: 1) charge-coupled device (CCD) or 2) a photomultiplier tube (PMT). Note that time-resolved cathodoluminescence (TRCL) is possible by replacing PMT by a hybrid PMT (D2) and by using the beam blanker. From [156].*

The CL setup consists of a SEM (FEI Inspect F50) equipped with a cryogenic stage allowing to work from 5 to 320 K. A parabolic mirror with a focal length of 12 mm was internally designed and is controlled by piezoelectric actuators, allowing fine positioning. The light is then focused on the entrance slit of a spectrometer (Horiba iHR550) using a second parabolic mirror with a focal length of 300 mm. This duet of mirrors acts as a microscope with a 25× magnification. This high magnification helps to make a precise alignment of the parabolic mirror. The spectrometer is equipped with several gratings but for these measurements, a 600 gr/mm grating was used. Two exit ports are available. On the first exit port, a charge-coupled device (Andor Newton DU940 BU2 CCD) is mounted and is used for optical alignment, spectra acquisition, or hyperspectral mapping, i.e., the e-beam scans a grid (or line) of points and a spectrum is recorded at each point. Thus, in order to have both spatial and spectral resolutions, hyperspectral mapping has been used for these measurements. To correct a possible drift during the acquisition, a full secondary electron image is acquired before and after the mapping. On the second exit port, it is possible to mount either a photomultiplier (Peltier-cooled Hamamatsu R10699 PMT) to acquire CL images with the same resolution as the secondary electron image. More information regarding this setup can be found in the work of S.Finot [156]. As Institut Néel mainly focused on III-N materials, this CL setup was at the limit of resolution for the infrared range during these measurements. Nevertheless, measurements were made on single NW at a temperature of 5 K with an acceleration voltage of 2 keV. At this accelerating voltage, the interaction depth is approximately 50 nm. It should be noted that I did not carry out the CL measurements but I analyzed the mappings thanks to the program used at Institut Néel (python with the Lumispy package).

Results are shown in Figure II.28. Intensity mapping is shown (Figure II.28.a.c) for two different corresponding spectral bands (in red in Figure II.28.b.d). Thus, we can compare the intensity distribution according to given wavelength ranges in order to see if there are distinct regions within the NW.

There are clearly two main emissions: one around 840 nm (1.48 eV) and one around 855 nm (1.45 eV). First, concerning the emission at 840 nm, if we look at the mapping in Figure II.28.a, almost all of the signal comes from the top of the NW. Therefore, based on the growing conditions, it is reasonable to presume that this signal comes from the n-doped area. The emission at 855 nm is more distributed in the entire NW except the top. Thus, it is reasonable to say that it could correspond to the p-doped area. These observations suggest that there are two distinct contributions in the NW: a n-doped corresponding signal coming from the NW top and a p-doped corresponding signal more

distributed in the NW. Thus, it would seem that the NWs present an axial junction rather than a radial one because, given the small interaction depth, if the n layer was present as a shell we should have had an uniform signal over the entire NW. However, CL is not a method of direct measurement of doping so we cannot conclude on this point. It should be noted that the multiple peaks observed beyond 860 nm could be a useful signal but it is modulated by the spectrometer grating. Thus, this signal is not usable in practice.

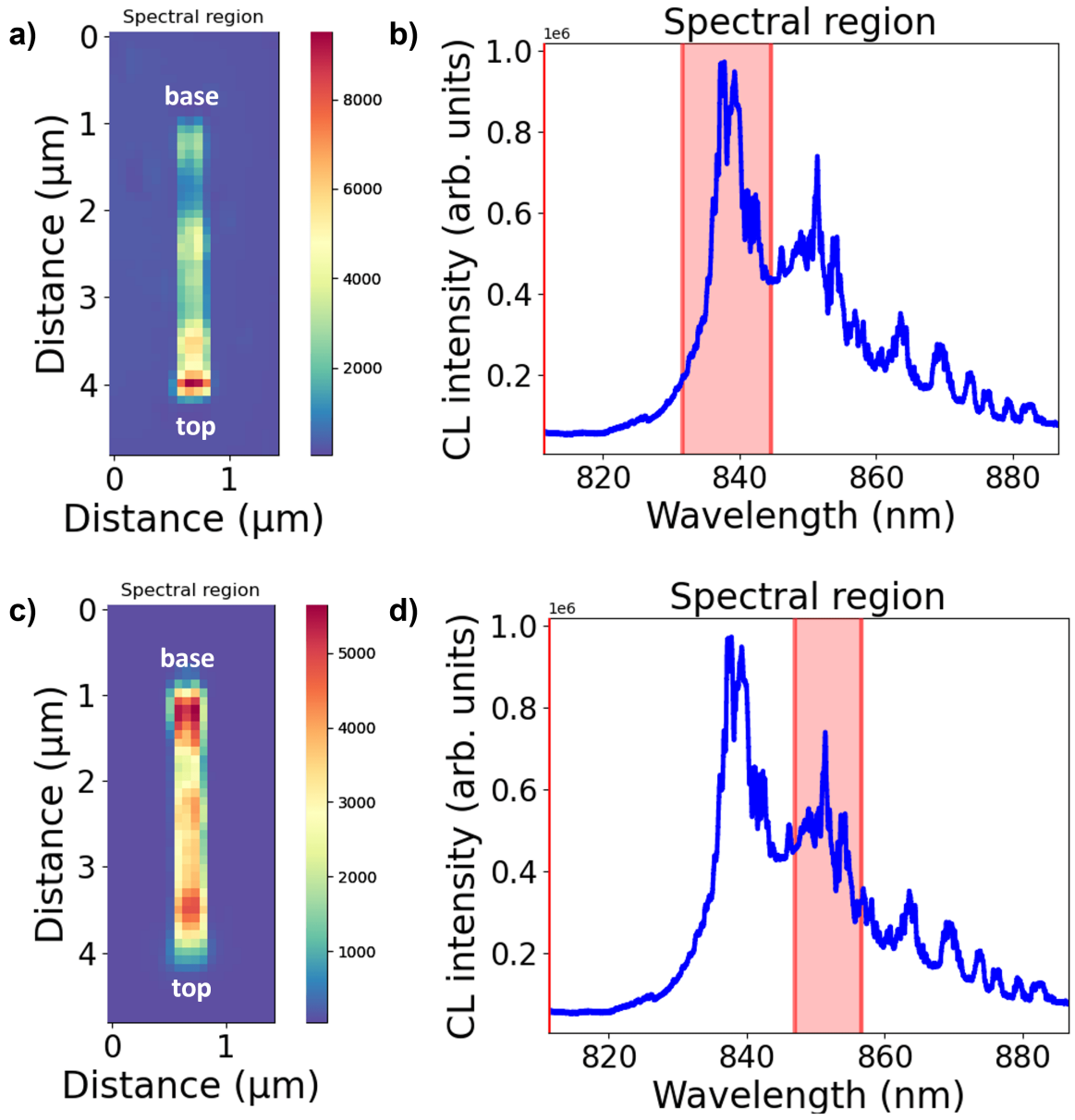


Figure II.28 – *5K Cathodoluminescence spectra of a single NW with their respective intensity mapping for two different wavelength ranges: a-b) 840 nm and c-d) 855 nm. The wavelength range width represented in red in the spectra is 10 nm.*

It is difficult to conclude on the nature of these two areas. For example, it could be two p-doped areas (or two n-doped areas) but with a significantly different doping rate. Moreover, we cannot directly compare these measurements with the results of μ-PL of section II.2.5 (on page 71) because of the following reasons: 1) the substrates are different, #Bath is undoped whereas #IBM1 is p-doped, 2) the dopant precursors flows are different (10 sccm of $SiH_4$ versus 3 sccm), 3) the temperature of the DEZ bath is significantly different here $\theta_{DEZ} = -22$ °C than for the p-doping growth of the section II.2.5 which was $\theta_{DEZ} = -27$ °C and this could have impacted the p-doping rate. In addition, the NWs exhibit most likely ZB/WZ polytypism, which impacts the CL spectra as much as the PL spectra as demonstrated by Spirkoska et.al [136]. They showed that, at a temperature of 4.2 K, pure ZB NWs exhibit a main peak at 1.52 eV while ZB NWs with 30% $\pm$ 10% of WZ exhibit several peaks ranging from 1.52 eV to 1.46 eV. Thus the polytypism greatly impacts the spectrum of CL which makes its exploitation difficult. However, the CL measurements seem to confirm our hypotheses based on the SEM images, namely the NWs present two distinct areas and perhaps axial p-i-n junctions. Thus, these preliminary results are encouraging for the realization of future p-i-n junctions by HVPE.

# II.4 Conclusion

In this chapter, we studied the selective area growth of vertically aligned GaAs NWs on GaAs (111)B substrate. The goal of this study was to determine the mechanisms involved during the growth and find the optimal growth conditions leading to long NWs. These results were the subject of a dedicated model which takes into account the kinetics of growth. These results shed light on different phenomena, namely the presence of As trimers on the top surface and the Ga adatoms diffusion on the NWs sidewalls. This is the first time that this diffusion is introduced in the growth modeling of GaAs NWs by HVPE. The crystalline quality of these NWs was investigated by HRTEM measurements and they exhibit a high density of random stacking faults related to ZB/WZ polytypism.

The optimal growth conditions leading to long NWs has been carried out for a doping study of GaAs NWs. This study was part of the collaboration with Professor Ray LaPierre with the aim to demonstrate the first GaAs NW p-i-n junction by HVPE for photovoltaic and betavoltaic applications. The results show a strong influence of doping on the morphology of NWs. These NWs were analyzed by HRTEM and it seems that the n-doping slightly influences the crystallographic quality. The NWs were then characterized by μ-PL and the interpretation of the emission lines is consistent with the dopants used.

Based on these encouraging first doping results, it was decided to conduct the first-ever NW p-i-n junction growth by HVPE. The NWs obtained were then processed to make a photovoltaic device at McMaster University in collaboration with Amanda Thomas (PhD student at McMaster University). The efficiencies obtained are very poor. Nevertheless, the diode effect is present which is encouraging for the future. Many ways of improvement have been proposed and this offers good prospects for the realization of future NW p-i-n junction by HVPE. Finally, a new p-i-n junction was made with the maximum flow of $SiH_4$ in order to achieve higher n-doping rate. The results by cathodoluminescence clearly show two distinct areas seeming to correspond to the different doping areas. The experimental procedure (HVPE growth and device processing) developed in the present thesis will be the base of future work between McMaster University and Institut Pascal dedicated to the manufacture of betavoltaic devices.

Chapter III

# SAG-HVPE of InAs and $In_xGa_{1-x}As$ nanowires

This chapter is devoted to the growth of InAs and InGaAs NWs for potential infrared applications as detailed in chapter I. In particular, with the aim of integrating III/V materials on Si as explained in section I.4.2.4 (page 32), we have focused our growth studies on patterned Si(111) substrate. However, a patterned GaAs(111)B substrate is used to demonstrate the feasibility of growing InGaAs NWs by HVPE.

Firstly, we will study the growth of InAs NWs on patterned Si(111) substrate. Parallel observations are made at high partial pressure of $As_4$, suggesting that the growth suppression under As-rich atmosphere concerns all III-As NWs growing along the [111]B direction.

Secondly, the growth of InGaAs NWs on patterned GaAs(111)B and Si(111) substrates is presented. To our knowledge, this is the first time that the growth of InGaAs NWs by HVPE is reported. The composition of the NWs and the homogeneity are investigated by EDX (energy-dispersive X-ray spectroscopy). The NW morphology and composition are discussed based on growth conditions. The crystallographic and optical properties were checked by HRTEM analysis and PL measurements. This study highlights the effect of growth parameters such as growth temperature or the indium content in the vapor phase. Finally, a theoretical model based on thermodynamic and kinetic considerations is developed to link the indium content in the vapor phase $z$ with the InAs fraction in the solid $x$.

# III.1 Selective area growth of long InAs nanowires

One of the main results of chapter I is that at high partial pressure of $As_4$ (in other words at low III/V ratio), a saturation of the NWs length appears due to the presence of As trimers on the (111)B facet. However, the growth conditions between GaAs and InAs materials are different (nature of group III precursors, growth temperature). Thus, a similar study in order to get the optimal growth conditions to obtain long InAs NWs is needed.

The growth was performed on #AC121A substrate. The pattern consists of holes with a diameter of 350 nm and a pitch of 1.75 µm. The dielectric mask is a 100 nm $SiN_x$ layer deposited on a 20 nm $SiO_x$ layer. For this study, $P_{InCl}$ is fixed at $4.8 \times 10^{-4}$ atm, the growth temperature is 640 °C and the growth time is 15 min. In order to remove native oxide formed in the openings and increase the NWs growth yield, the substrates are etched in a 5% HF solution for 15s and then rinsed with deionized water. As explained in chapter I (section I.3.2, page 14), due to the non-polarity of the Si(111) substrate, a pre-treatment under arsenic atmosphere is performed. Indeed, under As and In (or Ga) environment, different Si(111) surface reconstructions can be observed. Tomioka et al. showed that As-terminated and In-incorporated Si(111) surface correspond to (111)A oriented surface while As-incorporated and In-terminated Si(111) correspond to (111)B oriented surface [63]. NWs on (111)A surface grow along 3 equivalent (111)B direction forming an angle of 19.6° with respect to the substrate surface. Thus, it is assumed that the pre-treatment under an arsenic atmosphere made it possible to obtain an As-incorporated structure and vertical NWs. Here, the pre-treatment begins at 520 °C and the amount of arsenic is gradually increased to growth temperature. Figure III.1.a represents the evolution of InAs NWs lengths and diameters as a function of $P_{As_4}$. The corresponding SEM images are shown in Figure III.1.b-d. The uncertainties were calculated in the same way as in section II.1.1 (page 50).

First of all, we can clearly see the impact of $P_{As_4}$ on the length of NWs. The NWs mean length goes from 15 µm to less than 2 µm when increasing $P_{As_4}$. The same observation was made in section II.1.3 regarding the growth of GaAs NWs. For InAs NWs growing along the [111]B direction, a too high $P_{As_4}$ induces the formation of As trimers on the top surface. This phenomenon has also been reported for growth of InAs NWs by MOVPE [66, 68]. Concerning the evolution of the NWs diameter, several points should be underlined. If we exclude the third datapoint in Figure III.1.a ($P_{As_4} = 7.2 \times 10^{-4}$ atm), we can assume that the diameter varies slightly within uncertainty range. This remains consistent with the low lateral growth rates previously observed on NWs III-As by

HVPE [74, 157]. The deviation of the third datapoint could be explained by its yield which is very low compared to the other experiments. As it can be seen on the SEM images, the yield varies significantly between the experiments which may have had an impact on the local input material between the experiments. This could mainly be related to the quality of the dielectric mask and remaining oxide in the holes. Moreover, yield problems can also appear due to the random quality of the piece of cleaved substrate.

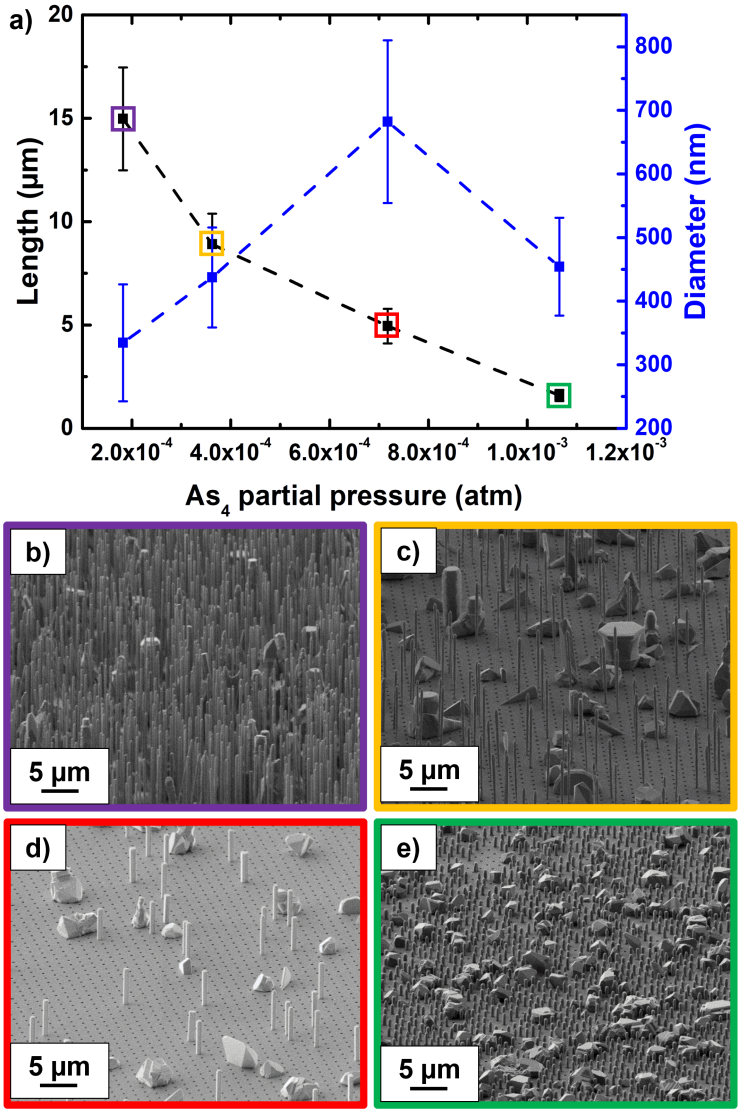


Figure III.1 – *a) Mean NWs length and diameter according to $P_{As_4}$ at a fixed $P_{InCl} = 4.8 \times 10^{-3}$ atm. Lines are guides for the eye. b-e) Corresponding tilted-view SEM images of as-grown NWs on #AC121A substrate.*

The main result that should be underlined is that we succeed to obtain long InAs NWs by HVPE (> 10 µm) as this was the main objective. Nevertheless, due to the lack of good quality substrates with different patterns, we were not able to carry out adequate experiments for multispectral detection.

These experiments will be carried out in a future collaboration with McMaster University which can characterize the samples by Fourier transform infrared spectroscopy (FTIR).

To conclude, we have successfully demonstrated the growth of long GaAs and InAs NWs by HVPE. A wide range of growth conditions with different patterns were studied. This allows good control of the growth of these two binaries by HVPE. All of these results make it possible to consider the growth of the ternary InGaAs NWs by HVPE for which the control of the composition is a significant challenge. This is the subject of the next section.

# III.2 Selective area growth of InGaAs nanowires

This section is divided into two parts. First, we present the growth of InGaAs NWs on patterned GaAs(111)B substrate by HVPE. Indeed, as the nucleation on Si substrate is still a significant challenge, it is necessary to first demonstrate the feasibility of growing InGaAs NWs by HVPE on GaAs substrate. We discuss the composition, the crystallographic quality and the optical properties of these NWs. Afterwards, we present the growth of InGaAs NWs on patterned Si(111) substrate with various $x$ which is the InAs fraction in the solid. This study is supported with a dedicated model.

## III.2.1 Growth on patterned GaAs(111)B substrate

The patterned GaAs(111)B substrate is #IBM2. It has been patterned by EBL and consists of a $SiO_x$ dielectric mask with 60 nm holes with a pitch of 2 µm. The substrate was stabilized under $As_4$ atmosphere during the heating phase. The growth starts when GaCl and InCl valves are turned-on simultaneously and ends by turning-off GaCl and InCl simultaneously. The substrate is then cooled down under $As_4$ atmosphere until the temperature reaches 560 °C. The first step is to find growth conditions which enable the growth of InGaAs NWs, no matter the indium composition. Thus, the growth was carried out at an intermediate growth temperature for the two binaries at 715 °C with a much higher flow rate of InCl than GaCl to counteract the indium desorption. The partial pressures are $P_{As4} = 7.5 \times 10^{-4}$ atm, $P_{GaCl} = 6.6 \times 10^{-4}$ atm and $P_{InCl} = 1.0 \times 10^{-2}$ atm, respectively. This leads to an In content in vapor phase $z = P_{InCl}/(P_{InCl} + P_{GaCl})$ of 0.94 and to a III/V ratio of 3.55. The InAs fraction in the solid $In_xGa_{1-x}As$ is noted $x$. The growth time was 10 min.

Figure III.2 shows SEM images of as-grown InGaAs NWs and three EDX profiles along a single NW. The SEM images in Figure III.2.a reveals pencil-like shape NWs grown in the [111]B direction with a diameter of 370 nm at the top of the NW and a length of 8.7 µm, corresponding to a remarkable

axial growth rate of more than 50 µm/h. This value is notable in SAG compared to the growth rate below 10 µm/h observed in MOVPE [82, 158] and in MBE [84, 159]. The NWs morphology is pencil-like because the intrinsic growth rate of the (111)B facet is greatly superior to the lateral facets assumed to be {-110}. The radial growth rate on the {-110} side facets, which consist of Ga-As rows, is generally very low over a wide range of HVPE conditions because of the low adsorption of GaCl on the {-110} surface [117]. However, it cannot be excluded that this morphology could also be interpreted by the formation of element III droplets at the top of InGaAs NWs which shrink at the end of growth.

In order to estimate the distribution of composition within the NWs, EDX profiles were performed. These EDX experiments were carried out by Catherine Bougerol at the Institut Néel in the framework of the ENNORA project (research project financed by region AURA). Figure III.2.b shows EDX profiles along the length of singles NW. The EDX results show an InAs fraction in the solid of $x = 0.84$, highlighting that these NWs are In-rich InGaAs. The difference between the In content in the vapor phase ($z = 0.93$) and the average In composition in the solid ($x = 0.84$) is a well-known phenomenon for the growth of ternary NWs. This is mainly explained by the different transport of Ga and In atoms into the NW, due to the different diffusion lengths on the NW sidewalls and different desorption rates [118]. The Ga and In concentrations were nearly homogeneous along the length of NWs along the length of the three different NWs analyzed. Such composition has already been demonstrated by MBE and MOVPE but on shorter NWs [83, 84].

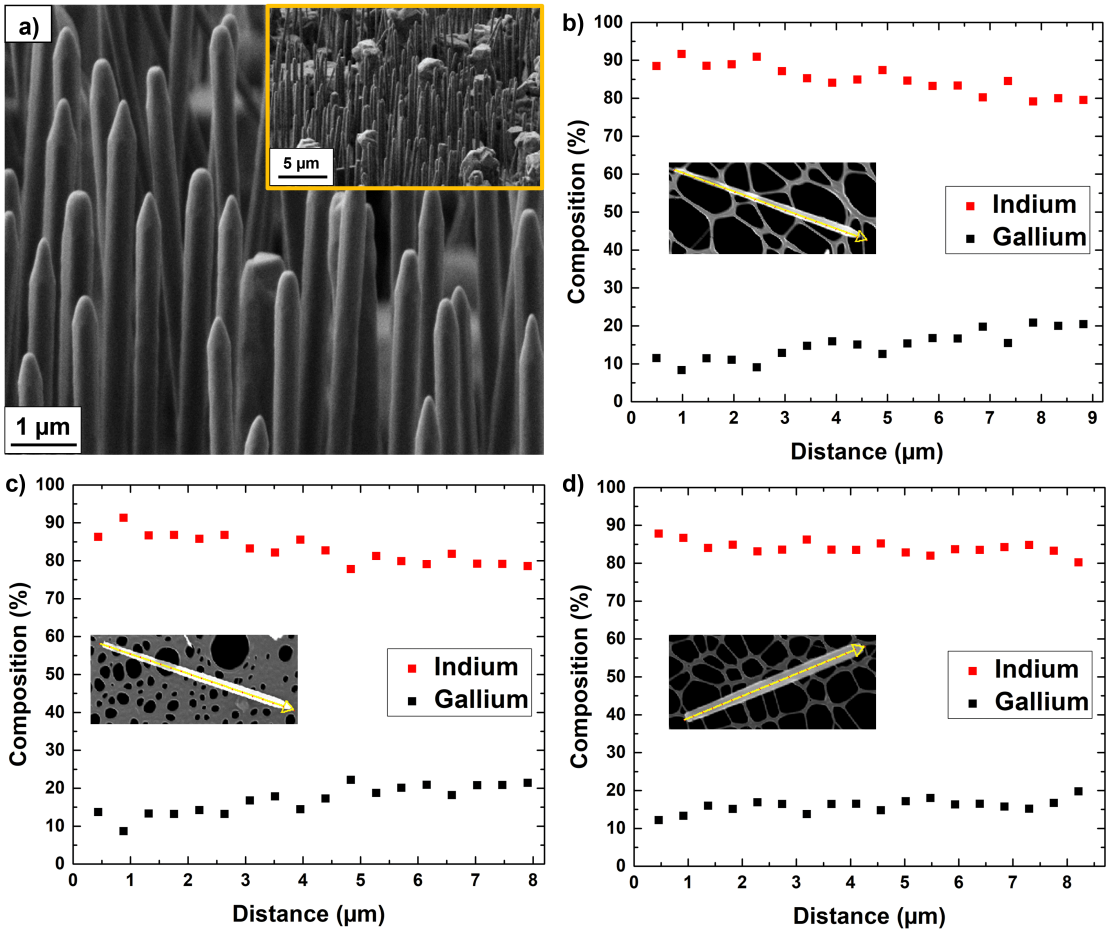


Figure III.2 – *a) 20° tilted-view SEM image of InGaAs NWs with an inset that shows a wide field SEM image. EDS profiles along the [111]B direction of single InGaAs NWs showing an average InAs fractions of b)* $x = 0.85$*, c)* $x = 0.83$ *and d)* $x = 0.84$*. Points run from base to top of the NW.*

The crystal structure of the NWs was characterized using a FEI-TECNAI high resolution transmission electron microscopy (HRTEM) operated at an acceleration voltage of 200 kV. The HRTEM images are shown in Figure III.3. Random stacking faults related to the zinc-blende/wurtzite (ZB/WZ) polytypism are observed. As explained previously in section I.3.1 (page 11), this polytypism is commonly observed during the growth of III-As NWs along the [111]B direction [84, 160, 161]. The effect is attributed to a small difference in the internal formation energies of the two phases (around 10 meV), which comes mainly from the electrostatic interaction between the third-nearest neighbor atoms [42, 133, 134].

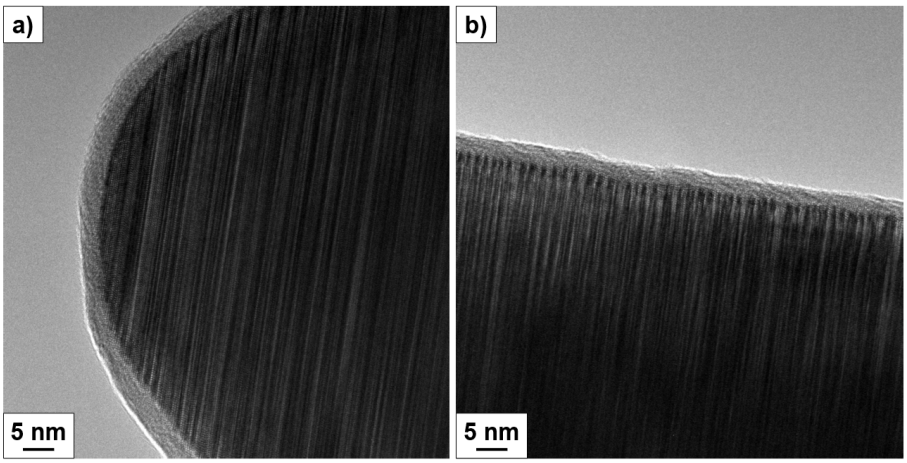


Figure III.3 – *HRTEM images of InGaAs NW at a) the top and b) the bottom of the NW. The shell visible on the NW is an oxide layer. The incident electron beam was along* $\langle 1-10 \rangle$.

In order to confirm the composition, photoluminescence (PL) spectroscopy was performed using a Brucker-Vertex 70 FTIR spectrometer equipped with a KBr beamsplitter and a cooled InSb detector. PL was excited by a 780 nm laser diode. The spot diameter was 200 µm and the power was 5 mW. The sample was cooled to reach a low temperature of 14 K using a closed cycle He flow cryostat. The spectrum in Figure III.4 shows a main broad peak at 0.58 eV with a secondary peak at 0.50 eV. The main peak is likely due to either a band-to-band or exciton-related transition and the low energy peak may be due to unintentional impurity-related transitions. The full width at half maximum (FWHM) of 0.042 eV of the main peak is similar to observations made on InGaAs NWs grown by MOVPE and MBE [78, 83, 84]. Two hypotheses could explain the width of the main emission peak. As TEM measurements have shown, the as-grown NWs exhibit a high density of stacking faults related to the ZB/WZ polytypism. Consequently, the presence of both ZB/WZ phases could result in an increase of the emission peak width due to difference in the bandgap energy of these two phases [78, 162]. The second reason relates to the homogeneity of composition between the NWs, a variation of the composition of a few percent leads to different energy emissions.

To determine the composition from the main peak of the PL spectrum, Equation (I.1) from section I.3.1 taken from Ref [44] is used:

$$E_g(x_{Ga},T) = 0.42 + 0.625x_{Ga} + [\frac{5.8}{(T+300)} - \frac{4.19}{(T+271)}].10^{-4}T^2x_{Ga} - \frac{4.19.10^{-4}T^2}{(T+271)} + 0.475x_{Ga}^2 \quad \text{(III.1)}$$

where $E_g$ is the InGaAs bandgap in eV, $x_{Ga}$ is the GaAs fraction in the solid and $T$ is the absolute temperature. From this equation, the indium composition is estimated at $x = 0.78$. This is close to the indium composition of $x = 0.84$ measured by EDX. However, we note that this equation was verified

for unstrained cubic ZB material. The NWs are expected to be elastically relaxed and thus unstrained and they exhibit a ZB/WZ polytypism. As a consequence, the WZ phase of InGaAs NWs may affect the position of the PL peak PL peak position and therefore Equation (III.1) does not provide the precise value of the composition.

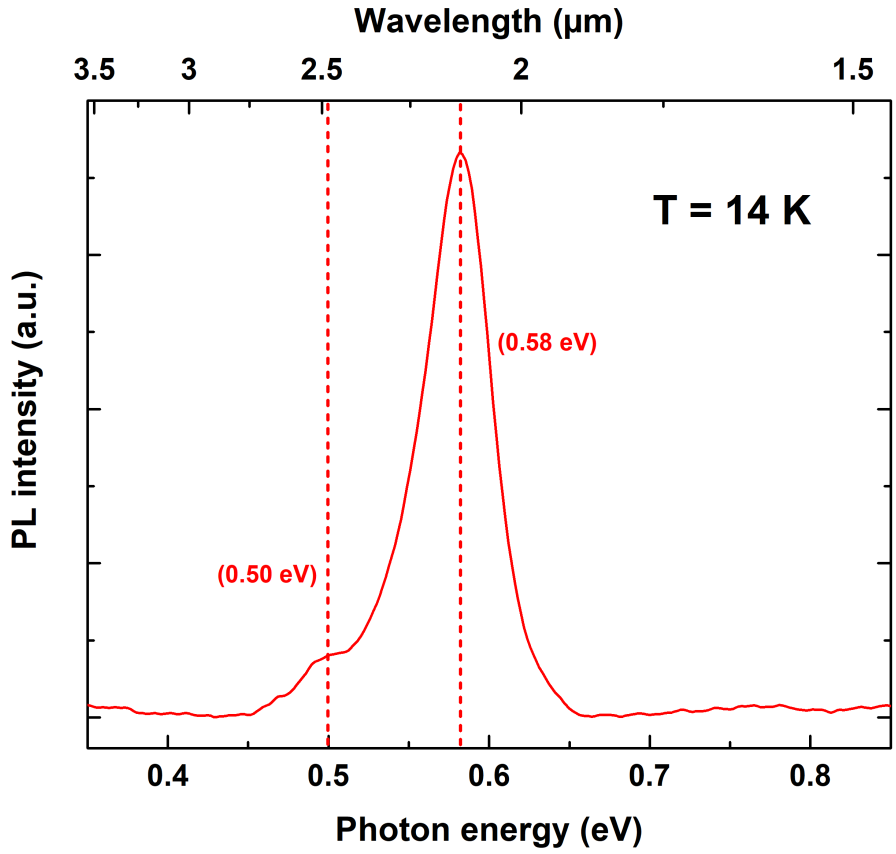


Figure III.4 – *14 K PL spectrum of InGaAs NWs array.*

In conclusion, we have demonstrated the SAG of InGaAs NWs on GaAs (111)B substrate with good selectivity using the HVPE technique. A high growth rate was observed of more than 50 µm/h leading to high aspect ratio NWs. The TEM measurements confirmed the presence of stacking faults in the NWs. The composition was investigated by EDX profile along a single NW, resulting in an average indium composition of $x = 0.84$ with nearly homogeneous concentrations along the NW length. The estimated composition by PL of $x = 0.78$ is consistent with the EDX results. Overall, SAG of InGaAs NWs by HVPE provides a new platform for the fabrication of homogeneous InGaAs NW arrays with high aspect ratios.

Now that we have demonstrated that the growth of InGaAs NWs is achievable by HVPE on GaAs(111)B substrate, we will study it on Si(111) substrate in the next section.

## III.2.2 Growth on patterned Si(111) substrate

We decided to study the SAG of InGaAs NWs on Si(111) substrate, with a view to integrating III-V based devices on silicon platform. SAG of InGaAs NWs on patterned Si(111) was performed on #AC121A substrate. The substrate is covered with dielectric masks that consisted of a 100 nm layer of $SiN_x$ on a 20 nm layer of $SiO_x$. These layers were deposited by plasma-enhanced chemical vapor deposition. The growth template consisted of hexagonal arrays of circular openings with a diameter of 350 nm and a pitch of 3.5 µm. The substrate and the chemical etching are the same as for the growth of InAs NWs on Si(111) seen in section III.1. The growth time was 15 min for all samples and the growth temperature was 690 °C for most samples. However, some samples were grown at 670 °C, 710 °C and 730 °C.

### III.2.2.1 Effect of GaCl partial pressure

Figure III.5.a shows the schematic of InGaAs SAG on patterned $SiN_x/SiO_x$/Si(111) substrates. We first investigated the effect of $P_{GaCl}$ on the NW morphology and composition, with the aim of growing long NWs. In these experiments, the growth temperature T was fixed at 690 °C, and the partial pressures $P_{As4}$ and $P_{InCl}$ were fixed at $3.6 \times 10^{-4}$ atm and $4.8 \times 10^{-3}$ atm, respectively. The composition of as-grown InGaAs NWs was investigated by EDX in a SEM and Figure III.5.b-d shows the SEM images of InGaAs NWs grown under different $P_{GaCl}$ with their respective InAs fraction $x$.

As expected, the growth is highly selective due to the low adsorption of chloride precursors on the mask surface. However, some unfilled holes are observed, which are clearly seen in Figure III.5.d. This is likely due to an oxide residue in the holes preventing the NW nucleation. The fraction of InAs in InGaAs NWs, $x$, gradually decreases from $x = 0.68$ to $x = 0.34$ with increasing $P_{GaCl}$ at a constant $P_{InCl}$. This is explained by the reduced fraction of In in the vapor and hence the lower incorporation rate of In atoms relative to Ga atoms [78, 161, 163, 164]. Interestingly, the NW length strongly decreases with increasing $P_{GaCl}$, from almost 8 µm at $P_{GaCl} = 3.2 \times 10^{-4}$ atm to less than 1 µm at $P_{GaCl} = 1.3 \times 10^{-3}$ atm. Hence, the closer we get to binary InAs composition, the longer the NWs are. The growth temperature of 690 °C is very low for the deposition of GaAs material by HVPE, which explains the short length of Ga-rich NWs due to a lower decomposition efficiency of GaCl [74, 165]. The effect may be enhanced by In adatoms which diffuse less on the NW facets in the presence of Ga adatoms. Furthermore, formation of In droplets on top of In-rich InGaAs NWs and the corresponding transition from the VS to VLS growth mode cannot be excluded. We can also see

that In-rich NWs exhibit a "pencil-like" shape, while Ga-rich NWs have flat tops. Since In adatoms diffuse more to the NW tops at low $P_{GaCl}$, the intrinsic growth rate of the (111)B facet is greater than on the lateral NW facets, which explains the observed pencil-like shape. At high $P_{GaCl}$, the In diffusivity is reduced and the pencil-like shape disappears.

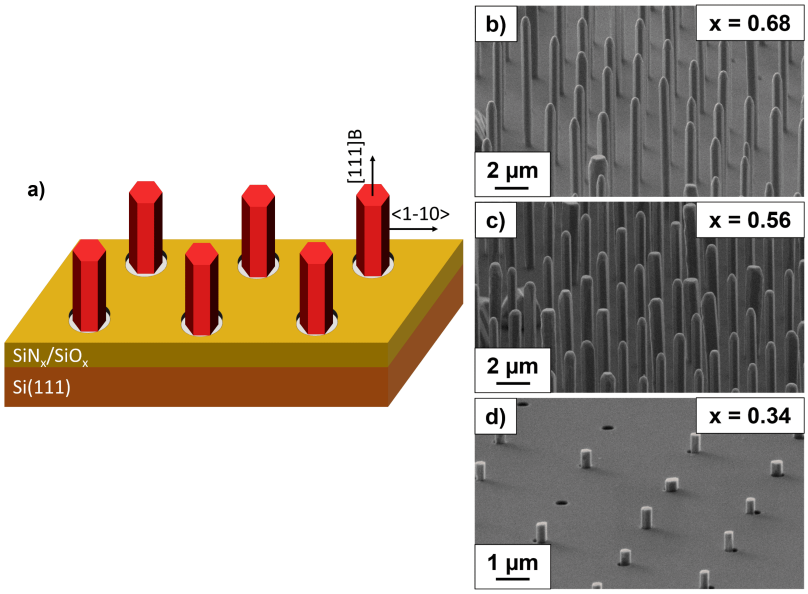


Figure III.5 – *a) Schematic representation of SAG of InGaAs NWs on patterned $SiN_x/SiO_x$/Si(111) substrates. 20° tilted-view SEM images of InGaAs NWs grown on #AC121A substrate with different $P_{GaCl}$: b) $3.2 \times 10^{-4}$ atm, c) $4.8 \times 10^{-4}$ atm, and d) $1.3 \times 10^{-3}$ atm. The average InAs fractions x measured by SEM EDX are b) 0.68, c) 0.56 and d) 0.34.*

### III.2.2.2 Investigations of compositional homogeneity

To access the compositional homogeneity of InGaAs NWs, additional EDX measurements in a scanning transmission electron microscope (STEM) were carried out by Ethan Diak at McMaster University. These images were taken using a Talos 200X STEM working at an acceleration voltage of 200 kV. Figure III.6 shows the high-angle annular dark-field (HAADF) images of two representative InGaAs NWs with the respective atomic mappings of As, Ga and In. The TEM-EDX spectra along the NW length and radially in the center of NWs are also presented. The growth conditions for NW1 in Figure III.6.a-c were: $P_{GaCl} = 3.2 \times 10^{-4}$ atm, $P_{InCl} = 4.8 \times 10^{-3}$ atm, $P_{As4} = 3.6 \times 10^{-4}$ atm, and T = 690 °C. For NW2 in Figure III.6.d-f, the growth conditions were: $P_{GaCl} = 1.3 \times 10^{-3}$ atm, $P_{InCl} = 4.7 \times 10^{-3}$ atm, $P_{As4} = 7.1 \times 10^{-4}$ atm, and T = 730 °C.

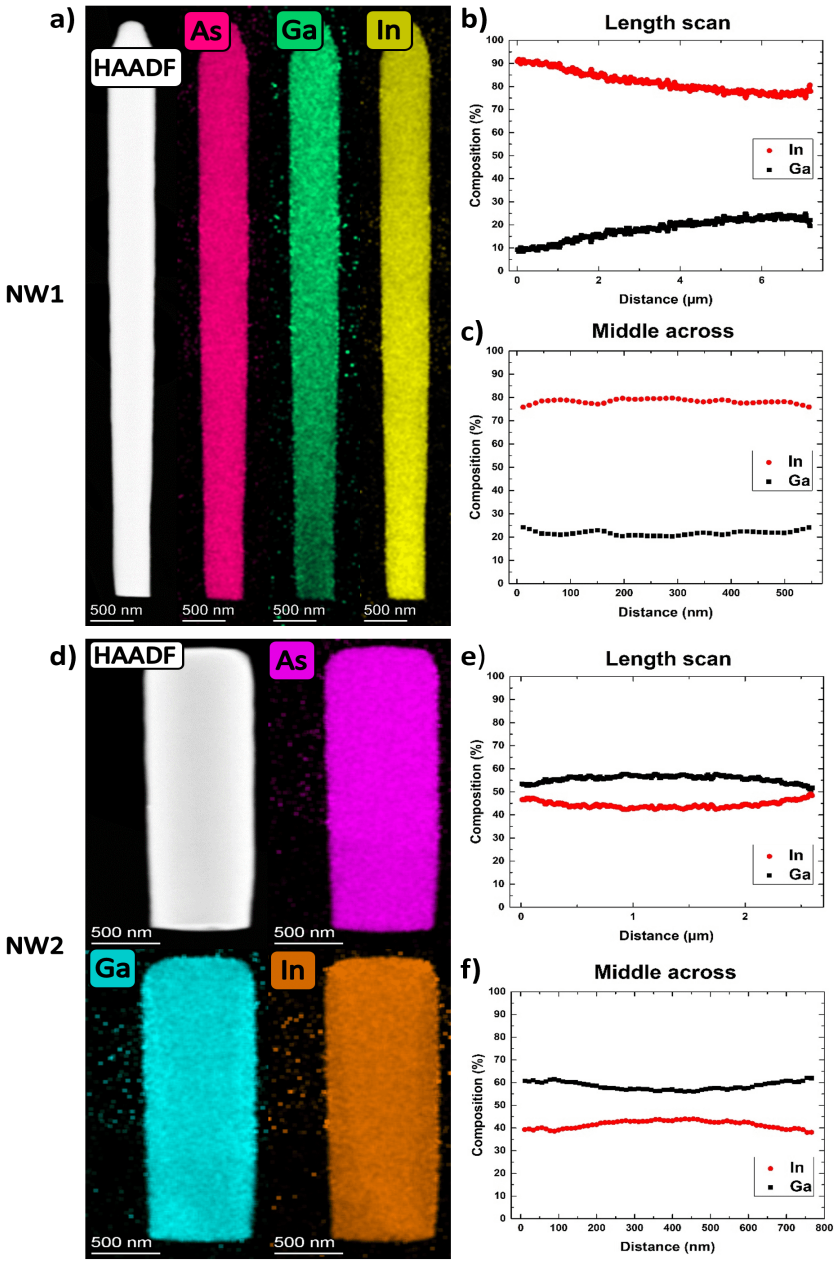


Figure III.6 – *a) HAADF image and the corresponding EDX mapping of As, Ga and In of NW1. EDX profile b) along the NW length showing an average InAs fraction of* $x = 0.82$ *with a decrease from* $x = 0.90$ *to* $x = 0.76$ *toward the NW top, and c) across the middle length showing an average InAs fraction of* $x = 0.78$. *d) HAADF image and the corresponding EDX mapping of As, Ga and In of NW2. EDX profile e) along the NW length showing an average InAs fraction of* $x = 0.44$, *and f) across the middle length showing an average InAs fraction of* $x = 0.45$.

For both NWs, a good homogeneity over the entire NWs is observed despite their significant lengths ($\sim$ 7 µm for NW1 and $\sim$ 3 µm for NW2). However, for NW1 the base is slightly richer in In. This is confirmed by Figure III.6.b, where the InAs fraction is larger at the NW base ($x = 0.90$) and

gradually decreases to $x = 0.76$. The average InAs fraction in NW1 equals $x = 0.82$. The In enrichment of the NW base has already been observed [6, 76], and attributed to different diffusion mechanisms of In and Ga adatoms for short and long NWs [118]. Figure III.6.c shows the radial distribution of In and Ga across the middle length of NW1, revealing a good homogeneity with no core-shell structure within the resolution limit. For a shorter NW2, Figure III.6.e reveals a more homogeneous composition along the NW length, where Ga and In concentrations vary only slightly. The In enrichment of the NW base is not present. This can be explained by (i) a higher growth temperature of 730 °C compared to NW1, which is too high for deposition of InAs material by HVPE due to enhanced In desorption [164], and (ii) a high input of Ga which limits the In surface diffusion. The radial profile in Figure III.6.f shows a quasi-constant composition. The average InAs fraction in NW2 equals 0.44, which is almost twice lower than in NW1.

### III.2.3 Modeling the vapor-solid distribution of InGaAs nanowires

In this section, we present a growth model of InGaAs NWs based on thermodynamics and kinetics. The aim of this model is to study the vapor-solid distribution, i.e. the relation which exists between indium content in the vapor $z$ and InAs fraction in the solid $x$. This will make it possible to link the partial pressures to the composition of the solid to have an optimal control of the composition of the InGaAs alloy by HVPE. Finally, this could make it possible to know whether, under the growth conditions used in HVPE, the growth of InGaAs material is governed by kinetics, by thermodynamics or both. This model was developed jointly with Professor Vladimir Dubrovskii. Table III.1 summarizes the growth conditions and compositions of InGaAs NWs measured by different techniques. The total atomic III/V flux ratio $I_3/I_5$ was calculated as:

$$\frac{I_3}{I_5} = \frac{1}{4}\frac{(P_{InCl} + P_{GaCl})}{P_{As4}} \tag{III.2}$$

and the In content in vapor $z$ were calculated as:

$$z = \frac{P_{InCl}}{P_{InCl} + P_{GaCl}} \tag{III.3}$$

| No. | $P_{GaCl}$ ($10^{-3}$ atm) | $P_{InCl}$ ($10^{-3}$ atm) | $P_{As4}$ ($10^{-3}$ atm) | $I_3/I_5$ | T (°C) | $z$ | $x$ by SEM | $x$ by TEM | L (µm) | D (nm) |
|---|---|---|---|---|---|---|---|---|---|---|
| 1 | 0.16 | 4.76 | 0.36 | 3.42 | 690 | 0.97 | 0.86 | 0.90 | 12.3 | 525 |
| 2 | 0.32 | 4.76 | 0.36 | 3.53 | 690 | 0.94 | 0.68 | 0.82 | 8.4 | 525 |
| 3 | 0.48 | 4.76 | 0.36 | 3.64 | 690 | 0.91 | 0.56 | | 4.5 | 740 |
| 4 | 0.63 | 4.76 | 0.36 | 3.75 | 690 | 0.88 | 0.50 | | 5.3 | 630 |
| 5 | 0.95 | 4.76 | 0.36 | 3.97 | 690 | 0.83 | 0.42 | | 0.9 | 340 |
| 6 | 1.27 | 4.76 | 0.36 | 4.19 | 690 | 0.79 | 0.34 | | 0.5 | 295 |
| 7 | 0.31 | 9.17 | 0.70 | 3.42 | 690 | 0.97 | 0.83 | | 3.5 | 940 |
| 8 | 0.32 | 4.76 | 0.36 | 3.53 | 670 | 0.94 | 0.75 | | 3.8 | 530 |
| 9 | 1.25 | 4.71 | 0.71 | 2.10 | 710 | 0.79 | 0.40 | | 1.3 | 515 |
| 10 | 1.25 | 4.74 | 0.71 | 2.10 | 730 | 0.79 | 0.40 | 0.44 | 4.0 | 900 |

Table III.1 – *Parameters of InGaAs NWs grown under different conditions. The InAs fractions in the solid x were measured by EDX in a SEM and in a TEM.*

## III.2.3.1 Theory on vapor-solid growth of ternary

### III.2.3.1.1 Vapor-solid distribution

In this model, we consider SAG of a $In_xGa_{1-x}As$ NW from the atomic vapor fluxes $I_{In}$, $I_{Ga}$ and $I_{As}$, with the pyrolysis efficiencies of In and Ga precursors $\chi_{In}$ and $\chi_{Ga}$, respectively, and the characteristic desorption times of In and Ga adatoms $\tau_{In}$ and $\tau_{Ga}$, respectively. Thus, in this model, it is only taken into account the atomic species on the surface which are the In and Ga adatoms and not molecules as it is the case in HVPE. The dechlorination steps of the AsInCl and AsGaCl molecules are actually included in the $\chi_{In,Ga}$ and in the $\tau_{In,Ga}$. However, in section III.2.3.2, a complete model will be detailed which takes into account all the reactions involved in the HVPE and we obtain the same conclusions. An illustration of the diffusion-induced growth with the main parameters of the model is shown in Figure III.7. The model considers a terrace as we did previously in chapter I in Figure I.24 (page 43).

The In content in vapor is given by:

$$z = \frac{I_{In}}{I_{In} + I_{Ga}} \tag{III.4}$$

The InAs fraction in solid x is determined by:

$$x = \frac{j_{In}}{j_{In} + j_{Ga}} \tag{III.5}$$

with $j_{In}$ and $j_{Ga}$ the diffusion fluxes entering the step of partial monolayer which grows on the NW top, as shown in Figure III.7. The aim is to find the vapor-solid distribution, i.e. the relation $z = f(x)$.

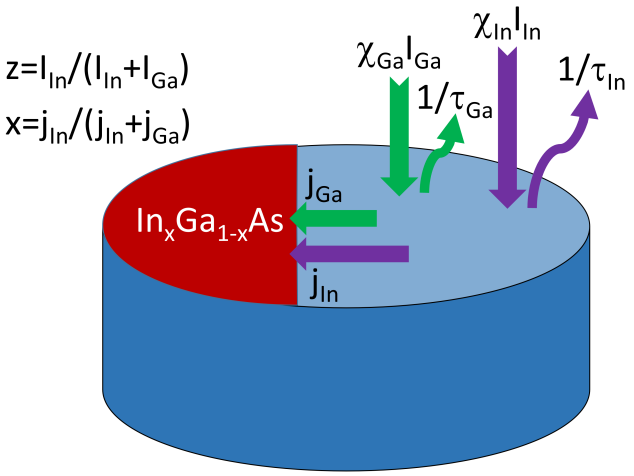


Figure III.7 – *Illustration of the diffusion-induced growth of $In_xGa_{1-x}As$ NW showing the main parameters of the model.*

To calculate the diffusion fluxes, $j_{In}$ and $j_{Ga}$, we consider the stationary diffusion equations for the group III adatom concentrations on the NW top $n_k$:

$$D_k \frac{d^2 n_k}{d\xi^2} + \chi_k I_k - \frac{n_k}{\tau_k} = 0 \tag{III.6}$$

for k= In and Ga, where $D_k$ are the surface diffusion coefficients and $\xi$ is the distance from the step. This approach is consistent with what has been done previously in Figure I.24 (page 43). We choose the boundary conditions in the form:

$$n_k(\xi \to \infty) = \chi_k I_k \tau_k, \;\; n_k(\xi = 0) = n_k^* \tag{III.7}$$

Here, $n_k^*$ are different for k=In and Ga, and account for interaction of InAs and GaAs pairs in solid. From these boundary conditions, we obtain the adatom surface concentrations by:

$$n_k = \chi_k I_k \tau_k - (\chi_k I_k \tau_k - n_k^*) e^{-\frac{\xi}{\lambda_k}} \tag{III.8}$$

with $\lambda_k = \sqrt{D_k \tau_k}$ are the desorption-limited adatom diffusion lengths which may include surface diffusion from the NW sidewalls to its top.

In order to determine the expressions of $n^*_{In}$ and $n^*_{Ga}$, we use the previous results demonstrated in section I.5.2.2 (page 39) and we consider the activities on the surface equal to the concentrations. Thus, we can write the equation (I.51) for InAs as:

$$\Delta\mu = k_B T ln\left(\frac{(a_{reactants}/a_{products})_{equilibrium}}{(a_{reactants}/a_{products})}\right) = k_B T ln\left(\frac{(n_{In}n_{As})_{equilibrium}}{n^*_{In}n_{As}} x\alpha_{InAs}\right) \tag{III.9}$$

with $\alpha_{InAs} = exp\left(\frac{(1-x)^2\Omega}{k_B T}\right)$ within the regular solution model which takes into account the interaction of InAs and GaAs pairs in the solid (demonstrated in section I.5.2.2).

As $\Delta\mu = 0$ at $\xi = 0$, we can write:

$$n^*_{In} = \frac{(n_{In}n_{As})^{eq}}{n_{As}} x e^{\omega(1-x)^2} \tag{III.10}$$

with $\omega = \frac{\Omega}{k_B T}$ the pseudo-binary interaction parameter in thermal units.

The same method is applied for $n^*_{Ga}$, we get:

$$n^*_{Ga} = \frac{(n_{Ga}n_{As})^{eq}}{n_{As}} (1-x) e^{\omega x^2} \tag{III.11}$$

Now we can determine the diffusion fluxes by taking the derivative of $n_k$ (Equation III.8) at $\xi = 0$:

$$j_k = D_k \frac{dn_k}{d\xi}\bigg|_{\xi=0} = \lambda_k\left(\chi_k I_k - \frac{n^*_k}{\tau_k}\right) \tag{III.12}$$

Using the definitions for $z$ and $x$ given by Equations (III.4) and (III.5) and dividing Equation (III.12) for In to Equation (III.12) for Ga, we get:

$$\frac{x}{1-x} = \frac{c(z-a)}{1-z-b} \tag{III.13}$$

with a and b values depend on $x$ but are independent of $z$ if the total flux of group III atoms $I_{tot}$=$I_{In}$+$I_{Ga}$ is kept constant:

$$a = \frac{n^*_{In}}{\chi_{In}\tau_{In}(I_{In}+I_{Ga})} \quad b = \frac{n^*_{Ga}}{\chi_{Ga}\tau_{Ga}(I_{In}+I_{Ga})} \tag{III.14}$$

and c, which is a fundamental parameter which will be analyzed more deeply subsequently (section III.2.3.1.4), which is defined as:

$$c = \frac{\chi_{In}\lambda_{In}}{\chi_{Ga}\lambda_{Ga}} \tag{III.15}$$

Expressing $z$ as a function of $x$ from Equation (III.13) and using Equations (III.10 and III.11), we obtain the vapor-solid distribution, which has the same form as in Refs [118, 166] given by:

$$z = \frac{x}{c+(1-c)x}[1+\Gamma(1-x)(ce^{\omega(1-x)^2} - \beta_g e^{\omega x^2})] \tag{III.16}$$

This equation is notable because it describes the relationship between z and x taking into account both the kinetics and thermodynamics of growth. The parameters $\Gamma$ and $\beta_g$ defined as:

$$\beta_g = \frac{\chi_{In}\tau_{In}}{\chi_{Ga}\tau_{Ga}} \frac{(n_{Ga}n_{As})^{eq}}{(n_{In}n_{As})^{eq}} \tag{III.17}$$

$$\Gamma = \frac{(n_{In}n_{As})^{eq}}{n_{As}\chi_{In}\tau_{In}(I_{In}+I_{Ga})} = \frac{(n_{In}n_{As})^{eq}}{\chi_{As}I_{As}\tau_{As}\chi_{In}\tau_{In}(I_{In}+I_{Ga})} \tag{III.18}$$

with the supersaturation parameter $\Gamma$ inversely proportional to the level of supersaturation in vapor with respect to solid, and the affinity parameter $\beta_g$ related to the differences of chemical potentials of pure elements. The last expression for $\Gamma$ applies if $n_{As} = \chi_{As}I_{As}\tau_{As}$. Note that a more complex form of the vapor-solid distribution for a $z$-dependent $I_{tot}$ has been demonstrated by Dubrovskii et.al [118].

#### III.2.3.1.2 Equilibrium vapor-solid distribution

The equilibrium vapor-solid distribution, which sets a limit for the solid composition under no-growth conditions, is obtained from:

$$j_k^+ = j_k^- \tag{III.19}$$

with k=In and Ga. Therefore, we get:

$$\lambda_k\chi_k I_k = \lambda_k \frac{n_k^*}{\tau_k} \tag{III.20}$$

Then:

$$I_k = \frac{n_k^*}{\chi_k\tau_k} \tag{III.21}$$

By using these expressions of $I_k$ in the expression of $z$ (Equation (III.4)), we obtain:

$$z = \frac{1}{1+f(x)}, \;\; f(x) = \beta_g \frac{(1-x)}{x} e^{\omega(2x-1)} \tag{III.22}$$

This equilibrium vapor-solid distribution (same as the nucleation-limited distribution) has the same form as the well-known equilibrium liquid-solid distribution [118, 166, 167, 168, 169] but with modified parameters which correspond to the vapor rather than the liquid phase.

#### III.2.3.1.3 Purely kinetic Langmuir-McLean equation

In the general form of the vapor-solid distribution (Equation III.16), the $\Gamma$ parameter is inversely proportional to the level of supersaturation in vapor with respect to solid. In the regimes corresponding to very high vapor supersaturations (at $\Gamma \to 0$), Equation (III.16) is reduced to the purely kinetic Langmuir-McLean formula:

$$z = \frac{x}{c+(1-c)x} \tag{III.23}$$

without any thermodynamic factors left in the distribution. Concretely, this corresponds to neglecting the rejected fluxes leading to a new expression for the diffusion fluxes: $j_k = \lambda_k \chi_k I_k$. Any vapor-solid distribution between the two limiting shapes given by Equation (III.16) and (III.23) is possible and depends on the level of vapor supersaturation and total III/V ratio.

#### III.2.3.1.4 Modeling results

The vapor-solid distribution $x(z)$ connecting the InAs fraction in $In_xGa_{1-x}As$ NWs $x$ with the In content in vapor $z$ for all the data points from Table III.1 is shown in Figure III.8. The dashed line shows the equilibrium vapor-solid distribution, i.e. Equation (III.22), for InGaAs material at 690 °C with $\omega = 1.556$ and $\beta_g = 0.0477$ according to Refs [170, 171]. This distribution does not vary significantly in the investigated temperature range for HVPE process from 670 °C to 730 °C.

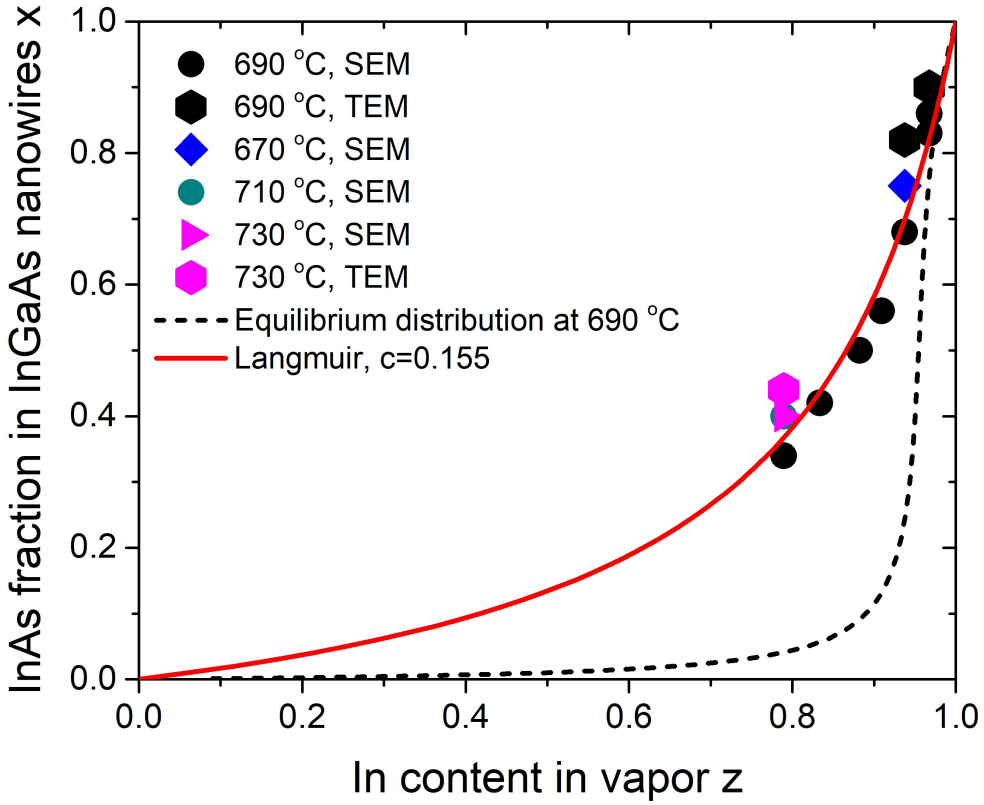


Figure III.8 – *Vapor-solid distribution of $In_xGa_{1-x}As$ NWs obtained under the growth conditions of Table III.1 Dashed line shows the equilibrium vapor-solid distribution at 690 °C. The data points are obviously far from the equilibrium curve, and well-fitted by the purely kinetic Langmuir-McLean curve at $c = 0.155$.*

Although the HVPE growth temperatures are much higher than the critical temperature of 543 °C [164, 168] and hence no miscibility gap is present in the equilibrium distribution, its shape is non-

linear and features an almost vertical section between $x = 0.2$ and $x = 0.8$. If the growth were close-to-equilibrium, the intermediate compositions of $In_xGa_{1-x}As$ would correspond to a very narrow range of vapor compositions $z$ and other growth parameters, and quite difficult to achieve. Our data points are obviously far from the equilibrium shape. The measured $x(z)$ dependence at 690 °C is rather smooth, and well-fitted by the purely kinetic Langmuir-McLean shape given by Equation (III.23) with $c = 0.155$. Furthermore, the data points at other temperatures (670 °C, 710 °C and 730 °C) are very close to the curve at 690 °C. Non-zero $\Gamma$ in Equation (III.16) worsen the correspondence between the data and the theory. Thus, one of the conclusions that can be drawn is that it seems that under the growth conditions used in this study, SAG of $In_xGa_{1-x}As$ NWs takes place at high supersaturations of the binaries ($\gamma_{InAs} \gg 1$, $\gamma_{GaAs} \gg 1$). This is consistent with the supersaturations calculated using Equations (I.32) and (I.33) (page 37) for the data in Table III.1 (page 103), the values found are bounded as $13 \leq \gamma_{GaAs} \leq 88$ and $29 \leq \gamma_{InAs} \leq 70$.

Consequently, the composition of the NWs is kinetically controlled and far from equilibrium. Therefore, based on this conclusion, an important perspective of this work would be to explore the conditions with $z < 0.7$ in order to completely cover the composition domain from 0 to 100% by HVPE.

Concerning the value of $c$ of 0.155: $c$ is defined by Equation (III.15) which is $c = \chi_{In}\lambda_{In}/\chi_{Ga}\lambda_{Ga}$. Given the high supersaturations, it is reasonable to assume that the ratio of the pyrolysis efficiency of gaseous precursors $\chi_{In}/\chi_{Ga}$ is close to 1. Thus, a low $c$ value of 0.155 obtained from the fit in Figure III.8 shows that the effective diffusion length of In adatoms is much smaller compared to Ga. In atoms are known to diffuse faster but desorb at much lower temperatures than Ga atoms, so the condition $\lambda_{In} \ll \lambda_{Ga}$ is very plausible at the high temperatures employed in the HVPE growth. The vapor-solid distributions of Au-catalyzed VLS InGaAs NWs grown by MOVPE on InAs(111)B substrates at temperatures 450 °C and 470 °C [172] were fitted by the kinetic shapes in Refs. [118, 168], with $c$ = 0.35-1.2 depending on the NW density and position at the NW top or bottom. InGaAs epi-layers of Ref. [171] were grown by vapor phase epitaxy in an (In-Ga)-$AsCl_3$-As-$H_2$ system with In-Ga metal source producing the chloride precursors InCl and GaCl, and $As_4$ vapor in the carrier gas $H_2$ at 750 °C. Their vapor-solid distributions were fitted by the kinetic shape in Ref.[118], with $c$ = 0.12, which is only slightly lower than our value of $c$ = 0.155. Therefore, our data confirm the trend for a decrease of $c$ from $\sim$ 1 at 450 °C to $\sim$ 0.1 at $\sim$ 700 °C, which should be due to the enhanced desorption of In atoms at higher temperatures. The excellent fit of the whole set of data for the compositions of NWs with very different morphologies using one-parametric Langmuir-McLean

formula is remarkable. It reveals the kinetically controlled formation of InGaAs NWs on Si substrates in SAG by HVPE technique, which enables a good control over the widely tunable composition of such structures.

Finally, this model fits the data very well but it only takes into account atomic species such as In and Ga adatoms. Thus, in the following section, we develop a model that takes into account the HVPE reactions and we demonstrate the link that exists between these two approaches.

### III.2.3.2 Discussion on the model: link with HVPE kinetics

In the model presented previously, only atomic species are considered which are In and Ga adatoms and not gaseous molecules as detailed in the kinetics of HVPE (section I.6 on page 42). Thus, in order to verify the veracity and consistency of the model, it would be interesting to reconsider it based on the HVPE reactions. In this section, we demonstrate the link that exists between the kinetic considerations of HVPE and the kinetic model presented in section III.2.3.1. We will limit ourselves to the purely kinetic regime, and consequently, the objective is to obtain the Lamgmuir-McLean equation previously demonstrated which is:

$$z = \frac{x}{c + (1-c)x} \tag{III.24}$$

with $z$ the In content in vapor, $x$ the InAs fraction in solid and $c$ the kinetic parameter expressed as $c = \chi_{In}\lambda_{In}/\chi_{Ga}\lambda_{Ga}$ where for k = In or Ga, $\lambda_k = \sqrt{D_k\tau_k}$ are the desorption-limited adatom diffusion lengths and $\chi_k$ are the pyrolysis efficiencies.

We consider that the surface is made up of a number $N_s$ of potential wells per unit of surface, of depth $\varepsilon_{ad}$. In the mother vapor phase, a molecule has an interaction potential energy $\varepsilon_m$ (Figure III.9). Eyring's theory [173] describes the transition from the mother phase to the crystalline state and vice versa, by the formation of an activated complex with energy $\varepsilon^*$ greater than the initial and final potential energies. To pass from the vapor phase to the crystalline state, the molecules cross a height potential barrier $(\varepsilon^* - \varepsilon_m)$ defining the adsorption activation energy. The total energy of molecules passing from the crystalline state to the parent phase crosses the height potential barrier $(\varepsilon^* - \varepsilon_{ad})$.

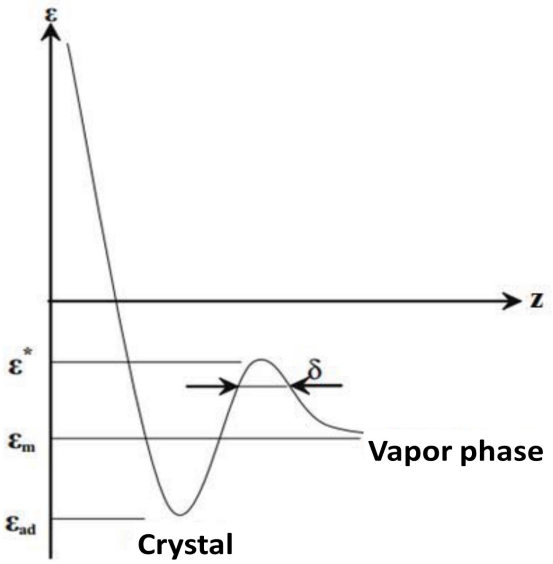


Figure III.9 – *Variation of molecules potential energy along the growth direction z ($\delta$ is the width of the potential barrier).*

We apply the Eyring theory to the most kinetically significant step, namely the slowest step of the set of diverse processes that lead to InGaAs deposition. The limiting step that governs the growth kinetics process is the dechlorination of AsIIICl molecules as explained in section I.6 (page 42). The adsorption and desorption reactions of InAs are written:

$$\textbf{adsorption}: \ AsInCl + H_{2_g} \rightleftharpoons InAs_c + Cl - H - H^* \rightarrow InAs_c + \frac{1}{2}H_{2_g} + HCl_g \tag{III.25}$$

$$\textbf{desorption}: \ InAs_c + Cl - H - H^* \rightleftharpoons InAs + \frac{1}{2}H_{2_g} + HCl_g \tag{III.26}$$

with $Cl - H - H^*$ that represents the activated molecule, of energy $\varepsilon^*_{In}$. The same reactions are written for GaAs with AsGaCl.

#### III.2.3.2.1 Adsorption flux $J_+$ for InAs

We consider the following reaction:

$$AsInCl + H_{2_g} \rightleftharpoons InAs_c + Cl - H - H^* \tag{III.27}$$

We can write the equality of chemical potentials:

$$\mu_{AsInCl} + \mu_{H_{2_g}} = \mu_{InAs_c} + \mu_{(Cl-H-H^*)} \tag{III.28}$$

The chemical potentials of the species (in the crystal, on the surface and in the mother phase) can be expressed according to their respective partition functions, then we obtain:

$$\frac{N_{AsInCl}}{N_v\, z_{AsInCl}} \frac{N_{H_{2g}}}{z_{H_{2g}}} = \frac{1}{z_{InAs_c}} \frac{N^*_{Cl-H-H}}{N_v\, z^*_{Cl-H-H}} \tag{III.29}$$

with $N_v$ the number of vacant sites on the surface, $N_i$ the number of adsorbed molecule $i$ and $z_i$ the partition function of molecule $i$.

The adsorption flux per unit area is defined as:

$$J_+ = \frac{1}{S} \frac{dN^*_{(Cl-H-H)}}{dt} = \frac{1}{S} N^*_{(Cl-H-H)} \frac{\overline{v}^*}{\delta_{In}} \tag{III.30}$$

with $\overline{v}^*$ the activated molecules mean speed which overcome the potential barrier of width $\delta_{In}$. For a 1D translation, $\overline{v}^*$ is defined as:

$$\overline{v}^* = \sqrt{\frac{k_B T}{2\pi m^*_{(Cl-H-H)}}} \tag{III.31}$$

with $m^*_{(Cl-H-H)}$ the mass of the activated complex.

We can write the partition function of the activated molecule isolating the 1D translation along the potential barrier:

$$z^*(In) = z^*_0(In)\, \delta_{In} \sqrt{\frac{2\pi m^*_{(Cl-H-H)} k_B T}{h^2}} \tag{III.32}$$

where $z^*_{Cl-H-H}$ is written as $z^*(In)$ for simplicity. Thus:

$$J_+ = \frac{1}{S} \frac{k_B T}{h} \frac{z^*_0(In)\, z_{InAs_c}}{z_{AsInCl}\, z_{H_{2g}}} N_{AsInCl}\, N_{H_{2g}} \tag{III.33}$$

The coverage ratio $\theta_i$ of a species $i$ is defined as $\theta_i = \frac{N_i}{N}$ where $N$ is the total number of surface sites. Using the number of sites per surface unit $N_s = \frac{N}{S}$ and the ideal gas law, we get:

$$J_+ = N_s \theta_{AsInCl} \frac{k_B T}{h} \frac{z^*_0(In)\, z_{InAs_c}}{z_{AsInCl}\, z_{H_{2g}}} \frac{P_{H_{2g}}}{\frac{k_B T}{V}} \tag{III.34}$$

The number of adsorbed InAsCl molecules is given by chemical potential equality of the reaction:

$$\frac{1}{4} As_{4g} + InCl_g \rightleftharpoons AsInCl \tag{III.35}$$

Then:

$$\frac{N_{AsInCl}}{N_v\, z_{AsInCl}} = \frac{P^{1/4}_{As_{4g}}}{(\frac{k_B T}{V}\, z_{As_{4g}})^{\frac{1}{4}}} \frac{P_{InCl_g}}{\frac{k_B T}{V}\, z_{InCl_g}} \tag{III.36}$$

$$\theta_{AsInCl} = \theta_v \left[ \frac{P_{As_{4g}}^{1/4}}{(\frac{k_BT}{V} z_{As_{4g}})^{\frac{1}{4}}} \frac{P_{InCl_g}}{\frac{k_BT}{V} z_{InCl_g}} \right] z_{AsInCl} \tag{III.37}$$

Finally:

$$J_+ = N_s \theta_v \frac{k_BT}{h} \frac{z_0^*(In)\, z_{InAs_c}}{z_{InCl_g}\, z_{H_{2g}}\, z_{As_{4g}}^{1/4}} \frac{P_{H_{2g}}\, P_{As_{4g}}^{1/4}\, P_{InCl_g}}{(\frac{k_BT}{V})^{\frac{9}{4}}} \tag{III.38}$$

As expected, the adsorption flux $J_+$ is a function of the coverage ratio of vacant sites on the surface $\theta_v$.

#### III.2.3.2.2 Desorption flux $J_-$ for InAs

The desorption flux is calculated using the chemical potential equality of the reaction:

$$InAs_c + Cl - H - H^* \rightleftharpoons InAs + \frac{1}{2} H_{2_g} + HCl_g \tag{III.39}$$

Based on the same calculation as for the adsorption flux $J_+$ we obtain:

$$J_- = N_s \theta_{InAs} \frac{k_BT}{h} \frac{z_0^*(In)}{z_{H_{2g}}^{1/2}\, z_{HCl_g}} \frac{P_{H_{2g}}^{1/2}\, P_{HCl_g}}{(\frac{k_BT}{V})^{\frac{3}{2}}} \tag{III.40}$$

We can see that the desorption flux $J_-$ is a function of the coverage ratio of InAs molecules $\theta_{InAs}$. Finally, by using the definition of the surface concentration $n_{InAs} = N_s \theta_{InAs}$ (page 45), we can write:

$$J_- = n_{InAs} \frac{k_BT}{h} \frac{z_0^*(In)}{z_{H_{2g}}^{1/2}\, z_{HCl_g}} \frac{P_{H_{2g}}^{1/2}\, P_{HCl_g}}{(\frac{k_BT}{V})^{\frac{3}{2}}} \tag{III.41}$$

#### III.2.3.2.3 Diffusion equation and total diffusion flux $j$

By combining Equations (I.62) and (I.66) from Chapter I (pages 44-45 of this manuscript) and using the notation of the model (concentration $n$ and distance $\xi$), we can write the following diffusion equation:

$$-D_{InAs} \frac{\partial^2 n_{InAs}}{\partial \xi^2} = J_+ - J_- \tag{III.42}$$

We choose the boundary conditions as the same form as purely kinetic growth:

$$n_{InAs}(\xi \to \infty) = n_0, \;\; n_{InAs}(\xi = 0) = 0 \tag{III.43}$$

with $n_0$ the limiting concentration which is a constant as it was the case previously in Equation (III.7) (page 104).

Then, we can write $n_{InAs}$ as:

$$n_{InAs} = n_0(1 - e^{-\frac{\xi}{\lambda_{InAs}}}) \tag{III.44}$$

By injecting this expression into Equation (III.42) and by assuming that there are enough vacant sites on the surface to incorporate all species whatever the growth conditions, i.e. $\theta_V$ does not depend on $\theta_{InAs}, \theta_{GaAs}$ (in other words $\theta_V \to 1 \gg \theta_{InAs}, \theta_{GaAs}$ and $J_+$ is independent of $n_{InAs}$), we get:

$$D_{InAs}\frac{n_0}{\lambda_{InAs}^2}e^{-\frac{\xi}{\lambda_{InAs}}} = J_+ - n_0(1 - e^{-\frac{\xi}{\lambda_{InAs}}})\frac{k_BT}{h}\frac{z_0^*(In)}{z_{H_{2g}}^{1/2}z_{HCl_g}}\frac{P_{H_{2g}}^{1/2}P_{HCl_g}}{(\frac{k_BT}{V})^{\frac{3}{2}}} \tag{III.45}$$

By taking the boundary conditions ($\xi = 0$ and $\xi \to \infty$), we get the expressions of $n_0$ and $\lambda_{InAs}$:

$$n_0 = J_+\frac{h}{k_BT}\frac{z_{H_{2g}}^{1/2}z_{HCl_g}}{z_0^*(In)}\frac{(\frac{k_BT}{V})^{\frac{3}{2}}}{P_{H_{2g}}^{1/2}P_{HCl_g}} \tag{III.46}$$

$$\lambda_{InAs} = \sqrt{D_{InAs}\frac{n_0}{J_+}} = \sqrt{D_{InAs}\frac{h}{k_BT}\frac{z_{H_{2g}}^{1/2}z_{HCl_g}}{z_0^*(In)}\frac{(\frac{k_BT}{V})^{\frac{3}{2}}}{P_{H_{2g}}^{1/2}P_{HCl_g}}} \tag{III.47}$$

Now that we have the expressions of $n_0$ and $\lambda_{InAs}$, we can determine $j_{InAs}$ which is defined by:

$$j_{InAs} = D_{InAs}\left.\frac{dn_{InAs}}{d\xi}\right|_{\xi=0} = D_{InAs}\frac{n_0}{\lambda_{InAs}} \tag{III.48}$$

$$j_{InAs} = J_+\sqrt{D_{InAs}\frac{h}{k_BT}\frac{z_{H_{2g}}^{1/2}z_{HCl_g}}{z_0^*(In)}\frac{(\frac{k_BT}{V})^{\frac{3}{2}}}{P_{H_{2g}}^{1/2}P_{HCl_g}}} \tag{III.49}$$

$$j_{InAs} = N_s\frac{k_BT}{h}\frac{z_0^*(In)\,z_{InAs_c}}{z_{InCl_g}\,z_{H_{2g}}\,z_{As_{4g}}^{1/4}}\frac{P_{H_{2g}}P_{As_{4g}}^{1/4}P_{InCl_g}}{(\frac{k_BT}{V})^{\frac{9}{4}}}\sqrt{D_{InAs}\frac{h}{k_BT}\frac{z_{H_{2g}}^{1/2}z_{HCl_g}}{z_0^*(In)}\frac{(\frac{k_BT}{V})^{\frac{3}{2}}}{P_{H_{2g}}^{1/2}P_{HCl_g}}} \tag{III.50}$$

$$j_{InAs} = N_s\sqrt{D_{InAs}}\sqrt{\frac{k_BT}{h}}\frac{1}{(\frac{k_BT}{V})^{\frac{3}{2}}}\frac{z_{InAs_c}\,z_{HCl_g}}{z_{InCl_g}\,z_{H_{2g}}^{1/2}\,z_{As_{4g}}^{1/4}}\frac{z_0^{*1/2}(In)}{z_{HCl_g}^{1/2}\,z_{H_{2g}}^{1/4}}\frac{P_{InCl_g}\,P_{As_{4g}}^{1/4}\,P_{H_{2g}}^{1/2}}{P_{HCl_g}^{1/2}} \tag{III.51}$$

We find the statistical expression of the equilibrium constant defined thermodynamically in the section I.5 (page 33):

$$K_{InAs}^{eq}(T) = \left(\frac{k_BT}{V}\right)^{\frac{3}{4}}\frac{z_{InCl_g}\,z_{H_{2g}}^{1/2}\,z_{As_{4g}}^{1/4}}{z_{InAs_c}\,z_{HCl_g}} \tag{III.52}$$

Thus, we arrive at the final expression of $J_{InAs}$ which is:

$$j_{InAs} = N_s\sqrt{\frac{D_{InAs}}{h}}\frac{V^{\frac{3}{4}}}{(k_BT)^{\frac{1}{4}}}\frac{1}{K_{InAs}^{eq}(T)}\frac{z_0^{*1/2}(In)}{z_{HCl_g}^{1/2}\,z_{H_{2g}}^{1/4}}\frac{P_{InCl_g}\,P_{As_{4g}}^{1/4}\,P_{H_{2g}}^{1/2}}{P_{HCl_g}^{1/2}} \tag{III.53}$$

By applying the same treatment for the GaAs deposition, we find:

$$j_{GaAs} = N_s \sqrt{\frac{D_{GaAs}}{h}} \frac{V^{\frac{3}{4}}}{(k_B T)^{\frac{1}{4}}} \frac{1}{K^{eq}_{GaAs}(T)} \frac{z_0^{*1/2}(Ga)}{z^{1/2}_{HCl_g} z^{1/4}_{H_{2g}}} \frac{P_{GaCl_g} P^{1/4}_{As_{4g}} P^{1/2}_{H_{2g}}}{P^{1/2}_{HCl_g}} \tag{III.54}$$

#### III.2.3.2.4 Purely kinetic distribution

Now that we have expressed the diffusion fluxes of InAs and GaAs, we can link the InAs fraction in the solid $x$ with the In content in vapor $z$:

$$x = \frac{1}{1 + \frac{j_{GaAs}}{j_{InAs}}} \tag{III.55}$$

$$x = \frac{1}{1 + \frac{\sqrt{D_{GaAs}}}{\sqrt{D_{InAs}}} \frac{K^{eq}_{InAs}(T)}{K^{eq}_{GaAs}(T)} \frac{z_0^{*1/2}(Ga)}{z_0^{*1/2}(In)} \frac{P_{GaCl_g}}{P_{InCl_g}}} \tag{III.56}$$

As $z$ is defined as the ratio $P_{InCl_g}/(P_{InCl_g} + P_{GaCl_g})$, we finally get the purely kinetic Langmuir-McLean equation:

$$z = \frac{x}{c' + (1-c')x} \quad \text{with} \quad c' = \frac{\sqrt{D_{InAs}}}{\sqrt{D_{GaAs}}} \frac{z_0^{*1/2}(In)}{z_0^{*1/2}(Ga)} \frac{K^{eq}_{GaAs}(T)}{K^{eq}_{InAs}(T)} \tag{III.57}$$

Thus, in a purely kinetic analysis, whether we consider atomic species (In and Ga adatoms) or the reactions that are involved in HVPE, we obtain the same dependence between $z$ and $x$. This suggests that the model used previously is indeed valid and consistent with HVPE growth modeling. Only the expression of the parameter $c'$ is modified and we discuss it in more detail in the following paragraph.

Let's focus on the dependence of $c'$ with respect to temperature to find out if this is consistent with the experimental results. According to the literature, we know that the parameter $c$ decreases with temperature (from $\sim 1$ at 450 °C to $\sim 0.1$ at $\sim 700$ °C as explained in section III.2.3.1.4 (page 107). For clarity, we will discuss the evolution of each term of $c'$ as a function of temperature.

- **The ratio** $\sqrt{D_{InAs}}/\sqrt{D_{GaAs}}$: the higher the temperature, the more easily indium desorbs. This suggests that $D_{InAs} < D_{GaAs}$. In addition, high temperatures are favorable for the growth of GaAs (740 °C vs 640 °C for InAs in HVPE). Thus, it is reasonable to assume that this ratio will decrease with temperature.

- **The ratio** $z_0^{*1/2}(In)/z_0^{*1/2}(Ga)$: to detail the evolution of this ratio with the temperature, it is necessary to discuss the dechlorination energies. Indeed, it can be shown that $z_0^*(In)$ and $z_0^*(Ga)$ can be written as the form $z_0^*(In/Ga) = z_0^{*\prime}(In/Ga) e^{\frac{-\varepsilon^*_{In/Ga}}{k_B T}}$ with $\varepsilon^*_{In}$ and $\varepsilon^*_{Ga}$ the dechlorination

energies of AsInCl and AsGaCl molecules, respectively. As a first approximation, we can assume that $z_0^{*\prime}(In) \approx z_0^{*\prime}(Ga)$. Consequently, the ratio depends mainly on $e^{\frac{\Delta\varepsilon^*}{k_BT}}$ with $\Delta\varepsilon^* = \varepsilon^*_{Ga} - \varepsilon^*_{In}$. In previous experiments on InGaAs layers by HVPE carried out by A.Porte and E.Gil [174, 175], the values obtained for delta $\Delta\varepsilon^*$ in several composition domains were always found positive (around 1000 cal/mol). Thus, the exponential decreases with temperature and the ratio $\frac{z_0^{*1/2}(In)}{z_0^{*1/2}(Ga)}$ as well.

– **The ratio** $K^{eq}_{GaAs}(T)/K^{eq}_{InAs}(T)$: in order to easily estimate its variation as a function of temperature, the evolutions of $K^{eq}_{GaAs}(T)$ and $K^{eq}_{InAs}(T)$ according to temperature were plotted and are shown in Figure III.10. We clearly see that this ratio decreases with temperature.

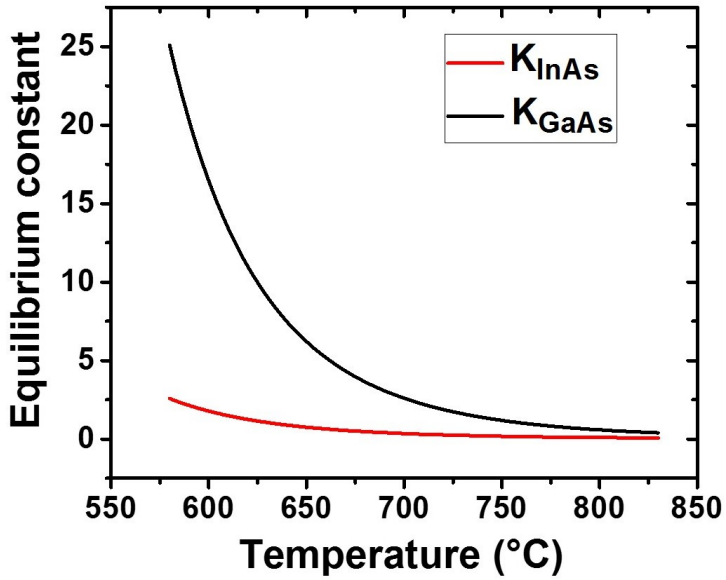


Figure III.10 – *Evolution of the equilibrium constants related to InAs and GaAs condensation from III-Cl and $As_4$ molecules as a function of temperature. Note that K are calculated here as (solid/gaseous species).*

Thus, the parameter $c'$ of the Equation (III.57) decreases with temperature, which is in agreement with the literature and which supports the consistency of this model. In theory, adjusting this parameter could make it possible to extrapolate some parameters such as diffusion coefficients or partition functions but there are still some unknowns to determine. However, we have successfully demonstrated the Langmuir-McLean equation based on kinetic considerations specific to HVPE. In perspective, it would be interesting to complete the model by taking into account the activity of the solid (i.e. thermodynamics) or by considering a dependence between $\theta_V$ and $\theta_{InAs,GaAs}$.

In summary, we have demonstrated SAG by HVPE of InGaAs NWs in regular arrays on patterned Si(111) substrates. The InAs fraction in InGaAs NWs was tuned in the range from $x = 0.34$ to $x = 0.90$, which is relevant for optoelectronic applications. The EDX mapping of individual NWs confirmed the homogeneous composition along the entire NW length. The NW composition was shown to be controlled by the growth kinetics rather than thermodynamic factors, which considerably simplifies the compositional control in a wide range of HVPE parameters. Kinetically controlled and widely tunable vapor-solid distributions have been known for a long time for InGaAs epi-layers [171] and obtained more recently in Au-catalyzed VLS InGaAs NWs on InAs substrates [161, 176] or catalyst-free InGaAs NWs on graphene [177]. However, none of these structures were grown on highly mismatched Si substrates. Overall, these findings reveal the capability of cost-effective HVPE techniques for fabrication of regular arrays of InGaAs NWs on Si with widely tunable and spatially uniform compositions.

# III.3 Conclusion

In this chapter, I have demonstrated that the growth suppression effect due to As trimers on the top (111)B surface also occurs for the growth of InAs NWs. Thus, this effect seems to concern more generally every III-As NWs which grow in the [111]B direction under high partial pressure of $As_4$ (or low III/V ratio). By adjusting $P_{As_4}$, we have demonstrated the growth of 12 µm-long InAs NWs which was the main objective regarding the perspective of multispectral devices by HVPE. These results are encouraging for the development of multispectral photodetector devices which will be performed during a forthcoming collaboration with McMaster University.

Secondly, I have studied the growth of InGaAs NWs on both patterned GaAs(111)B and Si(111) substrates. NW arrays were successfully obtained and, to our knowledge, this is the first time that the growth of InGaAs NWs is demonstrated by HVPE (two articles are in progress). First of all, the results obtained on patterned GaAs(111)B substrate showed the feasibility of growing InGaAs NWs. A remarkably high growth rate (more than 50 µm/h) was obtained. Like GaAs NWs, InGaAs NWs have a high density of stacking faults. The composition was investigated by EDX profile along a single NW, resulting in an average InAs fraction of $x = 0.84$ with nearly homogeneous concentrations along the NW length. This composition is consistent with the composition estimated by PL of $x = 0.78$. This demonstration of the feasibility of the SAG of InGaAs NWs on GaAs(111)B substrate allowed us to consider growth on Si(111) substrate.

Regarding the growth on Si, we have successfully demonstrated SAG by HVPE of InGaAs NWs in regular arrays on Si(111) substrates. A wide range of InAs fractions in InGaAs NWs has been obtained from $x = 0.34$ to $x = 0.90$. The EDX mapping of individual NW confirmed the homogeneous composition along the entire NW length. The NW composition was shown to be controlled by the growth kinetics rather than thermodynamic factors, which considerably simplifies the compositional control in a wide range of HVPE parameters. Kinetically controlled and widely tunable vapor-solid distributions have been known for a long time for InGaAs epi-layers and obtained more recently in Au-catalyzed VLS InGaAs NWs on InAs substrates or catalyst-free InGaAs NWs on graphene. However, none of these structures were grown on highly mismatched Si substrates. Overall, these findings reveal the capability of the cost-effective HVPE technique for the fabrication of regular arrays of InGaAs NWs on Si(111) with widely tunable and spatially uniform compositions.

# General conclusion

This thesis work focused on the study of the growth of catalyst-free III-As NWs by HVPE. After introducing the context and the HVPE method in chapter I, the thesis was oriented on two main axes: the growth of GaAs NWs in chapter II and the growth of InAs and InGaAs NWs in chapter III.

In chapter I, the context of my thesis has been introduced. The main advantages of NW geometry were presented as well as the different methods for growing NWs that are employed. Then, we have discussed a state of the art of the growth of III-As NWs and especially the difficulties encountered during the growth of ternary InGaAs. Afterwards, the main motivations for the growth of NWs III-As at Institut Pascal, notably betavoltaic cells for GaAs NWs and infrared photodetectors for InAs and InGaAs NWs were presented. In the last part of the chapter, the experimental HVPE set-up used at Institut Pascal has been described. We discussed the gaseous species present in the reactor in order to further develop the thermodynamics and the kinetics of HVPE growth. In particular, the concept of supersaturation was introduced which allowed us to determine the growth conditions for the condensation of III-As materials. Finally, the problems related to the supply of high quality patterned substrates were introduced, which impacted the number of substrates used during this work.

In Chapter II, we have described the SAG of GaAs NWs. The NW morphology was investigated versus the growth conditions and template geometry. This study revealed that As-rich conditions are highly undesirable for SAG of GaAs NWs by HVPE. Indeed, a saturation of the NW lengths was observed at high partial pressures of $As_4$, explained by the presence of As trimers on the (111)B surface at the NW top surface. Afterwards, optimal conditions for the growth of long GaAs NWs were determined which made it possible to obtain long NWs ($\sim$ 6 µm) with a high aspect ratio of around 50. These observations were supported by a dedicated kinetic model which takes into account the diffusion of Ga adatoms from the NW sidewalls to the top. In the second section, we have reported the first study of doping of catalyst-free GaAs NWs by HVPE. The influence of dopants on NW morphology, optical and crystallographic properties was discussed. These preliminary results made it possible to conduct the first growth of p-i-n junction NW by HVPE. The NWs obtained were then

processed to make a photovoltaic device at McMaster University. The efficiencies obtained are very poor but this study highlighted several ways of improvement in a perspective of a future p-i-n junction by HVPE. Finally, a new junction prototype was tested with a very high flow of n-dopant. This was characterized by cathodoluminescence and showed two distinct areas seeming to correspond to the different doping areas. These results are encouraging for the realization of NW p-i-n junction by HVPE.

In chapter III, we first discussed on the SAG of InAs NWs on Si(111). In the same way as the growth of GaAs NWs, optimal conditions for growing long InAs NWs were determined. This allowed to obtain 15 µm long NWs as well as a remarkable axial growth rate of 60 µm/h. These results are encouraging for the development of multispectral photodetectors devices on patterned Si(111) substrate by HVPE. This will be performed during a forthcoming collaboration with McMaster University. Afterwards, we focused on the growth of InGaAs NWs on patterned GaAs(111)B substrate. Indium-rich InGaAs NWs were obtained with a high growth rate of more than 50 µm/h. The indium composition was estimated at $x = 0.84$ by EDX and $x = 0.78$ by PL. Finally, we explored the growth of InGaAs NWs on patterned Si(111) substrate which represents a significant challenge in obtaining various compositions and which has never been reported by HVPE. A wide range of InAs fractions in InGaAs NWs was successfully obtained from $x = 0.34$ to $x = 0.90$. The EDX mapping of individual NWs confirmed the homogeneous composition along the entire NW length. A dedicated growth model has been developed and the NW composition was shown to be controlled by the growth kinetics rather than thermodynamic factors, which considerably simplifies the compositional control in a wide range of HVPE parameters. Thus, these findings provides HVPE as a new platform for the fabrication of homogeneous InGaAs NW arrays with widely tunable compositions.

In conclusion of this thesis, we have successfully demonstrated the SAG of III-As NWs by HVPE. This work has modestly contributed to the understanding of new aspects related to the growth of NWs by HVPE and opens up many perspectives. The results remain preliminary and require further study and investigation. Thus, the fruitful collaboration between Institut Pascal and McMaster University will continue in the perspective of obtaining promising NW-based devices.

# Ma Thèse en 180 secondes / Three Minute Thesis

Je souhaite conclure mon manuscrit de thèse avec la planche qui a été réalisée par Anne Bernardi (illustratrice scientifique) lors de la finale clermontoise du concours « Ma Thèse en 180 secondes », à laquelle j'ai participé en mars 2023. Cette planche permet d'illustrer et de vulgariser mon sujet de thèse, ainsi que de garder un souvenir scientifique de mon passage sur scène, qui a été filmé et que vous pouvez retrouver sur YouTube !

I would like to conclude my thesis manuscript with the drawing board which was produced by Anne Bernardi (scientific illustrator) during the final of the competition "Three Minute Thesis" in Clermont-Ferrand, in which I took part in March 2023. This board allows me to illustrate and popularize my thesis subject, as well as to keep a scientific memory of my performance on stage, which was filmed and that you can find on YouTube!


Chapter IV

# Summary in french

Dans ce chapitre, le contexte et les principaux résultats du travail de thèse sont résumés en français. En effet, l'article 19 du règlement intérieur de l'École Doctorale Sciences Fondamentales (EDSF) de l'Université Clermont Auvergne (UCA) stipule que : "*Dans le cas où l'autorisation de rédiger en anglais est obtenue, la thèse doit inclure un résumé substantiel [...] de 25 pages environ si le doctorant ou la doctorante est francophone, présentant le détail des contributions originales de la thèse replacées dans le contexte de la recherche*". Ainsi, dans un premier temps, le contexte et les objectifs de la thèse sont introduits. Puis, les principaux résultats et contributions des chapitres de ce manuscrit sont discutés.

## IV.1 Contexte de la thèse

Au cours des dernières décennies, les nanofils (NFs) semiconducteurs de matériaux III/V ont grandement intéressé la communauté scientifique en raison de leurs propriétés physiques uniques et de leurs potentielles applications en nanoélectronique et en optoélectronique. Depuis leur découverte par Wagner et Ellis en 1964 [6], une grande variété de dispositifs à base de NFs a été développée comme des transistors, des cellules solaires, des lasers ou encore des photodétecteurs. À ce jour, les principales techniques utilisées pour faire croître les NFs sont la MBE (molecular beam epitaxy) et la MOVPE (metal organic vapor phase epitaxy). Dans cette thèse, j'ai utilisé la HVPE (hydride vapor phase epitaxy). À l'Institut Pascal, ce procédé est utilisé depuis les années 1980 pour la croissance de couches planaires III-V. Au cours de la dernière décennie, l'équipe de croissance HVPE a démontré avec succès la croissance de NFs III-As et III-N par croissance catalysée [1, 2, 3] et par croissance non catalysée [4, 5].

Ces travaux de thèse s'inscrivent principalement dans le projet NANOSPRING (*Pack ambition international DRV_PIP_2021-252_IP_NANOSPRING*) en collaboration avec le professeur Ray LaPierre de McMaster University (Ontario, Canada). Le but de ce projet est la croissance de NFs d'InAs et d'InGaAs par HVPE pour des applications de photodétecteurs infrarouges. De plus, ce projet s'intéresse également aux NFs de GaAs pour des conversions d'énergie via les cellules bêtavoltaïques. Pour résumer, mes travaux portent sur l'étude de la croissance non catalysée de NFs III-As par HVPE et sont détaillés dans ce manuscrit qui contient trois chapitres.

Le chapitre I introduit le contexte global en présentant d'abord les avantages de la géométrie NF et les différentes façons qui existent pour les faire croître : croissance catalysée, croissance non catalysée et croissance sélective SAG (selective area growth). L'état de l'art est discuté ce qui permet de détailler les propriétés particulières des NFs III-As et le vaste champ d'application qui en résulte. En détaillant les potentielles applications visées du projet, il ressort un objectif commun et qui constitue un axe majeur de cette thèse, qui est la croissance de réseaux de longs NFs III-As (plusieurs µm). Après avoir décrit le réacteur utilisé au laboratoire, les aspects thermodynamiques et cinétiques de la croissance HVPE sont détaillés. Ceci permet d'appréhender les mécanismes de la croissance HVPE ainsi que les espèces présentes pendant la croissance.

Le chapitre II se concentre sur la SAG de NFs de GaAs sur des substrats de GaAs(111)B. Les caractéristiques des NFs sont étudiées en fonction des conditions de croissance et du motif du réseau. Cette étude révèle que les conditions riches en As sont hautement indésirables pour la SAG de NFs de GaAs par HVPE. En effet, des trimères d'As se forment sur la facette supérieure ce qui inhibe la croissance axiale des NFs. De plus, des conditions optimales pour la croissance des longs NFs sont déterminées et permettent l'obtention de longs NFs ($\sim$ 6 µm) avec un rapport de forme élevé ($\sim$ 50). Ces observations ont été appuyées par un modèle cinétique dédié qui, pour la première fois en HVPE, prend en compte la diffusion des adatomes de Ga depuis les parois latérales vers le haut du NF. Dans un second temps, il est présenté une étude du dopage de NFs de GaAs non catalysés par HVPE. L'influence des dopants sur la morphologie des NFs, sur les propriétés optiques et cristallographiques est discutée. Cette étude préliminaire du dopage a permis de réaliser une première croissance de jonction p-i-n dans des NFs de GaAs. Ces NFs ont été utilisés pour fabriquer un dispositif photovoltaïque à McMaster University. Malheureusement, les efficacités obtenues sont très faibles. Cependant, cette étude met en évidence plusieurs pistes d'amélioration en perspective de futures jonctions p-i-n par HVPE. Enfin, un nouveau prototype de jonction p-i-n est testé avec un très fort débit de dopants n. Des caractérisations par cathodoluminescence montrent deux zones distinctes semblant correspondre

aux différentes zones de dopage. Ces résultats sont encourageants quant à la réalisation de jonction p-i-n dans des NFs par HVPE.

Le chapitre III présente la SAG de NFs d'InAs sur substrat de Si(111) et la SAG de NFs d'InGaAs sur substrats de GaAs(111)B et de Si(111). Concernant l'InAs, de la même façon que pour le GaAs, des conditions de croissances optimales sont déterminées ce qui permet d'obtenir des NFs d'environ 15 µm. Ces résultats sont prometteurs pour le développement de photodétecteurs multispectraux qui seront étudiés lors d'une prochaine collaboration avec McMaster University. En ce qui concerne les NFs d'InGaAs, il est démontré la faisabilité sur substrat de GaAs(111)B avec une vitesse de croissance remarquablement élevée (plus de 50 µm/h) et des NFs riches indium avec une composition en indium $x$ estimée à $x = 0,84$ par EDX et $x = 0,78$ par photoluminescence. Sur substrat de Si(111), la SAG de NFs d'InGaAs est démontrée avec succès. Une large gamme de fractions d'InAs dans les NFs d'InGaAs est obtenue de $x = 0,34$ à $x = 0,90$. La cartographie EDX de NFs individuels confirme l'homogénéité de composition sur toute la longueur des NFs. Un modèle de croissance dédié est développé et la composition des NFs s'avère être essentiellement contrôlée par les cinétiques de croissance plutôt que par des facteurs thermodynamiques, ce qui simplifie considérablement le contrôle de la composition par HVPE. Pour conclure, ces résultats révèlent la capacité de la HVPE pour la fabrication de réseaux réguliers de NFs d'InGaAs sur Si avec des compositions uniformes et facilement ajustables.

# IV.2 Résumé du chapitre I : la méthode HVPE pour la croissance de nanofils III-As

## IV.2.1 Les avantages de la géométrie nanofil

**Que sont les nanofils ?** Les nanofils (NFs) sont des structures quasi-1D d'un diamètre de l'ordre de plusieurs nm jusqu'à des dizaines de nm et avec un haut rapport de forme. Grâce à leur géométrie, les NFs ont des propriétés très spécifiques en matière de relaxation des contraintes, d'interaction avec la lumière et de transport électrique. Depuis leur découverte en 1964 par Wagner et Ellis [6], l'intérêt pour la croissance des NFs n'a cessé d'augmenter. Les NFs se sont déjà révélés très efficaces dans de nombreux domaines d'applications tels que les cellules solaires, les diodes électroluminescentes (DEL) ou les photodétecteurs [7, 8, 9]. Les principaux avantages des NFs sont décrits ci-dessous.

**L'épitaxie sur substrat à fort désaccord de maille :** le problème majeur concernant la croissance de matériaux semiconducteurs sur hétérosubstrat est la difficulté à obtenir des cristaux sans défaut. En effet, le désaccord de maille entre le substrat et le semiconducteur provoque une contrainte à l'interface entre les deux matériaux. En épitaxie de couches minces, cela se traduit par une détérioration de la qualité cristalline avec une densité élevée de dislocations. Ces dislocations agissent comme des centres de recombinaison non radiatifs qui ont un impact important sur les propriétés électriques et optiques du matériau. Pour les NFs, leur faible diamètre permet de relaxer les contraintes à travers les facettes latérales comme illustré en Figure IV.1. Ainsi, même dans les configurations à fort désaccord de maille, telle que l'épitaxie de semiconducteurs III-V sur substrat Si, des matériaux sans dislocation peuvent être obtenus [10, 11].

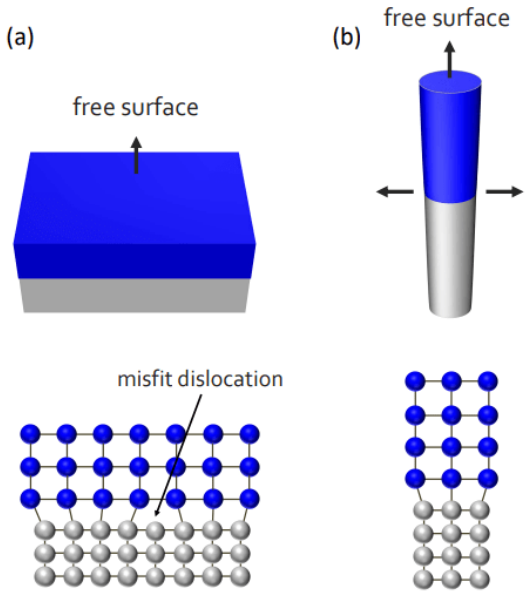


Figure IV.1 – *Schéma a) d'une croissance planaire et b) d'une croissance de nanofil sur hétérosubstrat. Pour la couche 2D, la relaxation des contraintes induit des dislocations, alors que pour le nanofil la contrainte est relaxée à travers les facettes latérales [13].*

**La croissance d'hétérostructures axiales et radiales :** la géométrie NF permet la fabrication de deux différents types d'hétérostructures : l'hétérojonction axiale et l'hétérojonction radiale (ou cœur/coquille) où les matériaux semiconducteurs peuvent être épitaxiés autour d'un noyau de NF [14, 15]. Pour obtenir ces structures particulières, il est nécessaire de contrôler les conditions de croissance afin d'augmenter la croissance radiale aux dépens de la croissance axiale. Les différentes possibilités d'hétérojonctions à base de NF sont schématisées dans la Figure IV.2.

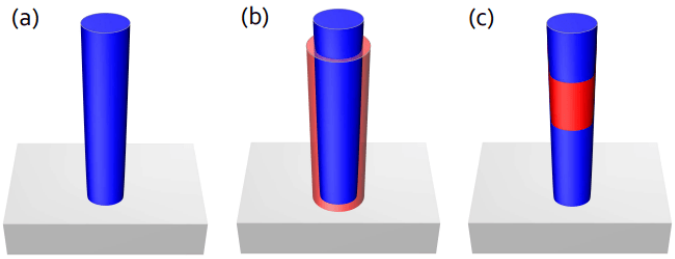


Figure IV.2 – *Schéma des différentes configurations d'hétérostructures à base de nanofils : a) NF seul sur un substrat, b) hétérostructure radiale (cœur/coquille) et c) hétérostructure axiale. Adapté de [13].*

**Une interaction lumière-matière particulière :** les NFs se comportent comme des antennes et concentrent la lumière incidente dans leur petit volume [16]. Des phénomènes de résonances apparaissent pour l'absorption de la lumière par des réseaux de NFs comme des modes Fabry-Pérot ou des modes de guides d'ondes. Il en résulte des propriétés antireflets améliorées et un piégeage de la lumière dans le réseau de NFs. Ainsi, en fonction de la longueur des NFs, de leur diamètre ou encore du motif du réseau, la réflexion peut être minimisée et une large bande d'absorption peut être obtenue, ce qui a été étudié théoriquement [17, 18, 19, 20, 21, 22] et expérimentalement [23, 24, 25, 26].

## IV.2.2 La croissance sélective : SAG

Que ce soit par MBE, MOVPE ou HVPE, il existe plusieurs méthodes pour faire croître des NFs. À ce jour, la méthode la plus utilisée est la croissance avec catalyseur, aussi appelée croissance VLS (vapeur-liquide-solide) [7, 9, 28]. Le catalyseur métallique le plus utilisé est l'or (Au-assisted growth), mais ce peut aussi être l'élément III comme un catalyseur Ga pour des NFs de GaAs (self-assisted growth). Cependant, la méthode VLS peut être compliquée à mettre en œuvre et il a été rapporté que des atomes d'Au peuvent s'incorporer dans les NFs. Les atomes agissent ainsi comme des impuretés ce qui introduit des centres de recombinaison profond et qui dégrade les propriétés électriques et optiques des NFs [30, 31]. Par conséquent, des efforts importants ont été déployés pour faire croître des NFs sans catalyseur par la méthode « catalyst-free » via le mécanisme VS (vapeur-solide). C'est cette méthode qui est utilisée dans mes travaux de thèse.

Pour obtenir des réseaux de NFs réguliers et ordonnés sur de grandes surfaces, il est nécessaire de faire de la croissance sélective ou SAG (selective area growth). En effet, si la croissance est auto-organisée (sur substrat nu), les germes de croissances sont de densité et de taille aléatoires ce qui conduit à des inhomogénéités de diamètre, de longueur, de position et de direction de croissance des

NFs. Ceci induit des inhomogénéités de propriétés électroniques et optiques, rendant la fabrication des dispositifs très difficile. Afin de surmonter ces difficultés, la SAG a été développée. La SAG consiste en la croissance de NFs dans des emplacements prédéfinis ce qui permet l'obtention de réseaux de NFs très homogènes et ce, à grande échelle.

Cette technique nécessite le pré-dépôt d'une couche de masque diélectrique (en général $SiN_x$ ou $SiO_x$) sur le substrat. Ensuite, des ouvertures avec un diamètre spécifique sont obtenues par lithographie. Elles sont espacées d'une distance qui est le pas du masque (ou pitch) déterminé. Aujourd'hui, l'EBL (electron beam litography) permet d'obtenir des trous de quelques dizaines de nanomètres, ce qui donne lieu à des réseaux NFs très denses. Les substrats obtenus sont appelés substrats « patternés ». Le processus de SAG typique est illustré en Figure IV.3.

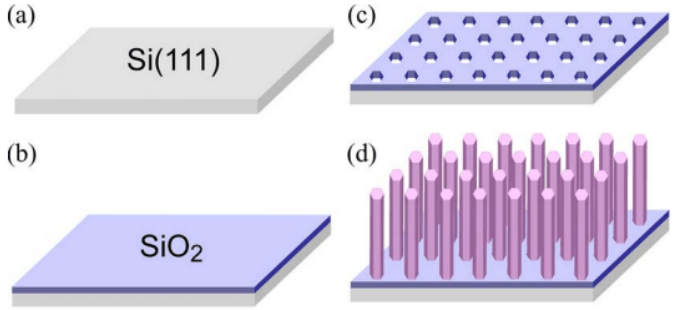


Figure IV.3 – *Schéma du processus de SAG : (a) substrat nu de Si(111), (b) dépôt d'un masque diélectrique $SiO_2$, (c) définition du motif par EBL et gravure chimique, (d) croissance des NFs. Adapté de [7].*

## IV.2.3 Objectifs de la thèse

Comme explicité précédemment, l'objectif principal de cette thèse est la SAG de NFs III-As sans catalyseur par HVPE. Ceci s'inscrit dans les projets dans lesquels est impliqué l'Institut Pascal avec des perspectives de cellules bêtavoltaïques pour les NFs de GaAs, et de photodétecteurs infrarouges (IR) pour les NFs d'InAs et d'InGaAs. Nous allons brièvement présenter ces applications, le lecteur est invité à se reporter à la section I.3.4 (page 22) pour plus de détails.

– **Les NFs de GaAs pour des cellules bêtavoltaïques :** les cellules bêtavoltaïques (BV) sont des sources d'alimentation potentielles pour les applications qui nécessitent une source de faible puissance et de longue durée [92]. Les générateurs BV fonctionnent de la même manière que les générateurs photovoltaïques : les paires électron-trou sont excitées dans une jonction p-i-n semiconductrice et collectées pour créer de l'électricité. Cependant, contrairement au photo-

voltaïque, les BV exploitent l'énergie des particules $\beta$ provenant de sources radioactives plutôt que des photons [93]. Les BV présentent l'avantage d'avoir une très longue durée de vie (qui dépend du temps de demi-vie de la source radioactive) et de pouvoir fonctionner à des températures ou des pressions extrêmes sans souci de dysfonctionnement ou panne [96]. Les applications concernées par de telles propriétés sont les implants biomédicaux, les capteurs à distance, la microélectronique mobile et l'exploration spatiale [92, 97, 98]. Les travaux théoriques de Devan Wagner, au sein du groupe du professeur Ray LaPierre, ont mis en évidence l'intérêt des NFs de GaAs comme cellules bêtavoltaïques [100]. En simulant des jonctions p-i-n au sein des NFs de GaAs, il a montré que la longueur de ces NFs impactait grandement l'efficacité des dispositifs BV avec une longueur optimale autour des 10 µm. Ainsi, un de mes objectifs principaux de thèse est de déterminer des conditions de croissance permettant l'obtention de NFs de GaAs de plusieurs µm de long et d'étudier le dopage de NFs de GaAs. Ceci constitue le premier axe de mes recherches et est présenté dans le chapitre II de ce manuscrit.

– **Les nanofils d'InAs pour les photodétecteurs multispectraux IR :** un photodétecteur multispectral infrarouge (IR) possède différentes bandes d'absorption dans le spectre IR [105, 107]. Cette détection multispectrale offre la capacité de détecter les différences de température dans divers objets permettant un meilleur contraste dans l'IR [107]. Contrairement aux couches minces, la position du pic d'absorption des NFs peut être contrôlée en modifiant la géométrie des NFs et la configuration du réseau. Ainsi, ces paramètres peuvent être ajustés pour obtenir une bande d'absorption spectrale étroite. Cela rend naturellement les photodétecteurs multispectraux à base de NFs attractifs, car la géométrie peut être adaptée pour absorber fortement à une longueur d'onde spécifique sans avoir à modifier l'énergie de la bande interdite du matériau ou d'utiliser des filtres spectraux supplémentaires au-dessus du photodétecteur [110]. De plus, l'utilisation de NFs permet une intégration des photodétecteurs directement sur substrat Si et de faire des hétérojonctions directement au sein des NFs. Par conséquent, non seulement les NFs absorbent la lumière dans des bandes spectrales spécifiques, mais ils peuvent également convertir les photons absorbés en courant. Des études théoriques menées par Khalifa Azizur-Rahman au sein du groupe du professeur Ray LaPierre ont mis en évidence l'intérêt des NFs d'InAs pour des photodétecteurs multispectraux [108]. Une de ses études a montré que l'absorption était grandement affectée par la longueur des NFs, avec une absorption maximale pour des NFs de 2 µm. Ainsi, à l'instar des NFs de GaAs pour les dispositifs BV, un de mes objectifs vise à obtenir des NFs d'InAs de plusieurs µm.

– **Les nanofils d'InGaAs pour des applications IR :** un intérêt particulier se porte dans la croissance du ternaire InGaAs en raison de son énergie de bande interdite qui est ajustable en contrôlant la fraction d'In (ou de Ga). À 300 K, les énergies de bande interdite $E_g$ pour l'InAs et le GaAs sont de 0,354 eV et 1,424 eV, ce qui correspond respectivement à des longueurs d'onde de 3 500 nm et 880 nm [44]. Ainsi, en obtenant plusieurs compositions, il est possible de couvrir une large gamme de longueurs d'onde dans le domaine IR. De plus, à notre connaissance, la croissance de NFs d'InGaAs par HVPE n'a jamais été rapportée.

Pour conclure, la majorité des applications présentées dans cette section requiert des dimensions de NFs spécifiques ce qui nécessite un contrôle précis des conditions de croissance. Maintenant que nous avons présenté les principaux objectifs de cette thèse, nous allons décrire le réacteur HVPE utilisé à l'Institut Pascal.

## IV.2.4 Le réacteur HVPE

Le réacteur HVPE utilisé dans notre laboratoire est un réacteur « home-made » à murs chauds opérant à pression atmosphérique. Le réacteur est en quartz ce qui garantit une grande stabilité thermique même à haute température (jusqu'à 1000 °C). La géométrie du réacteur et les débits des gaz assurent un écoulement laminaire au-dessus du substrat et un mélange homogène de la phase vapeur. Le réacteur est divisé en trois zones qui sont chauffées à différentes températures grâce aux six thermocouples du four. Un schéma du réacteur HVPE est illustré en Figure IV.4.

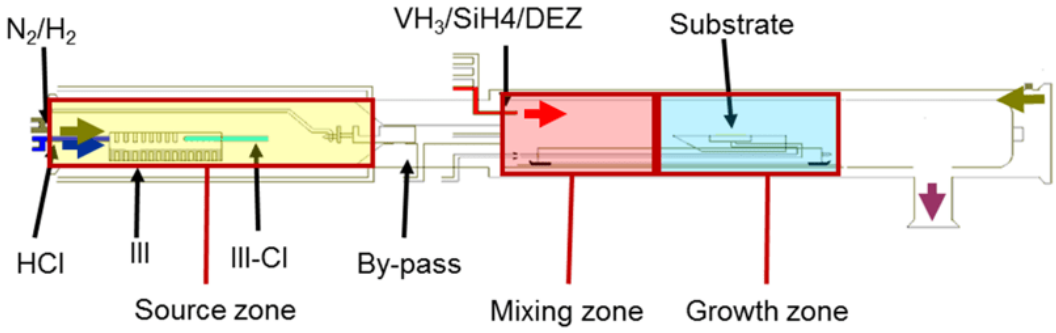


Figure IV.4 – *Schéma du réacteur HVPE utilisé à l'Institut Pascal pour la croissance de NFs III-As.*

Dans la zone source (en jaune), le gaz vecteur $H_2$ est introduit. Les précurseurs chlorés d'éléments III gazeux (InCl et GaCl) sont produits en faisant réagir de l'HCl gazeux avec des sources d'indium et de gallium liquides à 730 °C. Afin de contrôler la sursaturation (qui contrôle le dépôt de matière) de la réaction de croissance, de l'HCl additionnel peut être introduit dans cette zone. Concernant les précurseurs en élément V, de l'arsine gazeux ($AsH_3$) est introduit dans la zone de mélange en aval

du réacteur (en rouge). Cette zone est chauffée à plus haute température pour assurer un mélange homogène de la phase gazeuse et réduire la nucléation parasite en amont du substrat, les réactions impliquant des molécules de chlorure étant exothermiques. Le dopage est possible en introduisant dans cette zone du diéthylzinc (DEZ : $(C_2H_5)_2Zn$) pour le dopage p ou du silane ($SiH_4$). Il est à noter que le DEZ est maintenu dans un bain thermostaté, ainsi, le débit de DEZ dépend fortement de la température du bain $\theta_{DEZ}$. Enfin, la dernière zone est la zone dépôt (en bleue) qui est chauffée à la température la plus basse afin que la réaction soit favorisée sur le substrat. Les zones de mélange et de dépôt sont reliées à la zone source via une vanne tiroir à commande manuelle. Cette dernière permet la préparation des différentes espèces sans aucun dépôt parasite en amont du substrat. Les flux des gaz sont contrôlés à l'aide de vannes manuelles et de débitmètres, les débits de gaz sont exprimés en sccm (standard cubic centimeters per minute). Un des avantages majeurs de la HVPE pour la SAG est la faible adsorption des précurseurs chlorés sur le masque diélectrique. Ceci permet, lorsque le masque est bien ouvert et de bonne qualité, d'obtenir une très haute sélectivité sur une grande surface, ce qui est crucial pour la fabrication de dispositifs optoélectroniques à base de NFs.

## IV.2.5 Préambule expérimental

Dans cette section, il ne sera pas détaillé les considérations thermodynamiques et cinétiques dans leur globalité. Le lecteur est invité à se référer aux sections I.5 et I.6 (pages 33 et 42). Ici, nous allons uniquement présenter les notions les plus importantes qui sont utilisées dans les chapitres II et III. Ainsi, que ce soit pour les expériences ou les modélisations, il est nécessaire de présenter les notions suivantes :

- **Les espèces mises en jeu :** les précurseurs en éléments III sont $GaCl_{(g)}$ et $InCl_{(g)}$, et en élément V est l'$As_{4(g)}$ (l'$AsH_3$ se décompose à partir de 600 °C). Les pressions partielles [GaCl], [InCl] et [$As_4$] sont respectivement notées $P_{GaCl}$, $P_{InCl}$ et $P_{As4}$ dans ce chapitre.
- **Le rapport III/V :** une fois que les pressions partielles des différentes espèces sont calculées, nous pouvons calculer le rapport III/V :

$$III/V = \frac{P_{III-Cl}}{P_{As_4}} \tag{IV.1}$$

  Ce rapport est notamment utilisé pour les modélisations. Le rapport III/V atomique, noté $I_3/I_5$, est également utilisé et est défini par :

$$\frac{I_3}{I_5} = \frac{1}{4}\frac{P_{III-Cl}}{P_{As_4}} \tag{IV.2}$$

– **La sursaturation $\gamma$ :** la sursaturation de la phase vapeur, notée $\gamma$, détermine si la réaction de dépôt est favorisée ou non [114, 115]. Si $\gamma > 0$ il y a dépôt du solide, si $\gamma = 0$ il y a équilibre entre les réactifs et les produits et si $\gamma < 0$ il y a attaque du solide. Elle dépend de la température de croissance $T$, de la constante d'équilibre $K^{eq}_{III-As}$ et du rapport des pressions partielles. Ainsi, les sursaturations pour le GaAs et l'InAs sont données par :

$$\gamma_{GaAs} = \frac{[GaCl][As_4]^{1/4}[H_2]^{1/2}}{[HCl]K^{eq}_{GaAs}(T)} - 1 \; ; \; \gamma_{InAs} = \frac{[InCl][As_4]^{1/4}[H_2]^{1/2}}{[HCl]K^{eq}_{InAs}(T)} - 1 \tag{IV.3}$$

Enfin, la SAG a été réalisée sur des substrats patternés de GaAs (111)B et de Si (111). Le détail des substrats patternés utilisés dans ce manuscrit peut être trouvé dans le Tableau IV.1.

| | **Nom du substrat** | **Nature du substrat** | **Pitch (µm)** | **Diamètre (nm)** | **Masque diélectrique** | **Technique de patterning** |
|---|---|---|---|---|---|---|
| **Chapitre II** | #Bath | GaAs(111)B non dopé | 1 | 340 | 35 nm $SiN_x$ | PECVD + DTL |
| | #IBM1 | GaAs (111)B dopé p | 1 ou 2 | 80 | 35 nm $SiO_x$ | PECVD + EBL |
| **Chapitre III** | #IBM2 | GaAs(111)B non dopé | 2 | 60 | 35 nm $SiO_x$ | PECVD + EBL |
| | #AC121A | Si(111) dopé p | 1,75 ou 3,50 | 350 | 100 nm $SiN_x$ / 20 nm $SiO_x$ | PECVD + EBL |

Table IV.1 – *Détails des substrats patternés utilisés dans ce manuscrit.*

Pour l'ensemble des substrats, les couches ont été déposées par PECVD (plasma-enhanced chemical vapor deposition). Les motifs ont été obtenus soit par DTL (displacement talbot lithography) ou par EBL (electron beam lithography). Plus de détails sur la technique DTL peuvent être trouvés dans Coulon et al [111]. Le substrat #Bath est le résultat de collaborations avec Philip Shields (University of Bath) et les substrats #IBM1 et #IBM2 sont le résultat d'une collaboration avec Heinz Schmid (IBM Zurich). En raison d'un manque de substrats patternés de Si(111) de bonne qualité, j'ai dû utiliser le substrat #AC121A fabriqué il y a plus de 10 ans dans le cadre d'une collaboration avec le CEA-Leti (Grenoble). Ceci a probablement impacté les croissances sur substrat Si(111).

# IV.3 Résumé du chapitre II : SAG-HVPE de NFs de GaAs sur substrat de GaAs(111)B

Dans cette section, les principaux résultats du chapitre II qui portent sur la SAG de NFs de GaAs par HVPE sont discutés. Nous allons d'abord présenter des études expérimentales qui ont mis en évidence de nouveaux phénomènes comme la suppression de la croissance à haute pression partielle d'$As_4$ ce qui conduit à une saturation de la longueur des NFs, et la diffusion des adatomes de Ga sur les facettes latérales des NFs qui n'avait jamais été prise en compte auparavant en HVPE. Ces résultats ont été appuyés par un modèle cinétique dédié et de longs NFs ont été obtenus avec succès. Puis, dans un second temps, nous discutons brièvement du dopage des NFs de GaAs ainsi que des premières croissances de jonction p-i-n dans des NFs de GaAs.

## IV.3.1 Comment obtenir de longs nanofils ?

Dans un premier temps, l'effet du temps de croissance sur la dimension des NFs a été étudié dans le but de faire croître de longs NFs. En effet, généralement, plus le temps de croissance est long, plus les NFs sont longs. Dans ces expériences de croissance, $P_{As_4}$ et $P_{GaCl}$ ont été respectivement fixées à $1,0 \times 10^{-3}$ atm et $1,6 \times 10^{-3}$ atm. Le substrat est #Bath et le temps de croissance varie entre 5 minutes et 20 minutes. La Figure IV.5.a montre un schéma de la SAG sur un substrat patterné $SiN_x$/GaAs(111)B. La Figure IV.5.b montre l'évolution des longueurs et diamètres moyens déduits à partir des images MEB des Figure IV.5.c-e.

Nous pouvons voir que la croissance est parfaitement sélective en raison de la faible adsorption des précurseurs chlorés sur le masque. Par ailleurs, nous constatons que la longueur des NFs sature à environ 550 nm à partir de 5 min de croissance. À 5 min, les NFs ne sont pas clairement facettés et présentent une morphologie « en crayon ». Après 10 min et 20 min, les NFs ont un diamètre uniforme de la base au sommet, avec une section transversale hexagonale typique limitée par les facettes latérales {-110} et la facette (111)B sur le dessus [120]. La vitesse de croissance des facettes latérales {-110} qui est liée aux rangées de Ga-As, est généralement très faible dans une large gamme de conditions HVPE en raison du faible adsorption de GaCl sur la surface {-110} [74, 117]. Par conséquent, la vitesse de croissance radiale des NFs reste faible quelles que soient les conditions de croissance. Ainsi, la chute de la vitesse axiale après 5 min est attribuée à un effet de suppression de croissance sur la surface supérieure (111) B des NFs de GaAs, ce qui est confirmé par l'étude suivante.

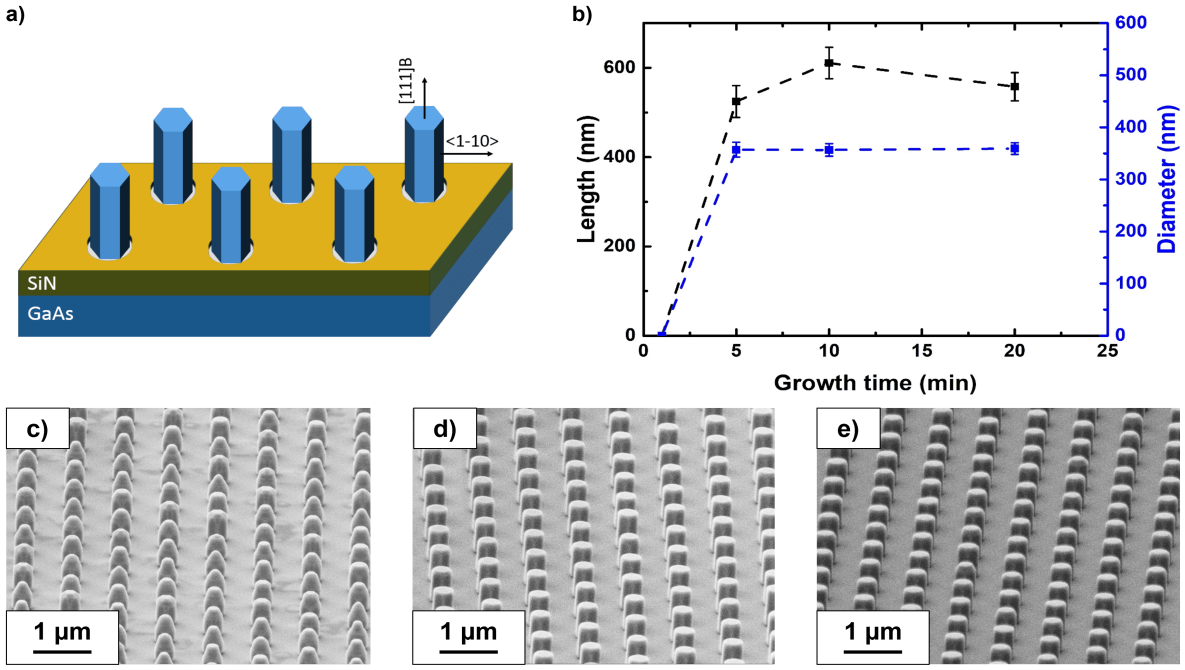


Figure IV.5 – *a) Schéma représentant la SAG de NFs de GaAs sur le substrat #Bath. b) Évolution des longueurs et diamètres moyens des NFs en fonction du temps de croissance. c) Images MEB du réseaux de NFs après : c) 5 min, d) 10 min et e) 20 min de croissance. Pour un temps de 1 min, aucune croissance n'a été observée. Les lignes en b) servent de guide visuel.*

Pour comprendre l'origine de la suppression de la croissance des NFs, une étude en fonction des précurseurs en élément V a été effectuée. Le substrat est toujours #Bath, le temps de croissance est de 10 min à une température de 742 °C. La Figure IV.6.a montre l'influence de $P_{As_4}$ à $P_{GaCl}$ fixée avec les images MEB respectives en Figure IV.6.b-c. Les conditions optimales à faible $P_{As_4}$, favorisant la croissance de NFs longs (en rouge), ont permis de débloquer la croissance axiale et d'obtenir des NFs de 6,8 µm en 30 min comme illustré en Figure IV.6.d.

Cette étude montre clairement l'importance de $P_{As_4}$ pour l'obtention de longs NFs de GaAs en SAG par HVPE. En effet, les NFs les plus longs ne peuvent être obtenus qu'à faible $P_{As_4}$ comme le montre la Figure IV.6.a. Selon certaines études [120, 122, 123, 124, 125, 126], la croissance de la facette supérieure (111)B des NFs de GaAs peut être supprimée par des trimères d'As stables lorsque le flux d'As est trop important. Pour les NFs épitaxiés à forte $P_{As_4}$ ($1,0 \times 10^{-3}$ atm), comme sur la Figure IV.6.c, la longueur des NFs est rapidement saturée et la partie supérieure de ces NFs est entièrement recouverte de trimères As. Aucune croissance supplémentaire ne peut se produire sur de telles surfaces [127, 128]. Pour les NFs épitaxiés à faible $P_{As_4}$ ($3,0 \times 10^{-4}$ atm), la croissance axiale se

produit sur une partie de la surface (111)B exempte de trimères As, ou sur toute la facette supérieure s'il y a absence de trimères As. En conclusion, cette étude a montré l'influence significative de $P_{As_4}$ dans l'obtention de longs NFs de GaAs, qui est un objectif important de cette thèse.

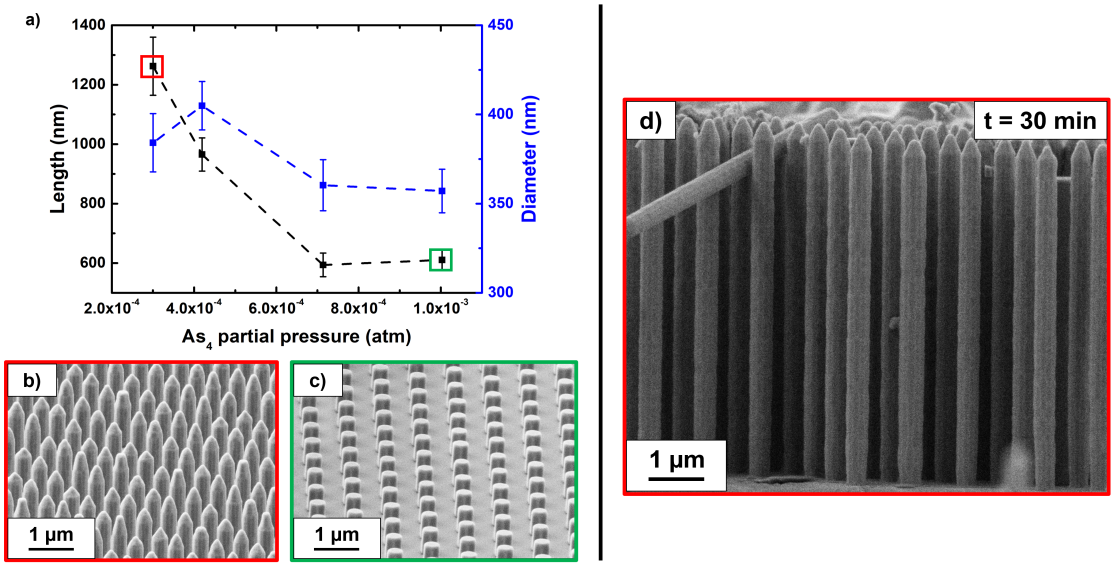


Figure IV.6 – *a) Longueur et diamètre moyens des NFs en fonction de $P_{As_4}$ à $P_{GaCl}$ fixée à* $1,6 \times 10^{-3}$ *atm. Images MEB des NFs à $P_{As_4}$ de : b)* $3,0 \times 10^{-4}$ *atm et c)* $1,0 \times 10^{-3}$ *atm. d) Image MEB des NFs après 30 min de croissance avec les conditions optimales (en rouge).*

Les conditions optimales ont été utilisées sur le substrat #IBM1 qui possède de faibles diamètres d'ouvertures et deux pitches différents : 1 et 2 µm. Les images MEB sont illustrées en Figure IV.7.

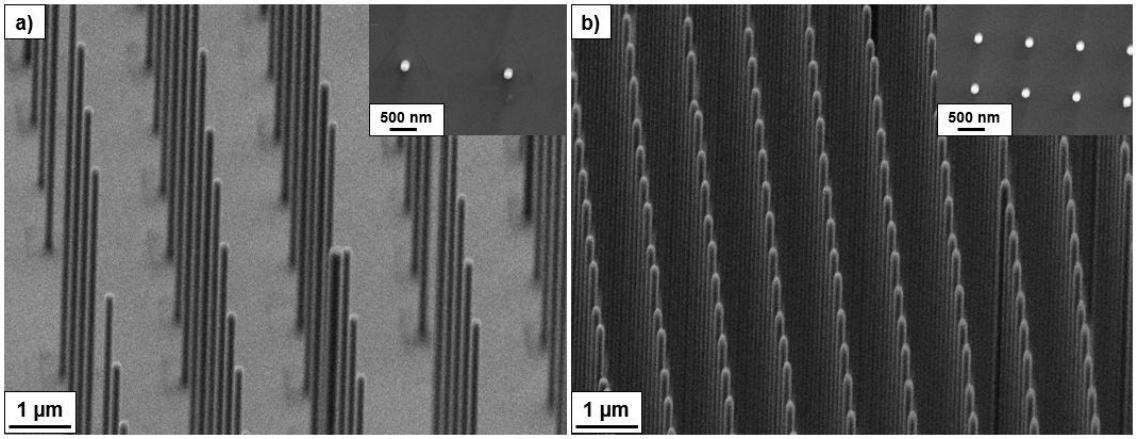


Figure IV.7 – *Images MEB des NFs de GaAs le substrat #IBM1 avec deux pitches différents : a) 2 µm et b) 1 µm. Le temps de croissance est de 10 min et la température est de 740 °C. Les pressions partielles sont de* $P_{GaCl} = 1,6 \times 10^{-3}$ *atm et* $P_{As_4} = 3,0 \times 10^{-4}$ *atm. Les inserts montrent des images MEB vue du dessus des NFs hexagonaux.*

Nous constatons une parfaite sélectivité qui s'explique, à nouveau, par l'adsorption négligeable des précurseurs chlorés sur le masque diélectrique quelle que soit sa nature chimique ($SiN_x$ ou $SiO_x$). Ces NFs sont remarquablement longs avec une longueur moyenne de 5,6 µm en seulement 10 min de croissance. Le diamètre moyen de 144 nm induit un rapport de forme remarquablement élevé de 39. Il s'avère que la vitesse de croissance axiale des NFs est 2,2 fois plus élevée que la vitesse de la couche 2D. En supposant que la croissance axiale des NFs soit contrôlée par le transport de Ga dans des conditions riches As, comme c'est le cas ici, trois flux différents de Ga doivent être considérés [137] : (i) le flux direct arrivant de la phase vapeur sur le sommet du NF, (ii) le flux de diffusion des adatomes de Ga depuis les parois latérales du NF vers le sommet, et (iii) le flux de diffusion des adatomes de Ga depuis la surface du masque vers le sommet du NF. Le flux direct (i) est identique pour les NFs et les couches car aucun transfert de masse notable n'a été observé pour la croissance de GaAs par HVPE [138]. Le flux de diffusion provenant du masque (iii) est négligeable en raison de la très faible adsorption des précurseurs chlorés sur le masque diélectrique. Par conséquent, la seule raison expliquant la différence de vitesse axiale entre les couches et les NFs est le flux de diffusion des adatomes de Ga à partir des parois latérales des NFs (ii). Ce résultat est d'une importance majeure car cette diffusion n'a jamais été prise en compte dans la croissance HVPE auparavant.

Désormais, nous sommes en mesure d'analyser et de comprendre expérimentalement les phénomènes régissant la croissance de NFs de GaAs sans catalyseur. Afin de mieux comprendre la croissance d'un point de vue cinétique, un modèle a été développé en collaboration avec le professeur Vladimir Dubrovskii qui nous a aidé à intégrer le flux (ii) qui est plus courant en MBE.

## IV.3.2 Modèle de croissance cinétique

Dans cette partie, nous allons brièvement discuter des principes physiques régissant le modèle, le détail des calculs peut être trouvé en section II.1.4 (page 59) de ce manuscrit. Le modèle cinétique est illustré en Figure IV.8.a. Si nous négligeons la croissance radiale, qui est usuellement faible en HVPE, et que nous prenons en compte la diffusion des adatomes de Ga sur les facettes latérales, la vitesse axiale peut s'écrire de la forme :

$$\frac{dL}{dt} = v_{2D}(1+\frac{2\lambda_3}{R})(1-\theta_5) \tag{IV.4}$$

avec $L$ la longueur du NF, $t$ le temps de croissance, $v_{2D}$ la vitesse de croissance 2D de la facette (111)B du sommet, $\lambda_3$ la longueur de diffusion effective des adatomes de Ga, $R$ le rayon moyen du NF et $\theta_5$ le taux de recouvrement de la facette (111)B par des trimères d'As.

En supposant que $\theta_5$ suit une loi de décroissance exponentielle (modèle de Kolmogorov [139]) du type $\theta_5 = 1 - e^{-(t-t_{inc})/\tau_5}$ avec $t_{inc}$ = 1 min le temps d'incubation pour la croissance de NFs au-dessus du masque (déduit des expériences) et $\tau_5$ le temps caractéristique pour former les As trimères sur la facette supérieure qui dépend du rapport III/V, nous obtenons :

$$L = v_{2D}(1 + \frac{2\lambda_3}{R})\tau_5[1 - e^{-(t-t_{inc})/\tau_5}] \tag{IV.5}$$

Par ailleurs, nous pouvons écrire :

$$\tau_5 = \tau_0 \frac{I_3}{I_5}(1 + \frac{2\lambda_3}{R}) \tag{IV.6}$$

en supposant que $\tau_5$ soit simplement proportionnel au rapport III/V atomique effectif au sommet des NFs $(I_3/I_5)(1+ 2\lambda_3/R)$ qui prend en compte la diffusion des adatomes de Ga en surface avec une constante $\tau_0$.

Grâce à ces équations et aux données expérimentales (voir le Tableau II.1 page 61), nous pouvons étudier l'évolution de la longueur des NFs en fonction du temps et du rapport III/V. La Figure IV.8.b montre les ajustements obtenus avec l'Équation (IV.5) pour les longueurs des NFs avec $I_3/I_5$ = 0,40 et 0,95. Les points expérimentaux sont remarquablement bien ajustés avec différents $\tau_5$ qui augmentent avec $I_3/I_5$. Ainsi, plus nous sommes sous atmosphère riche As, plus les trimères d'As se forment rapidement. La Figure IV.8.c montre le résultat principal du modèle. Sur cette dernière, il est comparé les longueurs des NFs avec les épaisseurs des couches 2D de GaAs(111)B obtenues avec les mêmes conditions de croissance. Les ajustements sont faits à l'aide de l'Équation (IV.5). Nous voyons que le modèle ajuste très bien les données, y compris la suppression de la croissance axiale par les trimères As à de faibles rapports III/V effectifs, et l'augmentation de la croissance axiale au-dessus du niveau 2D en raison de la diffusion des adatomes de Ga vers le sommet des NFs les plus fins. La longueur de diffusion effective des adatomes de Ga sur les parois des NFs, $\lambda_3$, était un paramètre d'ajustement pour lequel une valeur de 44 nm a été obtenue. Cette valeur est très proche de 45 nm, qui a été rapportée en MBE pour des températures de croissance de 770 °C à 810 °C [141]. En conclusion, les résultats expérimentaux et le modèle cinétique ont mis en lumière de nouveaux phénomènes apparaissant lors de la SAG de NFs de GaAs par HVPE. Les conditions de croissance optimales pour la croissance de longs NFs sont utilisées pour l'étude préliminaire du dopage des NFs de GaAs.

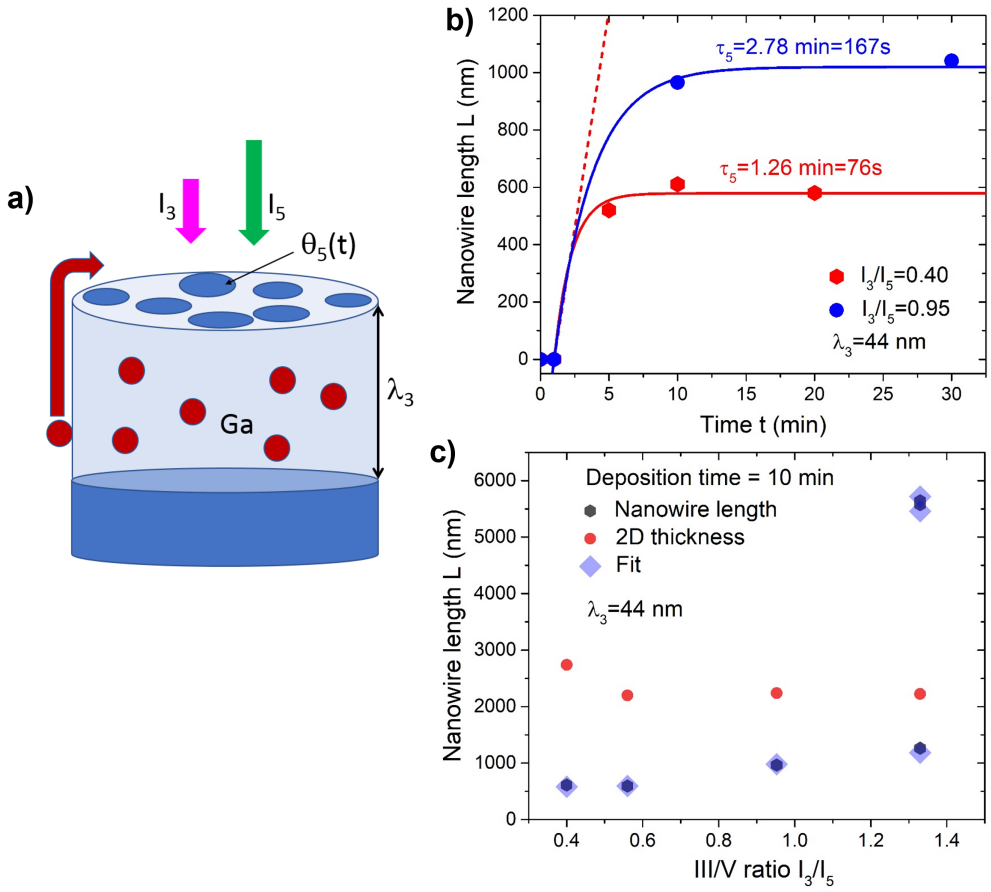


Figure IV.8 – *a) Illustration du modèle dans lequel la facette supérieure (111)B du NF est recouverte par des trimères d'As selon un taux de recouvrement $\theta_5(t)$ dépendant du temps et du rapport III/V. La longueur de diffusion effective des adatomes de Ga sur les parois latérales des NFs est égale à $\lambda_3$. b) Longueurs des NFs de GaAs en fonction du temps avec deux rapports $I_3/I_5$ différents de 0,40 et 0,95 correspondant à la suppression de la croissance par les trimères As au sommet des NFs (losanges), ajustées par le modèle avec les paramètres indiqués dans la légende (lignes) avec $\tau_5$ le temps caractéristique de formation des trimères sur la facette supérieure du NF. La ligne droite en pointillée correspond à l'épaisseur de couche sur un substrat nu de GaAs(111)B à $I_3/I_5 = 0{,}40$. c) Longueurs des NFs de GaAs après $t = 10$ min, ajustées par le modèle et comparées à l'épaisseur de la couche.*

## IV.3.3 Dopage des nanofils de GaAs

Comme explicité en section IV.2.4 (page 130), les dopants p sont les atomes Zn (précurseurs DEZ) et les dopants n sont les atomes Si (précurseurs $SiH_4$). Deux expériences ont été menées : un dopage p avec 30 sccm de DEZ et un dopage n avec 3 sccm de $SiH_4$. Les conditions de croissance

sont les mêmes que les conditions pour obtenir de longs NFs de GaAs. L'impact du dopage sur la morphologie est illustré en Figure IV.9. Tout d'abord, le premier constat que nous pouvons faire est que, quel que soit le dopant, une parfaite sélectivité et une très bonne homogénéité dans la morphologie des NFs sont observées. De plus, quel que soit le pitch, les NFs présentent une forme hexagonale définie par la famille des 6 facettes {-110}. Cependant, les dopants semblent avoir une influence sur la morphologie des NFs. En effet, les NFs dopés n sont beaucoup plus courts et plus épais que ceux non dopés. Cela pourrait s'expliquer par une modification de la structure de la surface due aux dopants Si [153]. Quoi qu'il en soit, pour le pitch de 1 µm, les NFs présentent une forme parfaitement hexagonale. Cependant, nous remarquons que pour le pitch de 2 µm, la forme des NFs est significativement différente et les NFs ne présentent plus une forme hexagonale. La seule chose qui change entre la Figure IV.9.c et la Figure IV.9.d étant le pitch, une hypothèse possible est que les atomes de Si issus du $SiH_4$ diffusent sur le masque contrairement aux précurseurs chlorés. Le cas échéant, cet effet serait prépondérant pour le pas de 2 µm. Concernant le dopage p, la longueur moyenne mesurée est inférieure à celle des NFs non dopés mais le diamètre moyen est sensiblement égal. Par ailleurs, aucune influence du pitch sur la morphologie des NFs n'est observée. Ainsi, contrairement au $SiH_4$ qui semble interagir avec le masque diélectrique $SiO_x$, il ne semble pas y avoir un effet significatif de la diffusion du DEZ dans ces conditions de croissance.

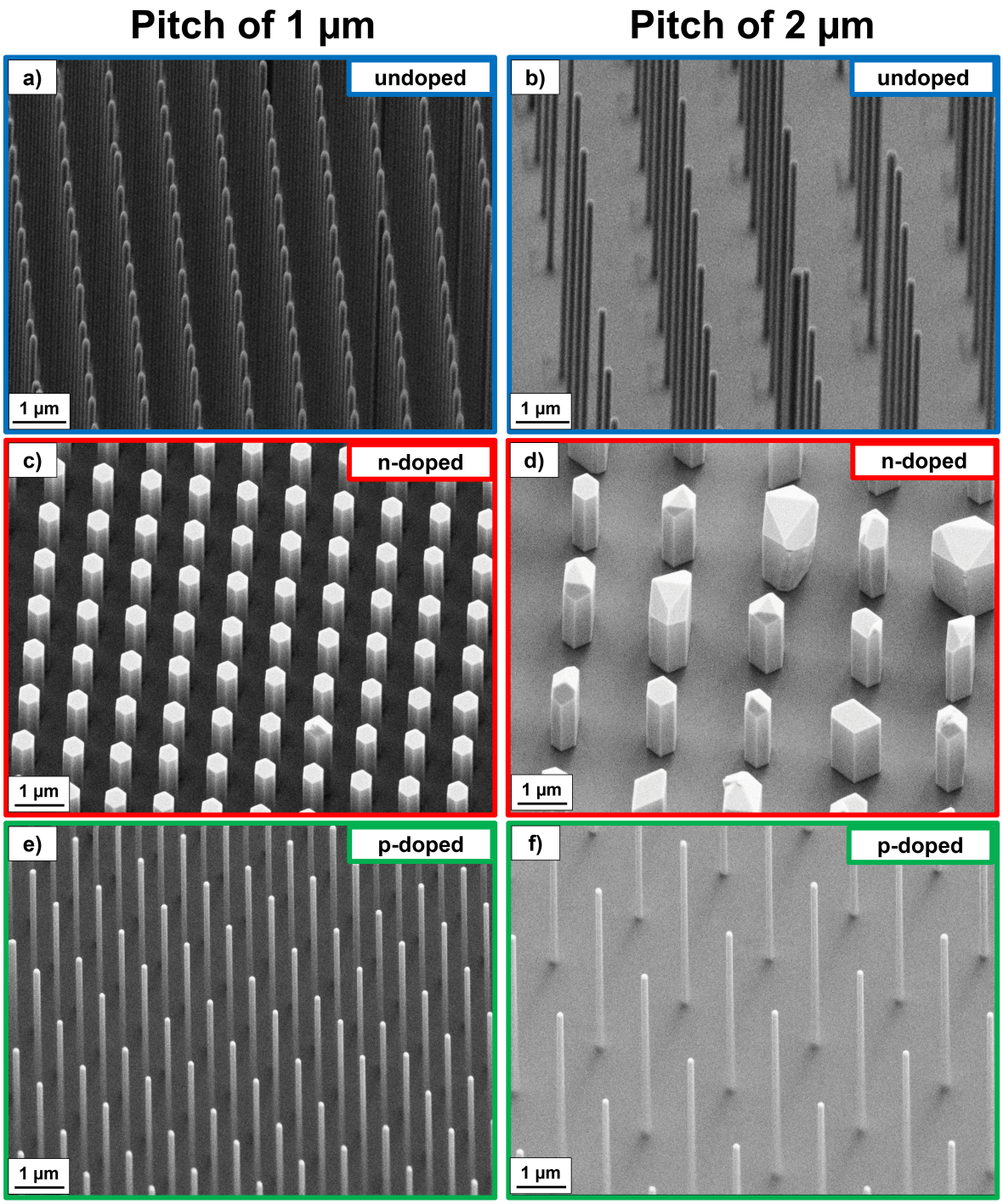


Figure IV.9 – *Images MEB à 20° : des NFs non dopés sur le substrat #IBM1 avec un pitch de a) 1 µm, b) 2 µm, des NFs dopés n avec un pitch de c) 1 µm, d) 2 µm et des NFs dopés p avec un pitch de e) 1 µm, f) 2 µm. Les flux des dopants n et p sont respectivement de : 3 sccm de $SiH_4$ et 30 sccm de DEZ.*

Les propriétés cristallographiques et optiques de ces NFs ont été analysées à McMaster University en collaboration avec Nebile Goktas, Amanda Thomas et Ethan Diak. Concernant les propriétés cristallographiques, il ne semble pas y avoir un effet du dopage sur la qualité du cristal (voir section II.2.4, page 70). Ici, nous allons essentiellement discuter des propriétés optiques de ces NFs. Des caractérisations par µ-photoluminescence (µ-PL) à une température de 7,5 K ont été menées sur des NFs individuels. Les spectres sont montrés en Figure IV.10.

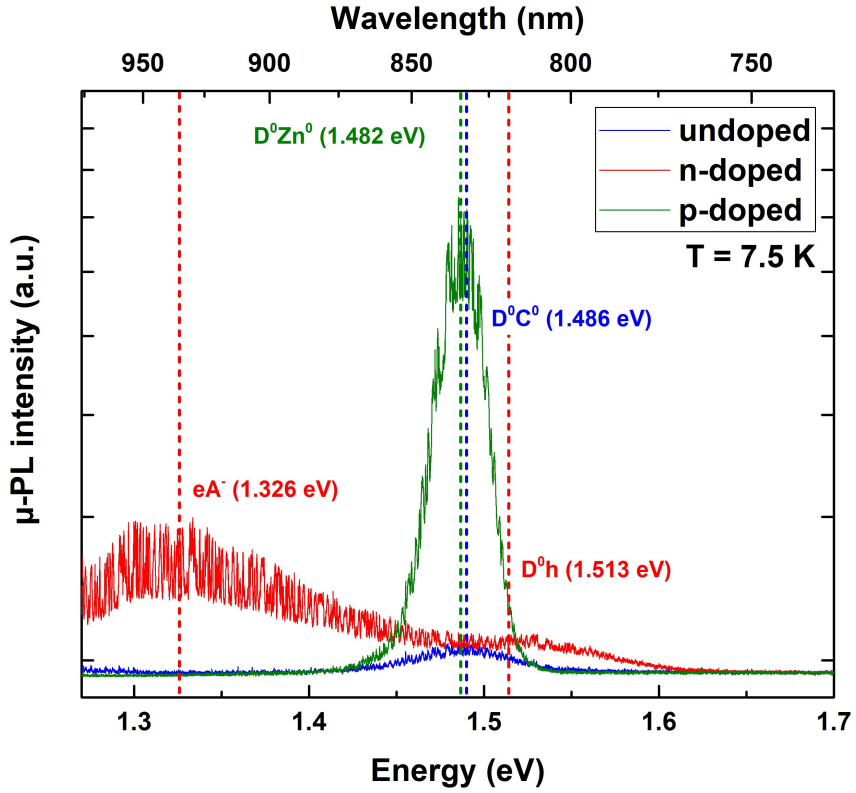


Figure IV.10 – *Spectre de µ-photoluminescence à 7,5 K d'un NF de GaAs non dopé (bleu), dopé n (rouge) et dopé p (vert). L'axe y est en échelle logarithmique.*

Tout d'abord, nous remarquons que l'intensité de µ-PL dépend du dopage. Le signal du NF non dopé a une intensité inférieure à celle des NFs dopés, ce qui est cohérent avec un faible dopage résiduel. De plus, l'échantillon non dopé présente un pic qui correspond à une transition donneur-accepteur liée au carbone ($D^0C^0$) à 1,486 eV. Ainsi, les NFs non dopés semblent être non intentionnellement dopés p en raison du carbone résiduel dans le réacteur. Ce carbone résiduel provient probablement d'impuretés et du fait que le DEZ contient du carbone ($(C_2H_5)_2Zn$). Récemment, cela a également été observé dans l'équipe sur des NFs non dopés de GaAs [74]. Ce dopage p non intentionnel tend à limiter l'incorporation des dopants n. En effet, lors du dopage n des NFs, un effet de compensation a probablement lieu avant d'atteindre une certaine quantité de dopants n. Concer-

nant le dopage p, un léger redshift est observé. Le pic observé à 1,482 eV tend à correspondre à une transition donneur-accepteur liée au Zn ($D^0Zn^0$). À propos du dopage n, un pic de haute énergie apparaît vers 1,513 eV correspondant à une transition $D^0h$. Un pic de faible énergie à 1,326 eV apparaît uniquement pour le dopage n. Ainsi, nous avons tendance à penser que ce pic est lié à un effet des dopants Si. Dans la littérature [152], ce pic semble attribué à une transition électron libre-accepteur ionisé $eA^-$, impliquant un niveau profond lié aux défauts d'antisites Ga. En conclusion, ces analyses montrent qu'il y a bien une incorporation efficace des dopants, ce qui a un impact sur les propriétés optiques des NFs. Ces résultats préliminaires sont encourageants pour la réalisation d'une jonction p-i-n, qui est l'objet de la section suivante.

### IV.3.4 Vers des jonctions p-i-n par HVPE ?

Les conditions de croissance utilisées pour le test d'une croissance de jonction p-i-n dans des NFs de GaAs sont $P_{GaCl} = 1,6 \times 10^{-3}$ atm et $P_{As_4} = 3,0 \times 10^{-4}$ atm, T = 740 °C, le cœur p a été épitaxié pendant 10 min de croissance avec 30 sccm de *DEZ*, la coquille i pendant 30 secondes sans dopants et la coquille n pendant 2 min 30 sec avec 3 sccm de $SiH_4$. Les images MEB des NFs obtenus sont montrées en Figure IV.11

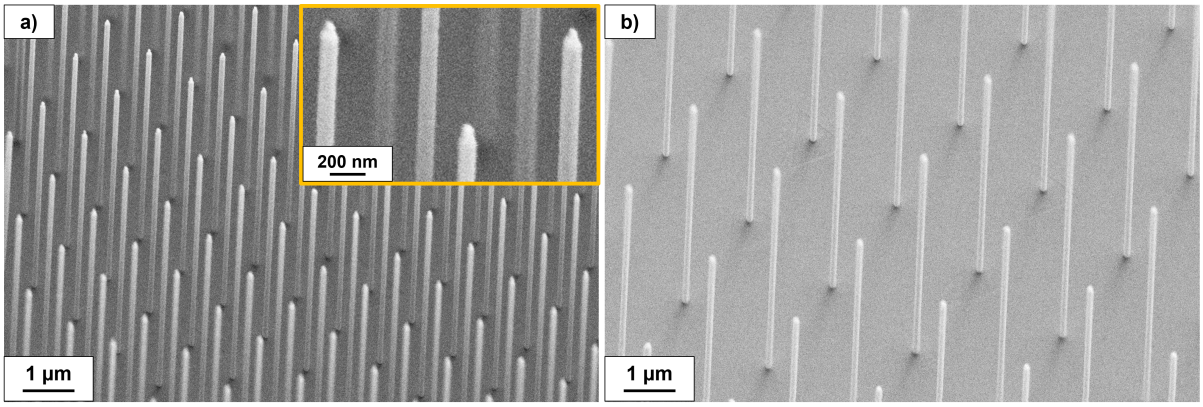


Figure IV.11 – *Images MEB à 20° des jonctions p-i-n dans des NFs épitaxiés sur le substrat #IBM1 avec a) un pitch de 1 µm et b) un pitch de 2 µm. L'encadré en a) montre une vue rapprochée du sommet des NFs.*

La longueur et le diamètre moyens des NFs sont L = 3,82 µm et D = 110 nm pour le pitch de 1 µm et L = 3,90 µm et D = 130 nm pour le pitch de 2 µm. Ainsi, aucune différence significative des dimensions des NFs n'est observée en fonction du pitch. Concernant la morphologie, le sommet des NFs présente une forme de « bougie » d'une hauteur d'environ 80 nm qui ne correspond pas tout

à fait à la hauteur estimée de la coquille n. Cependant, il pourrait toujours s'agir de la zone dopée n car la vitesse de croissance axiale pourrait être fortement impactée et différente de la vitesse de croissance axiale des NFs purement dopés n. De plus, nous avons vu que les morphologies des NFs dopés p et des NFs non dopés sont proches, cela renforce donc l'idée que cette forme de « bougie » pourrait être liée à la zone dopée n. Nous pouvons donc s'attendre à ce qu'il s'agisse d'une structure axiale mais l'hypothèse d'une structure cœur-coquille ne peut être exclue, car la vitesse radiale n'est pas maîtrisée.

Par la suite, nous avons décidé de réaliser un dispositif photovoltaïque à partir de ces réseaux de NFs. Cette procédure a été réalisée à McMaster University en collaboration avec la doctorante Amanda Thomas. Malheureusement, les efficacités obtenues sont extrêmement faibles (de l'ordre de $10^{-5}$ %). Néanmoins, ce travail préliminaire a été fondamental car il met en lumière plusieurs axes d'améliorations concernant la croissance par HVPE et le processus de fabrication du dispositif. Pour avoir plus de détails sur ces résultats, le lecteur est invité à consulter la section II.3.3 (page 80).

En perspective, il a été réalisé un deuxième essai de jonction p-i-n avec un débit de dopant n très élevé (10 sccm de $SiH_4$) et un substrat différent qui présente de plus grandes ouvertures (#Bath). Une différence majeure comparée au 1$^{er}$ test de jonction p-i-n est que $P_{GaCl}$ est augmentée entre chaque étape de croissance pour favoriser la croissance latérale. Entre chaque étape, une interruption de croissance de 2 min sous atmosphère As est réalisée pour éviter la désorption de l'As. Les conditions de croissance sont $P_{As_4} = 3,0 \times 10^{-4}$ atm, T = 740 °C, le coeur p a été épitaxié pendant 10 min avec $P_{GaCl} = 1,6 \times 10^{-3}$ atm et 30 sccm de DEZ, la coquille i pendant 30 sec avec $P_{GaCl} = 3,2 \times 10^{-3}$ atm et la coquille n pendant 30 sec avec $P_{GaCl} = 4,8 \times 10^{-3}$ atm et 10 sccm de $SiH_4$ qui est le maximum admissible par le débitmètre. Les images MEB de cette croissance sont illustrées en Figure IV.12. Une image avec le détecteur INLENS du MEB a été réalisée pour obtenir un meilleur contraste au sommet des NFs.

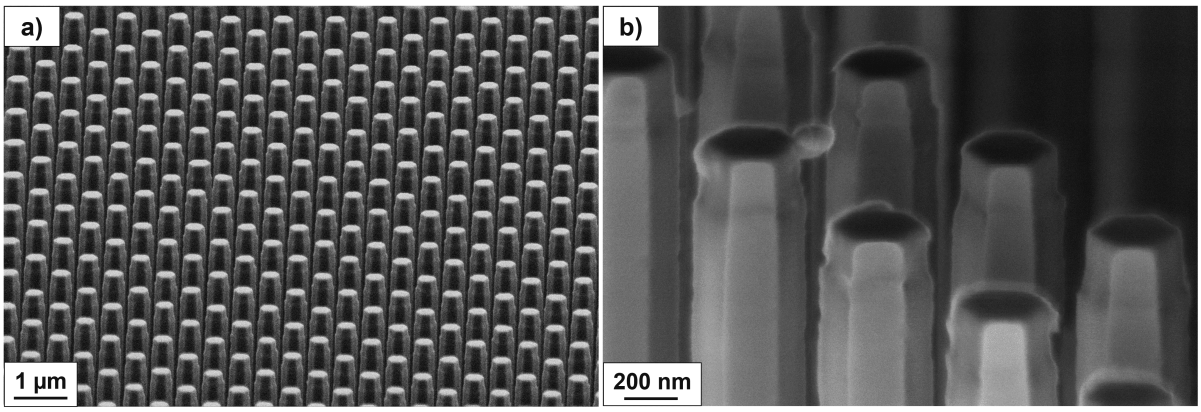


Figure IV.12 – *Images MEB à 20° des jonctions p-i-n dans des NFs épitaxiés sur le substrat #Bath avec a) un champ large et b) un champ proche avec le détecteur INLENS du MEB.*

Tout d'abord, nous constatons que malgré plusieurs interruptions de croissance et le recours à un dopage n élevé, une bonne sélectivité est conservée. Les NFs sont homogènes et présentent une forme hexagonale. La longueur moyenne des NFs est de 3,3 µm et les NFs présentent un rétrécissement du diamètre au sommet de 430 nm à 350 nm. La longueur de cette zone est d'environ 200 nm. À partir des images MEB, il n'est pas possible de déterminer exactement la nature de cette zone de rétrécissement. mais sur la base de nos résultats précédents, plusieurs hypothèses peuvent être émises. Premièrement, les NFs non dopés et les NFs dopés p sont très proches morphologiquement. Il n'y a aucune raison pour qu'un rétrécissement soudain se produise sauf à cause du dopage n. Le flux de $SiH_4$ étant très fort (10 sccm) il est envisageable que la vitesse de croissance radiale soit fortement impactée. Il semble donc concevable que cette zone de rétrécissement puisse être la zone dopée n. Enfin, comme la croissance radiale n'est pas totalement contrôlée, il est possible qu'une couche dopée n ait été déposée sur les parois latérales des NFs et qu'il y ait des structures cœur-coquille. Afin de déterminer la nature de cette zone de rétrécissement, et de savoir si nous sommes bien en présence d'une jonction p-i-n, des mesures de cathodoluminescence (CL) ont été réalisées par Gwénolé Jacopin à l'Institut Néel de Grenoble. Des mesures ont été effectuées sur un seul NF à une température de 5 K avec une tension d'accélération de 2 keV. Les résultats sont illustrés en Figure IV.13.

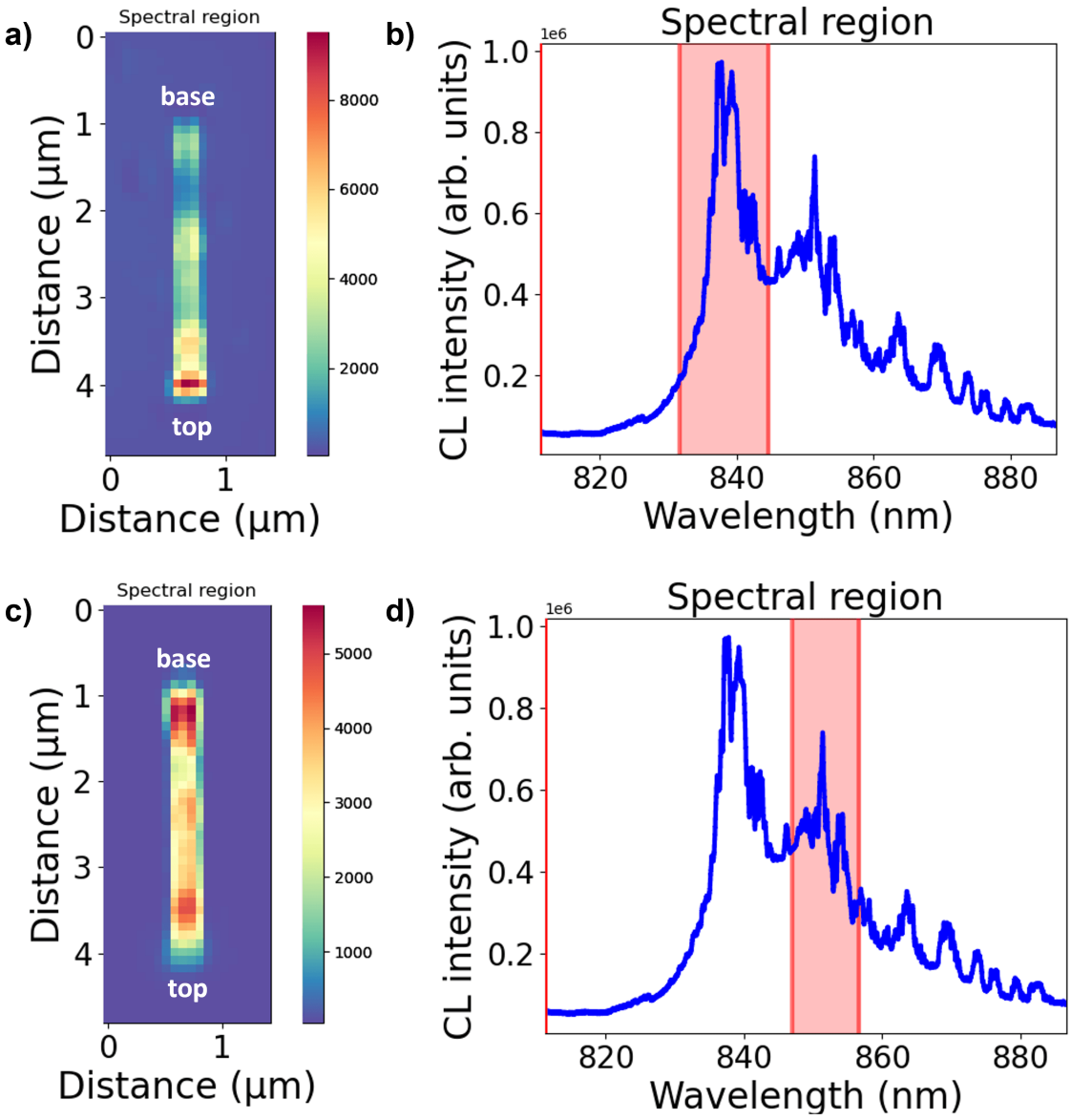


Figure IV.13 – *Spectres de cathodoluminescence à 5 K d'un NF unique avec leurs cartographies d'intensités respectives pour deux plages de longueurs d'onde différentes : a-b) 840 nm et c-d) 855 nm. La largeur de la plage de longueurs d'onde représentée en rouge dans les spectres est de 10 nm.*

Nous constatons clairement deux émissions principales : une à 840 nm (1,48 eV) et une à 855 nm (1,45 eV). Tout d'abord, concernant l'émission à 840 nm, si nous regardons la cartographie de la Figure IV.13.a, le signal provient essentiellement du sommet du NF. Par conséquent, si nous nous référons aux conditions de croissance, il est raisonnable de supposer que ce signal provienne de la zone dopée n. L'émission à 855 nm est plus répartie dans tout le NF excepté au sommet. Ainsi, il est raisonnable d'attribuer cette émission à la zone dopée p. Ces observations tendent à supposer qu'il existe deux contributions distinctes dans le NF : un signal correspondant à la zone dopée n venant du

sommet du NF et un signal correspondant à la zone dopée p plus réparti dans le NF. Cependant, la CL n'est pas une méthode de mesure directe du dopage, nous ne pouvons pas conclure sur ce point. Il est à noter que les pics multiples observés au-delà de 860 nm pourraient correspondre à un signal utile mais ce signal est modulé par le réseau du spectromètre. Ce signal n'est donc pas utilisable en l'état. Il est difficile de conclure sur la nature de ces deux domaines. Par exemple, il pourrait s'agir de deux zones dopées p (ou de deux zones dopées n) mais avec un taux de dopage significativement différent. De plus, nous ne pouvons pas comparer ces mesures avec les résultats de µ-PL pour les raisons suivantes : 1) les substrats sont différents (#Bath n'est pas dopé alors que #IBM1 est dopé p), 2) les flux des dopants sont différents (10 sccm de $SiH_4$ contre 3 sccm), 3) la température du bain DEZ est significativement différente ici ($\theta_{DEZ} = -22$ °C) comparée à celle de la croissance de NFs dopés p caractérisés par µ-PL ($\theta_{DEZ} = -27$ °C), cela peut ainsi affecter le taux de dopage p. De plus, les NFs présentent probablement du polytypisme ZB/WZ, ce qui impacte autant les spectres CL que les spectres PL comme démontré par Spirkoska et al. [136]. Les auteurs ont montré qu'à une température de 4,2 K, les NFs purs ZB présentent un pic principal à 1,52 eV, tandis que les NFs purs ZB avec 30% $\pm$ 10% de WZ présentent plusieurs pics allant de 1,52 eV à 1,46 eV. Ainsi, le polytypisme impacte grandement le spectre du CL ce qui rend son exploitation difficile. Cependant, les mesures de CL semblent confirmer nos hypothèses basées sur les images MEB, à savoir que les NFs présentent deux zones distinctes et peut-être des jonctions p-i-n axiales. Ces résultats préliminaires sont donc prometteurs pour la réalisation des futures jonctions p-i-n par HVPE.

## IV.4 Résumé du chapitre III : SAG-HVPE de nanofils d'InAs et d'$In_xGa_{1-x}As$

Dans cette section, les principaux résultats du chapitre III qui porte sur la SAG de NFs d'InAs et d'InGaAs par HVPE sont résumés. Tout d'abord, nous allons brièvement présenter une étude de la croissance des NFs d'InAs sur substrat patterné de Si(111) en fonction de la pression partielle d'$As_4$. Un comportement similaire à celui des NFs de GaAs est observé à forte pression partielle d'$As_4$. Ensuite, la faisabilité de la croissance de NFs d'InGaAs sur substrat de GaAs(111)B est démontrée. Cela permet, dans un second temps, de développer la croissance de NFs d'InGaAs sur substrat de Si(111) avec des compositions variées. Enfin, nous allons discuter d'un modèle qui prend en compte les considérations thermodynamiques et cinétiques afin de relier la teneur en indium dans la phase vapeur $z$ avec la fraction d'InAs dans le solide $x$.

### IV.4.1 Croissance sélective de longs nanofils d'InAs

Dans cette section, nous allons étudier la croissance de NFs d'InAs en fonction de $P_{As4}$ qui est la pression partielle d'$As_4$. La croissance a été réalisée sur le substrat #AC121A (voir section I.4.2.3, page 31). La température de croissance est de 640 °C, le temps de croissance est 15 min et $P_{InCl}$ a été fixée à $4,8 \times 10^{-4}$ atm. Les résultats sont illustrés en Figure IV.14. Tout d'abord, nous constatons clairement l'impact de $P_{As4}$ sur la longueur moyenne des NFs, la longueur passant de 15 µm à moins de 2 µm. La même observation a été faite dans la section IV.3.1 concernant la croissance des NFs de GaAs. Pour les NFs d'InAs se développant selon la direction [111]B, une $P_{As4}$ trop élevée induit la formation de trimères d'As sur la surface supérieure. Ce phénomène a également été observé pour la croissance de NFs d'InAs par MOVPE [66, 68]. Concernant l'évolution du diamètre des NFs, plusieurs points peuvent être soulignés. Si nous excluons le point de données rouge de la Figure IV.14.a ($P_{As_4} = 7,2 \times 10^{-4}$ atm), nous pouvons supposer que le diamètre varie peu. Cela reste cohérent avec les faibles vitesses de croissance radiales précédemment observées sur les NFs III-As par HVPE [74, 157]. La déviation du point de données rouge pourrait s'expliquer par son rendement qui est très faible par rapport aux autres expériences. Comme nous pouvons le voir sur les images MEB, le rendement varie considérablement entre les expériences et cela a pu avoir un impact significatif sur l'apport local de matière entre les expériences. Ceci pourrait être lié à la qualité du masque diélectrique et à un résidu d'oxyde dans les trous. De plus, cette variation du rendement peut également apparaître en raison de la qualité aléatoire du morceau de substrat clivé.

Le principal résultat à souligner est que nous avons réussi à obtenir de longs NFs d'InAs par HVPE (> 10 µm), ceci constituant un des objectifs principaux de cette thèse. Néanmoins, en raison d'un manque de substrats patternés de bonne qualité avec différents motifs, nous n'avons pas pu réaliser les expériences adéquates pour la détection multispectrale. Ces expériences seront réalisées dans le cadre d'une future collaboration avec McMaster University où il est possible de caractériser les échantillons par spectroscopie infrarouge à transformée de Fourier (FTIR).

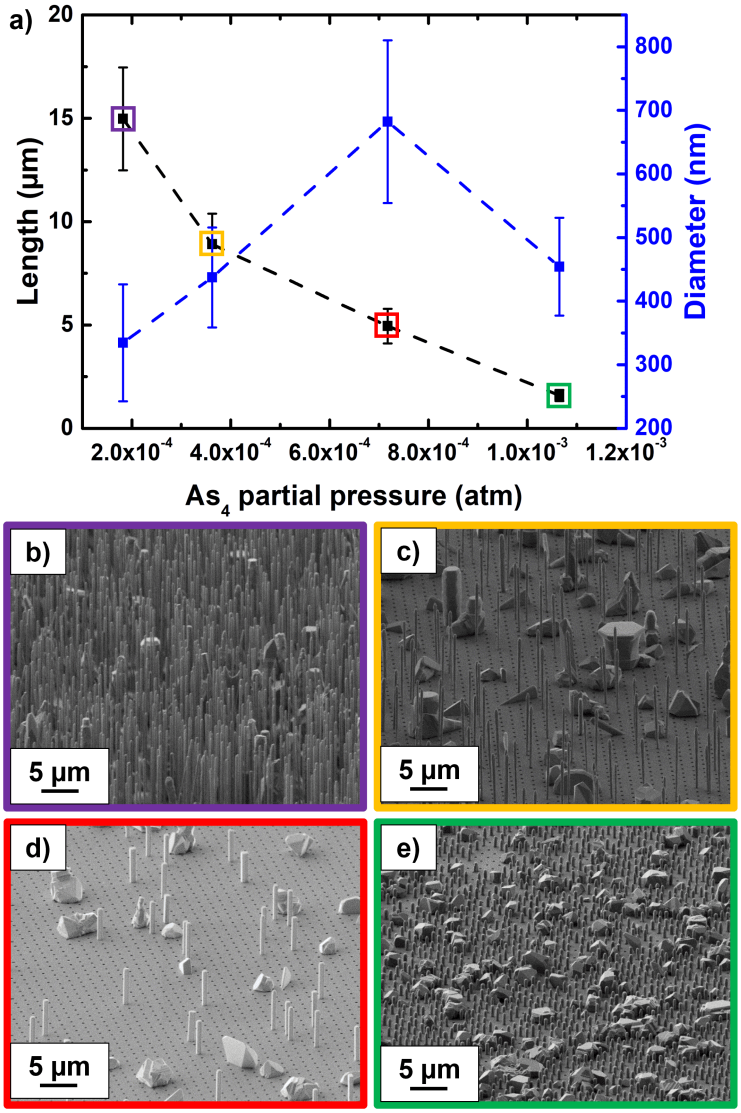


Figure IV.14 – *a) Longueur et diamètre moyens des NFs en fonction de $P_{As_4}$ à $P_{InCl} = 4,8 \times 10^{-3}$ atm fixée. Les lignes servent de guide visuel. b-e) Images MEB à 20° correspondantes de NFs épitaxiés sur le substrat #AC121A.*

Pour conclure, nous avons démontré avec succès la croissance de longs NFs de GaAs et d'InAs par HVPE. Un large éventail de conditions de croissance avec différents motifs a été étudié. Ainsi, nous avons développé une bonne maîtrise de la croissance des deux binaires par HVPE. L'ensemble de ces résultats permet d'envisager la croissance des NFs d'InGaAs par HVPE pour laquelle le contrôle de la composition représente un défi majeur. Ceci constitue le sujet de la section suivante.

## IV.4.2 Croissance sélective de nanofils d'InGaAs

Cette section est divisée en deux parties. Tout d'abord, nous présentons la croissance de NFs d'InGaAs sur substrat patterné de GaAs(111)B. En effet, comme la nucléation sur silicium reste un défi majeur, il est essentiel de démontrer au préalable la faisabilité de la croissance de NFs d'InGaAs sur substrat de GaAs. Nous discuterons de la composition et de la morphologie de ces NFs. Ensuite, nous démontrons la croissance de NFs d'InGaAs sur substrat patterné de Si(111) avec différentes fractions d'InAs dans le solide $x$. Cette étude est complétée par un modèle de croissance dédié.

### IV.4.2.1 Démonstration sur substrat de GaAs(111)B

Pour l'InGaAs, la croissance commence quand les vannes pneumatiques de GaCl et d'InCl sont ouvertes simultanément. Ici, le substrat est #IBM2. La température est de 715 °C, le temps de croissance est de 15 min et les pressions partielles valent respectivement $P_{As4} = 7,5 \times 10^{-4}$ atm, $P_{GaCl} = 6,6 \times 10^{-4}$ atm et $P_{InCl} = 1,0 \times 10^{-2}$ atm. Cela induit une teneur en indium dans la phase vapeur $z = P_{InCl}/(P_{InCl} + P_{GaCl})$ de 0,94. La fraction d'InAs dans le solide $In_xGa_{1-x}As$ est notée $x$.

La Figure IV.15 montre des images MEB des NFs d'InGaAs et trois profils EDX (energy-dispersive X-ray spectroscopy) le long de NFs uniques. Les images MEB en Figure IV.15.a révèlent des NFs verticaux en forme de « crayon » selon la direction [111]B avec un diamètre de 370 nm au sommet des NFs et une longueur de 8,7 µm, correspondant à une vitesse de croissance axiale remarquable de plus de 50 µm/h. Cette valeur est notable pour la SAG par rapport aux vitesses inférieures à 10 µm/h observées en MOVPE [82, 158] et en MBE [84, 159]. La morphologie des NFs est en forme de « crayon » car la vitesse de croissance intrinsèque de la facette (111)B est nettement supérieure à celle des facettes latérales supposées être {-110}. La vitesse de croissance des facettes latérales {-110}, constituées de rangées de Ga-As, est généralement très faible dans une large gamme de conditions HVPE en raison de la faible adsorption de GaCl sur la surface des facettes {-110} [117]. Cependant, il ne peut être exclu que cette morphologie puisse également être interprétée par la formation de gouttelettes d'élément III au sommet des NFs d'InGaAs qui se rétrécissent en fin de croissance.

Afin d'estimer l'homogénéité de composition au sein des NFs, des mesures EDX ont été réalisées par Catherine Bougerol à l'Institut Néel dans le cadre du projet ENNORA (projet de recherche financé par la région AURA). La Figure IV.15.b montre les profils EDX le long de NFs uniques. Les résultats

EDX montrent une fraction d'InAs dans le solide de $x = 0,84$, signifiant que ces NFs sont des NFs d'InGaAs riches indium. La différence entre la teneur en In dans la phase vapeur ($z = 0,93$) et la composition en In dans le solide ($x = 0,84$) est un phénomène bien connu pour la croissance des NFs ternaires. Ceci s'explique principalement par la différence de transport des atomes de Ga et d'In dans les NFs, en raison des longueurs de diffusion différentes sur les parois latérales des NFs et des différents taux de désorption [118]. Les concentrations de Ga et d'In sont pratiquement homogènes sur toute la longueur des trois NFs analysés.

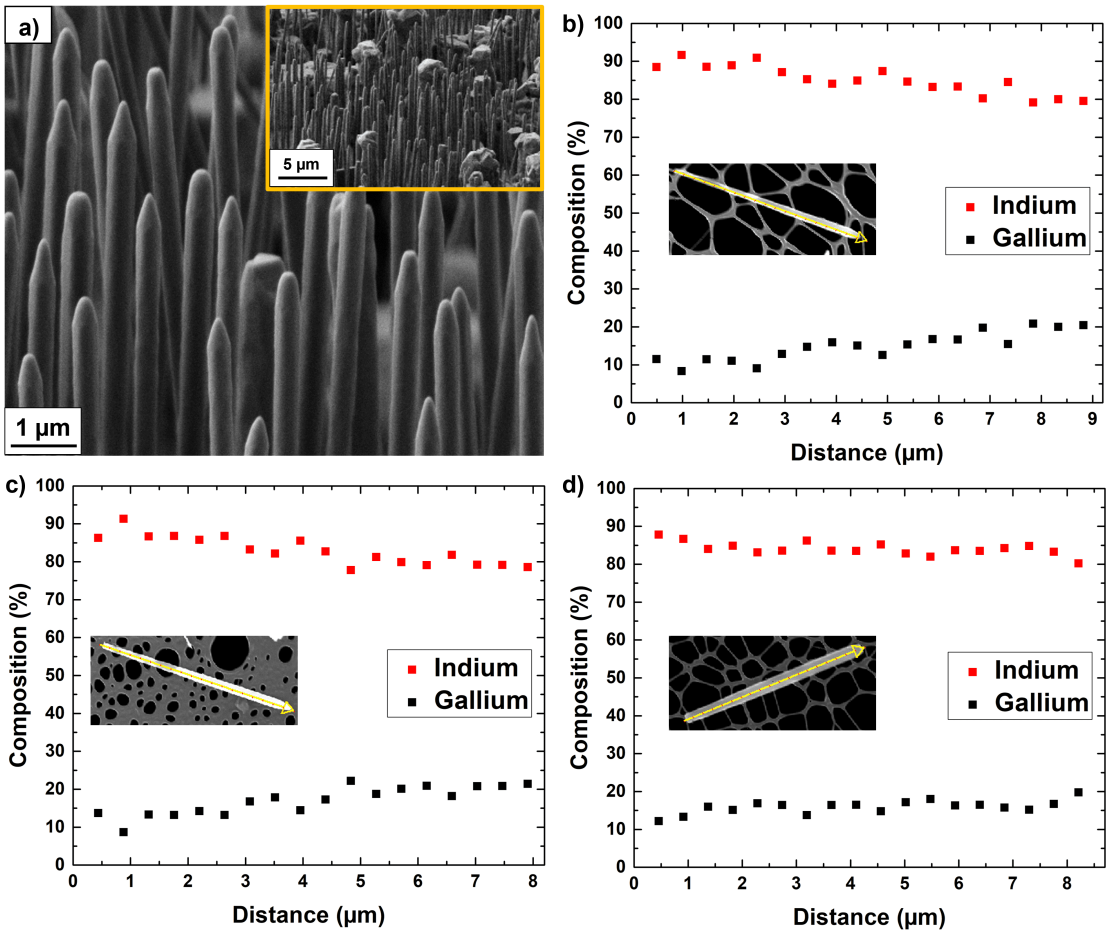


Figure IV.15 – *a) Image MEB à 20° des NFs d'InGaAs avec un insert montrant une image MEB grand champ. Profils EDX le long de la direction [111]B de NFs d'InGaAs uniques montrant une fraction d'InAs moyenne de b)* $x = 0.85$*, c)* $x = 0.83$ *and d)* $x = 0.84$*. Les points s'étendent de la base au sommet du NF.*

Les propriétés cristallographiques et optiques de ces NFs ont également été analysées. Pour plus de détails, le lecteur est invité à consulter la section III.2.1 (page 94). En conclusion, nous avons démontré la SAG de NFs d'InGaAs sur un substrat patterné de GaAs(111)B avec une bonne sélectivité par HVPE. Une vitesse de croissance élevée a été observée, supérieure à 50 µm/h, conduisant à des

NFs à haut rapport de forme. Ainsi, cette étude montre la capacité de la HVPE à fournir des réseaux de NFs d'InGaAs homogènes avec des rapports de forme élevés. Maintenant que nous avons démontré que la croissance de NFs d'InGaAs est réalisable par HVPE sur substrat de GaAs(111)B, nous allons l'étudier sur substrat de Si(111).

### IV.4.2.2 Croissance sur substrat de Si(111)

La SAG de NFs d'InGaAs sur substrat patterné de Si(111) a été réalisée sur le substrat #AC121A. Le temps de croissance est de 15 min pour tous les échantillons et la température de croissance était de 690 °C pour la plupart des échantillons. Cependant, certains échantillons ont été réalisés à 670 °C, 710 °C et 730 °C.

La Figure IV.16.a montre un schéma de la SAG de NFs d'InGaAs sur un substrat patterné de $SiN_x/SiO_x$/Si(111) qui correspond au substrat #AC121A. Nous avons étudié l'effet de $P_{GaCl}$ sur la morphologie et la composition des NFs. Dans ces expériences, la température de croissance T a été fixée à 690 °C et les pressions partielles $P_{As4}$ et $P_{InCl}$ ont été respectivement fixées à $3,6 \times 10^{-4}$ atm et $4,8 \times 10^{-3}$ atm. La composition des NFs d'InGaAs a été étudiée par EDX dans un MEB et la Figure IV.16.b-d montre les images MEB des NFs d'InGaAs obtenus sous différentes $P_{GaCl}$ avec les fractions d'InAs respectives $x$.

Comme attendu, la croissance est hautement sélective en raison de la faible adsorption des précurseurs chlorés sur la surface du masque diélectrique. Cependant, certains trous non remplis sont observés, ils sont clairement visibles sur la Figure IV.16.d. Cela est probablement dû à un résidu d'oxyde dans les trous empêchant la nucléation des NFs. La fraction d'InAs dans les NFs d'InGaAs, $x$, diminue progressivement de $x = 0,68$ à $x = 0,34$ avec l'augmentation de $P_{GaCl}$ à $P_{InCl}$ constante. Ceci s'explique par la fraction réduite d'In dans la vapeur et donc un taux d'incorporation plus faible des atomes d'In par rapport aux atomes de Ga [78, 161, 163, 164]. Il est intéressant de noter que la longueur des NFs diminue fortement avec l'augmentation de $P_{GaCl}$, de près de 8 µm à $P_{GaCl} = 3,2 \times 10^{-4}$ atm à moins de 1 µm à $P_{GaCl} = 1,3 \times 10^{-3}$ atm. Par conséquent, plus nous nous rapprochons de la composition du binaire InAs, plus les NFs sont longs. La température de croissance de 690 °C, très faible pour le dépôt de GaAs par HVPE, pourrait expliquer la courte longueur des NFs riches gallium en raison de la faible efficacité de décomposition de GaCl [74, 165]. De plus, cette diminution de longueur peut également être renforcée par les adatomes In qui diffusent moins sur les facettes des NFs en présence d'adatomes de Ga. Par ailleurs, la formation de gouttelettes In au-dessus des NFs d'InGaAs riches indium et la transition correspondante du mode de croissance

VS au mode de croissance VLS ne peuvent être exclues. Nous pouvons également voir que les NFs riches indium présentent une forme de « crayon », tandis que les NFs riches gallium ont des sommets plats. Étant donné que les adatomes diffusent davantage vers les sommets des NFs à faible $P_{GaCl}$, la vitesse de croissance intrinsèque de la facette (111)B est supérieure à celle des facettes latérales, ce qui explique la forme de « crayon » observée. À $P_{GaCl}$ élevée, la diffusivité de l'In est réduite et la forme de « crayon » disparaît.

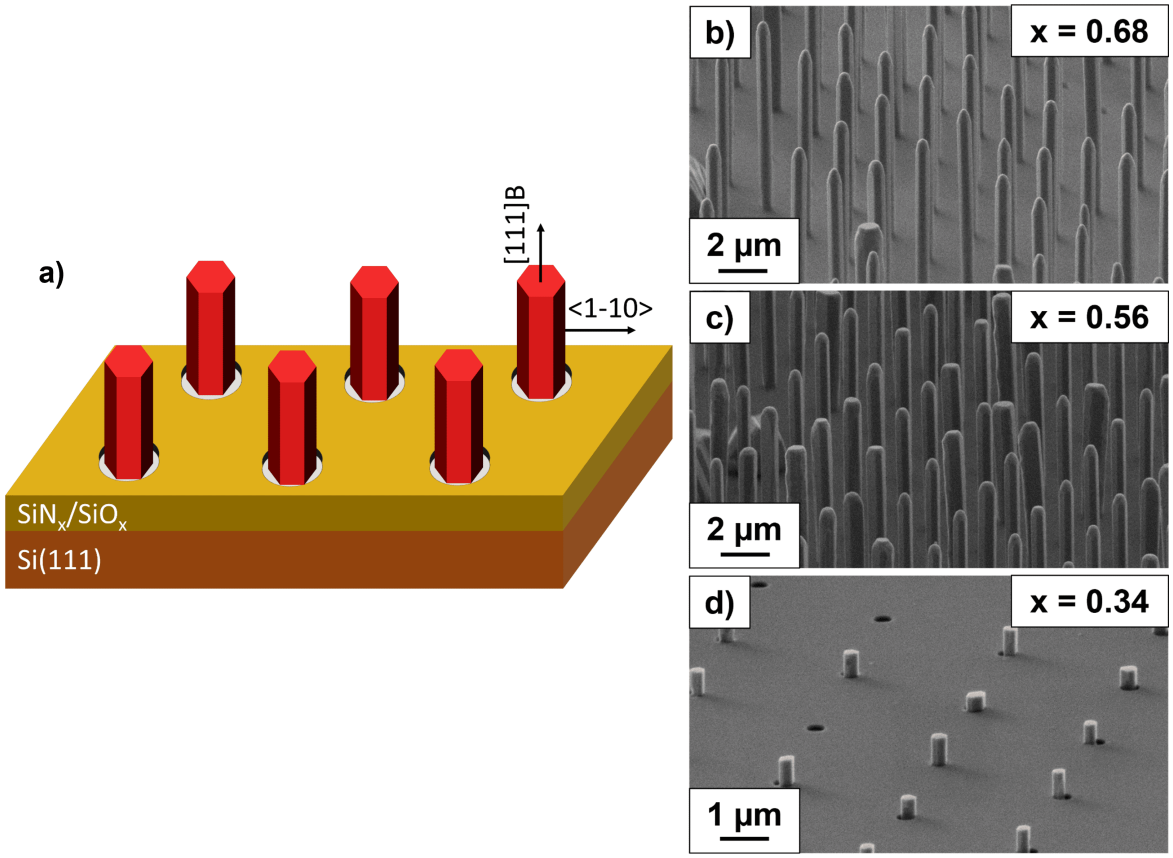


Figure IV.16 – *a) Schéma de la SAG de NFs d'InGaAs sur un substrat patterné $SiN_x$ / $SiO_x$ / Si(111). Images MEB à 20° des NFs d'InGaAs épitaxiés sur le substrat #AC121A avec différents $P_{GaCl}$ : b)* $3,2 \times 10^{-4}$ *atm, c)* $4,8 \times 10^{-4}$ *atm, et d)* $1,3 \times 10^{-3}$ *atm. Les fractions moyennes d'InAs x mesurées par EDX dans un MEB sont de b) 0,68, c) 0,56 et d) 0,34.*

La distribution de composition de ces NFs a été analysée par EDX dans un STEM (scanning transmission electron microscope). Ces résultats montrent une très bonne homogénéité de composition tout au long des NFs avec aucune coquille riche indium observée. Le lecteur est invité à consulter la section III.2.2.2 (page 100) pour plus de détails. Enfin, un modèle de croissance basé sur la thermodynamique et la cinétique a été développé. Le but de ce modèle est d'étudier la distribution vapeur-solide, c'est-à-dire la relation qui existe entre la teneur en indium dans la phase vapeur

$z$ et la fraction d'InAs dans le solide $x$. Celui-ci pourrait nous aider à déterminer quelles conditions de croissance viser afin d'obtenir une composition bien spécifique dans les NFs. Ce modèle a été développé conjointement avec le professeur Vladimir Dubrovskii. Le Tableau III.1 (page 103) résume les conditions de croissance et les compositions des NFs d'InGaAs mesurées par différentes techniques. Il est montré dans la section III.2.3 (page 102) que la distribution vapeur-solide suit la relation de Langmuir-McLean qui est purement cinétique et qui s'exprime telle que :

$$z = \frac{x}{c + (1-c)x} \tag{IV.7}$$

avec $c$ un paramètre cinétique qui dépend de la longueur de diffusion des atomes d'In et de Ga.

La distribution vapeur-solide $x(z)$ reliant la fraction d'InAs $x$ dans les NFs d'$In_xGa_{1-x}As$ avec la teneur en In dans la vapeur $z$ pour tous les points de données du Tableau III.1 est illustrée en Figure IV.17. La ligne en pointillée montre la distribution vapeur-solide à l'équilibre pour le matériau InGaAs à 690 °C. Cette distribution ne varie pas de manière significative pour le procédé HVPE dans la plage de températures étudiée de 670 °C à 730 °C. Tout d'abord, nous constatons que les points de données sont loin de la forme d'équilibre. La dépendance $x(z)$ mesurée à 690 °C est plutôt douce et bien ajustée par la relation purement cinétique de Langmuir-McLean donnée par l'Équation (IV.7) avec $c = 0,155$. L'excellent ajustement de l'ensemble des données de composition, pour des NFs présentant des morphologies très différentes, par la formule de Langmuir-McLean est remarquable. Il apparaît ainsi que la SAG de NFs d'InGaAs sur substrats de Si en HVPE est cinétiquement contrôlée. Cela permet une bonne maîtrise de la composition qui est facilement ajustable via les paramètres de croissance. Sur la base de cette conclusion, une perspective notable de ce travail consiste à explorer des conditions de croissance avec $z < 0,7$ afin de couvrir complètement le domaine de composition de 0 à 100% par HVPE.

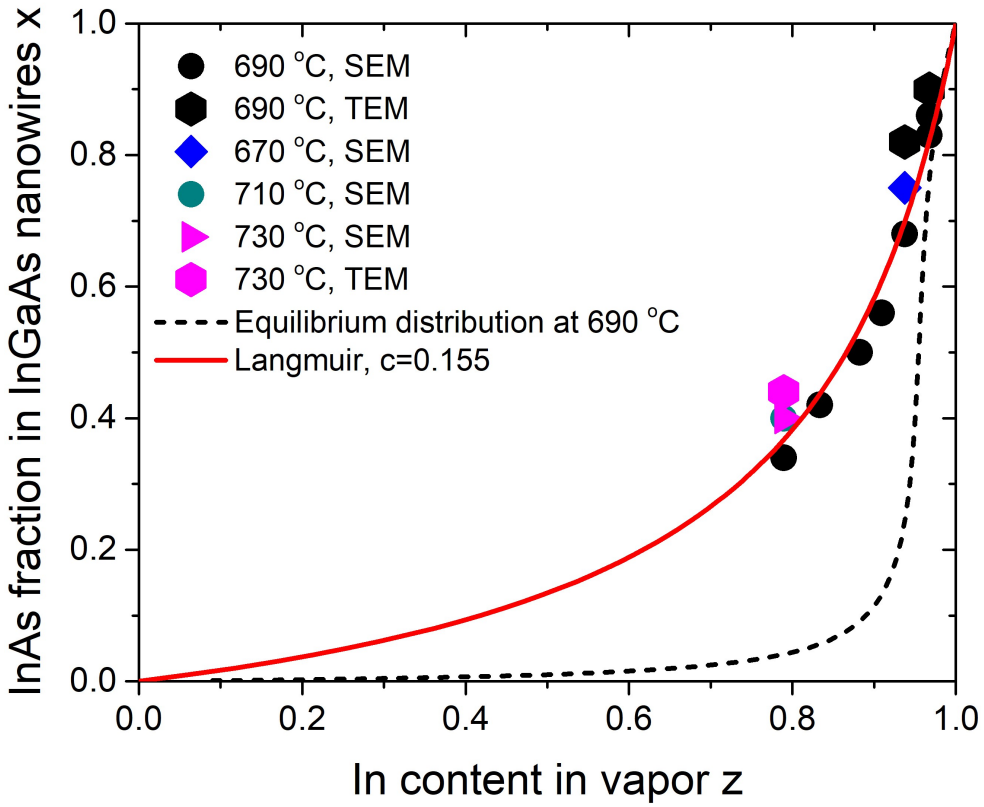


Figure IV.17 – *Distribution vapeur-solide des NFs d'$In_xGa_{1-x}As$ obtenus dans les conditions de croissance du Tableau III.1. La ligne en pointillée montre la distribution vapeur-solide à l'équilibre à 690 °C. Les points de données sont loin de la courbe d'équilibre et bien ajustés par la courbe purement cinétique de Langmuir-McLean avec* $c = 0,155$.

Néanmoins, ce modèle qui ajuste très bien les données, ne prend en compte que les espèces atomiques que sont les adatomes d'In et de Ga. Ainsi, un modèle complémentaire qui prend en compte les espèces et les réactions mises en jeu en HVPE a été développé et les mêmes conclusions sont obtenues (voir section III.2.3.2, page 109).

En résumé, nous avons démontré la SAG de NFs d'InGaAs par HVPE sur des substrats patternés de Si(111). La fraction d'InAs dans les NFs d'InGaAs a été ajustée dans une plage allant de $x = 0,34$ à $x = 0,90$, ce qui est approprié pour des applications optoélectroniques. Il a été démontré que la composition des NFs est contrôlée par la cinétique de croissance plutôt que par des facteurs thermodynamiques. Ceci simplifie considérablement le contrôle de la composition dans une large gamme de paramètres HVPE. En conclusion, ces résultats révèlent la capacité de la HVPE pour la fabrication de réseaux réguliers de NFs d'InGaAs sur silicium à faible coût et avec des compositions largement ajustables et spatialement uniformes.

# IV.5 Conclusion

Pour conclure, au cours de cette thèse, je me suis intéressé aux différents aspects de la SAG de NFs III-As par HVPE. Après avoir introduit le contexte et la technique HVPE dans le chapitre I, la thèse s'est orientée sur deux axes principaux : la croissance de NFs de GaAs dans le chapitre II et la croissance de NFs d'InAs et d'InGaAs dans le chapitre III. Tout au long de ce manuscrit, nous avons démontré avec succès la croissance de réseaux homogènes de NFs III-As que ce soit sur substrat patterné de GaAs(111)B ou de Si(111). Ces travaux ont modestement contribué à la compréhension de nouveaux aspects liés à la croissance des NFs par HVPE et ouvrent de nombreuses perspectives. Ces résultats restent préliminaires et nécessitent des études et des investigations plus approfondies. Ainsi, la collaboration fructueuse entre l'Institut Pascal et McMaster University va se poursuivre dans la perspective d'obtenir des dispositifs prometteurs à base de NFs III-As.

# Bibliography

[1] M. R. Ramdani, E. Gil, C. Leroux, Y. André, A. Trassoudaine, D. Castelluci, L. Bideux, G. Monier, C. Robert-Goumet, and R. Kupka, "Fast Growth Synthesis of GaAs Nanowires with Exceptional Length," *Nano Lett.*, vol. 10, pp. 1836–1841, May 2010. Publisher: American Chemical Society.

[2] H. Hijazi, V. G. Dubrovskii, G. Monier, E. Gil, C. Leroux, G. Avit, A. Trassoudaine, C. Bougerol, D. Castellucci, C. Robert-Goumet, and Y. André, "Influence of Silicon on the Nucleation Rate of GaAs Nanowires on Silicon Substrates," *The Journal of Physical Chemistry C*, vol. 122, pp. 19230–19235, Aug. 2018.

[3] G. Avit, K. Lekhal, Y. André, C. Bougerol, F. Réveret, J. Leymarie, E. Gil, G. Monier, D. Castelluci, and A. Trassoudaine, "Ultralong and Defect-Free GaN Nanowires Grown by the HVPE Process," *Nano Lett.*, vol. 14, pp. 559–562, Feb. 2014. Publisher: American Chemical Society.

[4] G. Grégoire, M. Zeghouane, C. Goosney, N. I. Goktas, P. Staudinger, H. Schmid, K. E. Moselund, T. Taliercio, E. Tournié, A. Trassoudaine, E. Gil, R. R. LaPierre, and Y. André, "Selective Area Growth by Hydride Vapor Phase Epitaxy and Optical Properties of InAs Nanowire Arrays," *Crystal Growth & Design*, vol. 21, pp. 5158–5163, Sept. 2021. Publisher: American Chemical Society.

[5] M. Zeghouane, G. Avit, Y. André, T. Taliercio, P. Ferret, E. Gil, D. Castelluci, P. Disseix, J. Leymarie, E. Tournié, and A. Trassoudaine, "Morphological Control of InN Nanorods by Selective Area Growth–Hydride Vapor-Phase Epitaxy," *Crystal Growth & Design*, vol. 20, pp. 2232–2239, Apr. 2020. Publisher: American Chemical Society.

[6] R. S. Wagner and W. C. Ellis, "Vapor-liquid-solid mechanism of single crystal growth," *Applied Physics Letters*, vol. 4, pp. 89–90, Mar. 1964.

[7] K. Tomioka, T. Tanaka, S. Hara, K. Hiruma, and T. Fukui, "III–V Nanowires on Si Substrate: Selective-Area Growth and Device Applications," *IEEE Journal of Selected Topics in Quantum Electronics*, vol. 17, pp. 1112–1129, July 2011. Conference Name: IEEE Journal of Selected Topics in Quantum Electronics.

[8] R. R. LaPierre, A. C. E. Chia, S. J. Gibson, C. M. Haapamaki, J. Boulanger, R. Yee, P. Kuyanov, J. Zhang, N. Tajik, N. Jewell, and K. M. A. Rahman, "III–V nanowire photovoltaics: Review of design for high efficiency," *physica status solidi (RRL) – Rapid Research Letters*, vol. 7, no. 10, pp. 815–830, 2013. _eprint: https://onlinelibrary.wiley.com/doi/pdf/10.1002/pssr.201307109.

[9] R. R. LaPierre, M. Robson, K. M. Azizur-Rahman, and P. Kuyanov, "A review of III–V nanowire infrared photodetectors and sensors," *Journal of Physics D: Applied Physics*, vol. 50, p. 123001, Feb. 2017.

[10] E. Ertekin, P. A. Greaney, D. C. Chrzan, and T. D. Sands, "Equilibrium limits of coherency in strained nanowire heterostructures," *Journal of Applied Physics*, vol. 97, p. 114325, June 2005.

[11] S. Raychaudhuri and E. T. Yu, "Critical dimensions in coherently strained coaxial nanowire heterostructures," *Journal of Applied Physics*, vol. 99, p. 114308, June 2006.

[12] "NSM Archive - Physical Properties of Semiconductors."

[13] D. V. Beznasyuk, *Axial GaAs/InAs nanowire heterostructures for photonic applications on Si*. PhD thesis, Université Grenoble Alpes, Sept. 2018.

[14] K. Tomioka, Y. Kobayashi, J. Motohisa, S. Hara, and T. Fukui, "Selective-area growth of vertically aligned GaAs and GaAs/AlGaAs core–shell nanowires on Si(111) substrate," *Nanotechnology*, vol. 20, p. 145302, Apr. 2009.

[15] M. Yao, N. Huang, S. Cong, C.-Y. Chi, M. A. Seyedi, Y.-T. Lin, Y. Cao, M. L. Povinelli, P. D. Dapkus, and C. Zhou, "GaAs Nanowire Array Solar Cells with Axial p–i–n Junctions," *Nano Letters*, vol. 14, pp. 3293–3303, June 2014.

[16] P. Krogstrup, H. I. Jørgensen, M. Heiss, O. Demichel, J. V. Holm, M. Aagesen, J. Nygard, and A. Fontcuberta i Morral, "Single-nanowire solar cells beyond the Shockley–Queisser limit,"

*Nature Photon*, vol. 7, pp. 306–310, Apr. 2013. Number: 4 Publisher: Nature Publishing Group.

[17] E. Garnett and P. Yang, "Light Trapping in Silicon Nanowire Solar Cells," *Nano Lett.*, vol. 10, pp. 1082–1087, Mar. 2010. Publisher: American Chemical Society.

[18] S. L. Diedenhofen, O. T. A. Janssen, G. Grzela, E. P. A. M. Bakkers, and J. Gómez Rivas, "Strong Geometrical Dependence of the Absorption of Light in Arrays of Semiconductor Nanowires," *ACS Nano*, vol. 5, pp. 2316–2323, Mar. 2011. Publisher: American Chemical Society.

[19] J. Kupec and B. Witzigmann, "Dispersion, Wave Propagation and Efficiency Analysis of Nanowire Solar Cells," *Opt. Express, OE*, vol. 17, pp. 10399–10410, June 2009. Publisher: Optica Publishing Group.

[20] N. Anttu and H. Q. Xu, "Efficient light management in vertical nanowire arrays for photovoltaics," *Opt. Express, OE*, vol. 21, pp. A558–A575, May 2013. Publisher: Optica Publishing Group.

[21] K. M. Azizur-Rahman and R. R. LaPierre, "Optical design of a mid-wavelength infrared InSb nanowire photodetector," *Nanotechnology*, vol. 27, p. 315202, Aug. 2016.

[22] N. Anttu, "Physics and design for 20% and 25% efficiency nanowire array solar cells," *Nanotechnology*, vol. 30, p. 074002, Dec. 2018. Publisher: IOP Publishing.

[23] O. M. Ghahfarokhi, N. Anttu, L. Samuelson, and I. Åberg, "Performance of GaAs Nanowire Array Solar Cells for Varying Incidence Angles," *IEEE Journal of Photovoltaics*, vol. 6, pp. 1502–1508, Nov. 2016. Conference Name: IEEE Journal of Photovoltaics.

[24] D. van Dam, N. J. J. van Hoof, Y. Cui, P. J. van Veldhoven, E. P. A. M. Bakkers, J. Gómez Rivas, and J. E. M. Haverkort, "High-Efficiency Nanowire Solar Cells with Omnidirectionally Enhanced Absorption Due to Self-Aligned Indium–Tin–Oxide Mie Scatterers," *ACS Nano*, vol. 10, pp. 11414–11419, Dec. 2016. Publisher: American Chemical Society.

[25] C. J. Goosney, V. M. Jarvis, D. P. Wilson, N. I. Goktas, and R. R. LaPierre, "InSb nanowires for multispectral infrared detection," *Semicond. Sci. Technol.*, vol. 34, p. 035023, Feb. 2019. Publisher: IOP Publishing.

[26] C. J. Goosney, V. M. Jarvis, J. F. Britten, and R. R. LaPierre, "InAsSb pillars for multispectral long-wavelength infrared absorption," *Infrared Physics & Technology*, vol. 111, p. 103566, Dec. 2020.

[27] F. Glas, "Critical dimensions for the plastic relaxation of strained axial heterostructures in free-standing nanowires," *Physical Review B*, vol. 74, p. 121302, Sept. 2006.

[28] X. Duan and C. M. Lieber, "General Synthesis of Compound Semiconductor Nanowires," *Advanced Materials*, vol. 12, no. 4, pp. 298–302, 2000.

[29] V. G. Dubrovskii, "Group V sensitive vapor–liquid–solid growth of Au-catalyzed and self-catalyzed III–V nanowires," *Journal of Crystal Growth*, vol. 440, pp. 62–68, Apr. 2016.

[30] S. Breuer, C. Pfüller, T. Flissikowski, O. Brandt, H. T. Grahn, L. Geelhaar, and H. Riechert, "Suitability of Au- and Self-Assisted GaAs Nanowires for Optoelectronic Applications," *Nano Letters*, vol. 11, pp. 1276–1279, Mar. 2011.

[31] M. Bar-Sadan, J. Barthel, H. Shtrikman, and L. Houben, "Direct Imaging of Single Au Atoms Within GaAs Nanowires," *Nano Letters*, vol. 12, pp. 2352–2356, May 2012.

[32] T. Grap, T. Rieger, C. Blömers, T. Schäpers, D. Grützmacher, and M. I. Lepsa, "Self-catalyzed VLS grown InAs nanowires with twinning superlattices," *Nanotechnology*, vol. 24, p. 335601, Aug. 2013.

[33] F. Matteini, G. Tütüncüoglu, H. Potts, F. Jabeen, and A. Fontcuberta i Morral, "Wetting of Ga on SiOx and Its Impact on GaAs Nanowire Growth," *Crystal Growth & Design*, vol. 15, pp. 3105–3109, July 2015.

[34] X. Wang, X. Yang, W. Du, H. Ji, S. Luo, and T. Yang, "Thickness influence of thermal oxide layers on the formation of self-catalyzed InAs nanowires on Si(111) by MOCVD," *Journal of Crystal Growth*, vol. 395, pp. 55–60, June 2014.

[35] M. Madsen, M. Aagesen, P. Krogstrup, C. Sørensen, and J. Nygård, "Influence of the oxide layer for growth of self-assisted InAs nanowires on Si(111)," *Nanoscale Research Letters*, vol. 6, no. 1, p. 516, 2011.

[36] D. S. Dhungana, A. Hemeryck, N. Sartori, P.-F. Fazzini, F. Cristiano, and S. R. Plissard, "Insight of surface treatments for CMOS compatibility of InAs nanowires," *Nano Research*, vol. 12, pp. 581–586, Mar. 2019.

[37] S. K. Jangir, H. K. Malik, A. Kumar, D. V. Sridhar Rao, R. Muralidharan, and P. Mishra, "Influence of Molecular Beam Epitaxy (MBE) Parameters on Catalyst-Free Growth of InAs Nanowires on Silicon (111) Substrate," *Journal of Electronic Materials*, Feb. 2019.

[38] H. Shtrikman, R. Popovitz-Biro, A. Kretinin, and M. Heiblum, "Stacking-Faults-Free Zinc Blende GaAs Nanowires," *Nano Lett.*, vol. 9, pp. 215–219, Jan. 2009. Publisher: American Chemical Society.

[39] M. M. Jansen, P. Perla, M. Kaladzhian, N. von den Driesch, J. Janßen, M. Luysberg, M. I. Lepsa, D. Grützmacher, and A. Pawlis, "Phase-Pure Wurtzite GaAs Nanowires Grown by Self-Catalyzed Selective Area Molecular Beam Epitaxy for Advanced Laser Devices and Quantum Disks," *ACS Appl. Nano Mater.*, vol. 3, pp. 11037–11047, Nov. 2020. Publisher: American Chemical Society.

[40] D. Jacobsson, F. Panciera, J. Tersoff, M. C. Reuter, S. Lehmann, S. Hofmann, K. A. Dick, and F. M. Ross, "Interface dynamics and crystal phase switching in GaAs nanowires," *Nature*, vol. 531, pp. 317–322, Mar. 2016. Number: 7594 Publisher: Nature Publishing Group.

[41] H. Hijazi, *HVPE-Grown GaAs Nanowires : Growth Modeling, Passivation and Transport Properties*. PhD thesis, Université Clermont Auvergne, Oct. 2019.

[42] V. G. Dubrovskii and N. V. Sibirev, "Growth thermodynamics of nanowires and its application to polytypism of zinc blende III-V nanowires," *Physical Review B*, vol. 77, p. 035414, Jan. 2008.

[43] M. E. Levinshteĭn, S. L. Rumyantsev, and M. Shur, eds., *Handbook series on semiconductor parameters*. Singapore ; New Jersey: World Scientific, 1996.

[44] S. Paul, J. B. Roy, and P. K. Basu, "Empirical expressions for the alloy composition and temperature dependence of the band gap and intrinsic carrier density in GaxIn1-xAs," *Journal of Applied Physics*, vol. 69, pp. 827–829, Jan. 1991. Publisher: American Institute of Physics.

[45] H. J. Joyce, Q. Gao, J. Wong-Leung, Y. Kim, H. H. Tan, and C. Jagadish, "Tailoring GaAs, InAs, and InGaAs Nanowires for Optoelectronic Device Applications," *IEEE Journal of Selected Topics in Quantum Electronics*, vol. 17, pp. 766–778, July 2011. Conference Name: IEEE Journal of Selected Topics in Quantum Electronics.

[46] K. A. Dick, K. Deppert, L. Samuelson, and W. Seifert, "Optimization of Au-assisted InAs nanowires grown by MOVPE," *Journal of Crystal Growth*, vol. 297, pp. 326–333, Dec. 2006.

[47] J. C. Harmand, M. Tchernycheva, G. Patriarche, L. Travers, F. Glas, and G. Cirlin, "GaAs nanowires formed by Au-assisted molecular beam epitaxy: Effect of growth temperature," *Journal of Crystal Growth*, vol. 301-302, pp. 853–856, Apr. 2007.

[48] K. A. Dick, K. Deppert, T. Mårtensson, B. Mandl, L. Samuelson, and W. Seifert, "Failure of the vapor-liquid-solid mechanism in Au-assisted MOVPE growth of InAs nanowires," *Nano Letters*, vol. 5, pp. 761–764, Apr. 2005.

[49] M. C. Plante and R. R. LaPierre, "Control of GaAs nanowire morphology and crystal structure," *Nanotechnology*, vol. 19, p. 495603, Nov. 2008. Publisher: IOP Publishing.

[50] H. J. Joyce, Q. Gao, H. H. Tan, C. Jagadish, Y. Kim, M. A. Fickenscher, S. Perera, T. B. Hoang, L. M. Smith, H. E. Jackson, J. M. Yarrison-Rice, X. Zhang, and J. Zou, "High Purity GaAs Nanowires Free of Planar Defects: Growth and Characterization," *Advanced Functional Materials*, vol. 18, no. 23, pp. 3794–3800, 2008. _eprint: https://onlinelibrary.wiley.com/doi/pdf/10.1002/adfm.200800625.

[51] Z. Zhang, Z.-Y. Lu, P.-P. Chen, W. Lu, and J. Zou, "Defect-free zinc-blende structured InAs nanowires realized by in situ two V/III ratio growth in molecular beam epitaxy," *Nanoscale*, vol. 7, pp. 12592–12597, July 2015.

[52] M. Tchernycheva, L. Travers, G. Patriarche, F. Glas, J.-C. Harmand, G. E. Cirlin, and V. G. Dubrovskii, "Au-assisted molecular beam epitaxy of InAs nanowires: Growth and theoretical analysis," *Journal of Applied Physics*, vol. 102, p. 094313, Nov. 2007.

[53] Z. Dong, Y. André, V. G. Dubrovskii, C. Bougerol, C. Leroux, M. R. Ramdani, G. Monier, A. Trassoudaine, D. Castelluci, and E. Gil, "Self-catalyzed GaAs nanowires on silicon by hydride vapor phase epitaxy," *Nanotechnology*, vol. 28, p. 125602, Feb. 2017.

[54] J. Becdelievre, X. Guan, I. Dudko, P. Regreny, N. Chauvin, G. Patriarche, M. Gendry, A. Danescu, and J. Penuelas, "Growing self-assisted GaAs nanowires up to 80 µm long by molecular beam epitaxy," *Nanotechnology*, vol. 34, p. 045603, Nov. 2022. Publisher: IOP Publishing.

[55] W. M. Haynes, *CRC Handbook of Chemistry and Physics*. CRC Press, June 2014.

[56] C. Chatillon and D. Chatain, "Congruent vaporization of GaAs(s) and stability of Ga(l) droplets at the GaAs(s) surface," *Journal of Crystal Growth*, vol. 151, pp. 91–101, May 1995.

[57] E. A. Anyebe, Q. Zhuang, A. M. Sanchez, S. Lawson, A. J. Robson, L. Ponomarenko, A. Zhukov, and O. Kolosov, "Self-catalysed growth of InAs nanowires on bare Si substrates by droplet epitaxy," *physica status solidi (RRL) – Rapid Research Letters*, vol. 8, no. 7, pp. 658–662, 2014. _eprint: https://onlinelibrary.wiley.com/doi/pdf/10.1002/pssr.201409106.

[58] U. P. Gomes, D. Ercolani, V. Zannier, J. David, M. Gemmi, F. Beltram, and L. Sorba, "Nucleation and growth mechanism of self-catalyzed InAs nanowires on silicon," *Nanotechnology*, vol. 27, no. 25, p. 255601, 2016.

[59] W. Yang, X. Ji, X. Wang, T. Li, T. Shi, T. Yang, and Q. Chen, "The effect of nanoscale steps on the self-catalyzed position-controlled InAs nanowire growth," *Journal of Micromechanics and Microengineering*, vol. 28, no. 1, p. 014002, 2018.

[60] B. Mandl, J. Stangl, E. Hilner, A. A. Zakharov, K. Hillerich, A. W. Dey, L. Samuelson, G. Bauer, K. Deppert, and A. Mikkelsen, "Growth Mechanism of Self-Catalyzed Group III-V Nanowires," *Nano Letters*, vol. 10, pp. 4443–4449, Nov. 2010.

[61] U. P. Gomes, D. Ercolani, N. V. Sibirev, M. Gemmi, V. G. Dubrovskii, F. Beltram, and L. Sorba, "Catalyst-free growth of InAs nanowires on Si (111) by CBE," *Nanotechnology*, vol. 26, p. 415604, Sept. 2015.

[62] B. Mandl, J. Stangl, T. Mårtensson, A. Mikkelsen, J. Eriksson, L. S. Karlsson, G. Bauer, L. Samuelson, and W. Seifert, "Au-Free Epitaxial Growth of InAs Nanowires," *Nano Letters*, vol. 6, pp. 1817–1821, Aug. 2006.

[63] K. Tomioka, J. Motohisa, S. Hara, and T. Fukui, "Control of InAs Nanowire Growth Directions on Si," *Nano Letters*, vol. 8, pp. 3475–3480, Oct. 2008.

[64] H. Kim, W.-J. Lee, A. C. Farrell, J. S. D. Morales, P. Senanayake, S. V. Prikhodko, T. J. Ochalski, and D. L. Huffaker, "Monolithic InGaAs Nanowire Array Lasers on Silicon-on-Insulator Operating at Room Temperature," *Nano Letters*, vol. 17, pp. 3465–3470, June 2017.

[65] L. C. Chuang, F. G. Sedgwick, R. Chen, W. S. Ko, M. Moewe, K. W. Ng, T.-T. D. Tran, and C. Chang-Hasnain, "GaAs-Based Nanoneedle Light Emitting Diode and Avalanche Photodi-

ode Monolithically Integrated on a Silicon Substrate," *Nano Letters*, vol. 11, pp. 385–390, Feb. 2011.

[66] K. Tomioka, P. Mohan, J. Noborisaka, S. Hara, J. Motohisa, and T. Fukui, "Growth of highly uniform InAs nanowire arrays by selective-area MOVPE," *Journal of Crystal Growth*, vol. 298, pp. 644–647, Jan. 2007.

[67] H. Paetzelt, V. Gottschalch, J. Bauer, G. Benndorf, and G. Wagner, "Selective-area growth of GaAs and InAs nanowires—homo- and heteroepitaxy using SiNx templates," *Journal of Crystal Growth*, vol. 310, pp. 5093–5097, Nov. 2008.

[68] C.-H. Song, M. Kong, H. Jang, S. Tae Lee, H.-H. Park, C. Zoo Kim, S. Hyun Jung, Y. Choi, S. Kim, D.-H. Ko, K. Seo, and C.-S. Shin, "Vertical growth characterization of InAs nanowires grown by selective area growth on patterned InP(1 1 1)B substrate by a MOCVD method," *Solid-State Electronics*, vol. 175, p. 107939, Jan. 2021.

[69] K. Ikejiri, T. Sato, H. Yoshida, K. Hiruma, J. Motohisa, S. Hara, and T. Fukui, "Growth characteristics of GaAs nanowires obtained by selective area metal–organic vapour-phase epitaxy," *Nanotechnology*, vol. 19, p. 265604, May 2008.

[70] H. Küpers, R. B. Lewis, A. Tahraoui, M. Matalla, O. Krüger, F. Bastiman, H. Riechert, and L. Geelhaar, "Diameter evolution of selective area grown Ga-assisted GaAs nanowires," *Nano Research*, vol. 11, pp. 2885–2893, May 2018.

[71] K. Tomioka, Y. Kobayashi, J. Motohisa, S. Hara, and T. Fukui, "Selective-area growth of vertically aligned GaAs and GaAs/AlGaAs core-shell nanowires on Si(111) substrate," *Nanotechnology*, vol. 20, p. 145302, Apr. 2009.

[72] H. Yoshida, K. Ikejiri, T. Sato, S. Hara, K. Hiruma, J. Motohisa, and T. Fukui, "Analysis of twin defects in GaAs nanowires and tetrahedra and their correlation to GaAs(111)B surface reconstructions in selective-area metal organic vapour-phase epitaxy," *Journal of Crystal Growth*, vol. 312, pp. 52–57, Dec. 2009.

[73] X. Wang, W. Yang, B. Wang, X. Ji, S. Xu, W. Wang, Q. Chen, and T. Yang, "Effect of nanohole size on selective area growth of InAs nanowire arrays on Si substrates," *Journal of Crystal Growth*, vol. 460, pp. 1–4, Feb. 2017.

[74] M. Zeghouane, G. Grégoire, E. Chereau, G. Avit, P. Staudinger, K. E. Moselund, H. Schmid, P.-M. Coulon, P. Shields, N. Isik Goktas, R. R. LaPierre, A. Trassoudaine, Y. André, and E. Gil, "Selective Area Growth of GaAs Nanowires and Microplatelet Arrays on Silicon by Hydride Vapor-Phase Epitaxy," *Crystal Growth & Design*, vol. 23, pp. 2120–2127, Apr. 2023. Publisher: American Chemical Society.

[75] C. D. Yerino, B. Liang, D. L. Huffaker, P. J. Simmonds, and M. L. Lee, "Review Article: Molecular beam epitaxy of lattice-matched InAlAs and InGaAs layers on InP (111)A, (111)B, and (110)," *Journal of Vacuum Science & Technology B*, vol. 35, p. 010801, Jan. 2017. Publisher: American Vacuum Society.

[76] Y. Kim, H. J. Joyce, Q. Gao, H. H. Tan, C. Jagadish, M. Paladugu, J. Zou, and A. A. Suvorova, "Influence of Nanowire Density on the Shape and Optical Properties of Ternary InGaAs Nanowires," *Nano Lett.*, vol. 6, pp. 599–604, Apr. 2006. Publisher: American Chemical Society.

[77] H. Ye, Z. Y. Yu, S. Kodambaka, and V. B. Shenoy, "Kinetics of axial composition evolution in multi-component alloy nanowires," *Applied Physics Letters*, vol. 100, p. 263103, June 2012.

[78] G. Koblmüller and G. Abstreiter, "Growth and properties of InGaAs nanowires on silicon," *physica status solidi (RRL) – Rapid Research Letters*, vol. 8, pp. 11–30, Jan. 2014.

[79] Y.-N. Guo, H.-Y. Xu, G. J. Auchterlonie, T. Burgess, H. J. Joyce, Q. Gao, H. H. Tan, C. Jagadish, H.-B. Shu, X.-S. Chen, W. Lu, Y. Kim, and J. Zou, "Phase Separation Induced by Au Catalysts in Ternary InGaAs Nanowires," *Nano Lett.*, vol. 13, pp. 643–650, Feb. 2013. Publisher: American Chemical Society.

[80] J. C. Shin, K. H. Kim, K. J. Yu, H. Hu, L. Yin, C.-Z. Ning, J. A. Rogers, J.-M. Zuo, and X. Li, "InxGa1-xAs Nanowires on Silicon: One-Dimensional Heterogeneous Epitaxy, Bandgap Engineering, and Photovoltaics," *Nano Letters*, vol. 11, pp. 4831–4838, Nov. 2011.

[81] S. Hertenberger, S. Funk, K. Vizbaras, A. Yadav, D. Rudolph, J. Becker, S. Bolte, M. Döblinger, M. Bichler, G. Scarpa, P. Lugli, I. Zardo, J. J. Finley, M.-C. Amann, G. Abstreiter, and G. Koblmüller, "High compositional homogeneity in In-rich InGaAs nanowire arrays on nanoimprinted SiO2/Si (111)," *Applied Physics Letters*, vol. 101, p. 043116, July 2012.

[82] Z. Azimi, A. Gopakumar, A. S. Ameruddin, L. Li, T. Truong, H. T. Nguyen, H. H. Tan, C. Jagadish, and J. Wong-Leung, "Tuning the crystal structure and optical properties of selective area grown InGaAs nanowires," *Nano Res.*, vol. 15, pp. 3695–3703, Apr. 2022.

[83] K. Chiba, K. Tomioka, A. Yoshida, and J. Motohisa, "Composition controllability of InGaAs nanowire arrays in selective area growth with controlled pitches on Si platform," *AIP Advances*, vol. 7, p. 125304, Dec. 2017.

[84] J. Treu, M. Speckbacher, K. Saller, S. Morkötter, M. Döblinger, X. Xu, H. Riedl, G. Abstreiter, J. J. Finley, and G. Koblmüller, "Widely tunable alloy composition and crystal structure in catalyst-free InGaAs nanowire arrays grown by selective area molecular beam epitaxy," *Applied Physics Letters*, vol. 108, p. 053110, Feb. 2016.

[85] I. Åberg, G. Vescovi, D. Asoli, U. Naseem, J. P. Gilboy, C. Sundvall, A. Dahlgren, K. E. Svensson, N. Anttu, M. T. Björk, and L. Samuelson, "A GaAs Nanowire Array Solar Cell With 15.3% Efficiency at 1 Sun," *IEEE Journal of Photovoltaics*, vol. 6, pp. 185–190, Jan. 2016. Conference Name: IEEE Journal of Photovoltaics.

[86] H. K. Kang, J. Y. Kim, M. S. Noh, C. Y. Kang, Y. D. Kim, M. H. Cho, and J. D. Song, "Growth of pure wurtzite InGaAs nanowires for photovoltaic and energy harvesting applications," *Nano Energy*, vol. 53, pp. 57–65, Nov. 2018.

[87] D. Saxena, S. Mokkapati, P. Parkinson, N. Jiang, Q. Gao, H. H. Tan, and C. Jagadish, "Optically pumped room-temperature GaAs nanowire lasers," *Nature Photon*, vol. 7, pp. 963–968, Dec. 2013.

[88] X. Dai, S. Zhang, Z. Wang, G. Adamo, H. Liu, Y. Huang, C. Couteau, and C. Soci, "GaAs/AlGaAs Nanowire Photodetector," *Nano Lett.*, vol. 14, pp. 2688–2693, May 2014.

[89] O.-P. Kilpi, J. Svensson, J. Wu, A. R. Persson, R. Wallenberg, E. Lind, and L.-E. Wernersson, "Vertical InAs/InGaAs Heterostructure Metal–Oxide–Semiconductor Field-Effect Transistors on Si," *Nano Letters*, vol. 17, pp. 6006–6010, Oct. 2017.

[90] A. W. Dey, J. Svensson, B. M. Borg, M. Ek, and L.-E. Wernersson, "Single InAs/GaSb Nanowire Low-Power CMOS Inverter," *Nano Letters*, vol. 12, pp. 5593–5597, Nov. 2012.

[91] K. Tomioka, J. Motohisa, S. Hara, K. Hiruma, and T. Fukui, "GaAs/AlGaAs Core Multishell Nanowire-Based Light-Emitting Diodes on Si," *Nano Lett.*, vol. 10, pp. 1639–1644, May 2010.

[92] S. Revankar, "Advances in Betavoltaic Power Sources," *Journal of Energy and Power Sources*, vol. 1, pp. 321–329, Jan. 2014.

[93] L. C. Olsen, P. Cabauy, and B. J. Elkind, "Betavoltaic power sources," *Physics Today*, vol. 65, pp. 35–38, Dec. 2012.

[94] F. K. Manasse, J. J. Pinajian, and A. N. Tse, "Schottky Barrier Betavoltaic Battery," *IEEE Transactions on Nuclear Science*, vol. 23, pp. 860–870, Feb. 1976. Conference Name: IEEE Transactions on Nuclear Science.

[95] M. A. Prelas, C. L. Weaver, M. L. Watermann, E. D. Lukosi, R. J. Schott, and D. A. Wisniewski, "A review of nuclear batteries," *Progress in Nuclear Energy*, vol. 75, pp. 117–148, Aug. 2014.

[96] G. R. Ghasemi Nejad, F. Rahmani, and G. R. Abaeiani, "Design and optimization of beta-cell temperature sensor based on 63Ni–Si," *Applied Radiation and Isotopes*, vol. 86, pp. 46–51, Apr. 2014.

[97] P. E. Sims, L. C. Dinetta, and A. M. Barnett, "High efficiency GaP power conversion for Betavoltaic applications," pp. 373–382, Sept. 1994. Conference Name: 13th Space Photovoltaic Research and Technology Conference (SPRAT 13) ADS Bibcode: 1994sprt.nasa..373S.

[98] T. H. Smith, J. Greenborg, and W. E. Matheson, "Benefit/Risk Analysis of Cardiac Pacemakers Powered by Betacel® Promethium-147 Batteries," *Nuclear Technology*, vol. 26, pp. 54–64, May 1975. Publisher: Taylor & Francis _eprint: https://doi.org/10.13182/NT75-A24404.

[99] D. L. Wagner, D. R. Novog, and R. R. LaPierre, "Design and optimization of nanowire betavoltaic generators," *Journal of Applied Physics*, vol. 127, p. 244303, June 2020.

[100] D. Wagner, *Simulation and Optimization of Nanowire-Based Betavoltaic Generators*. Master thesis, 2020. Accepted: 2020-08-07T17:08:51Z.

[101] G. Otnes and M. T. Borgström, "Towards high efficiency nanowire solar cells," *Nano Today*, vol. 12, pp. 31–45, Feb. 2017.

[102] S. McNamee, D. Wagner, E. M. Fiordaliso, D. Novog, and R. R. LaPierre, "GaP nanowire betavoltaic device," *Nanotechnology*, vol. 30, p. 075401, Dec. 2018. Publisher: IOP Publishing.

[103] S. O. Kasap, *Optoelectronics and Photonics: Principles and Practices*. Prentice Hall, 2001. Google-Books-ID: MaEeAQAAIAAJ.

[104] A. Rogalski, "HgCdTe infrared detector material: history, status and outlook," *Reports on Progress in Physics*, vol. 68, p. 2267, Aug. 2005.

[105] A. Rogalski, J. Antoszewski, and L. Faraone, "Third-generation infrared photodetector arrays," *Journal of Applied Physics*, vol. 105, p. 091101, May 2009.

[106] A. Rogalski, P. Martyniuk, and M. Kopytko, "Challenges of small-pixel infrared detectors: a review," *Reports on Progress in Physics*, vol. 79, p. 046501, Mar. 2016. Publisher: IOP Publishing.

[107] P. Martyniuk, J. Antoszewski, M. Martyniuk, L. Faraone, and A. Rogalski, "New concepts in infrared photodetector designs," *Applied Physics Reviews*, vol. 1, p. 041102, Nov. 2014.

[108] K. M. Azizur-Rahman, *Simulation of III-V Nanowires for Infrared Photodetection*. PhD thesis, 2016. Accepted: 2016-10-18T20:27:22Z.

[109] K. M. Azizur-Rahman and R. R. LaPierre, "Wavelength-selective absorptance in GaAs, InP and InAs nanowire arrays," *Nanotechnology*, vol. 26, p. 295202, July 2015. Publisher: IOP Publishing.

[110] A. Rogalski, "Infrared Detectors for the Future," *Acta Physica Polonica A*, vol. 116, pp. 389–406, Sept. 2009.

[111] P.-M. Coulon, B. Damilano, B. Alloing, P. Chausse, S. Walde, J. Enslin, R. Armstrong, S. Vézian, S. Hagedorn, T. Wernicke, J. Massies, J. Zúñiga-Pérez, M. Weyers, M. Kneissl, and P. A. Shields, "Displacement Talbot lithography for nano-engineering of III-nitride materials," *Microsyst Nanoeng*, vol. 5, pp. 1–12, Dec. 2019.

[112] V. S. Ban, "Mass Spectrometric Studies of Vapor-Phase Crystal Growth: II .," *J. Electrochem. Soc.*, vol. 119, p. 761, June 1972. Publisher: IOP Publishing.

[113] M. Harrous, L. Chaput, A. Bendraoui, M. Cadoret, C. Pariset, and R. Cadoret, "Phosphine and arsine decomposition in CVD reactors for InP and InGaAs growth," *Journal of Crystal Growth*, vol. 92, pp. 423–431, Oct. 1988.

[114] E. Gil-Lafon, J. Napierala, A. Pimpinelli, R. Cadoret, A. Trassoudaine, and D. Castelluci, "Direct condensation modelling for a two-particle growth system: application to GaAs grown by hydride vapour phase epitaxy," *Journal of Crystal Growth*, vol. 258, pp. 14–25, Oct. 2003.

[115] A. Pimpinelli, R. Cadoret, E. Gil-Lafon, J. Napierala, and A. Trassoudaine, "Two-particle surface diffusion-reaction models of vapour-phase epitaxial growth on vicinal surfaces," *Journal of Crystal Growth*, vol. 258, pp. 1–13, Oct. 2003.

[116] G. B. Stringfellow, "Fundamental aspects of vapor growth and epitaxy," *Journal of Crystal Growth*, vol. 115, pp. 1–11, Dec. 1991.

[117] E. Gil-Lafon, J. Napierala, D. Castelluci, A. Pimpinelli, R. Cadoret, and B. Gérard, "Selective growth of GaAs by HVPE: keys for accurate control of the growth morphologies," *Journal of Crystal Growth*, vol. 222, pp. 482–496, Jan. 2001.

[118] V. G. Dubrovskii and E. D. Leshchenko, "Kinetically controlled composition of III-V ternary nanostructures," *Phys. Rev. Mater.*, vol. 7, p. 056001, May 2023. Publisher: American Physical Society.

[119] D. W. Shaw, "Mechanisms in Vapour Epitaxy of Semiconductors," in *Crystal Growth: Theory and Techniques Volume 1* (C. H. L. Goodman, ed.), pp. 1–48, Boston, MA: Springer US, 1974.

[120] I. W. Yeu, G. Han, J. Park, C. S. Hwang, and J.-H. Choi, "Theoretical understanding of the catalyst-free growth mechanism of GaAs <111>B nanowires," *Applied Surface Science*, vol. 497, p. 143740, Dec. 2019.

[121] J. Napierala, E. Gil-Lafon, D. Castelluci, A. Pimpinelli, and B. Gérard, "Control of the growth morphologies of GaAs stripes grown on patterned substrates by HVPE," *Optical Materials*, vol. 17, pp. 315–318, June 2001.

[122] D. K. Biegelsen, R. D. Bringans, J. E. Northrup, and L.-E. Swartz, "Reconstructions of GaAs $(\bar{1}\bar{1}\bar{1})$ surfaces observed by scanning tunneling microscopy," *Phys. Rev. Lett.*, vol. 65, pp. 452–455, July 1990.

[123] K. Ikejiri, J. Noborisaka, S. Hara, J. Motohisa, and T. Fukui, "Mechanism of catalyst-free growth of GaAs nanowires by selective area MOVPE," *Journal of Crystal Growth*, vol. 298, pp. 616–619, Jan. 2007.

[124] T. Nishida, K. Uwai, Y. Kobayashi, and N. K. N. Kobayashi, "Phase Diagram of GaAs (111)B Surface during Metal-Organic Chemical Vapor Deposition Measured by Surface Photo-Absorption," *Jpn. J. Appl. Phys.*, vol. 34, p. 6326, Dec. 1995. Publisher: IOP Publishing.

[125] A. Ohtake, J. Nakamura, T. Komura, T. Hanada, T. Yao, H. Kuramochi, and M. Ozeki, "Surface structures of GaAs {111}A,B-{2×2}," *Phys. Rev. B*, vol. 64, p. 045318, June 2001. Publisher: American Physical Society.

[126] M. Yao, C. Sheng, M. Ge, C.-Y. Chi, S. Cong, A. Nakano, P. D. Dapkus, and C. Zhou, "Facile Five-Step Heteroepitaxial Growth of GaAs Nanowires on Silicon Substrates and the Twin Formation Mechanism," *ACS Nano*, vol. 10, pp. 2424–2435, Feb. 2016. Publisher: American Chemical Society.

[127] J. Johansson, B. A. Wacaser, K. A. Dick, and W. Seifert, "Growth related aspects of epitaxial nanowires," *Nanotechnology*, vol. 17, p. S355, May 2006.

[128] S. O. Mariager, C. B. Sørensen, M. Aagesen, J. Nygård, R. Feidenhans'l, and P. R. Willmott, "Facet structure of GaAs nanowires grown by molecular beam epitaxy," *Appl. Phys. Lett.*, vol. 91, p. 083106, Aug. 2007. Publisher: American Institute of Physics.

[129] V. Pankoke, P. Kratzer, and S. Sakong, "Calculation of the diameter-dependent polytypism in GaAs nanowires from an atomic motif expansion of the formation energy," *Phys. Rev. B*, vol. 84, p. 075455, Aug. 2011. Publisher: American Physical Society.

[130] N. Jiang, H. J. Joyce, P. Parkinson, J. Wong-Leung, H. H. Tan, and C. Jagadish, "Facet-Related Non-uniform Photoluminescence in Passivated GaAs Nanowires," *Frontiers in Chemistry*, vol. 8, 2020.

[131] N. Jiang, J. Wong-Leung, H. J. Joyce, Q. Gao, H. H. Tan, and C. Jagadish, "Understanding the True Shape of Au-Catalyzed GaAs Nanowires," *Nano Lett.*, vol. 14, pp. 5865–5872, Oct. 2014. Publisher: American Chemical Society.

[132] V. Pankoke, S. Sakong, and P. Kratzer, "Role of sidewall diffusion in GaAs nanowire growth: A first-principles study," *Phys. Rev. B*, vol. 86, p. 085425, Aug. 2012. Publisher: American Physical Society.

[133] P. Caroff, K. A. Dick, J. Johansson, M. E. Messing, K. Deppert, and L. Samuelson, "Controlled polytypic and twin-plane superlattices in iii–v nanowires," *Nature Nanotechnology*, vol. 4, pp. 50–55, Jan. 2009.

[134] M. Cantoro, G. Brammertz, O. Richard, H. Bender, F. Clemente, M. Leys, S. Degroote, M. Caymax, M. Heyns, and S. D. Gendt, "Controlled III/V Nanowire Growth by Selective-Area Vapor-Phase Epitaxy," *Journal of The Electrochemical Society*, vol. 156, p. H860, Oct. 2009. Publisher: IOP Publishing.

[135] K. Shimamura, Z. Yuan, F. Shimojo, and A. Nakano, "Effects of twins on the electronic properties of GaAs," *Appl. Phys. Lett.*, vol. 103, p. 022105, July 2013. Publisher: American Institute of Physics.

[136] D. Spirkoska, J. Arbiol, A. Gustafsson, S. Conesa-Boj, F. Glas, I. Zardo, M. Heigoldt, M. H. Gass, A. L. Bleloch, S. Estrade, M. Kaniber, J. Rossler, F. Peiro, J. R. Morante, G. Abstreiter, L. Samuelson, and A. Fontcuberta i Morral, "Structural and optical properties of high quality zinc-blende/wurtzite GaAs nanowire heterostructures," *Phys. Rev. B*, vol. 80, p. 245325, Dec. 2009. Publisher: American Physical Society.

[137] V. G. Dubrovskii and F. Glas, "Vapor–Liquid–Solid Growth of Semiconductor Nanowires," in *Fundamental Properties of Semiconductor Nanowires* (N. Fukata and R. Rurali, eds.), pp. 3–107, Singapore: Springer, 2021.

[138] M. R. Ramdani, *Croissance sélective HVPE et VLS-HVPE d'objets et de structures GaAs à morphologie contrôlée à l'échelle sub-micrométrique et nanométrique*. PhD thesis, Université Blaise Pascal - Clermont-Ferrand II, Mar. 2010.

[139] V. G. Dubrovskii and N. V. Sibirev, "Growth rate of a crystal facet of arbitrary size and growth kinetics of vertical nanowires," *Phys. Rev. E*, vol. 70, p. 031604, Sept. 2004. Publisher: American Physical Society.

[140] G. E. Cirlin, V. G. Dubrovskii, N. V. Sibirev, I. P. Soshnikov, Y. B. Samsonenko, A. A. Tonkikh, and V. M. Ustinov, "The diffusion mechanism in the formation of GaAs and AlGaAs nanowhiskers during the process of molecular-beam epitaxy," *Semiconductors*, vol. 39, pp. 557–564, May 2005.

[141] V. Consonni, V. G. Dubrovskii, A. Trampert, L. Geelhaar, and H. Riechert, "Quantitative description for the growth rate of self-induced GaN nanowires," *Phys. Rev. B*, vol. 85, p. 155313, Apr. 2012.

[142] M. López and Y. Nomura, "Surface diffusion length of Ga adatoms in molecular-beam epitaxy on GaAs(100)–(110) facet structures," *Journal of Crystal Growth*, vol. 150, pp. 68–72, May 1995.

[143] X.-Q. Shen, D. K. D. Kishimoto, and T. N. T. Nishinaga, "Arsenic Pressure Dependence of Surface Diffusion of Ga on Nonplanar GaAs Substrates," *Jpn. J. Appl. Phys.*, vol. 33, p. 11, Jan. 1994. Publisher: IOP Publishing.

[144] V. V. Fedorov, L. N. Dvoretckaia, D. A. Kirilenko, I. S. Mukhin, and V. G. Dubrovskii, "Formation of wurtzite sections in self-catalyzed GaP nanowires by droplet consumption," *Nanotechnology*, vol. 32, p. 495601, Sept. 2021. Publisher: IOP Publishing.

[145] E. Chereau, V. G. Dubrovskii, G. Grégoire, G. Avit, P. Staudinger, H. Schmid, C. Bougerol, P.-M. Coulon, P. A. Shields, A. Trassoudaine, E. Gil, R. R. LaPierre, and Y. André, "Importance of As and Ga Balance in Achieving Long GaAs Nanowires by Selective Area Epitaxy," *Crystal Growth & Design*, vol. 23, pp. 4401–4409, June 2023. Publisher: American Chemical Society.

[146] H. C. Casey and F. Stern, "Concentration-dependent absorption and spontaneous emission of heavily doped GaAs," *Journal of Applied Physics*, vol. 47, pp. 631–643, Feb. 1976. ADS Bibcode: 1976JAP....47..631C.

[147] D. Olego and M. Cardona, "Photoluminescence in heavily doped GaAs. I. Temperature and hole-concentration dependence," *Phys. Rev. B*, vol. 22, pp. 886–893, July 1980. Publisher: American Physical Society.

[148] E. Burstein, "Anomalous Optical Absorption Limit in InSb," *Phys. Rev.*, vol. 93, pp. 632–633, Feb. 1954. Publisher: American Physical Society.

[149] T. S. Moss, "The Interpretation of the Properties of Indium Antimonide," *Proc. Phys. Soc. B*, vol. 67, p. 775, Oct. 1954.

[150] H.-L. Chen, *Ultrathin and nanowire-based GaAs solar cells*. PhD thesis, Université Paris Saclay (COmUE), Oct. 2018.

[151] J. S. Blakemore, "Semiconducting and other major properties of gallium arsenide," *Journal of Applied Physics*, vol. 53, pp. R123–R181, Oct. 1982.

[152] J.-Y. Huang, L. Shang, S.-F. Ma, B. Han, G.-D. Wei, Q.-M. Liu, X.-D. Hao, H.-S. Shan, and B.-S. Xu, "Low temperature photoluminescence study of GaAs defect states*," *Chinese Phys. B*, vol. 29, p. 010703, Jan. 2020. Publisher: Chinese Physical Society and IOP Publishing Ltd.

[153] D. Ruhstorfer, M. Döblinger, H. Riedl, J. J. Finley, and G. Koblmüller, "Role of twin defects on growth dynamics and size distribution of undoped and Si-doped GaAs nanowires by selective area epitaxy," *Journal of Applied Physics*, vol. 132, p. 204302, Nov. 2022.

[154] N. Isik Goktas, A. Sokolovskii, V. G. Dubrovskii, and R. R. LaPierre, "Formation Mechanism of Twinning Superlattices in Doped GaAs Nanowires," *Nano Lett.*, vol. 20, pp. 3344–3351, May 2020. Publisher: American Chemical Society.

[155] J. P. Boulanger, A. C. E. Chia, B. Wood, S. Yazdi, T. Kasama, M. Aagesen, and R. R. LaPierre, "Characterization of a Ga-Assisted GaAs Nanowire Array Solar Cell on Si Substrate," *IEEE Journal of Photovoltaics*, vol. 6, pp. 661–667, May 2016. Conference Name: IEEE Journal of Photovoltaics.

[156] S. Finot, *Cathodoluminescence lifetime spectroscopy for efficient III-nitride LEDs*. PhD thesis, Université Grenoble Alpes, Nov. 2022.

[157] G. Grégoire, E. Gil, M. Zeghouane, C. Bougerol, H. Hijazi, D. Castelluci, V. G. Dubrovskii, A. Trassoudaine, N. I. Goktas, R. R. LaPierre, and Y. André, "Long catalyst-free InAs nanowires grown on silicon by HVPE," *CrystEngComm*, vol. 23, pp. 378–384, Jan. 2021.

[158] Y. Kohashi, T. Sato, K. Ikejiri, K. Tomioka, S. Hara, and J. Motohisa, "Influence of growth temperature on growth of InGaAs nanowires in selective-area metal–organic vapor-phase epitaxy," *Journal of Crystal Growth*, vol. 338, pp. 47–51, Jan. 2012.

[159] J. Treu, X. Xu, K. Ott, K. Saller, G. Abstreiter, J. J. Finley, and G. Koblmüller, "Optical absorption of composition-tunable InGaAs nanowire arrays," *Nanotechnology*, vol. 30, p. 495703, Sept. 2019. Publisher: IOP Publishing.

[160] J. C. Shin, K. J. Choi, D. Y. Kim, W. J. Choi, and X. Li, "Characteristics of Strain-Induced InxGa1–xAs Nanowires Grown on Si(111) Substrates," *Crystal Growth & Design*, vol. 12, pp. 2994–2998, June 2012. Publisher: American Chemical Society.

[161] J. Wu, B. M. Borg, D. Jacobsson, K. A. Dick, and L.-E. Wernersson, "Control of composition and morphology in InGaAs nanowires grown by metalorganic vapor phase epitaxy," *Journal of Crystal Growth*, vol. 383, pp. 158–165, Nov. 2013.

[162] S. Morkötter, S. Funk, M. Liang, M. Döblinger, S. Hertenberger, J. Treu, D. Rudolph, A. Yadav, J. Becker, M. Bichler, G. Scarpa, P. Lugli, I. Zardo, J. J. Finley, G. Abstreiter, and G. Koblmüller, "Role of microstructure on optical properties in high-uniformity In 1 - x Ga x As nanowire arrays: Evidence of a wider wurtzite band gap," *Physical Review B*, vol. 87, May 2013.

[163] A. S. Ameruddin, H. A. Fonseka, P. Caroff, J. Wong-Leung, R. L. O. h. Veld, J. L. Boland, M. B. Johnston, H. H. Tan, and C. Jagadish, "In x Ga 1- x As nanowires with uniform composition, pure wurtzite crystal phase and taper-free morphology," *Nanotechnology*, vol. 26, no. 20, p. 205604, 2015.

[164] V. G. Dubrovskii, A. A. Koryakin, and N. V. Sibirev, "Understanding the composition of ternary III-V nanowires and axial nanowire heterostructures in nucleation-limited regime," *Materials & Design*, vol. 132, pp. 400–408, Oct. 2017.

[165] E. Gil, Y. André, R. Cadoret, and A. Trassoudaine, "2 - Hydride Vapor Phase Epitaxy for Current III–V and Nitride Semiconductor Compound Issues," in *Handbook of Crystal Growth (Second Edition)* (T. F. Kuech, ed.), Handbook of Crystal Growth, pp. 51–93, Boston: North-Holland, Jan. 2015.

[166] V. G. Dubrovskii and E. D. Leshchenko, "Composition of III-V ternary materials under arbitrary material fluxes: The general approach unifying kinetics and thermodynamics," *Phys. Rev. Mater.*, vol. 7, p. 074603, July 2023. Publisher: American Physical Society.

[167] V. G. Dubrovskii, "Liquid-solid and vapor-solid distributions of vapor-liquid-solid III-V ternary nanowires," *Phys. Rev. Mater.*, vol. 7, p. 096001, Sept. 2023. Publisher: American Physical Society.

[168] V. G. Dubrovskii, "Composition of Vapor–Liquid–Solid III–V Ternary Nanowires Based on Group-III Intermix," *Nanomaterials*, vol. 13, p. 2532, Jan. 2023. Number: 18 Publisher: Multidisciplinary Digital Publishing Institute.

[169] M. Ghasemi, E. D. Leshchenko, and J. Johansson, "Assembling your nanowire: an overview of composition tuning in ternary III–V nanowires," *Nanotechnology*, vol. 32, p. 072001, Nov. 2020. Publisher: IOP Publishing.

[170] I. Ansara, C. Chatillon, H. L. Lukas, T. Nishizawa, H. Ohtani, K. Ishida, M. Hillert, B. Sundman, B. B. Argent, A. Watson, T. G. Chart, and T. Anderson, "A binary database for III–V compound semiconductor systems," *Calphad*, vol. 18, pp. 177–222, Apr. 1994.

[171] K. Kajiyama, "Vapor Pressure Dependence of the Relative Composition of III–V Mixed Crystals in Vapor Phase Epitaxy," *J. Electrochem. Soc.*, vol. 123, p. 423, Mar. 1976. Publisher: IOP Publishing.

[172] R. Sjökvist, D. Jacobsson, M. Tornberg, R. Wallenberg, E. D. Leshchenko, J. Johansson, and K. A. Dick, "Compositional Correlation between the Nanoparticle and the Growing Au-Assisted InxGa1–xAs Nanowire," *J. Phys. Chem. Lett.*, vol. 12, pp. 7590–7595, Aug. 2021. Publisher: American Chemical Society.

[173] S. Glasstone, K. J. Laidler, and H. Eyring, *The theory of rate processes : the kinetics of chemical reactions, viscosity, diffusion and electrochemical phenomena*. International Chemical Series, New York NY: McGraw-Hill, 1941.

[174] A. Porte, *Détermination des paramètres qui régissent la cinétique et la composition d'un dépôt de GaInAs/InP par la méthode aux hydrures*. These de doctorat, Clermont-Ferrand 2, Jan. 1988.

[175] E. Gil, *Réalisation par la méthode aux hydrures et étude de puits quantiques contraints* $Ga_xIn_{1-x}As/InP$. These de doctorat, Clermont-Ferrand 2, Jan. 1992.

[176] A. S. Ameruddin, H. A. Fonseka, P. Caroff, J. Wong-Leung, R. L. O. h. Veld, J. L. Boland, M. B. Johnston, H. H. Tan, and C. Jagadish, "InxGa1-xAs nanowires with uniform composition, pure wurtzite crystal phase and taper-free morphology," *Nanotechnology*, vol. 26, p. 205604, Apr. 2015. Publisher: IOP Publishing.

[177] P. K. Mohseni, A. Behnam, J. D. Wood, C. D. English, J. W. Lyding, E. Pop, and X. Li, "InxGa1–xAs Nanowire Growth on Graphene: van der Waals Epitaxy Induced Phase Segregation," *Nano Lett.*, vol. 13, pp. 1153–1161, Mar. 2013. Publisher: American Chemical Society.